Continuous Long Term Observations of Accreting Pulsars

Thesis by
Danny Towsian Koh

In Partial Fulfillment of the Requirements
for the Degree of
Doctor of Philosophy

California Institute of Technology
Pasadena, California
1998
(Submitted July 11, 1997)

Acknowledgements

I would like to express my sincere thanks and appreciation to Tom Prince for being an outstanding advisor. Aside from providing invaluable guidance on my thesis research, his boundless enthusiasm for science is absolutely contagious and has never failed to refresh and invigorate me in times of adversity. I have always been amazed by his ability to simultaneously tackle a truly mind-boggling array of research projects, spanning not only a wide range of the electromagnetic spectrum, but also involving novel tools from diverse technological frontiers. He will undoubtedly continue to be a source of inspiration even after my departure from Caltech.

Next, I would like to thank the many outstanding colleagues whom I had the good fortune of working with on the BATSE pulsar project. Special mention goes to Lars Bildsten, Deepto Chakrabarty, Rob Nelson and Brian Vaughan, all of whom have never hesitated to offer assistance and advice on the countless occasions when I was overwhelmed – whether it was getting stuck on a research problem, ignorance about how to prepare a talk or proposal, or simply feeling lost. Without them, this thesis could very well have been nothing more than a figment of my imagination.

Special thanks go out to the many members of the Space Radiation Laboratory (SRL) who have helped make my career at Caltech such an exciting, stimulating and rewarding experience. Without the fun–filled interaction I had with them, life at Caltech would have been much less bearable.

Last, but not least, I would like to thank my parents for the love, emotional and financial support which they have selflessly showered upon me over all these years.

Continuous Long Term Observations of Accreting Binary Pulsars

Danny T. Koh

California Institute of Technology

Abstract

The all–sky monitoring ability of the BATSE instrument on the *GRO* has enabled the first uniform, continuous and long term observations of the torque and fluxes of many known accreting pulsars. In the first part of this thesis, I describe the capabilities of BATSE for detecting hard X-rays, the techniques developed to perform timing and flux measurements, and the steps involved in reducing the raw data sets to a standardized database of data products for each accreting pulsar monitored by BATSE.

In the second part of this thesis, I describe several studies performed with this database. The first is a broad overview of all the accreting pulsars monitored by BATSE. For each source, I display the frequency and pulsed flux histories from $\approx$ five years of BATSE observations, and provide a brief summary of the BATSE findings.

I then focus on the wind-fed accreting pulsar GX 301–2. The most striking features in the pulsar frequency history are two steady and rapid spin-up episodes, with $\dot{\nu} \approx$ (3-5) $\times 10^{-12}$ Hz s^{-1}, each lasting for about 30 days. They probably represent the formation of transient accretion disks in this wind-fed pulsar. Except for these spin-up episodes, there are virtually no net changes in the neutron star spin frequency on long time scales. We suggest that the long-term spin-up trend observed since 1984 ($\dot{\nu} \approx 2 \times 10^{-13}$ Hz s^{-1}) may be due entirely to brief ($\approx$ 20 d) spin-up episodes similar to those we have discovered.

Next, I highlight the most significant trends revealed by the BATSE observations and discuss their implications for our current understanding of the spin–evolution and torque–luminosity relations in accreting pulsars. Alternating episodes of steady spin–up and spin–down were found to be a surprisingly common characteristic of many persistent sources. Pulsed flux and accretion torque are strongly correlated in outbursts of transient accreting pulsars, but uncorrelated, or even anticorrelated, in persistent sources. I describe the various competing models that currently exist and critically assess each model within the context of the BATSE observations.

Finally, I describe how BATSE observations of the recurrence rate of transient systems can be used to infer the galactic population of high–mass Be–transient systems.

Thesis supervisor: Thomas A. Prince, Professor of Physics

Contents

Acknowledgments iii

Abstract iv

Contents v

List of Figures ix

List of Tables xii

1 Accretion Powered Pulsars and BATSE 1

1.1 Introduction 1

1.2 Observed Characteristics 2

1.3 Spin–Evolution of Accreting Pulsars 6

1.4 The Role of BATSE 10

1.5 Thesis Roadmap 11

2 The Compton Gamma–Ray Observatory 13

2.1 BATSE – The Burst and Transient Source Experiment 14

2.1.1 BATSE LAD Response 16

3 BATSE Data Analysis 21

3.1 Introduction 21

3.2 Frequency Determination 21

3.3 Signal Estimation 23

3.3.1 Rigorous Statistical Approach for Single Harmonic Signal 23

3.3.2 Template Fitting Method for Multiple Harmonic Signals 24

3.4 Flux Determination 26
3.5 Background Subtraction 27
3.6 Post–Background Subtraction Steps 30
3.7 The BATSE Pulsed Source Catalog 33

4 BATSE Observations of Individual Sources 36
4.1 Introduction 36
4.2 Low-Mass Systems 44
4.3 High-Mass Supergiant Systems 50
4.4 High-Mass Transient Systems 57

5 Rapid Spin–Up Episodes in the Wind–Fed Accreting Pulsar GX 301–2 72
5.1 Introduction 72
5.2 BATSE Observations and Frequency Measurements 73
5.2.1 Measuring the Neutron Star Orbit 76
5.2.2 The Neutron Star Spin Frequency History 80
5.2.3 Hard X-Ray Spectrum and Flux Measurements 81
5.3 Inferences about the Optical Companion 85
5.3.1 Constraints on the Mass and Radius of the Optical Companion . . . 86
5.3.2 The Stellar Wind 89
5.4 Mass Transfer and Accretion onto the Neutron Star 91
5.4.1 The Two Rapid Spin-Up Episodes 91
5.4.2 Accretion from the Companion's Wind 93
5.5 Conclusions 95

6 Spin Evolution of Accretion Powered Pulsars 97
6.1 Introduction 97
6.2 Torque Switching in Persistent Sources 98
6.2.1 Prograde Accretion Disk Interacting with Pulsar Magnetosphere . . 101
6.2.2 Transitions Between Standard Keplerian disks and sub–Keplerian Advection–dominated Flow (ADAF) 108
6.2.3 Alternating Prograde and Retrograde Disks 109
6.2.4 Discussion 117
6.2.5 Observational Tests and Future Directions 121

6.3 Accretion Disks in non Roche–Lobe Overfilling Systems 123

7 Torque Luminosity Relations in Accreting Pulsars 124

7.1 Introduction 124

7.2 Strengths and Weaknesses of BATSE 125

7.3 Transient Sources 127

7.4 Persistent Sources 130

7.4.1 4U 1626–67 and GX 1+4 130

7.4.2 Cen X–3 and OAO 1657–415 131

7.5 Overall Assessment 139

7.6 Future Directions 140

8 The Population of Be Transients 142

8.1 Introduction 142

8.2 Motivation 143

8.3 Be–transient Population Estimation 144

9 Summary 149

APPENDICES 151

A GX 301–2 Time Delay Measurements Using the Cross Spectrum Technique 151

B Details of BATSE Data Analysis Techniques 155

B.1 Frequency Estimation 155

B.1.1 Frequency Estimation using Power Spectra 155

B.1.2 Frequency Estimation using Epoch Folding 157

B.1.3 Frequency Estimation from Fits to Pulse-Phase Measurements . . . 158

B.2 Pulsed Flux Estimation 158

B.2.1 What is Pulsed Flux and Pulsed Fraction? 158

B.2.2 Peak-to-Peak Pulsed Spectra and Flux 159

B.2.3 Daily RMS Flux 160

REFERENCES **163**

References 163

List of Figures

1.1 The Corbet diagram 7
1.2 The Galactic distribution of accreting pulsars. 8

2.1 The *Compton Gamma Ray Observatory.* 14
2.2 A BATSE detector module. 15
2.3 LAD CONT channel boundaries. 18
2.4 The normal incidence effective area of a BATSE LAD as a function of incident photon energy. 19
2.5 Angular response of a BATSE LAD to incident photons of different energies. 20

3.1 Typical power spectrum of BATSE LAD background before and after background subtraction. 29
3.2 1–day BATSE sensitivity as a function of CONT channel. 32
3.3 The 1-day BATSE 5σ detection threshold for CONT channels 1 to 4 summed 34
3.4 Evolution of CONT time series over the course of analysis 35

4.1 Long–term frequency history for all pulsars detected by BATSE that were previously known. 39
4.2 Pulse profiles of accreting pulsars from BATSE. 43
4.3 Her X-1 frequency and pulsed flux measurements from BATSE. 45
4.4 4U 1626-67 frequency and pulsed flux measurements from BATSE. 46
4.5 GX 1+4 frequency and pulsed flux measurements from BATSE. 47
4.6 GRO J1744-28 frequency and pulsed flux measurements from BATSE. . . . 48
4.7 Cen X–3 frequency and pulsed flux measurements from BATSE. 50
4.8 OAO 1657–415 frequency and pulsed-flux measurements from BATSE. . . . 52

4.9 Vela X-1 spin frequency and pulsed flux measurements from BATSE. 53
4.10 4U 1538-52 spin frequency and pulsed flux measurements from BATSE. . . 54
4.11 GX301–2 frequency and pulsed flux measurements from BATSE. 55
4.12 Outburst times for all transient accreting pulsars observed by BATSE. . . . 57
4.13 4U 0115+634 frequency and flux measurements from BATSE. 58
4.14 Measurements of the 4U 0115+63 periastron epoch. 59
4.15 GRO J1750-27 spin frequency and pulsed flux measurements from BATSE. 60
4.16 GS 0834-430 frequency and flux measurements from BATSE. 61
4.17 2S 1417–624 frequency and pulsed flux measurements from BATSE. 63
4.18 GRO J1948+32 frequency and pulsed flux measurements from BATSE. . . 64
4.19 EXO 2030+375 frequency and flux measurements from BATSE. 65
4.20 GRO J1008-57 frequency and flux measurements from BATSE. 66
4.21 A0535+262 frequency and pulsed flux measurements from BATSE. 67
4.22 Pulse Profile as a function of pulsed flux and energy for A0535+26. 68
4.23 GRO J2058+42 frequency and flux measurements from BATSE. 69
4.24 4U 1145-619 frequency and pulsed flux measurements from BATSE. 70
4.25 A 1118–616 frequency and pulsed flux measurements from BATSE. 71

5.1 Long–term pulse frequency history of GX 301–2 74
5.2 Pulse profiles as a function of energy for GX 301–2. 77
5.3 Orbit–induced frequency derivative in GX 301–2. 79
5.4 Time delays for the pulse arrival times as a function of the orbital phase of GX 301–2. 80
5.5 The intrinsic neutron star spin frequency in GX 301–2 from MJD 48370-49612. 81
5.6 The phase and time-averaged pulsed photon spectrum of GX 301–2 84
5.7 The 20-55 keV pulsed flux for GX 301–2 from MJD 48388-49612. 85
5.8 The 20-55 keV pulsed flux for GX 301–2 from MJD 48388-49612 as a function of orbital phase. 86
5.9 Mass-radius constraints to the optical companion of GX 301–2, Wray 977. . 88
5.10 Frequency, frequency derivative and pulsed flux during the spin-up episodes for GX 301–2. 90
5.11 A comparison of the GX 301–2 folded flux history and the fit obtained using a circumstellar disk model. 92

6.1 Frequency histories of Cen X–3. 99
6.2 Frequency histories of OAO 1657–415. 100
6.3 Histogram of frequency derivatives for Cen X–3 102
6.4 Distribution of durations of spin–up and spin–down episodes for Cen X–3 . 103
6.5 Histogram of frequency derivatives for OAO 1657–415 104
6.6 Distribution of durations of spin–up and spin–down episodes for OAO 1657–415 105
6.7 Anti–correlation between torque switching time scale and neutron star orbital velocity. 120

7.1 Observed relationships between fluxes and frequency derivatives for A 0535+262 and GRO J1744–28. 128
7.2 Correlation between the BATSE pulsed 20–50 keV flux and the *RXTE*/ASM bolometric 2–10 keV count rate for Cen X–3. 132
7.3 Absence of correlation between the BATSE pulsed 20–50 keV flux and the *RXTE*/ASM bolometric 2–10 keV count rate for OAO 1657–415. 133
7.4 Absence of correlation between pulsed flux and bolometric count rate with frequency derivative in Cen X–3 134
7.5 Absence of correlation between pulsed flux and frequency derivative in OAO 1657–415. 135
7.6 Absence of correlation between pulsed flux and frequency derivative averaged across individual spin–up/spin–down episodes for Cen X–3 137
7.7 Absence of correlation between pulsed flux and frequency derivative averaged across individual spin–up/spin–down episodes for OAO 1657–415 138

8.1 Galactic location of BATSE-detected giant outbursts from Be transients. . . 146
8.2 Cumulative b and ℓ distributions of Be–transients systems 147

A.1 The chi-square histogram for the GX 301–2 time delay measurements performed using the cross spectrum technique 154

List of Tables

1.1 Known Accretion-Powered Pulsars (as of Feb. 1997) 3
1.2 Orbital Parameters of Accretion-Powered Pulsar Systems 4

2.1 Energy Channels in BATSE DISCLA and CONT Data 17

3.1 Conversion to Pulsed Flux from Counts 31

4.1 Spectral Parameters Measured with BATSE 40

5.1 GX 301–2 Orbital Parameters 78
5.2 GX 301–2 Spectral Parameters 83

6.1 Characteristics of Torque Reversals 106
6.2 Inferred Properties of OAO 1657–415 113
6.3 Key Properties of Selected Accreting Pulsars 118

7.1 Torque Luminosity Index for Transient Sources 129

Chapter 1

Accretion Powered Pulsars and BATSE

1.1 Introduction

An accretion powered pulsar consists of a highly magnetized ($B \sim 10^{12}$ G) neutron star accreting matter from a stellar companion. The strong magnetic field results in anisotropic channeling of stellar material to the poles of the neutron star, resulting in beamed X–ray emission. If the neutron star rotational and magnetic axes are misaligned, an Earth–based observer will only detect emission when the beam intersects the line of sight, thus giving rise to the pulsing phenomenon.

As described in greater detail in section 1.3, the accretion of matter onto the neutron star results in the transfer of angular momentum, which changes the spin period of the neutron star. Measurements of such torques provide unique insights into the nature of the accretion process and also enable tests of different accretion models. Accreting pulsars are thus excellent laboratories for probing accretion physics. In fact, accreting pulsars are the only objects where torque measurements have been made repeatedly. Corresponding measurements for accreting magnetic white dwarfs require $\approx$ decade–long baselines due to the much larger moment of inertia.

The first observation of an accreting pulsar was made by *UHURU* in 1971 when it discovered 4.8 s X–ray pulsations from Cen X–3 (Giacconi et al. 1971; Schreier et al. 1972). This promptly motivated theoretical interpretation of these pulsations as sketched above (Pringle & Rees 1972; Davidson & Ostriker 1973; Lamb, Pethick, & Pines 1973). As of this writing, there are 44 known accreting pulsars in our Galaxy and Magellanic clouds, spanning a range of 0.069 s to 1413 s in spin period. Table 1.1 shows a list of all these pulsars while

Table 1.2 details the presently known orbital parameters. Recent comprehensive reviews of accreting pulsars can be found in Nagase (1989), White, Nagase & Parmar (1995) and Bildsten et al.(1997). The traditional picture of accreting pulsars painted by the first two references have been significantly revised by the last one, upon which the bulk of this thesis is based. In the next two sections, I briefly describe the properties of accreting pulsars, mainly concentrating on the traditional picture. Where appropriate, I will also briefly highlight the changes to this picture brought about by BATSE observations.

1.2 Observed Characteristics

Emission from accreting pulsars results from the release of gravitational potential energy from matter captured by the neutron star, giving rise to a luminosity of

$$L_{\rm acc} = \frac{GM_{\rm x}\dot{M}_{\rm acc}}{R_{\rm x}} = 10^{37}\,{\rm erg\ s^{-1}} \left(\frac{M_{\rm x}}{1.4\,M_\odot}\right) \left(\frac{\dot{M}_{\rm acc}}{10^{-10}\,M_\odot\ {\rm yr^{-1}}}\right) \left(\frac{R_{\rm x}}{10\ {\rm km}}\right)^{-1}, \qquad (1.1)$$

where $L_{\rm acc}$ is the accretion luminosity, $M_{\rm x}$ and $R_{\rm x}$ are the mass and radius of the neutron star, and $\dot{M}_{\rm acc}$ is the mass accretion rate. When $L_{\rm acc} \gtrsim 10^{36}$ ergs s^{-1}, a radiative shock forms at the neutron star surface (Basko & Sunyaev 1976; Wang & Frank 1981), yielding a shock temperature of $T_{\rm sh} \approx \frac{3}{8}\frac{GM_{\rm x}m_p}{kR_{\rm x}} \sim 50$ MeV. However, such high energy photons will only be observed if the post–shock gas is optically thin, which is usually not the case. For an optically thick accretion flow, the emitted radiation attains thermal equilibrium with the accreted material, resulting in black–body emission characterized by an emission temperature $T_{\rm rad} \gtrsim (L_{\rm acc}/4\pi R_{\rm x}^2\sigma)^{1/4} \sim 1$ keV for the observed range of $L_{\rm acc} \sim 10^{36}$–10^{37} ergs s^{-1} (see Nagase (1989)). We hence expect most of the emission to be in the $\sim$ few keV range. Indeed, the observed spectra in known accreting pulsars can generally be characterized by a flat power–law with index α of 0–1 up to a cut–off energy E_c, after which it falls off exponentially with an e–folding energy E_f. Both E_c and E_f are $\approx$ 10–20 keV (White, Swank, & Holt 1983).

We note in equation 1.1 that as $\dot{M}_{\rm acc}$ is increased, radiation pressure on the in-falling material becomes increasingly important and eventually inhibits accretion. Assuming spherical accretion of pure hydrogen, the Eddington luminosity, $L_{\rm Edd}$, at which radiation pressure balances gravitational attraction is given by

$$L_{\rm Edd} = \frac{4\pi c G M_{\rm x} m_p}{\sigma_{\rm T}} = 1.8 \times 10^{38}\ {\rm erg\ s^{-1}} \left(\frac{M_{\rm x}}{1.4\ M_\odot}\right) \qquad (1.2)$$

Table 1.1
Known Accretion-Powered Pulsars (as of Feb. 1997)

	System[a]	l_{II}	b_{II}	P_{spin} (s)	P_{orb}[b] (d)	Companion (MK Type)	References[d]
	Low-mass binaries						
◉	GRO J1744–28	0.0	+0.3	0.467	11.8		[1]
•	Her X-1	58.2	+37.5	1.24	1.70	HZ Her (A9-B)	[2],[3]
•	4U 1626–67	321.8	-13.1	7.66	0.0289	KZ TrA (low-mass dwarf)	[4],[5]
•	4U 1728–247 (GX 1+4)	1.9	+4.8	120		V2116 Oph (M6III)	[6],[7]
	High-mass supergiant and giant systems						
	SMC X-1	300.4	-43.6	0.717	3.89	Sk160 (B0 I)	[8]
•	Cen X-3	292.1	+0.3	4.82	2.09	V779 Cen (O6–8f)	[9],[10]
	RX J0648.1–4419	253.7	-19.1	13.2	1.54	HD 49798 (O6p)	[11]
	LMC X-4	276.3	-32.5	13.5	1.41	Sk-Ph (O7 III-V)	[12]
•	OAO 1657–415	344.4	+0.3	37.7	10.4	(B0–6Iab)	[13]
•	Vela X-1	263.1	+3.9	283	8.96	HD77581 (B0.5Ib)	[14]
	1E 1145–614	295.5	-0.0	297	5.65	V830 Cen (B2Iae)	[15]
	4U 1907+09	43.7	+0.5	438	8.38	(B I)	[16]
•	4U 1538–52	327.4	+2.1	530	3.73	QV Nor (B0Iab)	[17],[18]
•	GX 301–2	300.1	-0.0	681	41.5	Wray 977 (B1.5Ia)	[19],[20]
	Transient Be-binary systems						
	A 0538–67	276.9	-32.2	0.069	16.7	(B2 III-IVe)	[21]
•	4U 0115+63	125.9	+1.0	3.61	24.3	V635 Cas (Be)	[22],[23]
	V 0332+53	146.1	-2.2	4.37	34.2	BQ Cam (Be)	[24]
•	2S 1417–624	313.0	-1.6	17.6	42.1	(OBe)	[25]
•	EXO 2030+375	77.2	-1.3	41.7	46.0	(Be)	[26],[27]
◉	GRO J1008–57	283.0	-1.8	93.5	$\approx$ 248	(Be)	[28],[29]
•	A 0535+26	181.4	-2.6	105	110	HDE245770 (O9.7IIe)	[30]
	GX 304–1	302.1	+1.2	272	133 (?)	V 850 Cen (B2Vne)	[31]
•	4U 1145–619	295.6	-0.2	292	187	Hen 715 (B1Vne)	[32]
•	A 1118–616	292.5	-0.9	405		He3-640 (O9.5 III-Ve)	[33]
	4U 0352+309	163.1	-17.1	835		X Per (O9 III-Ve)	[34]
	RX J0146.9+6121	129.9	-0.5	1413		LSI +61° 235 (B5 IIIe)	[35]
	Persistent systems with an undetermined companion						
	RX J1838.4–0301	28.8	+1.5	5.45			[36]
	1E 1048–593	288.2	-0.5	6.44			[37]
	1E 2259+586	109.1	-1.0	6.98			[38]
	RX J0720.4-3125	244.2	-8.2	8.38			[39]
	4U 0142+614	129.4	-0.4	8.69			[40]
	Transient systems with an undetermined companion						
•	RX J0059.2–7138[c]	302.1	-45.5	2.76			[41]
	RX J0502.9–6626	277.0	-35.5	4.06			[42]
◉	GRO J1750–27	2.4	+0.5	4.45	29.8		[43]
	2E 0050.1–7247	302.9	-44.6	8.9			[11]
	2S 1553–54	327.9	-0.9	9.26	30.6		[44]
•	GS 0834–430	262.0	-1.5	12.3	106		[45],[46]
◉	GRO J1948+32	64.9	1.8	18.7			[47]
	GS 1843+00	33.1	+1.7	29.5			[48]
	GS 2138+56 (Cep X-4?)	99.0	+3.3	66.2			[49]
	GS 1843–024	30.2	-0.0	94.8			[50]
	Sct X-1	24.5	-0.2	111			[51]
◉	GRO J2058+42	83.6	-2.7	198			[52],[53]
	GPS 1722–363	351.5	-0.6	414			[54]

[a]Sources marked • have been detected with BATSE, sources marked with ◉ were discovered by BATSE.

[b]In those cases where no orbital parameters are given in Table 1.2, the orbital period has been inferred from pulse timing and/or outburst recurrence times and/or optical photometry.

[c]This source was detected by both BATSE and ROSAT on MJD 49120. It has not been studied with BATSE and is not discussed in this paper.

[d]REFERENCES: [1] Finger et al.1996; [2] Deeter et al.1991; [3] Wilson et al.1994a; [4] Chakrabarty et al.1997a; [5] Middleditch et al.1981; [6] Chakrabarty et al.1997b; [7] Makishima et al.1988; [8] Levine et al.1993; [9] Finger et al.1993; [10] Nagase et al.1992; [11] Israel et al.1995; [12] Safi-Harb, Ogelman & Dennerl 1996; [13] Chakrabarty et al.1993; [14] Deeter et al.1987; [15] Ilovaisky, Chevalier & Motch 1982; [16] Makishima et al.1984; [17] Rubin et al.1994; [18] Corbet et al.1993; [19] Koh et al.1997; [20] Sato et al.1986; [21] Skinner 1981; [22] Cominsky et al.1994; [23] Rappaport et al.1978; [24] Stella et al.1985; [25] Finger, Wilson & Chakrabarty 1996; [26] Stollberg et al.1994; [27] Parmar et al.1989; [28] Wilson et al.1994b; [29] Coe et al.1994a; [30] Finger, Wilson & Harmon 1996; [31] Priedhorsky & Terrell 1983; [32] Cook & Warwick 1987; [33] Ives, Sanford & Bell-Burnell 1975; [34] Murakami et al.1987; [35] Hellier 1994; [36] Schwentker 1994; [37] Seward, Charles & Smale 1986; [38] Iwasawa, Koyama & Halpern 1992; [39] Haberl et al.1996; [40] Israel, Mereghetti, & Stella 1994; [41] Hughes 1994; [42] Schmidtke et al.1995; [43] Scott et al., in preparation; [44] Kelley, Rappaport and Ayasli 1983; [45] Wilson et al.1997; [46] Aoki et al.1992; [47] Chakrabarty et al.1995; [48] Koyama et al.1990a; [49] Koyama et al.1991a; [50] Koyama et al.1990b; [51] Koyama et al.1991b; [52] Wilson, Strohmayer & Chakrabarty 1996; [53] Wilson et al.1995a; [54] Tawara et al.1989.

Table 1.2
Orbital Parameters of Accretion-Powered Pulsar Systems[a]

Source Name	Orbital epoch [MJD]	$P_{\rm orb}$ [d]	$a_{\rm x} \sin i$ [lt-sec]	e	ω [°]	$f_{\rm x}(M)$ [$M_\odot$]	Refs.[b]
Low-mass system							
GRO J1744-28	50079.1552(18)[c]	11.8337(13)	2.6324(12)	$< 1.1 \times 10^{-3}$ (90%)	···	$1.3638(17) \times 10^{-4}$	[1]
Her X-1	48799.61235(1)[c]	1.700167412(40)[d]	13.1853(2)	$< 1.3 \times 10^{-4}$ (3σ)	···	0.85145(4)	[2], [3]
High-mass supergiant systems							
LMC X-4	47741.9904(2)[c]	1.40841(2)[e]	26.31(3)	0.006(2)	···	9.86(3)	[4]
Cen X-3	48561.656702(71)[c]	2.08706533(49)[l]	39.627(18)	$< 1.6 \times 10^{-3}$ (90%)	···	15.343(21)	[5]
4U 1538-52	45625.719(18)[c]	3.72839(2)[f]	53.5(14)	< 0.058 (95%)	···	11.8(9)	[6]
SMC X-1	47740.35906(3) [c]	3.892116(1)[h]	53.4876(4)	$< 4 \times 10^{-5}$ (2σ)	···	10.8481(2)	[7]
4U 1907+09	45578.75(35)[c]	8.3745(42)	80.2(72)	$0.16^{+0.14}_{-0.11}$	330^{+18}_{-56}	7.9(21)	[8]
Vela X-1	48895.2186(12)[c]	8.964368(40)	113.89(13)	0.0898(12)	152.59(92)	19.74(07)	[9]
OAO 1657-415	48515.99(5)[c]	10.44809(30)[g]	106.0(5)	0.104(5)	93(5)	11.7(2)	[10], [11]
GX 301-2	48802.79(12)[i]	41.498(2)	368.3(37)	0.462(14)	310.4(14)	31.1(9)	[12]
Be-binary systems							
4U 0115+63 [k]	49279.2677(34)[i]	24.317037(62)	140.13(8)	0.3402(2)	47.66(9)	5.00(1)	[11], [13], [14]
V 0332+53	45651.5(10)[i]	34.25(10)	48(4)	0.31(3)	313(10)	0.10(2)	[15]
2S 1417-624	49713.62(5)[i]	42.12(3)	188(2)	0.446(2)	300.3(6)	3.9(1)	[16]
EXO 2030+375	48936.5(3)[i]	46.01(2)	264(21)	0.37(2)	223.4(39)	9.1(22)	[17]
A 0535+26	49058.7(6)[i]	110.3(3)	267(13)	0.47(2)	130(5)	1.64(23)	[18]
System with undetermined companion							
2S 1553-54	42596.67(3)[c]	30.2(1)	162.7(10)	< 0.09 (2σ)	···	5.0(1)	[19]
GRO J1750-27	49931.02(1)[i]	29.817(9)	101.8(5)	0.360(2)	206.3(3)	1.24(2)	[20]
GS 0834-430	48809.6(15)[j]	105.8(4)	128^{+47}_{-38}	$0.12^{+0.05}_{-0.04}$	140^{+35}_{-53}	$0.20^{+0.30}_{-0.10}$	[21]

[a] All confidence intervals are quoted at the 1σ level, except where noted. Epochs are quoted in TDB at the solar system barycenter. $P_{\rm orb}$=orbital period, $a_{\rm x} \sin i$=projected semimajor axis, e=eccentricity, ω=longitude of periastron, and $f_{\rm x}(M)$=X-ray mass function.

[b] REFERENCES: [1] Finger et al. 1996; [2] Deeter et al. 1991; [3] Wilson et al. 1994a; [4] Levine et al. 1991; [5] Finger et al. 1993; [6] Rubin et al. 1997; [7] Levine et al. 1993; [8] Cook & Page 1987; [9] Finger et al. in preparation; [10] Chakrabarty et al. 1993; [11] §4, this work; [12] Koh et al. 1997; [13] Rappaport et al. 1978; [14] Cominsky et al. 1994; [15] Stella et al. 1985; [16] Finger, Wilson & Chakrabarty 1996; [17] Stollberg et al., in preparation; [18] Finger et al. 1994a; [19] Kelley, Rappaport & Ayasli 1983; [20] Scott et al. 1997; [21] Wilson et al. 1997; [22] Nagase et al. 1992.

[c] $T_{\pi/2}$ = epoch of 90° mean orbital longitude.

[d] Orbital period for specified orbital epoch, computed using $\dot{P}_{\rm orb} = (-6.16 \pm 0.74) \times 10^{-11}$ d d^{-1} from [2].

[e] Orbital period for specified orbital epoch, computed using $\dot{P}_{\rm orb} = (4.2 \pm 3.1) \times 10^{-9}$ d d^{-1} from [4].

[f] Orbital period derivative constrained to -4.0×10^{-8} d d^{-1} $< \dot{P}_{\rm orb} < 2.1 \times 10^{-8}$ d d^{-1} (95% confidence) by [6].

[g] Revised orbital period from [11].

[h] Orbital period for specified orbital epoch, computed using $\dot{P}_{\rm orb} = (-3.58 \pm 0.02) \times 10^{-8}$ d d^{-1} from [7].

[i] T_0 = epoch of periastron passage.

[j] $T_2 = T_0 - \omega P_{orb}(4\pi)^{-1}$ where T_0 = epoch of periastron passage.

[k] $a_{\rm x} \sin i$ and e are from [13], and were held fixed by [14]. ω is from [14]. The epoch and $P_{\rm orb}$ are from [11].

[l] $\dot{P}_{\rm orb} = (-9.93 \pm 0.02) \times 10^{-9}$ d d^{-1} reported by [22].

where m_p is the proton mass and $\sigma_{\rm T}$ is the Thomson scattering cross-section. The presence of heavier elements in the accretion stream, coupled with non–spherical accretion, changes this estimate of $L_{\rm Edd}$ somewhat, although it remains a good benchmark.

The companion type of an accreting pulsar determines the mass transfer mechanism and the resultant evolution of the binary system. Hence, accreting pulsars can be broadly categorized into low–mass systems, for which the companion mass $M_{\rm c} \lesssim 2.5 M_{\odot}$ and high–mass systems, for which $M_{\rm c} \gtrsim 6 M_{\odot}$ (Shore, Livio, & van den Heuvel 1994). The high–mass systems have traditionally been further sub-divided into underfilled Roche Lobe supergiants, Roche Lobe filling supergiants and Be–transients. The main characteristics of these different systems are summarized as follows:

- **Low Mass systems**: The companion is of spectral type later than A, and can even be a white dwarf in some evolved systems. The absence of strong stellar winds led to the traditional belief that mass transfer could only occur through Roche–Lobe overflow. However, we show in Chapter 6 some of these systems may not overflow their Roche Lobes and that an X–ray excited thermal wind could be a more plausible mode of mass transfer. These systems typically have low luminosities of $L_{\rm acc} \lesssim 10^{35}$erg s^{-1}.

- **High–Mass underfilled Roche Lobe Supergiants**: The typical companion is an O or B star which underfills its Roche Lobe and which has substantial stellar wind with terminal velocity up to 2000 km s^{-1} which results in mass loss rates of $\sim 10^{-10}$–$10^{-6} M_{\odot}$ yr^{-1}. The mass transfer to the neutron star occurs through wind capture. The luminosities of these systems are typically $L_{\rm acc} \sim 10^{35} - 10^{37}$erg s^{-1}.

- **High–Mass Roche Lobe Filling Supergiants**: The typical companion is an O or B star. The *apparent* secular spin–up trend observed by pre–BATSE instruments, coupled with the typically high luminosities of $L_{\rm acc} \gtrsim 10^{37}$erg s^{-1}, led to the traditional belief that the companion in each of these systems overflows its Roche Lobe and that mass transfer to the neutron star is mediated by an accretion disk. However, we show in Chapter 6 that the apparent secular spin–up trend is due to sparse sampling of pre–BATSE instruments and that an X–ray excited thermal wind could be a more plausible mode of mass transfer in some of these systems.

- **High–Mass Be–transients**: The typical companion is a rapidly rotating Be–star which underfills its Roche Lobe and has a dense circumstellar disk along its equatorial

plane. These systems are generally quiescent and non-detectable except during outbursts, when their luminosities increase by up to several orders of magnitude for days to weeks, briefly making them the brightest X–ray sources in the sky. The neutron star in these systems are generally eccentric and the outbursts often occur close to periastron passage.

Corbet (1986) first pointed out that the three types of high–mass systems occupy distinct regions in the $P_{\rm spin}$–$P_{\rm orb}$ (spin period vs. orbital period) diagram. Figure 1.1 clearly shows that underfilled Roche Lobe systems (squares) are characterized by long spin periods of $P_{\rm spin} \sim 100$ s and orbital periods of $P_{\rm orb} \approx 4 - 40$ d, as opposed to those of the Roche Lobe filling systems (asterisks), for which $P_{\rm spin} \lesssim 10$ s and $P_{\rm orb} \lesssim 4$ d. The Be–transients not only span much wider ranges, with $P_{\rm spin} \approx 0.1$–300 s, and $P_{\rm orb} \approx 15$–200 d, but also exhibit a striking correlation between these two quantities. It has been suggested that this correlation arises from the fact that, given identical companion masses and mass loss rates, neutron stars in systems with longer orbital periods are further away from their companions, thus leading to lower mass accretion rates and higher equilibrium periods (see section 1.3). In addition, Waters & van Kerkwijk (1989) argue that selection effects favor the detection of Be systems which are in equilibrium with the slow equatorial wind of the companion. The observed anti–correlation of spin and orbital periods for the Roche-lobe filling supergiants is not understood. As Figure 1.2 shows, most of the high mass systems are found in the Galactic plane, consistent with the short lifetime of the massive companions.

Although this traditional classification scheme can successfully account for many characteristics of accreting pulsars observed by pre–BATSE instruments, we will show in subsequent chapters that BATSE observations blur the distinction between the various classes of accreting pulsars mentioned above.

1.3 Spin–Evolution of Accreting Pulsars

Despite the rather complicated physics which governs the detailed transfer of angular momentum from captured matter to the neutron star, the simple model pioneered by Pringle & Rees (1972) and Rappaport & Joss (1977) provides ample explanation for the gross features of neutron stars and predictive power.

Due to the strong ($\sim 10^{12}$ G) neutron star magnetic field, the accretion flow from the companion becomes disrupted at a distance r_A from the stellar surface, where the

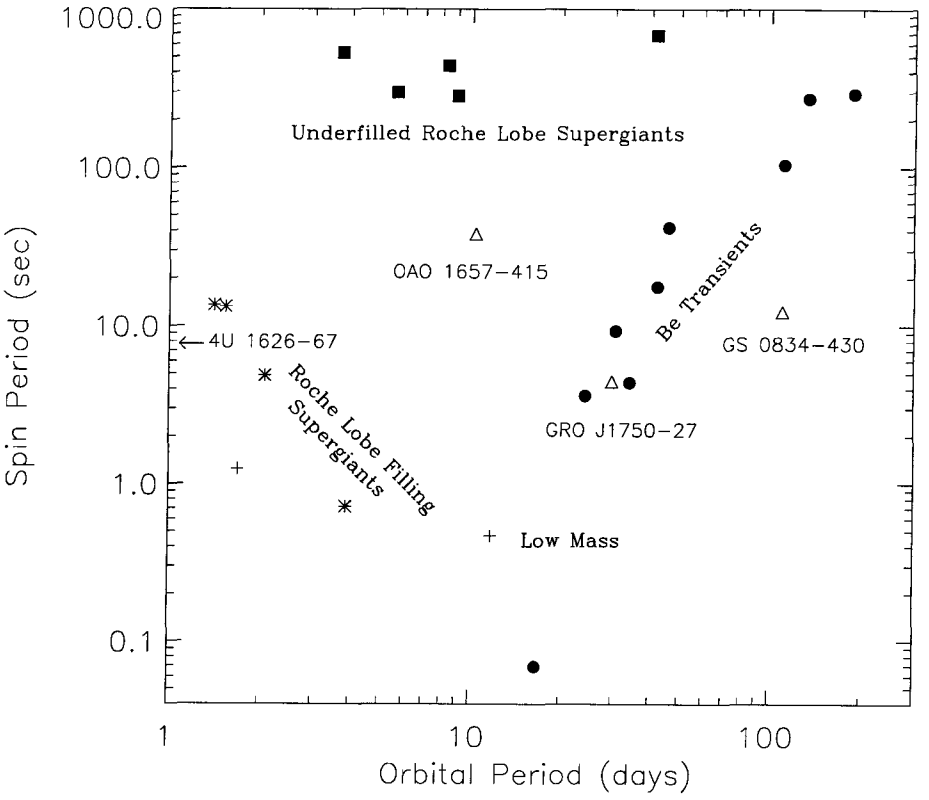

Figure 1.1: The spin period of the accreting neutron stars versus the binary period (the Corbet diagram). The different symbols refer to the type of binary the neutron star resides in. Asterisks are supergiant companions which are Roche-Lobe filling, squares are supergiant companions that underfill their Roche lobe, circles are confirmed Be transient binaries, and crosses are those with low mass ($\lesssim 2M_\odot$) companions (Her X-1, GRO J1744–28, 4U 1626–67). Triangles refer to sources for which there are no optical companions yet identified, though orbits have been measured (GS 0834–430, OAO 1657–415 and GRO J1750–27).

magnetic stress becomes comparable to the ram pressure of the accreting matter. Thus, r_A is given by (Pringle & Rees 1972; Lamb, Pethick, & Pines 1973)

$$\frac{B(r_A)^2}{8\pi} \approx \frac{1}{2}\rho(r_A)v(r_A)^2, \tag{1.3}$$

where ρ is the density of the accreting matter and v its velocity. Assuming a dipolar magnetic field, spherical accretion and free fall velocity of the accreting matter, r_A is given

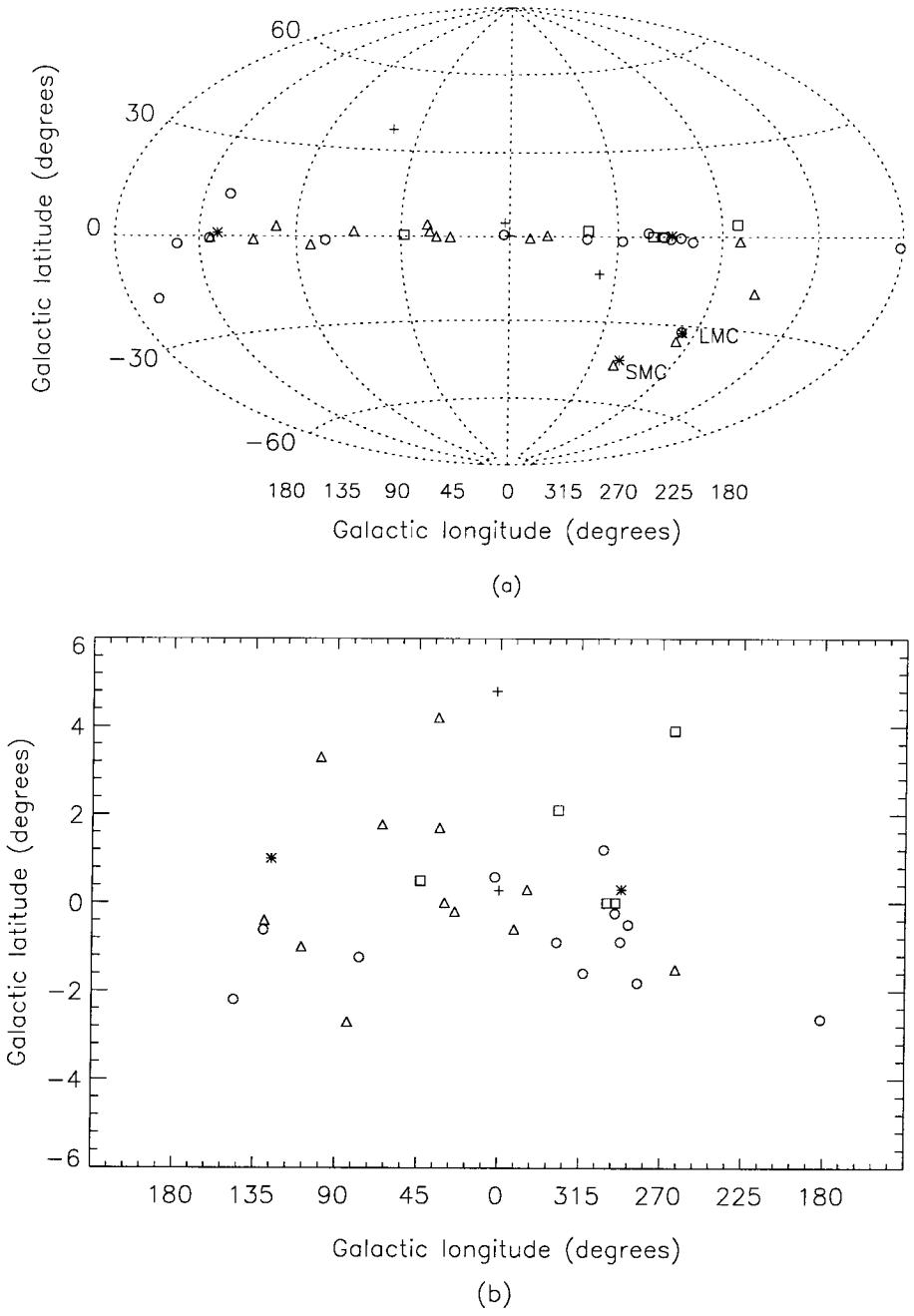

Figure 1.2: The Galactic distribution of accreting pulsars. We plot the known Be transients as open circles, the low-mass objects as pluses, the disk-fed OB supergiants with asterisks and the wind-fed OB supergiants with squares. This contains all pulsars listed in Table 1. Triangles denote sources with unknown companions and orbit. This symbol convention is the same as in Figure 1.1, except here the symbols are not filled.

by

$$r_{\rm A} = \left(\frac{\mu^4}{2GM_{\rm x}\dot{M}^2}\right)^{1/7} \simeq 6.8\times10^8 \text{ cm} \left(\frac{\mu}{10^{30} \text{ G cm}^3}\right)^{4/7} \left(\frac{10^{-10}\ M_\odot \text{ yr}^{-1}}{\dot{M}_{\rm acc}}\right)^{2/7} \left(\frac{1.4M_\odot}{M_{\rm x}}\right)^{1/7} \tag{1.4}$$

where $\dot{M}_{\rm acc}$ is the mass accretion rate and μ and $M_{\rm x}$ are respectively the magnetic moment and mass of the accreting star.

In many situations, the accreting matter possesses too much angular momentum to accrete radially, but first forms an accretion disk in which excess angular momentum is removed through viscous forces. In this case, the distance from the star at which the accretion flow becomes disrupted is modified to $r_{\rm m} = \xi r_{\rm A}$. Estimates for ξ range from 0.52 (Ghosh & Lamb 1979) to ≈ 1 (Arons 1993; Ostriker & Shu 1995; Wang 1996). As long as $r_{\rm m}$ is less than the co–rotation radius, $r_{\rm co} = (GM_{\rm x}P_{\rm spin}^2/4\pi^2)^{1/3}$, at which a Keplerian disk co–rotates with the neutron star, accretion can occur. However, when $\dot{M}_{\rm acc}$ is decreased, $r_{\rm m}$ increases and centrifugal inhibition of accretion occurs when $r_{\rm m} > r_{\rm co}$. In addition, if the material couples to the neutron star magnetic field which tries to enforce co–rotation, the former will be expelled, carrying away angular momentum and resulting in spin–down. This phenomenon is known as the propeller effect (Illarionov & Sunyaev 1975).

Accretion occurs when $r_{\rm m} < r_{\rm co}$. Assuming that the captured matter deposits all its angular momentum at the magnetospheric boundary and that this angular momentum is all transported by the field lines to the star, the latter will experience a spin–up torque of (Pringle & Rees 1972; Rappaport & Joss 1977)

$$N \approx \dot{M}_{\rm acc}\sqrt{GM_{\rm x}r_{\rm m}}, \tag{1.5}$$

and a corresponding spin–up rate of

$$\dot{\nu} = \frac{N}{2\pi I} \simeq 1.6\times10^{-13}\text{s}^{-2} \left(\frac{\dot{M}_{\rm acc}}{10^{-10}M_\odot \text{ yr}^{-1}}\right) \left(\frac{P_{\rm spin}}{\text{s}}\right)^{1/3} \left(\frac{r_{\rm m}}{r_{\rm co}}\right)^{1/2} \tag{1.6}$$

where $I \simeq 0.4M_{\rm x}R_{\rm x}^2$ is the neutron star's moment of inertia (Ravenhall & Pethick 1994). The time scale for spinning up the neutron star is then

$$t_{\rm spin-up} \equiv \frac{\nu}{\dot{\nu}} \simeq 2\times10^5 \text{ yr} \left(\frac{10^{-10}M_\odot \text{ yr}^{-1}}{\dot{M}_{\rm acc}}\right) \left(\frac{1 \text{ s}}{P_{\rm spin}}\right)^{4/3} \left(\frac{r_{\rm co}}{r_{\rm m}}\right)^{1/2}. \tag{1.7}$$

Spin–up cannot continue indefinitely, as the propeller effect kicks in when the neutron star magnetosphere rotates faster than the Keplerian frequency at the inner disk ($r_{\rm m} > r_{\rm co}$).

The spin period at which $r_m = r_{co}$ is the equilibrium spin period

$$P_{\rm spin,eq} \approx 8 \text{ s} \left(\frac{10^{-10} M_\odot \text{ yr}^{-1}}{\langle \dot{M}_{\rm acc} \rangle} \right)^{3/7} \left(\frac{\mu}{10^{30} \text{ G cm}^3} \right)^{6/7} . \quad (1.8)$$

Here $\langle \dot{M}_{\rm acc} \rangle$ is an appropriately averaged mass accretion rate. The significance of the equilibrium spin period is that it is the minimum neutron star spin period at which accretion can still occur.

1.4 The Role of BATSE

Though this simple model satisfactorily accounted for the sparsely sampled pre–1980 data on accreting pulsars, its inadequacy became apparent as new sources were discovered and frequency histories of known ones extended. For example, the propeller effect predicts that accretion cannot take place when a source undergoes spin–down, contrary to observations. Also, Cen X–3 and Her X–1 appeared to be spinning–up with a time scale much longer than that predicted by Equation 1.7. New models (Ghosh & Lamb 1979; Anzer & Borner 1980; Arons et al. 1984) were developed to resolve problems such as how accretion and spin-down can occur simultaneously. However, the older instruments are typically pointed ones which can only observe each source at $\approx$ yearly intervals, a time sampling much too sparse for tracking the frequency or luminosity changes required to probe the validity of these models. Although all–sky coverage was provided by scanning wide–field cameras on board some of the instruments, these typically suffer from poor sensitivity and time resolution. In addition, the different instruments used results in non-uniformity of the data sets which complicates long–term studies of these sources.

The launch of *GRO* in April 1991 addressed many of these problems and ushered in a new revolution in the study of accreting pulsars. The Burst and Transient Source Experiment (BATSE), one of the four instruments on board *GRO*, consists of eight identical detectors each situated on one corner of the spacecraft, thus providing uniform all–sky coverage. This, combined with the high time resolution of 1.024 s and the good sensitivity provided by the detectors, enables BATSE to monitor many known persistent accreting pulsars on $\approx$ daily time scales. Moreover, BATSE's all–sky monitoring ability makes it ideally suited to track the activities of known transient systems and discover new ones.

1.5 Thesis Roadmap

The goals of this thesis are to present the results of five years of continuous monitoring of accreting pulsars with BATSE, and to elucidate the implications of these results for our current understanding of accreting pulsars. The author pursued this work within the context of a Caltech–Marshall Space Flight Center (MSFC) collaboration to perform a comprehensive study of accreting pulsars with BATSE. Aside from the author, the other Caltech collaborators are Lars Bildsten (now at UC Berkeley), Deepto Chakrabarty (now at MIT), John Chiu, Robert Nelson, Thomas Prince and Brian Vaughan. The MSFC collaborators are Mark Finger, Bradley Rubin (now at the Institute for Physical and Chemical Research (RIKEN), Japan) Matt Scott, Mark Stollberg, Colleen Wilson and Robert Wilson.

The long–term dense sampling of frequencies and fluxes made possible by BATSE have enabled observations to confront theory aggressively and have yielded important new insights into the spin–evolution, accretion torques, and torque–luminosity relations for accreting pulsars. While good agreement between observations and theory exists in some instances, many of our observations paint a surprising picture of accreting pulsars that is difficult to account for by current models.

In Chapter 2, I provide a brief overview of the four instruments on board *GRO* and then discuss in greater detail the characteristics and capabilities of BATSE. Chapter 3 provides an overview of the data analysis techniques and describes the procedures used to process optimally the raw BATSE data sets (DISCLA and CONT) to yield the final standardized data products used in most of our investigations. Chapter 4 provides a synopsis of BATSE observations with frequency and flux histories for each accreting pulsar we continuously monitored. After this general overview, Chapter 5 brings the wind–fed system, GX 301–2, into sharp focus and describes the surprising discovery of rapid spin–up episodes in this system.

The BATSE observations cover many known accreting pulsars belonging to the different classes. This, coupled with the long–term monitoring and dense sampling capabilities of BATSE, greatly facilitates the investigation of several important scientific topics which has traditionally been hampered by the limited capabilities of pre–BATSE instruments. New trends in the spin–evolution of accretion powered pulsars, as revealed by BATSE observations, are discussed in Chapter 6. Chapter 7 presents a detailed study of the correlation between torque and luminosity in both transient and persistent systems.

Chapter 8 describes how the galactic population of high–mass Be transient systems can be inferred from BATSE observations of the recurrence rate of transient systems. Finally, Chapter 9 summarizes our key discoveries and the new insights into accreting pulsars gained from BATSE observations.

Chapter 2

The Compton Gamma–Ray Observatory

The *Compton Gamma Ray Observatory* was launched on 1991 April 5 aboard the space shuttle Atlantis and deployed into a 400 km orbit inclined at 28.5° with respect to the Earth's equator. It is the second of NASA's Great Observatories and, at 17 tons, is the heaviest astrophysical payload ever flown. *GRO* carries four instruments which cover the gamma ray spectrum from 30 keV to 30 GeV:

- **Burst and Transient Source Experiment (BATSE) (20 keV–1 MeV)** (Fishman et al. 1989a) BATSE was designed primarily to detect and monitor gamma–ray bursts and consists of 8 identical NaI crystals based detectors located on the corners of *GRO*. However, the resultant continuous all-sky monitoring ability allows BATSE to also detect and locate transient X-ray and gamma-ray sources and to monitor persistent ones.

- **Oriented Scintillation Spectrometer Experiment (OSSE) (50 keV–10 MeV)** (Johnson et al. 1993) OSSE consists of four NaI scintillation detectors, each of which can be individually pointed. OSSE has observed the energy spectrum of nuclear lines in solar flares, the radioactive decay of nuclei in supernova remnants, and the signature of (electron–positron) annihilation in the Galactic Center region.

- **Compton Telescope (COMPTEL) (1–30 MeV)** (Schonfelder et al. 1993) COMPTEL consists of two layers of gamma-ray detectors and utilizes the Compton effect to reconstruct images of gamma-ray sources. COMPTEL has studied gamma rays from active galaxies, radioactive supernova remnants, and diffuse gamma rays from giant molecular clouds.

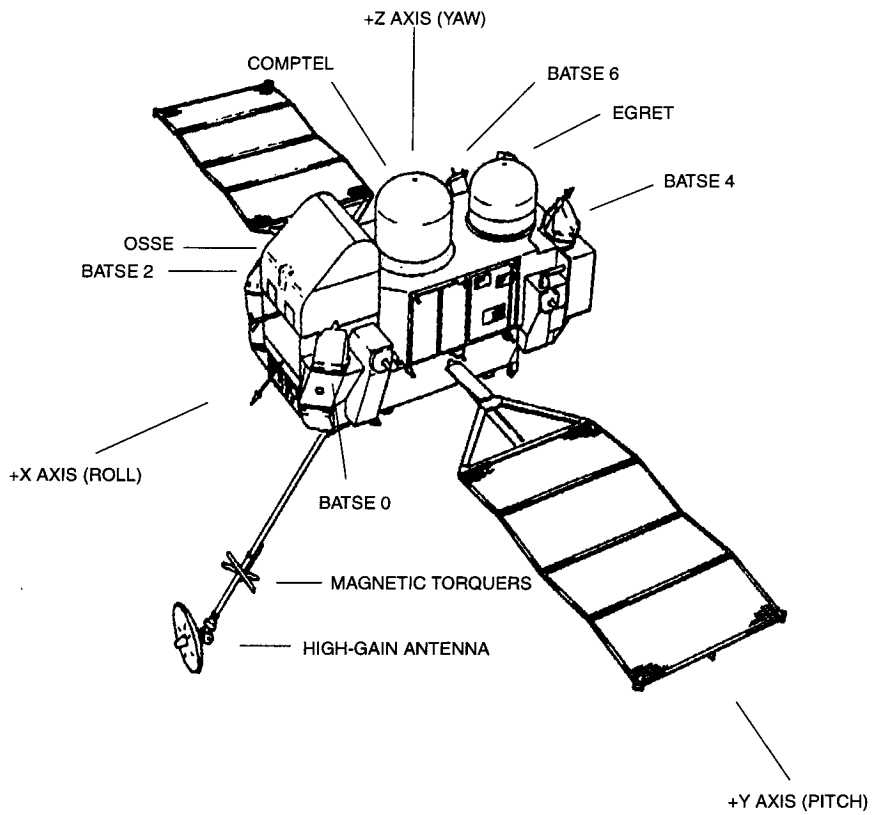

Figure 2.1: The *Compton Gamma Ray Observatory.* The 8 BATSE detector modules are situated on the corners of the spacecraft's main body. Modules 0, 2, 4, and 6 are visible in this diagram.

- **Energetic Gamma Ray Experiment Telescope (EGRET) (20 MeV–30 GeV)** (Thompson et al. 1993) EGRET consists of a NaI crystal beneath high voltage, gas filled, spark chambers which can determine the direction and energy of high-energy gamma rays. EGRET has observed high energy processes associated with pulsars, Active Galactic Nuclei (AGNs) and gamma–ray blazars.

2.1 BATSE – The Burst and Transient Source Experiment

Figure 2.2 shows one of BATSE's 8 identical detector modules which consists of a Large Area Detector (LAD) optimized for sensitivity and directional response, a Spectroscopy Detector (SD) optimized for energy coverage and energy resolution, and a Charged-

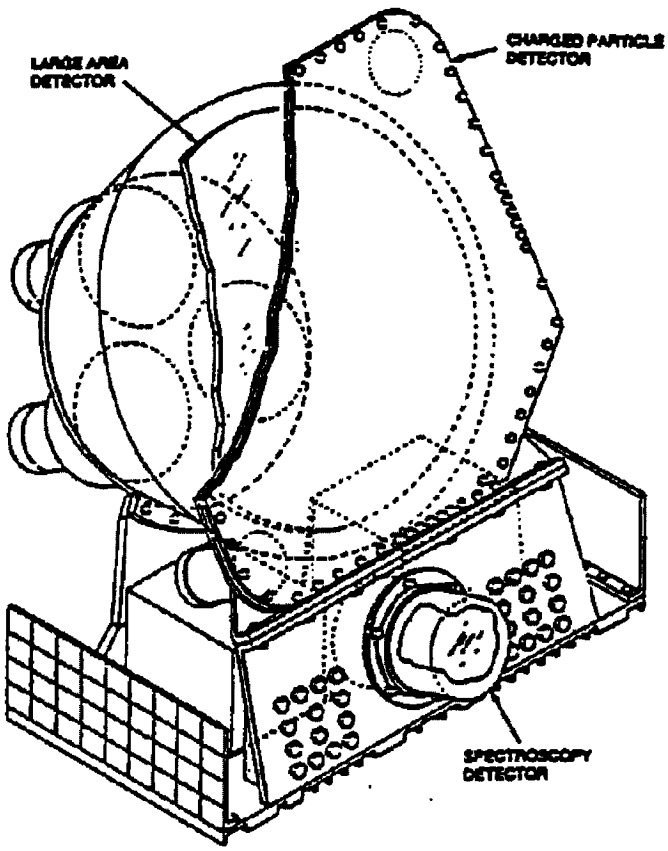

Figure 2.2: A BATSE detector module.

Particle Detector (CPD) which rejects charged–particle induced events in the LAD. The SD and CPD will not be described in detail as none of the analysis done in this work utilizes the data from these detectors.

Each LAD detector comprises a 1.27 cm thick, 50 cm diameter NaI scintillation crystal mounted on a 1.9 cm layer of quartz. Shielding each LAD is a 1 mm aluminum window and the 0.63 cm thick, polystyrene scintillator based CPD. Scintillation light generated by the interaction of high-energy photons with the NaI (Tl) crystal is brought by a light collector into three 12.7 cm diameter photo-multiplier tubes. The signals from the three tubes are then summed.

Scintillation pulses from the LADs are processed in parallel by a high-speed, four-channel discriminator circuit and by a slower pulse height analyzer system. The upper 3 discriminators have nominal equivalent energies of 60, 100 and 325 keV. The low-level discriminators are programmable and are currently set at $\approx$ 20 keV. Each BATSE detector

module sends data to a Central Electronics Unit (CEU), which contains hardware and software that accumulates data in several large RAM memory buffers. Use of commandable parameters and the re-programmability of flight software allow BATSE to respond to unforeseen conditions in orbit and newly discovered gamma–ray phenomena. Signals from the pulse-height converters are used to construct 128–channel spectra from LADs, which are mapped into the coarse resolution 16-channel CONT data. The CEU produces one packet every 2.048 s for telemetry and each packet contains the following 4 data types:

- **Background Data** This comprises the 16-channel continuous (CONT) data, sampled every 2.048 s and the 4-channel discriminator (DISCLA) data, sampled every 1.024 s. The typical energy channel edges for these data types are shown in Table 2.1. The mapping from the 128–channel LADs spectra onto the 16 CONT energy channels is programmable and allows for a tradeoff of time resolution for energy resolution in several of the data types.

- **Housekeeping Data** There are two types of housekeeping data: the HKG product and the QUAL product. The HKG product contains the *GRO* spacecraft orientation and geocentric position at 2.048 s intervals while the QUAL product contains diagnostic information on data quality to enable exclusion of bad data from analysis.

- **Scheduled Data** These data types are typically used to observe known sources and typically involve only 1 or 2 of the 8 BATSE LADs, thus allowing for higher time or spectral resolution. Such data types are collected based on an on-board schedule updated biweekly with each change in *GRO* orientation.

- **Burst Trigger Data** This is generated every time a gamma–ray burst is identified in the BATSE data stream. Such data are excluded from our analysis.

2.1.1 BATSE LAD Response

Figure 2.4 shows the effective area of a BATSE LAD as a function of incident photon energy. Incident photons with $E \lesssim 100$ keV, deposit virtually all their energy within the detector, thus resulting in almost identical effective areas for total response and the full energy deposition response. Photons with $E \gtrsim 100$ keV have larger penetration depths and only deposit part of their energy in the detector before escaping, thus leading to the

Table 2.1. Energy Channels in BATSE DISCLA and CONT Data

Channel	Nominal Energy Range (keV)	Background Rate (c s^{-1})
DISCLA 1	20–60	1500
DISCLA 2	60–110	1200
DISCLA 3	110–320	1000
DISCLA 4	>320	700
CONT 0	20–24	250
CONT 1	24–33	450
CONT 2	33–42	500
CONT 3	42–55	500
CONT 4	55–74	500
CONT 5	74–99	450
CONT 6	99–124	300
CONT 7	124–165	300
CONT 8	165–232	300
CONT 9	232–318	200
CONT 10	318–426	130
CONT 11	426–590	130
CONT 12	590–745	50
CONT 13	745–1103	80
CONT 14	1103–1828	80
CONT 15	>1828	200

NOTE: These channel boundaries are *approximate*, and are averaged over the eight detectors. Each detector has slightly different edges, as shown in Figure 2.3. The CONT edges are programmable; the displayed values are typical, and are computed using the calibration discussed in Preece et al. 1997. We have made use of CONT data through channel 7 in our analyses.

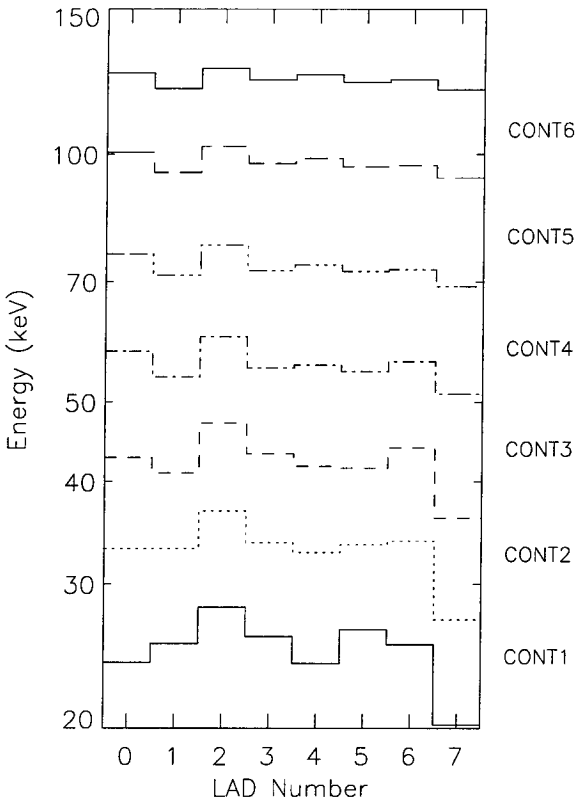

Figure 2.3: The energies of the Large Area Detector (LAD) channel boundaries for the CONT data. We display the lower and upper boundaries of CONT channels 1–6 for all detectors. The gain is stabilized on-board using the 511 keV background feature. These bin energies apply to two different intervals, MJD 48406.11 – 49400.69 and MJD 49419.69 – 50062.82, which together comprise most of the *GRO* mission.

observed discrepancy between the two effective area curves. The steep fall in the response at $E \lesssim 20$ keV arises from the attenuation induced by the aluminum shielding and the CPD.

Figure 2.5 shows the angular response of a BATSE LAD to incident photons of different energies. At low energies, a fall–off steeper than the geometric cos dependence on the viewing angle θ arises from the aluminum shielding and CPD induced attenuation, which increases with increasing θ. At high photon energies, this attenuation is less significant due to the increased penetration depth in the detector. In addition, the $\approx \cos\theta$ dependence of the penetration depth partially offsets the geometric $\cos\theta$ dependence, thus leading to a much gentler fall–off in response with increasing θ.

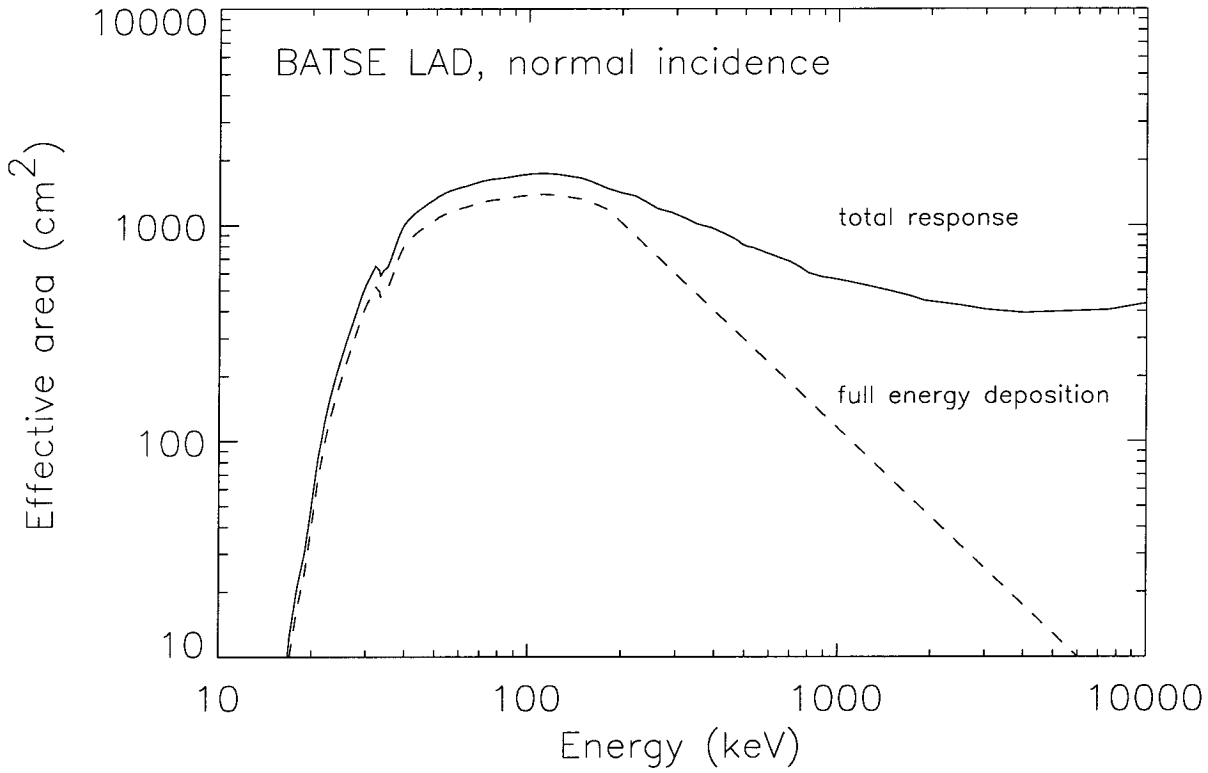

Figure 2.4: The normal incidence effective area of a BATSE LAD as a function of incident photon energy. The solid line represents the total response of the detector, while the dashed line represents the full energy deposition response. The discrepancy between the two arises from high energy incident photons not depositing their energy fully into the detector and then escaping. The increase in total response which begins at $\approx$ 5 MeV is attributable to pair production, the dominant contribution to the interaction cross section at these energies. The steep fall in the response at $E \lesssim 20$ keV arises from the attenuation induced by the aluminum shielding and the CPD. The dip in the effective area at $E \approx 30$ keV is attributable to the iodine K edge. Figure is from Chakrabarty (1996).

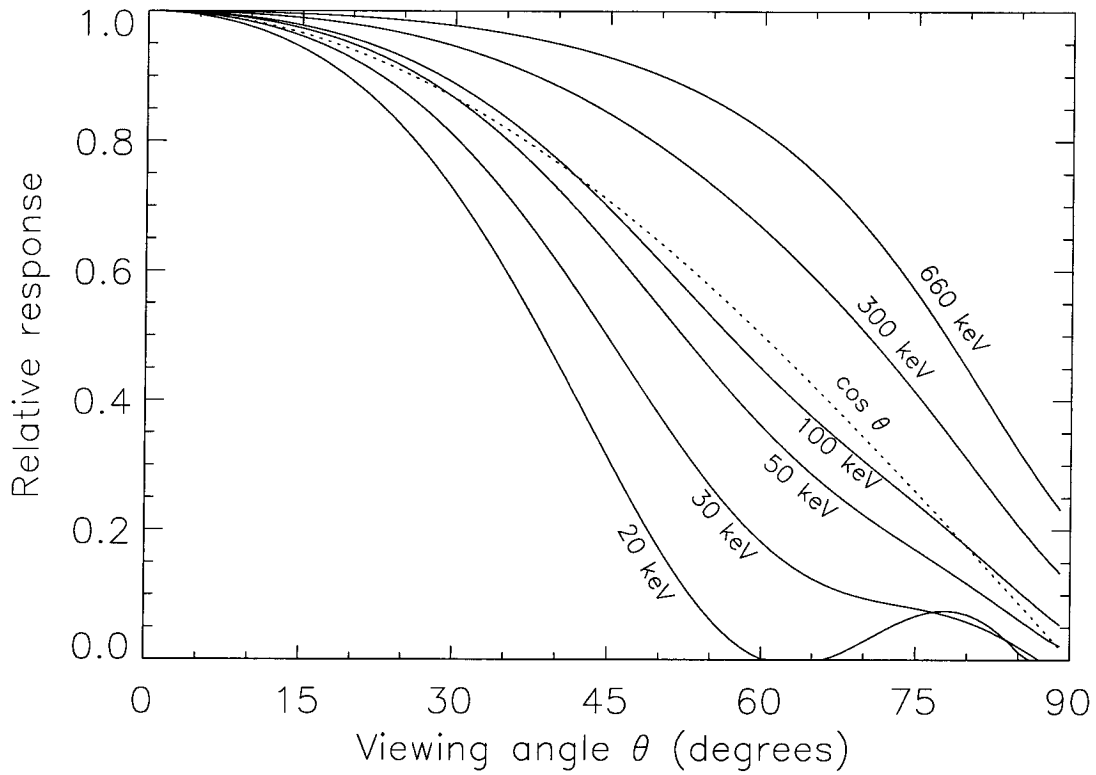

Figure 2.5: Angular response of a BATSE LAD to incident photons of different energies. The dotted line is the geometric $\cos\theta$ response. A gap in the detector support structure at the edge of the LADs is responsible for the secondary bump in the 20 keV response. Figure is from Chakrabarty (1996).

Chapter 3

BATSE Data Analysis

3.1 Introduction

The ability to address most of the science topics which form the focus of this thesis rests upon the accurate determination of frequency and signal strength on $\approx$ daily time scales. We shall hence provide a brief overview of the techniques to extract these quantities. Since these techniques have been covered in depth by numerous references, we will simply review the key concepts and point to the appropriate references.

3.2 Frequency Determination

The two most common techniques used for frequency determination in BATSE data analysis are epoch folding and Fourier analysis. Epoch folding typically involves folding the time series at a set of trial frequencies into a pulse profile containing N phase bins, and evaluating the χ^2 statistic S of each resultant profile, given by

$$S = \sum_{j=1}^{N} \frac{(x_j - \langle x \rangle)^2}{\sigma_j^2} \tag{3.1}$$

where x_j is value of the profile at the jth phase bin, $\langle x \rangle$ is the mean value of profile, and σ_j is the 1-σ error at the jth phase bin. S is a random variable χ^2 distributed with $N-1$ degrees of freedom and this can be used to assess objectively the presence of a signal. The source frequency is that which maximizes the χ^2.

A more sophisticated extension of this procedure is used in our BATSE analysis where epoch folding is generalized to encompass any technique which involves assigning a

phase, computed using a pulse phase model, to each time bin. Each time series segment, ranging in duration from 1–10 d, is fitted to the following model

$$C(t) = M(t) + \sum_{k=1}^{n} [A_k \cos 2\pi k\phi(t) + B_k \sin 2\pi k\phi(t)], \tag{3.2}$$

where $M(t)$ is a model of the background rate, A_k and B_k are the Fourier amplitudes of the pulse profile modeled typically by $n = 3$ harmonics, and $\phi(t)$ is the pulse phase where a constant frequency is generally assumed for the interval. The optimal frequency is determined using the Z_m^2 test, which measures the significance of the first m Fourier amplitudes. This technique was used to obtain the frequency histories of Cen X–3, 4U 1538–52, 4U 0115+634, GRO J1750-27, 2S 1417–624, GRO J2058+42, 4U 1145–619 and A 1118–616 shown in Chapter 4. More details on this technique can be found in Appendix B. Since the entire time series must be processed for each trial frequency, epoch folding is an order N^2 algorithm which is agonizingly inefficient.

In stark contrast to epoch folding, the Fast Fourier Transform (FFT) is an order $N \log N$ algorithm. Fourier analysis exploits the efficiency of the FFT algorithm to compute the Fourier amplitudes at a range of discrete frequencies. Given a time series of duration T, consisting of N samples evenly spaced at Δt, ($T = N\Delta t$) we compute

$$H_k = \sum_{j=0}^{N-1} h_j e^{2\pi ijk/N} \tag{3.3}$$

where H_k is the Fourier amplitude corresponding to frequency k/T, where k ranges from 0 to $N/2$. The maximum frequency $\nu = N/2T$ is also known as the Nyquist frequency. When the corresponding Fourier power,

$$P_k = |H_k|^2, \tag{3.4}$$

is normalized by the mean noise power $< P_k >$, we obtain the normalized power

$$\bar{P}_k = \frac{P_k}{\langle P \rangle}. \tag{3.5}$$

The probability that, purely by chance, the power in a spectral bin will exceed a pre–defined threshold, P_t, is given by

$$\Pr(\bar{P} > \bar{P}_t) = e^{-\bar{P}_t}. \tag{3.6}$$

The above global power normalization only works for the case when the noise power spectral density is flat. Otherwise, we need to normalize the power in each spectral bin with the

local noise power. For a power spectrum where the noise is locally flat, this procedure also yields a power spectrum with mean 1 and variance 1, for which Equation 3.6 remains valid.

Unfortunately, the finite width of each frequency bin translates into power distributed across neighboring bins for a signal whose frequency falls between 2 Independent Fourier Frequencies (IFFs). For the pathological case of a source frequency located equidistant between 2 IFFs, the power loss of the signal can be up to ≈ 50 %. One possible remedy for this problem, which is the one adopted for our analysis, is to over–resolve the power spectrum by padding the original (zero–meaned) time series with zeros and then perform the FFT. This decreases the width of each frequency bin, thus decreasing power loss for a signal not located at an IFF, and also increasing the precision with which the source frequency can be measured. The recovery of power through over–resolution saturates when the time series is padded to a length of $\approx 5N$. This technique was used to obtain the frequency histories of OAO 1657–415, GS 0834–430, GRO J1948+32, EXO 2030+375 and GRO J1008–52 shown in Chapter 4.

For more details on the topic of frequency determination, refer to van der Klis (1988) and Chapter 3 of Chakrabarty (1996) and references therein. Appendix B also describes other frequency estimation techniques used in BATSE data analysis but not covered here.

3.3 Signal Estimation

The process of flux determination begins with the estimation of the signal strength in the various DISCLA and CONT channels which register detections. We describe here two different methods for signal estimation. The first technique is adapted from statistical optics and allows for the rigorous estimation of the signal strength in a single harmonic pulse profile. The second technique works for pulse profiles which contain higher harmonics and assumes the pulse profile shape to be constant.

3.3.1 Rigorous Statistical Approach for Single Harmonic Signal

The problem of signal estimation in the presence of noise has been elegantly dealt with in statistical optics. Given a single-harmonic, periodic signal with measured amplitude a, true amplitude s and noise strength n, the probability distribution of a is given by

(Goodman 1985)

$$p(a|s,n)da = \frac{2a}{n^2}\exp\left[\frac{-(a^2+s^2)}{n^2}\right] I_0\left(\frac{2as}{n^2}\right) da \qquad (a>0). \tag{3.7}$$

The noise strength is defined to be $n = \sqrt{2P_n}$, where P_n is the local noise power computed from the power spectrum. Since we are primarily interested in inferring s given a and n, we apply Bayes theorem to obtain (Chakrabarty 1996)

$$p(s|a,n)ds = \frac{2}{n}\sqrt{\frac{1}{\pi}}\exp\left[\frac{-(a^2+2s^2)}{2n^2}\right]\frac{I_0\left(\frac{2as}{n^2}\right)}{I_0\left(\frac{a^2}{2n^2}\right)}ds \qquad (a>0), \tag{3.8}$$

where we assumed $p(s)$ = constant during the inversion. We refer the reader to de Jager (1994) for a discussion of the strengths and weaknesses of this choice to assume that all prior probabilities of the true amplitude strength s are equal. For the case of strong signal–to–noise ratio, $s, a \gg n$ and both of these expressions reduce to the familiar Gaussian distributions

$$p(a|s,n) \approx p(s|a,n) \approx \frac{1}{\sqrt{\pi n^2}}\exp\left[\frac{-(a-s)^2}{n^2}\right] \quad . \tag{3.9}$$

Hence, n is the 1–σ error in s. We note however that this method of estimating the intrinsic signal strength works easily only for single harmonic pulse profiles. Although the intrinsic signal strength can be estimated individually at each harmonic of a signal with higher harmonic content, the phase relations between the different harmonics are themselves not well defined since they too are contaminated by noise. This greatly complicates the applicability of this method to such pulse profiles. This technique was used to estimate the signal strengths GRO J1948+32 (Chakrabarty et al. 1995a), 4U 1626–67 (Chakrabarty et al. 1997a) and GX 1+4 (Chakrabarty et al. 1997b) as the pulse profiles of these sources are almost perfectly sinusoidal. For multiple harmonic signals, we propose an alternative approximate method, which depends on the assumption of a constant pulse profile over the observation interval.

3.3.2 Template Fitting Method for Multiple Harmonic Signals [1]

The continuous monitoring ability of BATSE allows us to generate a pulse profile for most sources on $\approx$ daily time scales. Assuming that the pulse profile shape is non–

[1]Extracted with changes from "Rapid Spin–Up Episodes in the Wind Fed Accreting Pulsar GX 301–2" in *The Astrophysical Journal*, 479, 933–947, by D. T. Koh, L. Bildsten, D. Chakrabarty, R. W. Nelson, T. A. Prince, B. A. Vaughan, M. H. Finger, R. B. Wilson and B. C. Rubin. Used by permission of the authors.

variable, we can construct a template by stacking together several hundred pulse profiles.

Define $x(j)$, $0 \leq j \leq N_b - 1$ to be a template with N_b phase bins. Since each phase bin has negligible variance, the count rate, C, in the template is given by

$$C = \frac{1}{N_b} \sum_{j=0}^{N_b-1} (x(j) - \min[x(j)]). \tag{3.10}$$

This technique cannot be applied to a typical profile due to the large variance of each phase bin, especially when the signal–to–noise ratio is low. Nevertheless, if the pulse shape of the source is approximately constant, then the count rate of a typical profile can be found by computing the intensity scaling I and the phase ϕ which relates the profile and the template amplitudes.

Define the complex Fourier amplitudes of the template and profile as T_j and a_j, the 1–σ uncertainties of the real and imaginary parts of a_j to be σ_j, the phase shift between the template and profile to be ϕ, and the number of harmonics retained in each pulse profile to be N_h. Assuming that a_j are independent Gaussian random variables, maximizing

$$\chi^2 = \sum_{j=1}^{N_h} \frac{|a_j - Ie^{ij\phi}T_j|^2}{{\sigma_j}^2} \tag{3.11}$$

dictates the maximum-likelihood value of I to be

$$I = \left(\sum_{j=1}^{N_h} \mathrm{Re}[a_j e^{-ij\phi} T_j^*]/\sigma_j^2 \right) \left(\sum_{j=1}^{N_h} |T_j|^2/\sigma_j^2 \right)^{-1}. \tag{3.12}$$

Since the profile is assumed to be a scaled version of the template, the most likely value of ϕ is that which brings the two in phase. Hence,

$$\arg[a_j e^{-ij\phi} T_j^*] = \arg[a_j] - \arg[e^{ij\phi} T_j] = 0 \tag{3.13}$$

and

$$\mathrm{Re}[a_j e^{-ij\phi} T_j^*] = a_j e^{-ij\phi} T_j^* = |a_j||T_j|. \tag{3.14}$$

Substitution of this into 3.12 yields

$$I = \left(\sum_{j=1}^{N_h} |a_j||T_j|/\sigma_j^2 \right) \left(\sum_{j=1}^{N_h} |T_j|^2/\sigma_j^2 \right)^{-1} \tag{3.15}$$

which we use to find I.

We assume that the template has been generated from a sufficient number of pulse profiles to render the statistical errors negligible. Assuming that noise introduces a Gaussian random deviate into the real and imaginary parts of the measured a_j, we write a_j as

$$a_j = a_j^s + n_j, \tag{3.16}$$

where a_j^s is the signal component and n_j is the 2–D Gaussian noise component. Substitution of this into 3.12 and taking its variance yields

$$\mathrm{var}[I] = \left(\sum_{j=1}^{N_h} \mathrm{var}(\mathrm{Re}[n_j e^{-ij\phi} T_j^*])/\sigma_j^4\right)\left(\sum_{j=1}^{N_h} |T_j|^2/\sigma_j^2\right)^{-2} = \left(\sum_{j=1}^{N_h} |T_j|^2/\sigma_j^2\right)^{-1} \tag{3.17}$$

which we use to find the errors.

This technique was used to obtain the count rates from which the fluxes in GX 301–2 (Figure 5.7) and those quoted in Table 4.1 were dervied. The cross spectrum technique (see Appendix A), which also assumes a constant pulse profile, was used to measure the time delays needed for orbit determination in GX 301–2 (see Chapter 5). The good correspondence between the observed and expected chi–square distribution for the linear fits performed supports the assumption of a constant pulse profile (see Figure A.1).

3.4 Flux Determination

Once the signal strengths were obtained, we computed the fluxes by folding either a power–law photon spectrum, $dN/dE \propto (E/30\mathrm{keV})^{-\gamma}$ or an exponential spectrum, $dN/dE \propto (1/E)\exp(-E/E_f)$ through the detector response matrix. Since the signal–to–noise ratio in a single day of BATSE observation is too low for detection in at least three channels needed to perform a fit, we typically stack together multiple days of data to determine the optimal spectral parameters, γ or E_f. Once these have been determined for a source, they can be assumed fixed and used to evaluate fluxes on shorter ($\approx$ daily) time scales.

The signal strengths obtained through the procedures described in Sections 3.3.1 and 3.3.2 are the peak–to—peak count rates which yield the the pulsed flux. Defining $F(\phi)$ to be the flux of a pulse profile at phase ϕ $(0 < \phi < 1)$, the pulsed flux can be expressed as

$$F_{\mathrm{pulsed}} = \int_0^1 (F(\phi) - F_{\mathrm{min}}) d\phi \tag{3.18}$$

where $F_{\rm min} = \min[F(\phi)]$. However, if the pulse profile is neither sinusoidal and we do not want to assume a constant pulse profile, neither of the signal estimation techniques discussed in Sections 3.3.1 and 3.3.2 can be used. In such instances, the Root–Mean–Square (RMS) flux, defined by

$$F_{\rm RMS} = \left[\int_0^1 (F(\phi) - \bar{F})^2 d\phi\right]^{1/2} \tag{3.19}$$

where $\bar{F} = \int_0^1 F(\phi) d\phi$, is a more reliable measure of the fluxes. This is especially so when the observation intervals are are short ($\lesssim$ days) and the signal–to–noise ratio low, since $\bar{F}$ can be measured more accurately than $F_{\rm min}$. For a square pulse profile, $F_{\rm pulsed} = F_{\rm RMS}$ while for a sinusoidal pulse profile, $F_{\rm pulsed} = \sqrt{2} F_{\rm RMS}$. All the fluxes for the various sources displayed in Chapter 4 are RMS fluxes. More details on the computation of $F_{\rm RMS}$ can be found in Appendix B.2.3. A comprehensive description of other techniques used to compute fluxes is given in Appendix B.

3.5 Background Subtraction

The un-collimated nature of BATSE LADs not only gives BATSE an all–sky monitoring ability, but also results in a manifold increase in the background, which is $\approx$ 2000 c s^{-1}in CONT channels 1–4 ($\approx$ 20–70 keV) summed. This background includes contributions from the diffuse cosmic gamma–ray background, atmospheric gamma-rays, a prompt background due to gamma–rays and neutrons produced by local cosmic rays, decays of radionuclides (activated by cosmic–ray bombardment), and transient events, such as solar flares and electron precipitation events. A detailed discussion of this background can be found in Dean, Lei & Knight (1991). The $\approx$ 90–min orbit of the spacecraft around the Earth modulates this background, resulting in many higher harmonics which severely degrade the detection sensitivity. Large gaps in the data stream occur when the detector high voltage is turned off during spacecraft passages through the South Atlantic Anomaly (SAA), a region with an extremely high flux of charged particles trapped by the Earth's radiation belts (see Tascione 1988). Such gaps and the presence of spikes, due mainly to charged–particle induced phosphorescence in the NaI crystal of the detector, introduce power at a wide range of frequencies, further deteriorating the detection sensitivity. Three techniques of varying degrees of sophistication have been developed to subtract this background.

The first technique (Chakrabarty et al. 1993; Chakrabarty 1996) begins with spike

removal and interpolation over gaps in the raw data. A low–pass filter of the form

$$R(\nu < \nu_0) = [1 + \cos(\pi\nu/\nu_0)]/2 \quad \text{for} \quad \nu < \nu_0 \qquad \text{and}$$
$$R(\nu > \nu_0) = 0 \quad \text{for} \quad \nu > \nu_0, \quad \text{with} \quad \nu_0 = 1.6 \times 10^{-3}\text{Hz} \tag{3.20}$$

is then applied to the Fourier transform of the spike–removed and smoothed data. The resultant product, when inverse Fourier transformed, is a good representation of the background which is then subtracted from the original time series. This technique works well for the faster ($P_{\rm spin} \lesssim 100$ s) pulsars. The frequency and flux histories for 4U 1626–67 and GX 1+4 shown in Chapter 4 were obtained from data background subtracted using this technique.

A more empirical method models the background in segments of ≈ 300 s using a spline function with quadratics in time. Within contiguous data sets, the spline function is continuous in value and slope at the segment boundaries. This model is fit simultaneously with a Fourier representation of the pulsed signal (see Appendix B.1.2). This technique extends the detection sensitivity to pulsars with $P_{\rm spin} \lesssim 400$ s. The frequency and flux histories of GRO J1744–28, Cen X–3, 4U 0115+63, 2S 1417–624, A 0535+26, 4U 1145–619 and A 1118–616 shown in Chapter 4 were obtained from data background subtracted using this technique.

To push the envelope of detection sensitivity to include pulsars with $P_{\rm spin} \gtrsim 400$ s, a model which phenomenologically accounts for each of the major contributions to the background was developed (Rubin et al. 1996). Instead of modeling each of these contributions in detail, approximate functional forms, scaled by coefficients determined from fitting the data, are used. Also, terms which account for the changing direction of the detector with respect to the Earth are included. The data in each LAD is fitted at 1/8 day intervals to the function

$$M(t_i) = \sum_{j=0}^{3}(a_j + b_j L)P_j(\cos\theta_i) + c\cos\phi_i + d\sin\phi_i \sum_{k=1}^{n_{\rm SAA}} f_k \exp\left[\frac{-(t_i - t_{\rm SAA})}{\tau_k}\right] + \sum_{l=1}^{n_{occ}} g_l T_{li} \tag{3.21}$$

where i labels the time bin corresponding to t_i, L is the McIlwain-L shell parameter, P_j is the Legendre polynomial of order j, θ is the angle from the detector normal to the center of the Earth, ϕ is the angle made by the projection of the detector normal onto a plane tangent to the Earth with an Eastern reference direction, $t_{\rm SAA}$ is the end time of the most recent SAA passage, τ_k is the decay time of ^{128}I, and T_{li} is the atmospheric transmission function of

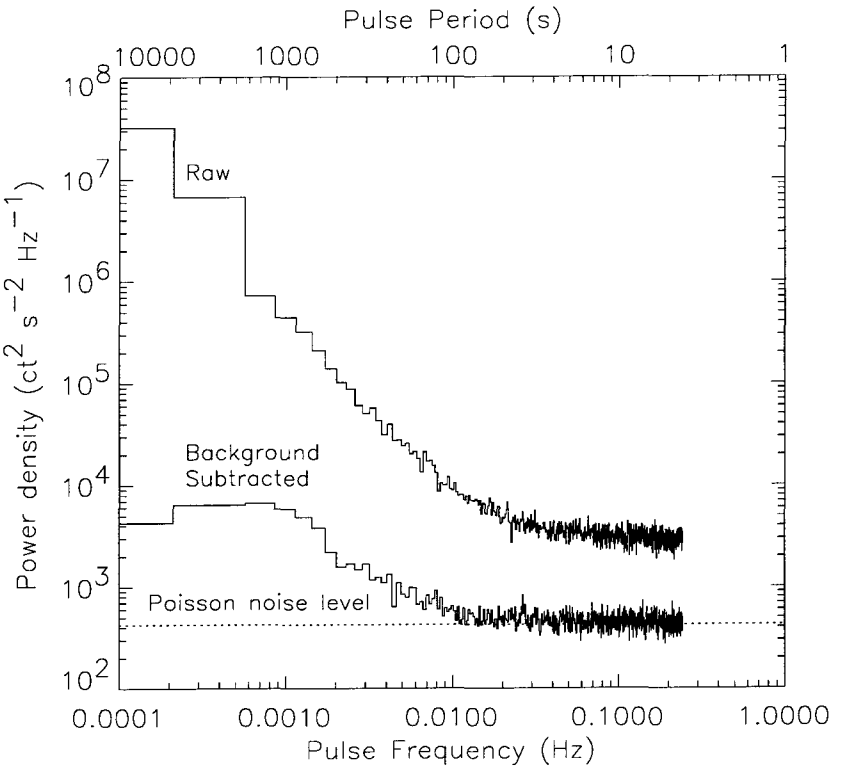

Figure 3.1: The typical power spectrum of the BATSE LAD background in the 25–33 keV range. The data shown are for CONT Channel 1 (25–33 keV) from LAD 2 on MJD 48851–48852 when the mean count rate was 423.7 c s^{-1}. The top curve is the unprocessed raw data, while the bottom curve is after background subtraction.

source l at the mean energy of bin i. These first three terms account for the atmospheric and prompt components of the background and the geometric effects due to changing detector orientation, the fourth takes care of the SAA passages, and the last models the appearance or disappearance of bright sources as the detector moves within or away from its view. The coefficients a_j, b_j, c, d, f_k and g_l are determined by a linear least-squares fit to the raw data. The frequency and flux histories of OAO 1657–415, Vela X-1, 4U 1538–52, GX 301–2, GS 0834–430, GRO J1948+32, EXO 2030+375 and GRO J1008–57 shown in Chapter 4 were obtained from data background subtracted using this technique.

Figure 3.1 shows the dramatic decrease in noise power achieved by this background subtraction, while Figure 3.2 shows the 1–day pulsed-intensity sensitivities of the CONT data as a function of energy for three representative pulse frequencies. We define the threshold sensitivity to be the count rate beneath which the error is larger than 20%, which is a more stringent criterion than that of detecting the pulse within a narrow frequency

range. The degradation of sensitivity at low frequencies is due to residual background not fully accounted for by the background subtraction process.

Since most of our searches are performed on time series summed over CONT channels 1–4, we show the corresponding 5–σ detection threshold in Figure 3.3. At frequencies of $\nu \gtrsim 0.02$ Hz, the noise is Poisson and the resulting sensitivity is

$$C_{\rm S} \approx 1.1 \text{ c s}^{-1} \left(\frac{C_{\rm B}}{2000 \text{ c s}^{-1}}\right)^{1/2} \left(\frac{42000 \text{ s}}{t}\right)^{1/2}, \tag{3.22}$$

where C_B is the background rate and t is the exposure time. Depending on how steep the spectrum is (see Table 3.1 for the conversion from BATSE LAD c s^{-1} to flux units) this is a flux of $\approx 10^{-10}$erg cm^{-2} s^{-1} in the 20-60 keV band. The corresponding luminosity at the Galactic center (8.5 kpc) is $L(20-60 \text{ keV}) \approx 8 \times 10^{35}$ erg s^{-1}, allowing detection of the majority of the known accretion powered pulsars.

3.6 Post–Background Subtraction Steps

After background subtraction, several important steps remain to be executed to construct an optimal time series for frequency searches for a particular source. We first summed CONT channels 0–3 (20–55 keV) data weighted by the cosine squared of the viewing angle to the source for each detector [2]. To further increase the signal–to–noise ratio, we zeroed out all segments in the time series where the source is occulted from view as the *GRO* spacecraft orbits the Earth. We then reduced all our timing observations to the solar system barycenter using the Jet Propulsion Laboratory DE-200 solar system ephemeris (Standish et al. 1992) and removed the best known orbit for the source. The pulse frequency for each 1-day data segment was then determined by searching the corresponding Fourier power spectrum for the strongest signal in a small range around the previously observed pulse frequency. Figure 3.4 highlights the evolution a typical CONT time series over the course of the analysis process.

[2]During any *GRO* pointing, an astrophysical source is visible to 4 of BATSE's 8 detectors. A weighted sum of the 4 detectors significantly enhances the signal–to–noise ratio in the time series. The optimal weighting function, $w(\theta)$, depends on the source sky position and detector angular response $r(\theta)$, where θ is the source viewing angle wrt the detector. Chakrabarty (1996) showed that for the range of spectrum observed in most accreting pulsars, the detector angular response is well approximated by $r(\theta) = \cos^2\theta$. For this $r(\theta)$, he showed that an adaptive weighting function, $w(\theta) = \cos^n\theta$, with $n = 0, 1, 2, 3, 4$ depending on the source position, maximizes the overall signal–to–noise ratio. All the results presented in this thesis utilized $w(\theta) = \cos^2\theta$.

Table 3.1. Conversion to Pulsed Flux from Counts

Power Law			
α^a	DISCLA[b]	CONT[c]	% Error[d]
2.0	0.84	0.79	5
3.0	0.94	0.87	10
4.0	1.05	0.95	15
5.0	1.17	1.02	20
OTTB			
kT (keV)[e]	DISCLA[b]	CONT[c]	% Error[d]
10	1.18	1.03	15
25	0.94	0.88	8
40	0.89	0.84	6
55	0.87	0.82	5

Note. — These conversions are for normal incidence. For other incident photon angles, see section 2.1.1 and Figure 2.5.

[a]Spectral model used is $dN/dE \propto E^{-\alpha}$.

[b]Energy flux in units of 10^{-10} ergs cm^{-2} s^{-1} corresponding to a pulsed intensity of 1 c s^{-1} in DISCLA Channel 1 (20–50 keV).

[c]Energy flux in units of 10^{-10} ergs cm^{-2} s^{-1} corresponding to a pulsed intensity of 1 c s^{-1} in CONT Channels 1–4 (20–70 keV) summed .

[d]Percentage error in energy flux due to variations in energy edges for different detectors.

[e]Spectral model used is $dN/dE \propto (1/E)\exp(-E/kT)g_{ff}(E,kT)$

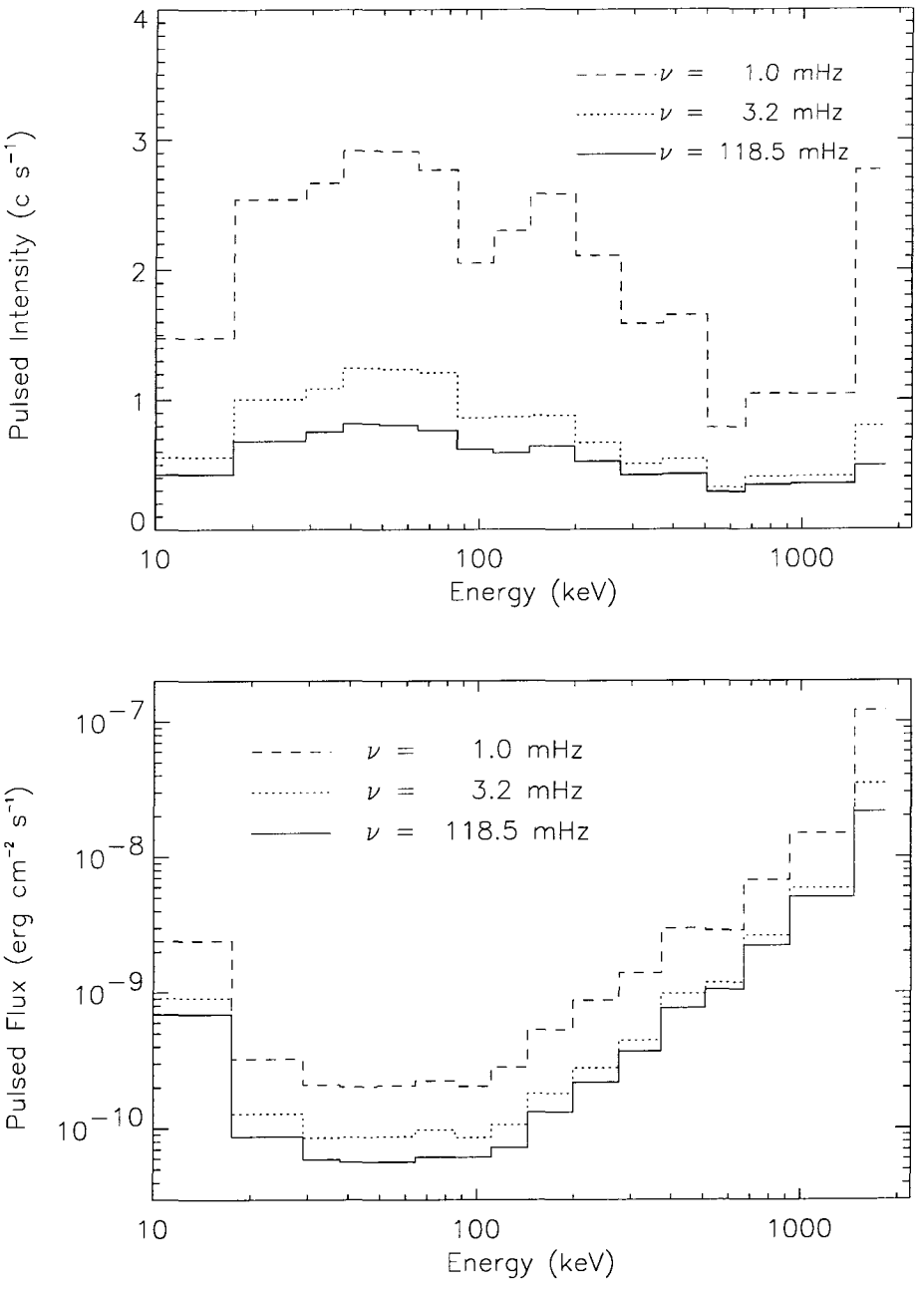

Figure 3.2: The 1-day BATSE sensitivity for a single large-area detector to an un-occulted pulsed source at three pulse frequencies. We define the threshold pulsed intensity (upper panel) as the count rate where the error in the measured rate is 20 %. The degradation in sensitivity at low frequencies is due to residual background not fully accounted for by the background subtraction process. The lower panel shows the energy flux corresponding to these threshold count rates, assuming that the source has a power-law spectrum with photon number index $\alpha = 4.0$ and is viewed at normal incidence. A typical live time of $\sim$ 42000 s is obtained per day.

3.7 The BATSE Pulsed Source Catalog

BATSE has harvested an unusually rich data set on accreting pulsars which is unprecedented in breadth, size and uniformity. Although this thesis deals in depth with several scientific topics which are especially suited for probing by the BATSE data sets, many other important topics remain unexplored. To allow the BATSE data set to be exploited fruitfully by the astrophysical community at large, we have created a standardized set of data products for each pulsar detected in the CONT data. For each source, the information stored in a FITS file on a daily basis includes: source pulse frequency, power spectrum in the vicinity of the spectral peak, the associated normalized power, pulse profiles for each [channel,detector] combination, and the local noise powers associated with each of the harmonics of the profile. These standard products are available daily for the persistent sources 4U 1626–67, GX 1+4, Vela X–1, OAO 1657–415, GX 301–2, and during outbursts for the transient sources GS 0834–430, 2S 1417–624, EXO 2030+375, A 0535+262, 4U 1145–619, A 1118–616, GRO J1750–27, GRO J2058+42. Up-to-date results on these sources are being made available through the public archive at the *Compton Observatory* Science Support Center (http://cossc.gsfc.nasa.gov/cossc/COSSC_HOME.html).

The sources monitored by BATSE for which the standardized products are not available are Cen X–3, Her X–1, GRO J1744–28, and 4U 1538–52. The first three have spin frequencies which are beyond the Nyquist limit of the CONT data while 4U 1538–52 is too weak to be detected on a daily basis.

In the next chapter, we present a brief overview of BATSE observations of individual accreting pulsars. For each source, a long–term frequency and flux history are shown. Aside from the few exceptions mentioned above, all these plots were generated from information extracted from the standardized daily data products, clearly illustrating the usefulness and versatility this database. In addition, we highlight that we have only used a small fraction of the data contained in the database and its potential for supporting other studies remain to be fully exploited.

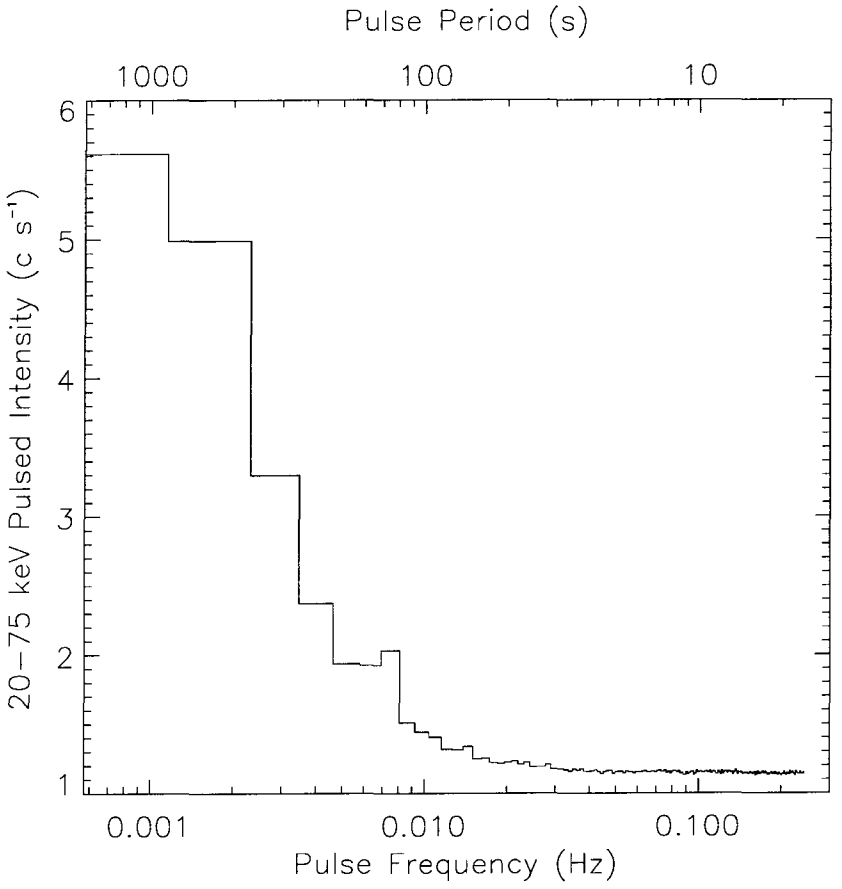

Figure 3.3: The 1-day BATSE 5σ detection threshold for an un-occulted source (CONT channels 1 to 4 summed) following background subtraction. The thresholds plotted were obtained by averaging the thresholds for each of the 8 BATSE detectors from MJD 49081 to 49093. A typical day is characterized by a mean background rate (CONT channels 1 to 4 summed) of $\approx$ 2000 c s^{-1} and $\approx$ 42000 seconds of useful data. At frequencies $\nu \gtrsim 0.02$ Hz, the background noise is essentially Poisson and the threshold is simply that given by equation (3.22). The thresholds at lower frequencies are found by assuming local Gaussian statistics for the measured noise strength. The anomalous rise in the thresholds at $\nu \approx 0.007$ Hz is attributable to the second harmonic of Vela X-1, which was not accounted for in the background subtraction model.

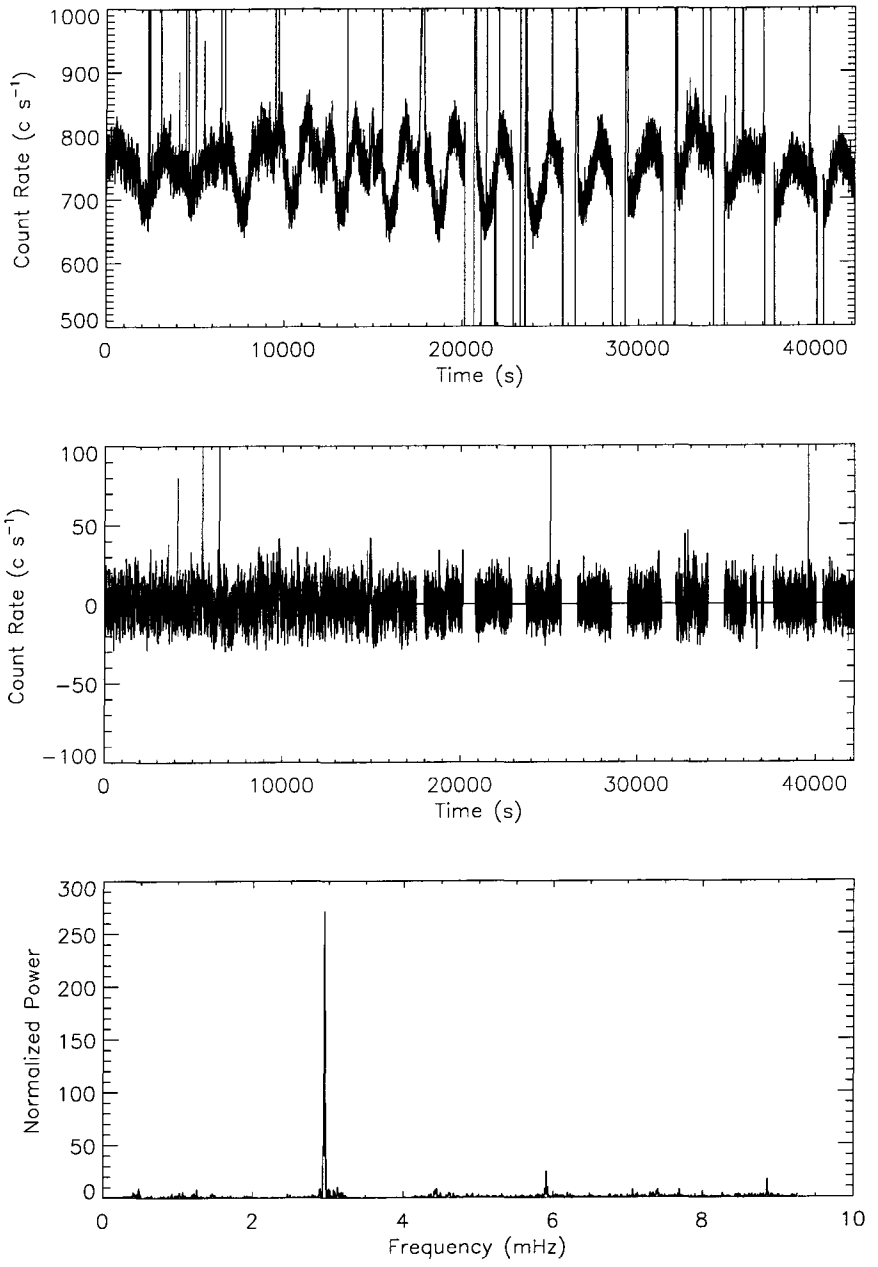

Figure 3.4: The evolution of a typical CONT time series over the course of the analysis process. Top panel: Raw CONT data (summed over channels 0–3) from BATSE LAD 7 on MJD 48635. The $\approx$ 90 min modulations associated with the *GRO* orbit are clearly visible, as are numerous spikes mainly attributable to charge-particle induced phosphorescence in the NaI. Middle Panel: The same time series, after background subtraction. The orbital modulations and most spikes have been removed from the time series, which now has zero-mean. Bottom Panel: Fourier power spectrum of the background subtracted, zero-meaned time series (after application of occultation window, barycentering, removal of known orbit). The second (dominant) harmonic of the wind-fed source GX 301–2, is clearly detected. Also visible are the 4th and 6th harmonics.

Chapter 4

BATSE Observations of Individual Sources [1]

4.1 Introduction

BATSE continuously monitors the spin frequency and pulsed flux of 3 low-mass systems (Her X-1, 4U 1626–67, and GX 1+4) and 5 high-mass systems (Cen X-3, OAO 1657–415, Vela X-1, 4U 1538–52, and GX 301–2). BATSE has also observed one or more outbursts from 7 known transient systems (4U 0115+63, GS 0834–430, 2S 1417–624, EXO 2030+375, A 0535+26, 4U 1145–619, and A 1118–616). In addition, it has discovered 5 new transients (GRO J1744–28, GRO J1750–27, GRO J1948+32, GRO J1008–57, and GRO J2058+42). In Figure 4.1 we display long-term frequency histories of all sources seen with BATSE that were known prior to BATSE, including archival data.

In this section, intrinsic spin frequency and flux histories for the persistently accreting binaries are presented for the first four years of BATSE monitoring, 1993 April 23–1995 Feb 11 (MJD 48370–49760). We also show frequency and flux histories of the outbursts for the transient sources. For those transients where we have yet to measure the orbital parameters, we display the observed frequencies, whereas we display the intrinsic spin frequencies for neutron stars with measured orbital parameters. Up-to-date results on these sources are being made available through the public archive at the *Compton Observatory* Science Support Center (http://cossc.gsfc.nasa.gov/cossc/COSSC_HOME.html).

[1] Extracted with changes from "Observations of Accreting Pulsars", of which I was a major contributing author, to appear in the Astrophysical Journal Supplements 1997, 113, #2, by L. Bildsten, D. Chakrabarty, J. Chiu, M. H. Finger, D. T. Koh, R. W. Nelson, T. A. Prince, B. C. Rubin, D. M. Scott, M. Stollberg, B. A. Vaughan, C. A. Wilson and R. B. Wilson. Used by permission of the authors. I wrote the individual source descriptions for GRO J1744–28, GX 301–2, GRO J1750–27, 2S 1417–624, GRO J1948+32, GRO J1008–57, GRO J2058+42, 4U 1145–619 and A 1118–616. The remaining descriptions were contributed by the other co–authors.

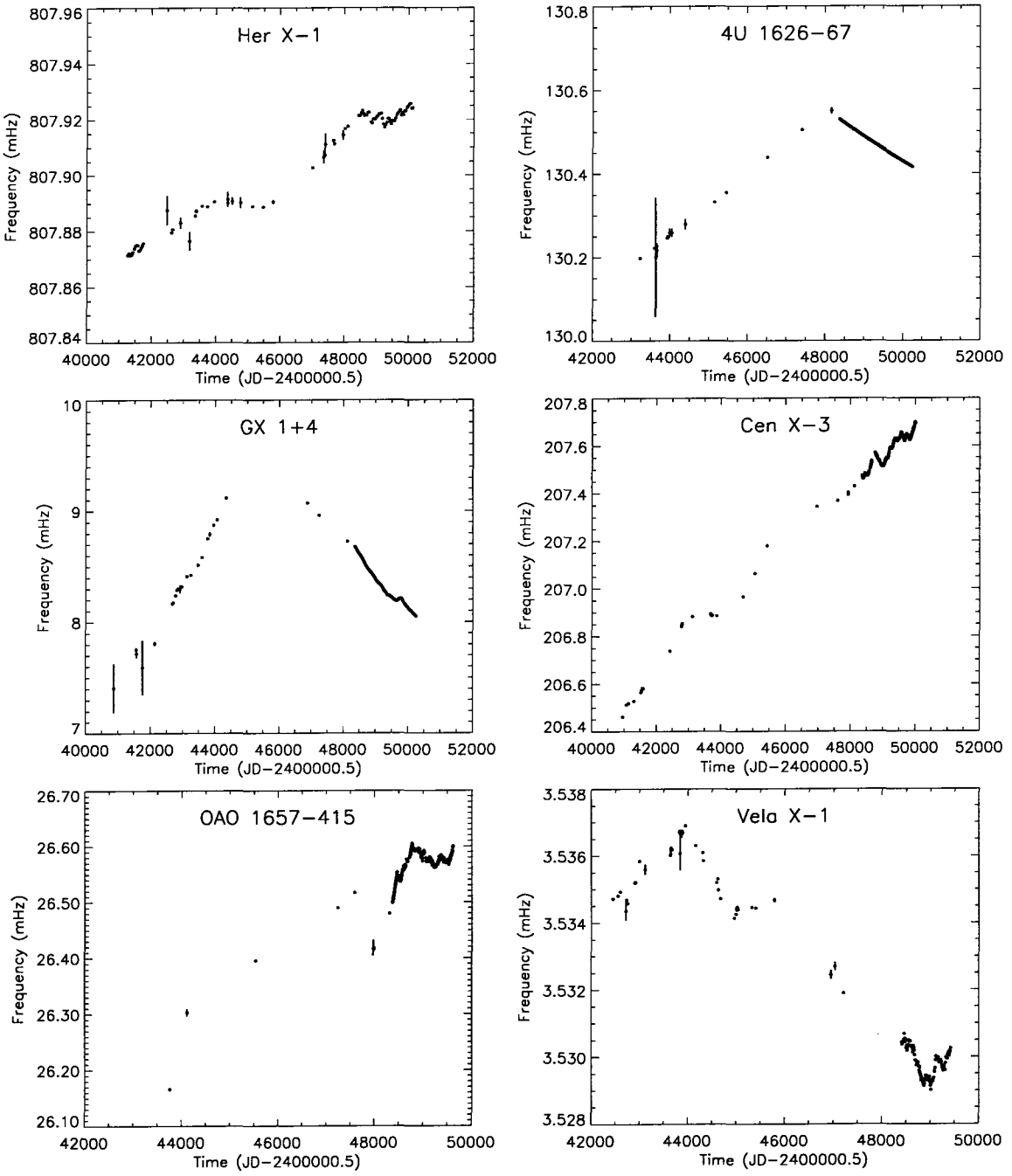
Her X−1
4U 1626−67
GX 1+4
Cen X−3
OAO 1657−415
Vela X−1
Frequency (mHz)
Time (JD−2400000.5)

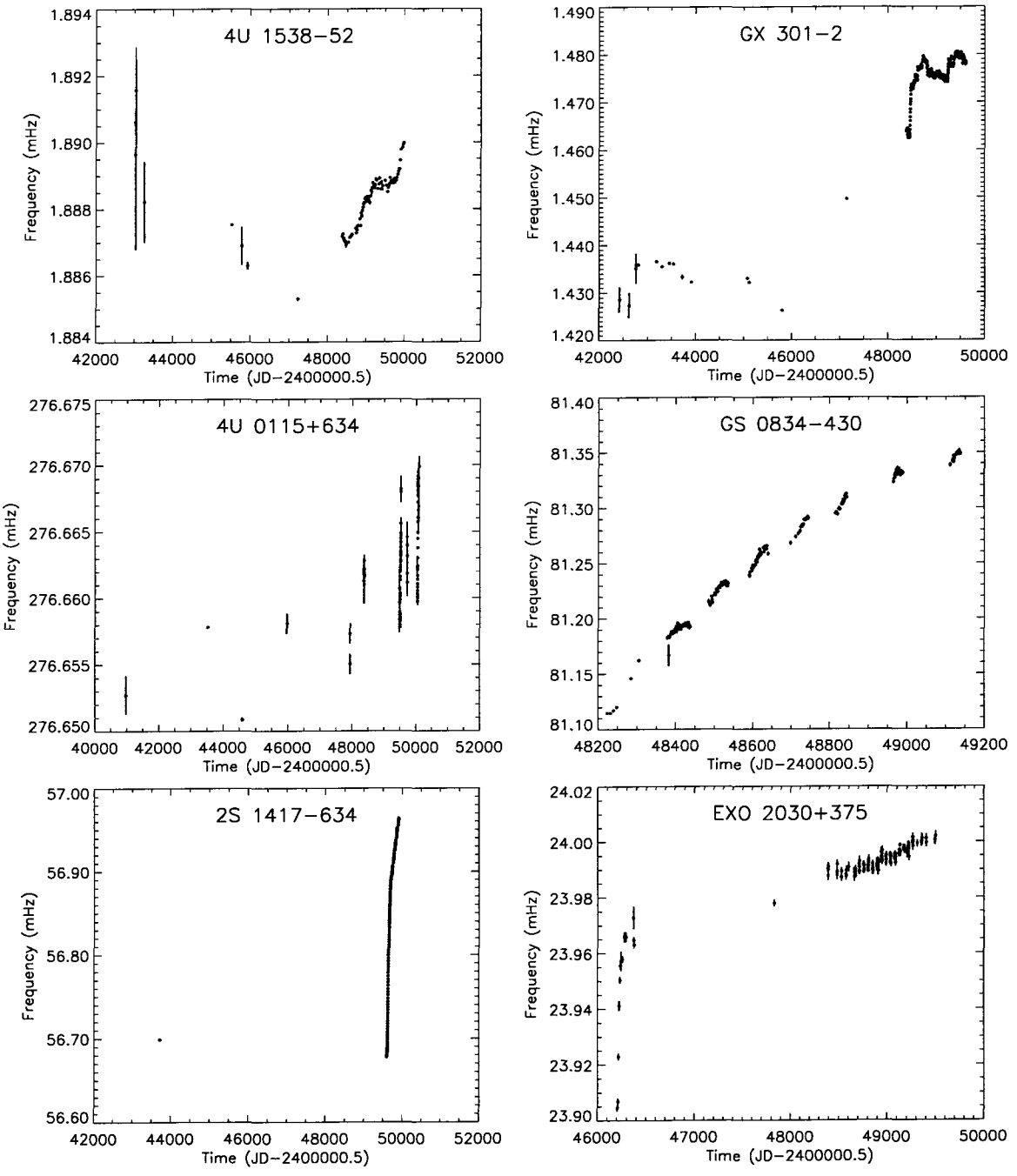
4U 1538−52
Frequency (mHz)
1.894
1.892
1.890
1.888
1.886
1.884
42000
44000
46000
48000
50000
52000
Time (JD−2400000.5)
GX 301−2
Frequency (mHz)
1.490
1.480
1.470
1.460
1.450
1.440
1.430
1.420
42000
44000
46000
48000
50000
Time (JD−2400000.5)
4U 0115+634
Frequency (mHz)
276.675
276.670
276.665
276.660
276.655
276.650
40000
42000
44000
46000
48000
50000
52000
Time (JD−2400000.5)
GS 0834−430
Frequency (mHz)
81.40
81.35
81.30
81.25
81.20
81.15
81.10
48200
48400
48600
48800
49000
49200
Time (JD−2400000.5)
2S 1417−634
Frequency (mHz)
57.00
56.90
56.80
56.70
56.60
42000
44000
46000
48000
50000
52000
Time (JD−2400000.5)
EXO 2030+375
Frequency (mHz)
24.02
24.00
23.98
23.96
23.94
23.92
23.90
46000
47000
48000
49000
50000
Time (JD−2400000.5)

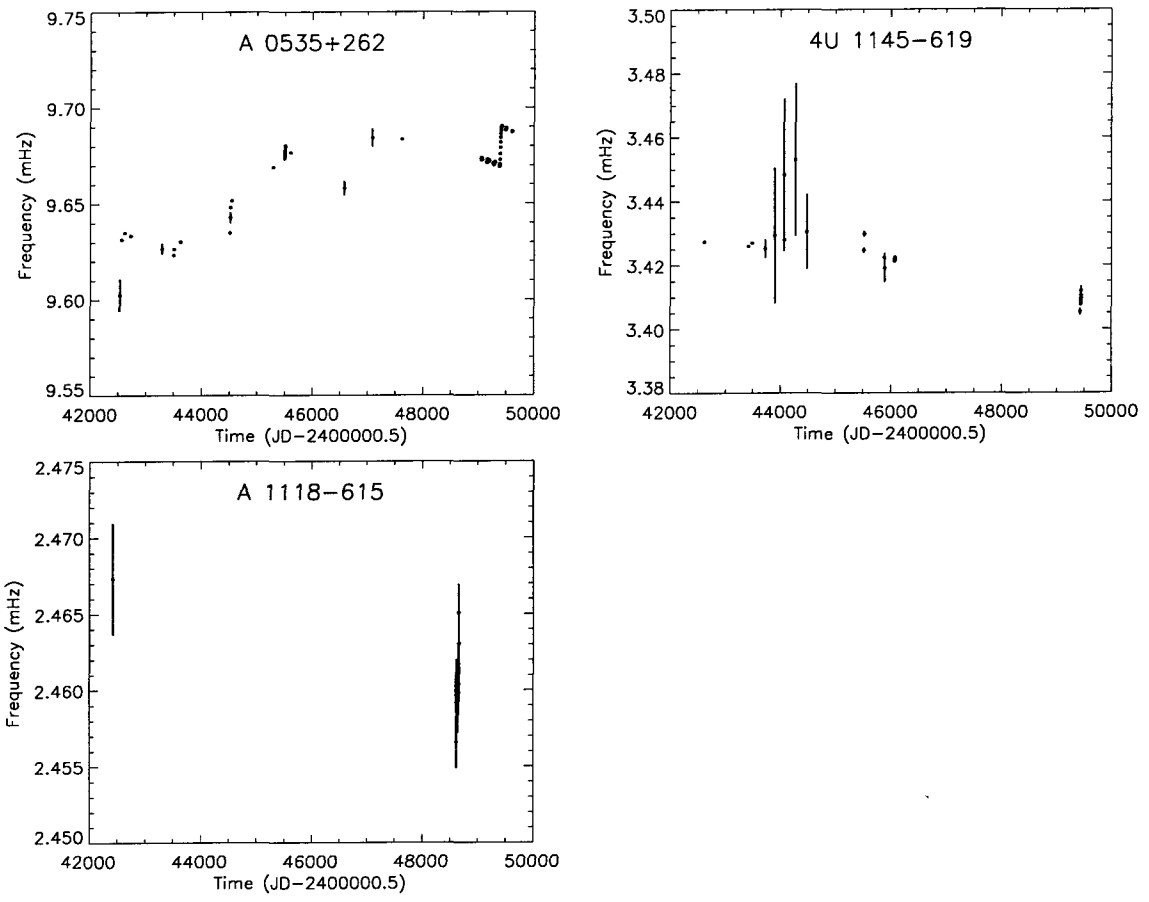

Figure 4.1: The long-term frequency history for all pulsars detected by BATSE that were previously known. The squares show the pre-BATSE data taken from Nagase (1989) and additional references. The line is the BATSE data, which we discuss later in great detail. The long term frequency history for X-ray pulsars observed by BATSE that were known prior to the *Compton Observatory* launch commences April 1991. For Her X-1, Cen X-3, Vela X-1, 4U 1538–52, GX 301–2, 4U 0115+634, and EXO 2030+375 all frequencies have been orbitally corrected. For OAO 1657–415, GS 0834–430, 2S 1417–62, and A 0535+262 orbital corrections have been applied only to the BATSE observations. No orbital corrections have been applied for 4U 1626–67, GX 1+4, 4U 1145–619, or A1118–615, which have unknown, or incompletely known, orbital elements. The BATSE frequencies for OAO 1657–415, GS 0834–430, EXO 2030+375, 4U 1145–619 and A 1118–615 are from the daily frequency history files we have deposited at the *Compton Observatory* archive. For the remainder of the objects, the frequencies are from source specific studies: Her X-1 (Wilson, et al., in prep.) 4U 1626–67 (Chakrabarty et al. 1997), GX 1+4 (Chakrabarty et al., in prep.), Cen X-3 (Finger et al. in preparation); Vela X-1 (Finger et al. in preparation); 4U 1538–52, (Rubin et al. in preparation); GX 301–2 (Koh et al. 1997); 4U 0115+634 (Cominsky et al. in preparation); 2S 1417–624 (Finger et al.(1996); and A 0535+262 (Finger et al. 1996).

Table 4.1
Spectral Parameters measured with BATSE

Source Name	Start [MJD]	End [MJD]	C_{30}[a] (PL)	α[b] (PL)	C_{30}[c] (EXP)	kT[d] (EXP)	Energy Range[e]	Pulsed Flux[f]
Low-mass systems								
Her X-1[g]	48376	50114	62–199	3.5–5.8	61-201	7.7–19	25–165	7.4–25
4U 1626–67	48450	48715	17.6(6)	4.66(17)	17.7(6)	10.8(6)	26–76	2.2
GX 1+4	48450	48715	57.3(6)	2.95(2)	49.6(5)	28.4(3)	26–126	6.2
High-mass supergiant and giant systems								
OAO 1657–415	48450	48715	45.6(6)	3.12(3)	40.7(6)	24.7(4)	26–125	5.1
Vela X-1	48450	48715	249(1)	4.05(1)	254(1)	13.56(3)	24–97	30.8
GX 301–2	48450	48715	127(1)	4.26(2)	130(1)	12.1(1)	25–74	15.8
Transient Be-binary systems								
GRO J1750–27	49960	49967	22(4)	5(1)	23(4)	10(3)	26–72	2.9(7)
2S 1417–624	49623	49698	37.8(7)	2.92(3)	33.9(6)	28.1(6)	26–124	4.3
EXO 2030+375	49170	49360	54.8(17)	3.60(8)	46.6(15)	23.0(1)	23–71	12.1
GRO J1008–57	49182	49215	103(1)	3.11(2)	99(1)	22.1(3)	25–96	12.2
A0535+26	49379	49430	451(1)	2.99(1)	392(1)	26.3(1)	27–100	49.2
4U 1145–619	49428	49439	219(1)	3.48(1)	205(1)	19.3(2)	26–123	25.1
A 1118–616	48621	48633	114(1)	3.66(4)	113(2)	16.2(3)	24–76	13.7
Transient systems with an undetermined companion								
GRO J1948+32	49448	49482	25.8(10)	2.88(8)	25.5(8)	22.9(11)	24–76	3.2
GRO J2058+42	49987	49993	113(8)	4.35(16)	87(6)	15.3(9)	35–100	10.5

[a]Normalization: 10^{-5} ph cm^{-2} s^{-1} keV^{-1} at 30 keV, photon power-law (PL) model $C_{30}(E/30\,\mathrm{keV})^{-\alpha}$
[b]Photon index, PL model
[c]Normalization: 10^{-5} ph cm^{-2} s^{-1} keV^{-1} at 30 keV, exponential (EXP) model $C_{30}(30\,\mathrm{keV/E})\exp[(\mathrm{E} - 30\,\mathrm{keV})/\mathrm{kT}]$
[d]Temperature (keV), EXP model
[e]Energy range used in fitting (keV)
[f]10^{-10} erg cm^{-2} s^{-1}, 20–50 keV, from EXP model. Highly variable for most sources.
[g]Fitted during Main Highs. Spectral shape varies. Table gives range of observed values.

In the following sections, we categorize the accreting pulsars by the type of star they are accreting from: low mass stars ($M \lesssim 2M_\odot$), OB supergiants, and main sequence Be stars. We then briefly summarize the BATSE observations of each individual binary, focusing on those results obtained from continuous timing and pulsed flux monitoring.

Spectral fits to the pulsed flux are tabulated in Table 4.1 for most sources. These are typical spectra. Exposure varies from source to source. The interval used for spectral fitting is not always the brightest the source displayed. For some sources, spectra could not be determined because the spin frequency was too high, the pulse profile varied with energy and/or luminosity, or the source was too weak.

Pulse profiles for all sources seen with BATSE are displayed in Figure 4.2. High energy pulse profiles in accretion-powered pulsars are generally simpler and smoother than those $\lesssim$10 keV, as they are less affected by circumstellar scattering and absorption. Thus,

they may be more indicative of the intrinsic radiation pattern from the neutron star. The profiles in Figure 4.2 can be classified broadly as single or double peaked. Cases where the pulse shape changes dramatically with energy or flux are discussed individually. Fluxes measured with BATSE have been found using both power-law and simple exponential models (see Appendix B).

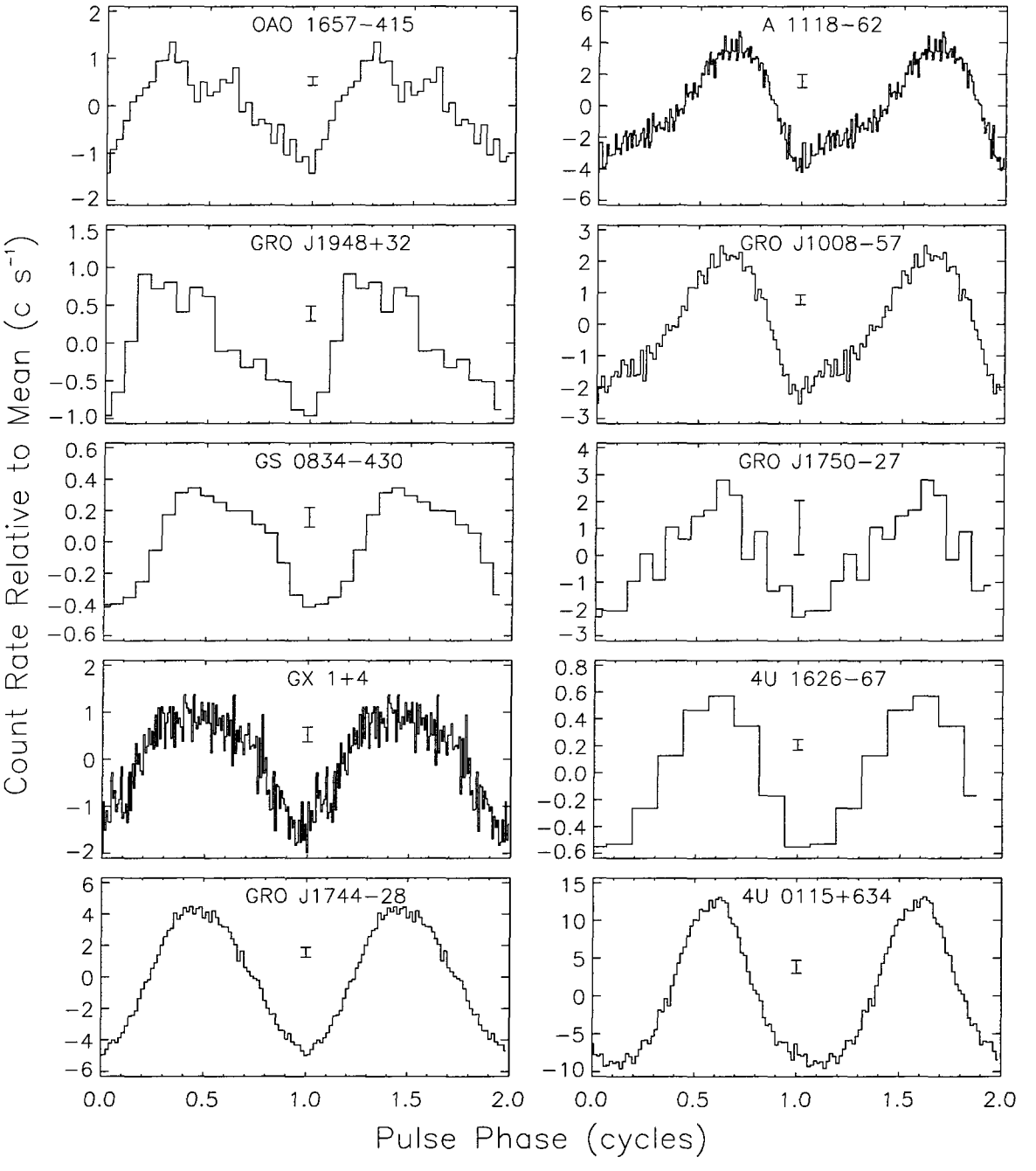
OAO 1657−415
A 1118−62
GRO J1948+32
GRO J1008−57
GS 0834−430
GRO J1750−27
GX 1+4
4U 1626−67
GRO J1744−28
4U 0115+634
Count Rate Relative to Mean (c s⁻¹)
Pulse Phase (cycles)

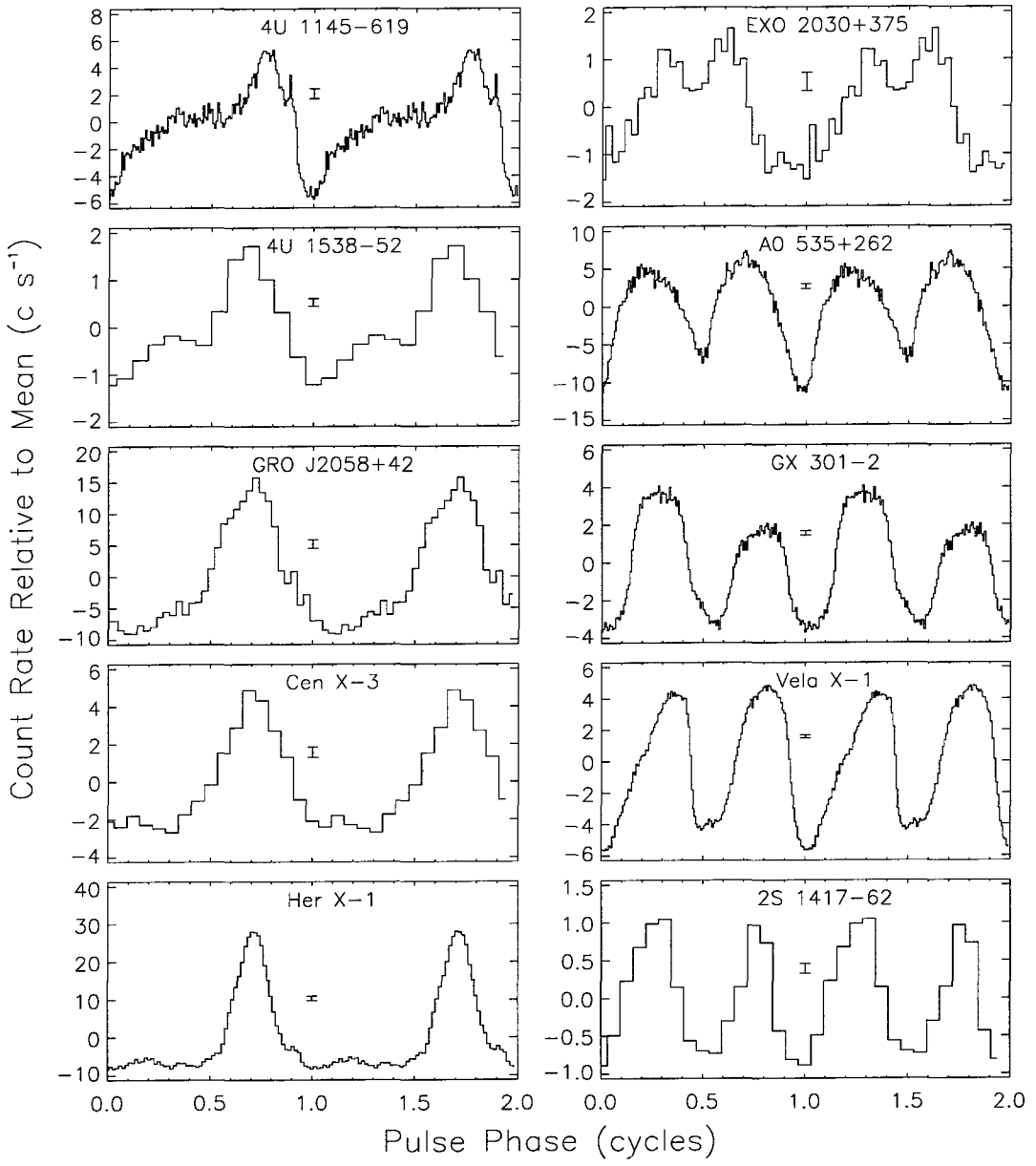

Figure 4.2: Pulse profiles of accreting pulsars from BATSE, in 20–35 keV except as noted. The 1σ error bar in each phase bin is also shown. The profile for GS 0834-430 was constructed using bin splitting rather than whole binning (see Wilson et al.1997). The range of days (in MJD) summed to construct the profiles for each of the sources (and energy range if different from above) are: a. OAO 1657–415 (48450–48715), A 1118–62 (48621–48633), GRO J1948+32 (49448–49482), GRO J1008–57 (49182–49215), GS 0834–430 (48518–48522), GRO J1750–27 (49960–49967; 20–70 keV), GX 1+4 (48450–48715), 4U 1626–67 (48450–48715), GRO J1744–28 (50092–50098), 4U 0115+634 (50049–50057; 20–40 keV) b. 4U 1145–619 (49428–49439), EXO 2030+375 (48450–48715), 4U 1538–52 (49350–9421; 20–50 keV), A0 535+262 (49379–49430), GRO J2058+42 (49987–49993; 20–40 keV), GX 301–2 (48450–48715), Cen X-3 (48985–48992), Vela X-1 (48450–48715), Her X-1 (49586–49593; 20–40 keV), 2S 1417–62 (49623–49698).

4.2 Low-Mass Systems

Only four accreting pulsars are definitely known to be orbiting low mass ($M \lesssim 2M_\odot$) stars: Her X-1 and GRO J1744–28 on the basis of timing-based measurements of their companions' mass functions (Tananbaum et al. 1972; Finger et al. 1996), 4U 1626–67 from optical photometry (Middleditch et al. 1981; Chakrabarty 1997), and GX 1+4 from spectroscopy (Davidsen, Malina, & Bowyer 1977; Chakrabarty & Roche 1997). This is a very heterogeneous class of objects: the mass donors are a main sequence A star (Her X-1), a probable $M_c < 0.1M_\odot$ helium or carbon-oxygen degenerate dwarf inferred from pulse timing (4U 1626–67), and two red giants (GX 1+4, GRO J1744–28). The absence of an observable companion in very deep optical and IR searches and the lack of orbital detections also suggest low mass companions for 4U 0142+61, 1E 1048.1–5937, RX J1838.4–0301 and 1E 2259+589 (see Mereghetti & Stella 1995 and references therein). We now discuss the BATSE observations of Her X-1, 4U 1626–67, GX 1+4, and GRO J1744–28.

Hercules X-1. — *Uhuru* discovered 1.2 s pulsations from Her X-1 (4U1656+354) in 1971 (Tananbaum et al. 1972) and the pulsar was subsequently found to be in an eclipsing, circular, 1.7 d orbit (Deeter, Boynton, & Pravdo 1981) around the low–mass companion HZ Her (Doxsey et al. 1973; Gottwald et al. 1991). This disk-fed system exhibits "super-cycles" of intensity modulated with a period of ≈35 d (Giacconi et al. 1973; Soong et al. 1990). At energies of 1-10 keV, the source is observed during both a "Main High" and "Short High" interval of the 35 day cycle. Detailed discussion of BATSE observations have appeared elsewhere (Wilson et al. 1994d; Wilson et al. 1994c).

BATSE detects pulsations for 5–10 days during each Main High interval. We report an average frequency for each Main High interval since reliable measurements of $\dot{\nu}$ within a Main High are hampered by the low signal-to-noise ratio of the BATSE data as well as pulse shape variations. Analyses of 20 Her X-1 Main High Observations through July 1993 found that the pulsed 20–70 keV luminosity varied by a factor of ∼4, and that the pulsar was spinning down during 35d cycles when the immediately preceding Main High interval luminosity (averaged over the peak days of the interval), and presumably the mass accretion rate, was low (Wilson et al. 1994d). Subsequent observations do not universally show a significant correlation of luminosity and $\dot{\nu}$, with some episodes of spin-

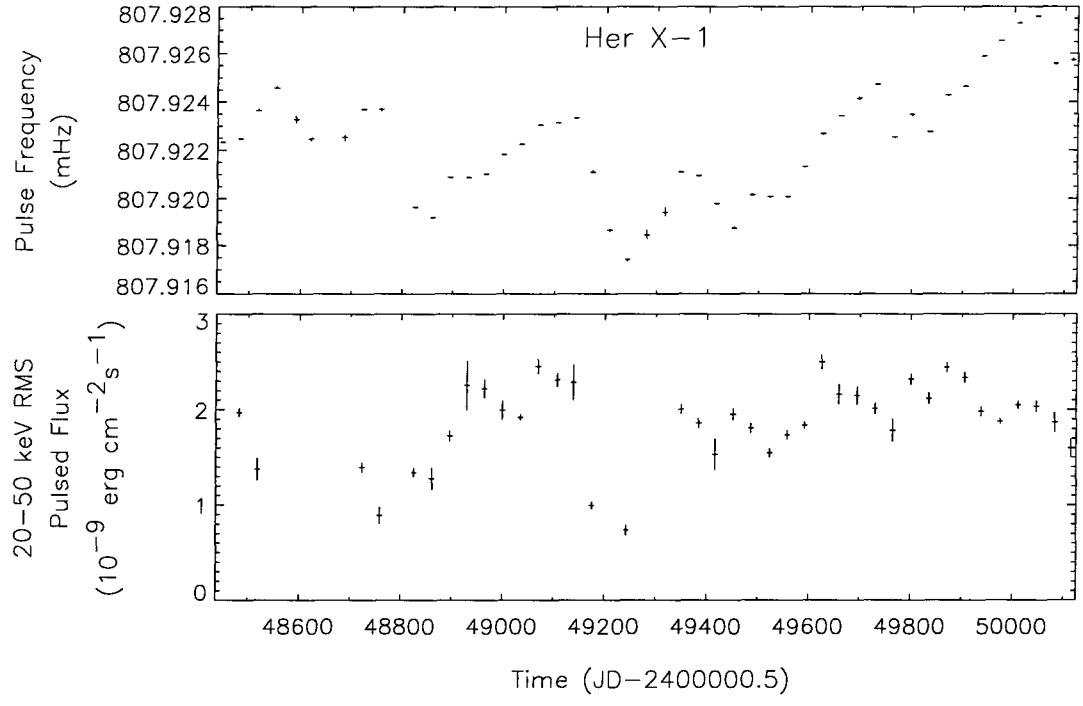

Figure 4.3: Her X-1 frequency and pulsed flux measurements from BATSE. A mean frequency has been determined for each Main High state for which adequate scheduled folded-on-board data was available. The frequencies, which have been orbitally corrected using parameters from Wilson et al.(1994a), were obtained using linear fits to pulse phases of 20–70 keV data (see Appendix B.1.3). Pulsed fluxes are the pulse phase-averaged flux obtained during one orbital period (averaged from eclipse egress to eclipse ingress) during the brightest portion of each available Main High state. An exponential model, with the e–folding energy allowed to vary, was used to obtain the fluxes (see Appendix B.2.3).

down following intervals with high flux levels. The neutron star is usually spinning up with $\dot{\nu}$ between zero and a maximum of 5×10^{-13} Hz s^{-1} between 32 of the 48 observed intervals. As is evident in Figure 4.3, the maximum spin-down rates are larger in magnitude, reaching 7×10^{-13} Hz s^{-1}.

4U 1626-67. — *SAS-3* discovered 7.68 s pulsations from 4U 1626-67 in 1977 (Rappaport et al. 1977) and the optical counterpart was later identified to be KZ TrA (McClintock et al. 1977). X-ray timing limits imply an ultra-compact binary with an extremely low-mass companion (Levine et al. 1988; Chakrabarty et al. 1997a). There is optical photometric evidence for a 42-min orbital period (Middleditch et al. 1981; Chakrabarty 1997), suggesting a mass of $< 0.1 M_{\odot}$ for the mass donor.

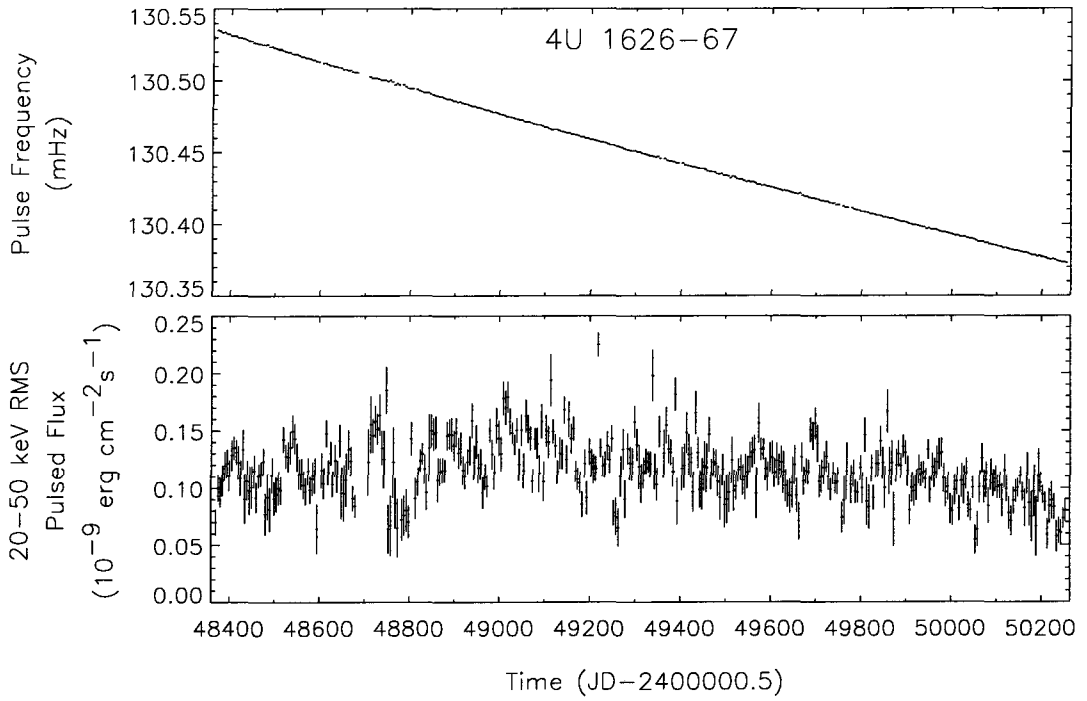

Figure 4.4: 4U 1626-67 frequency and pulsed flux measurements from BATSE. The spin frequencies, which have not been orbitally corrected since the orbit is unknown, were determined at 5–day intervals by searching the Fourier power spectrum of the 20-50 keV DISCLA data for the strongest signal in a small range around 7.7 s (see Appendix B.1.1). The pulsed fluxes were obtained by assuming a power law spectral model with a photon number index of 4.9 (see Appendix B.2.3).

Detailed discussion of BATSE observations have appeared elsewhere (Bildsten et al. 1994; Chakrabarty et al. 1997a). The neutron star was observed to spin up steadily during 1977-1991 and made a transition to steady spin-down at nearly the same rate of $|\nu/\dot{\nu}| \approx 5000\,\mathrm{yr}$ by the start of BATSE observations in 1991. Despite this torque reversal, there is no evidence for a large change in the bolometric flux from the source. The torque exerted on the neutron star is quiet, in the sense that the torque-fluctuation power measured by BATSE is the lowest measured for any X-ray pulsar and is comparable to the timing noise observed in young rotation-powered radio pulsars.

GX 1+4. — An 18–50 keV X-ray balloon experiment discovered ≈ 2 min pulsations from GX 1+4 in 1970 (Lewin, Ricker, & McClintock 1971). It is now known to be orbiting an M5 III giant (Davidsen, Malina, & Bowyer 1977; Chakrabarty & Roche 1997), making

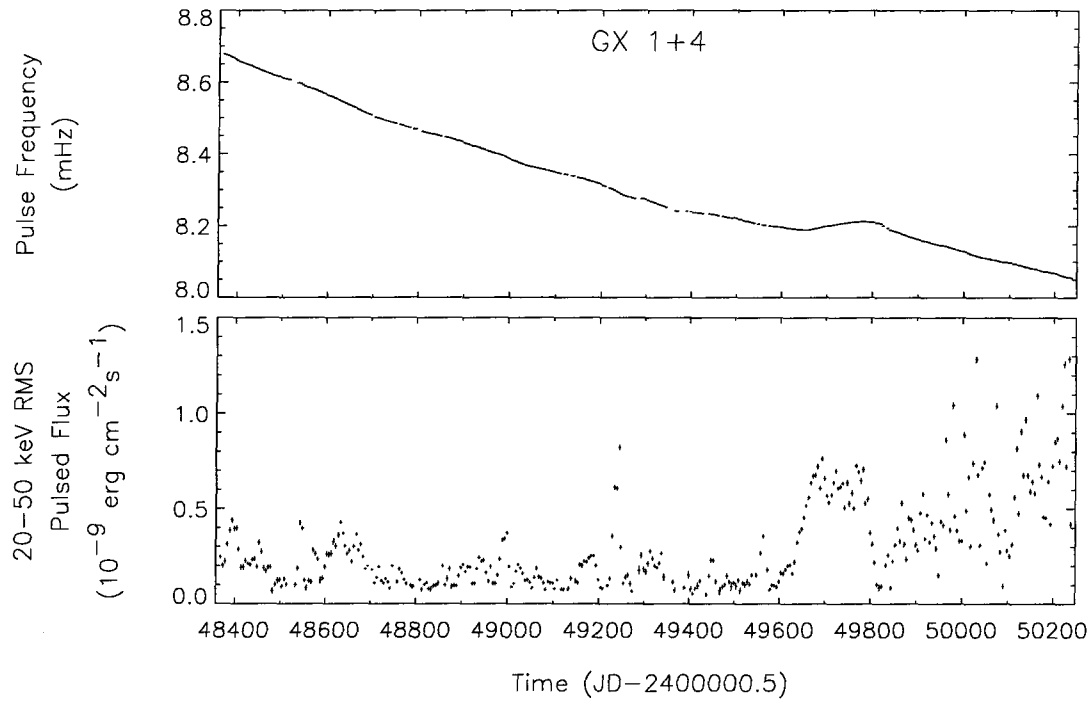

Figure 4.5: GX 1+4 frequency and pulsed flux measurements from BATSE. The spin frequencies, which have not been orbitally corrected since the orbit is unknown, were determined at 5–day intervals by searching the Fourier power spectrum of the 20–50 keV DISCLA data for the strongest signal in the pulse period range 110 s $\lesssim P_{\rm spin} \lesssim$ 130 s (see Appendix B.1.1). The pulsed fluxes were determined at 5–day intervals by assuming a power law spectral model with a photon number index of 2.5 (see Appendix B.2.3).

it the only accreting pulsar with a verified red giant donor. The binary period is unknown but believed to be of order years (Chakrabarty & Roche 1997). Throughout the 1970s, GX 1+4 was persistently bright and was spinning up on a time scale $|\nu/\dot{\nu}| \sim 40\,\mathrm{yr}$, increasing in frequency from $\sim$7.5 mHz to $\sim$9 mHz between 1970 and 1980 (Nagase 1989). After decreasing in flux by at least two orders of magnitude in the early 1980s, GX 1+4 was found by *GINGA* to be rapidly spinning down (Makishima et al. 1988).

Detailed discussions of the BATSE observations of GX 1+4 have appeared elsewhere (Chakrabarty et al. 1994a; Chakrabarty et al. 1997b) These observations found GX 1+4 to have the hardest spectrum of any accretion-powered pulsar, with pulsations clearly detected up to energies of 160 keV (Chakrabarty et al. 1997b). GX 1+4 is spinning down on average, on a time scale $|\nu/\dot{\nu}| \approx 40\,\mathrm{yr}$. During 1991–1994, BATSE observed a number of bright flares in the hard X-ray (20–100 keV) band which were accompanied by episodes of enhanced spin-down. A smooth torque reversal to spin-up accompanied an

extended bright state during late 1994 and early 1995 (Chakrabarty et al. 1994b), followed by a return to spin-down and a lower average hard X-ray flux (Chakrabarty et al. 1995b). During spin-down, the torque fluctuations exhibit a $1/f$ power density spectrum, similar to that seen in Cen X-3.

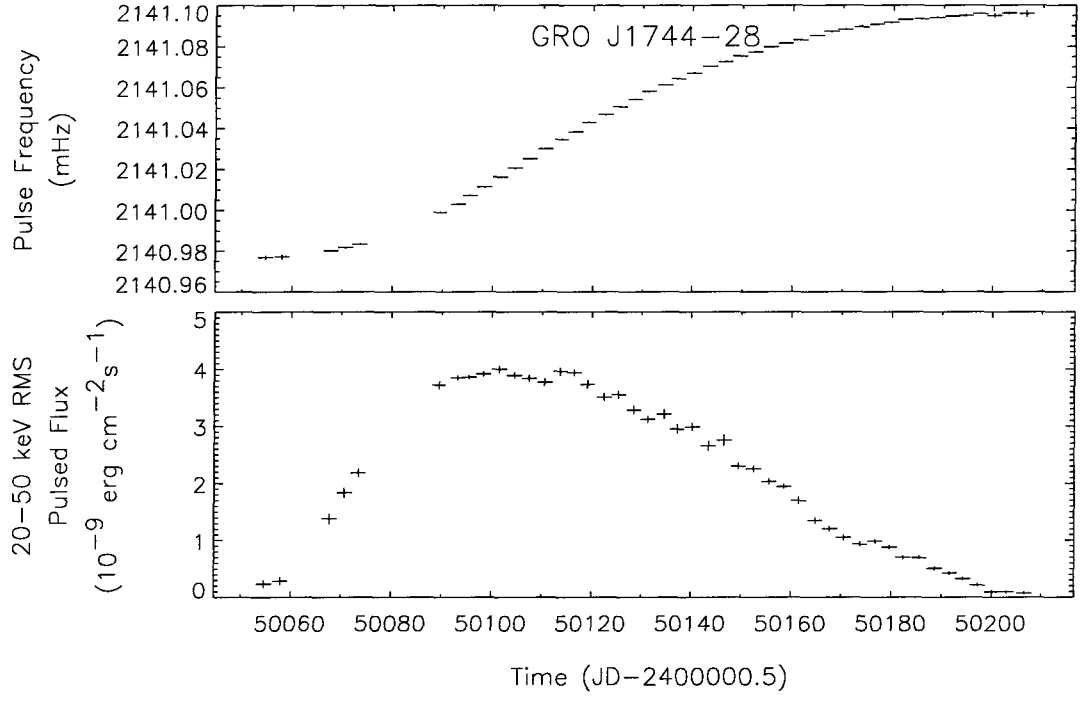

Figure 4.6: GRO J1744-28 frequency and pulsed flux measurements from BATSE. The spin frequencies, which have been orbitally corrected using parameters from Finger et al. (1996), were determined at 2–day intervals by fitting pulse phases derived from pulsar folded-on-board data in the 20-40 keV band (see Appendix B.1.3). The pulsed fluxes were obtained by assuming a spectra of the form $F(E) = AE^{-\lambda}\exp(-E/kT)$ with $\lambda = 2.0$ and $kT = 15$ keV, as determined by OSSE measurements (Strickman et al. 1996) (see Appendix B.2.3).

GRO J1744-28. — GRO J1744-28 was initially discovered by BATSE as an unusual bursting source in the direction of the Galactic Center (Kouveliotou et al. 1996). The discovery of coherent 467 ms pulsations by BATSE, and subsequent pulse timing unambiguously established GRO J1744-28 to be a neutron star in a circular 11.8–day orbit around a low–mass companion and indicated that the neutron star was spun–up by an accretion disk during the outburst (Finger et al. 1996). These are the first persistent pulsations seen in a

bursting X-ray source.

Detailed discussions of the BATSE observations of GRO J1744–28 have appeared elsewhere (Finger et al. 1996). One major outburst has been observed to date, spanning $\approx$ MJD 50053–50223. Another outburst which began on $\approx$ MJD 50253 lasted for only $\approx$ 1 week. The initial outburst showed enough dynamic range that the relation between accretion torque and pulsed flux could be tested directly (see Chapter 7). The 20–40 keV pulse profile is nearly sinusoidal, in stark contrast to the more complicated pulse shapes seen in other accretion powered pulsars (see Figure 4.2). Simultaneous 20–40 keV pulsed and Earth occultation DC flux measurements on 10–16 January 1996 (MJD 50092–50098) yielded a peak-to-peak pulsed fraction of $\approx$ 25% (Finger et al. 1996).

4.3 High-Mass Supergiant Systems

BATSE continuously monitors 5 pulsars which accrete from high-mass evolved supergiants: Cen X-3, OAO 1657–415, Vela X-1, 4U 1538–52 and GX 301–2. The long-term spin frequency evolution of these pulsars has revealed several surprises which challenge the standard model of such systems, as we discuss in Chapter 6. For example, Cen X-3 (the only high-mass supergiant system in the Roche Lobe filling region of the Corbet diagram observed by BATSE) exhibits short term ($\sim$ 50 d) spin–up and spin–down episodes. Moreover, the underfilled Roche-Lobe system GX 301-2 exhibits transient spin–up episodes, also of $\sim$ 50 d durations.

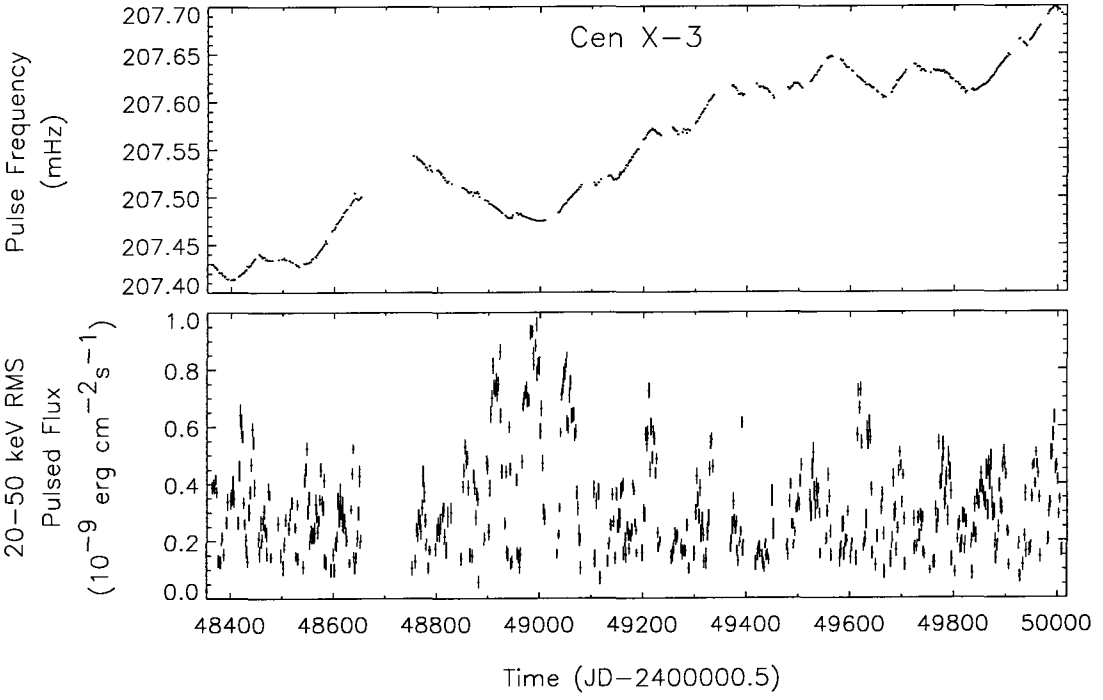

Figure 4.7: Cen X–3 frequency and pulsed flux measurements from BATSE. The intrinsic spin frequencies, which have been orbitally corrected using parameters from Finger et al.(1993), were determined at 2.1–day intervals by epoch-folding the 20-50 keV DISCLA data (see Appendix B.1.2). The pulsed fluxes were determined at 2.1–day intervals by assuming an exponential spectrum with a e–folding energy of 12 keV (see Appendix B.2.3).

Centaurus X-3. — *Uhuru* discovered 4.8 s pulsations from Cen X-3 in 1971, the first observation of an accreting pulsar (Giacconi et al. 1971). This bright, persistent, eclipsing pulsar is in a 2.1 d orbit (Kelley et al. 1983) around the O6–8 supergiant V779

Cen (Krzeminski 1974; Rickard 1974; Hutchings et al. 1979). An accretion disk is apparent from the optical light-curve (Tjemkes, Zuiderwijk, & van Paradijs 1986). Pre-BATSE observations by numerous pointed instruments found the neutron star to be gradually spinning up, although episodes of spin-down have been observed (Nagase 1989).

Detailed discussions of the BATSE observations of Cen X-3 have appeared elsewhere (Finger et al. 1992; Finger, Wilson, & Fishman 1994). These continuous observations found that the long term (~years) spin-up trend is actually the average effect of alternating 10~100 d intervals of spin-up and spin-down at a constant rate (Finger, Wilson, & Fishman 1994). Large excursions in the X-ray intensity occur on time scales of days to weeks, including bright flares lasting 10–40 days. A comparison of the orbital measurements made over the last 20 years reveals that the orbital period is decreasing (Kelley et al. 1983; Nagase et al. 1992). BATSE confirms this orbital decay (Finger et al. 1993), which is thought to be due to the tidal interaction of the neutron star with its companion.

OAO 1657–415. — *HEAO 1* discovered 38.22 s pulsations from OAO 1657-415 in 1978 (White & Pravdo 1979). BATSE observations revealed a 10.4 d binary orbit with a 1.7 d eclipse by the stellar companion (Chakrabarty et al. 1993), making it the seventh eclipsing X-ray pulsar discovered. The intrinsic spin frequency history reveals strong, stochastic variability and alternating episodes of steady spin-up and spin-down lasting 10–200 d, similar to what is seen in Cen X-3. Although the companion remains unidentified, it is inferred to be an OB supergiant from the neutron-star orbit (Table 1.2) and eclipse duration (Chakrabarty et al. 1993).

Chakrabarty et al. (1993) measured the binary orbital parameters using BATSE data spanning 1991 April 24 to 1992 July 23 (MJD 48370–48460). For the spin frequency history presented here, which extends far beyond the data used in the original orbital analysis, it was necessary to refine the orbital period. For this purpose the pulse frequencies obtained between 1991 April 24 and 1994 September 20 (MJD 48370–49615) were fitted using the Chakrabarty et al. (1993) orbital elements, with $P_{\rm orb}$ as a free parameter. The contribution to the uncertainty in $P_{\rm orb}$ from stochastic variations in accretion torque was estimated by assuming that ν performed a random walk with a strength of 2.5×10^{-17} Hz^2 s^{-1}, as estimated from the power spectrum of the frequency derivative measured at $P_{\rm orb}$ (Bildsten et al. 1997). The revised orbital period is $P_{\rm orb} = 10.44809(30)$ d, consistent

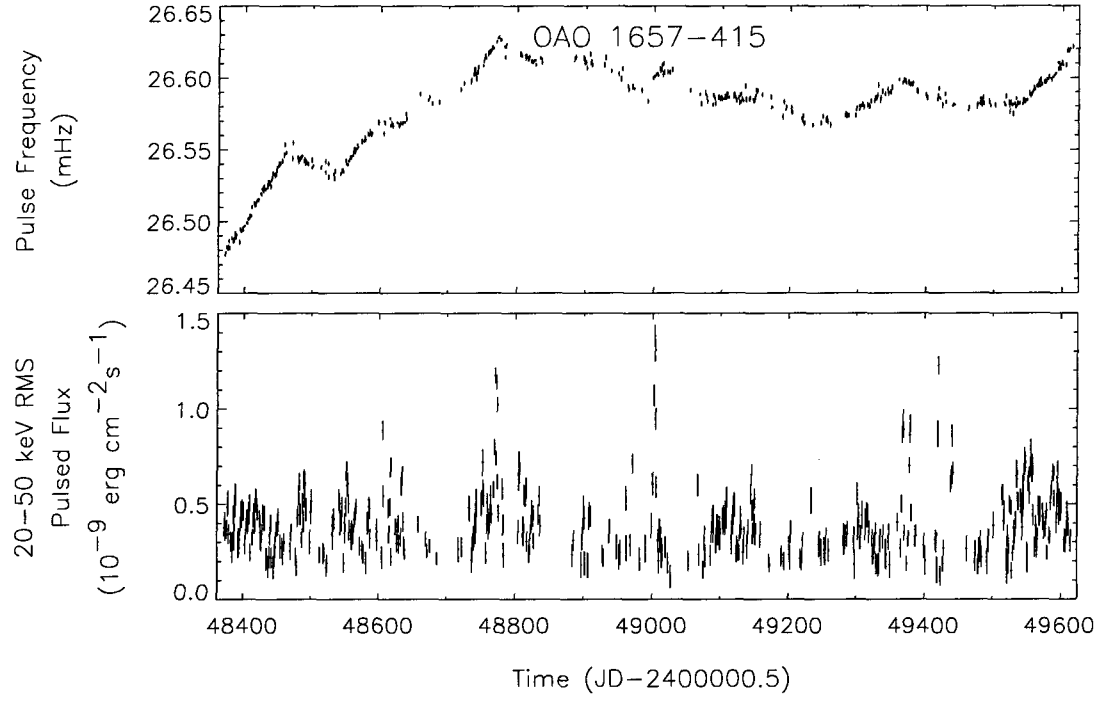

Figure 4.8: OAO 1657–415 frequency and pulsed-flux measurements from BATSE. The intrinsic spin frequencies, which have been orbitally corrected using parameters from Chakrabarty et al.(1993) and a refined orbital period of $P_{\rm orb}$ = 10.44809(30) d (see text below for details), were measured at 1–day intervals from the power spectra of the 15–55 keV CONT data (see Appendix B.1.1). The pulsed fluxes were measured at 1–day intervals by assuming an exponential spectrum with a e–folding energy of 20 keV (see Appendix B.2.3).

with the value measured by Chakrabarty et al. (1993), but of improved accuracy.

Vela X-1. — *SAS-3* discovered 283 s pulsations from the eclipsing binary Vela X-1 in 1975 (McClintock et al. 1976) and pulse timing revealed this pulsar to be in an 8.96 d eccentric orbit (Rappaport, Joss, & McClintock 1976, Finger et al.(1997), in preparation) around the B0.5Ib supergiant HD77581 (Hiltner, Werner, & Osmer 1972; van Kerkwijk et al. 1995). The optical light-curve of the companion shows ellipsoidal variations, indicating that the star is substantially distorted by the tidal field from the neutron star (Tjemkes, Zuiderwijk, & van Paradijs 1986).

Vela X-1 is the brightest persistent accretion-powered pulsar in the 20–50 keV energy band. Individual pulses are often visible in the raw data. BATSE observations

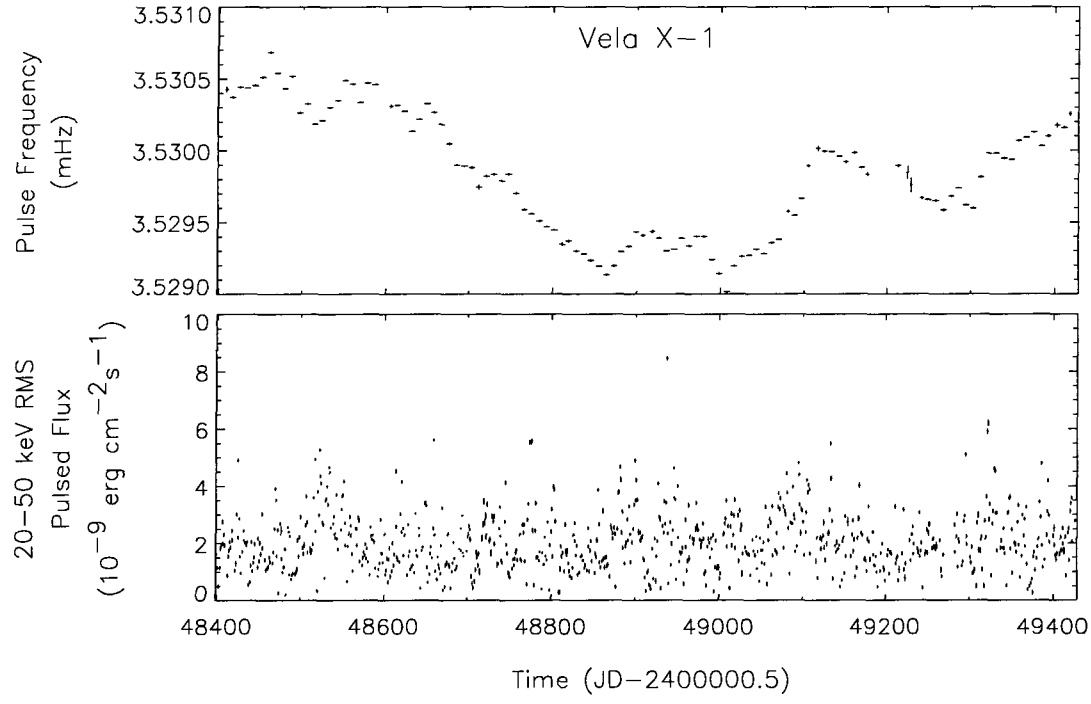

Figure 4.9: Vela X-1 spin frequency and pulsed flux measurements from BATSE. The intrinsic spin frequencies, which have been orbitally corrected using parameters from Finger et al. (1997), in preparation, were determined by fitting pulse phase measurements (see Appendix B.1.3). Each point uses the uneclipsed data of the 8.96 d binary orbit. The pulsed fluxes were determined at 1–day intervals by assuming an exponential spectrum with a e–folding energy of 20 keV (see Appendix B.2.3).

showed Vela X-1 alternating between spin-up and spin-down, with no long-term trend in spin frequency, consistent with pre-BATSE observations of a random-walk in spin frequency (Deeter et al. 1989). Pulse profiles in the BATSE energy range are double peaked and vary slightly with both energy and time, with some evidence for a correlation between luminosity and pulse shape. At lower energies the pulse profiles are more complex, showing dramatic changes with energy (Raubenheimer 1990).

4U 1538–52. — *Ariel 5* discovered 530 s pulsations from 4U 1538-52 in 1976 (Davison, Watson, & Pye 1977) and pulse timing revealed this pulsar to be in a 3.7 d circular orbit (Davison, Watson, & Pye 1977; Corbet, Woo, & Nagase 1993) around the B0 supergiant companion, QV Nor (Parkes, Murdin, & Mason 1978), which most likely underfills its Roche lobe (Crampton, Hutchings, & Cowley 1978). Pre-BATSE data shows

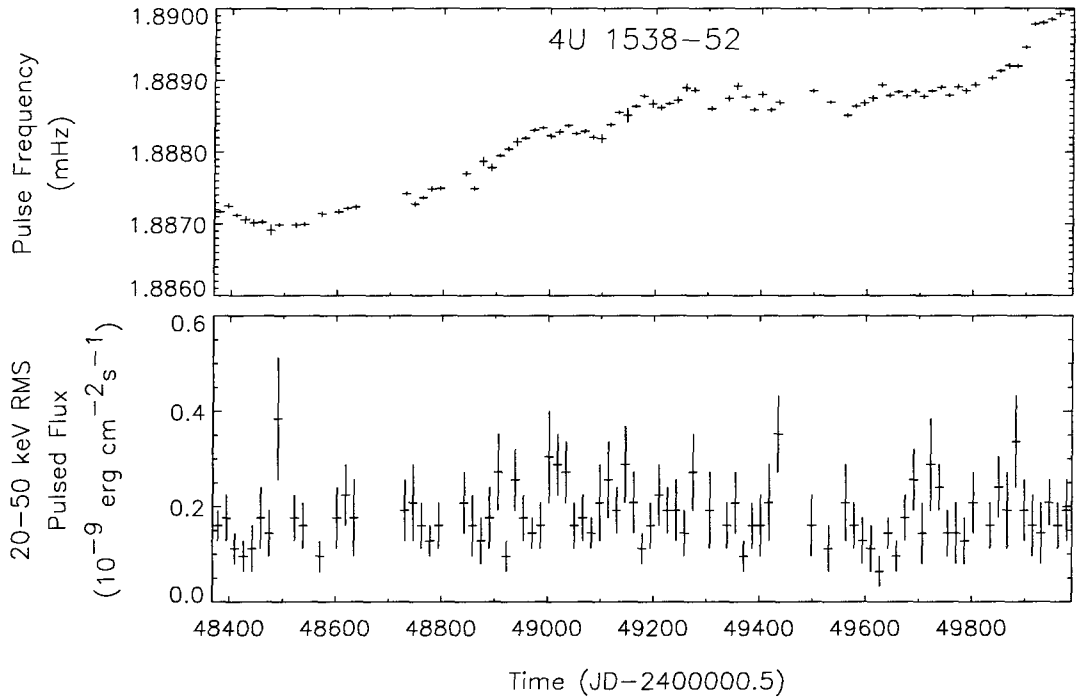

Figure 4.10: 4U 1538-52 spin frequency and pulsed flux measurements from BATSE. The intrinsic spin frequencies, orbitally corrected using parameters from Rubin et al.(1997), were determined at 16 d intervals by epoch folding the 20–50 keV DISCLA data at a range of trial frequencies after subtracting the background model of Rubin et al.(1996) (see Appendix B.1.2). Measurements are obtained only once every 16 days due to the low flux from the object and BATSE's poor sensitivity at long periods.

a long term spin down trend with random pulse period variations on shorter time scales (Nagase 1989).

Detailed BATSE observations of 4U 1538–52 have appeared in Rubin et al.1994. These observations revealed a reversal of the secular torque to long-term spin-up at an average rate of $\dot{\nu} = 1.8 \times 10^{-14}$ Hz s^{-1}. However, the change in ν is comparable in magnitude to what one would predict from the observed torque-noise strength of $\sim 10^{-20}$ Hz^2 s^{-2} Hz^{-1} (Bildsten et al. 1997), and is thus consistent with being the result of a random walk in frequency. Combining orbital epochs measured with BATSE with those determined from previous experiments has led to an improved value for the orbital period (see footnote to Table 1.2) and a 95% confidence limit on the rate of change of $\dot{P}_{\rm orb}$ of $-3.9 \times 10^{-6} < \dot{P}_{\rm orb}/P_{\rm orb} < 2.1 \times 10^{-6}$ yr^{-1} (Rubin et al. 1997).

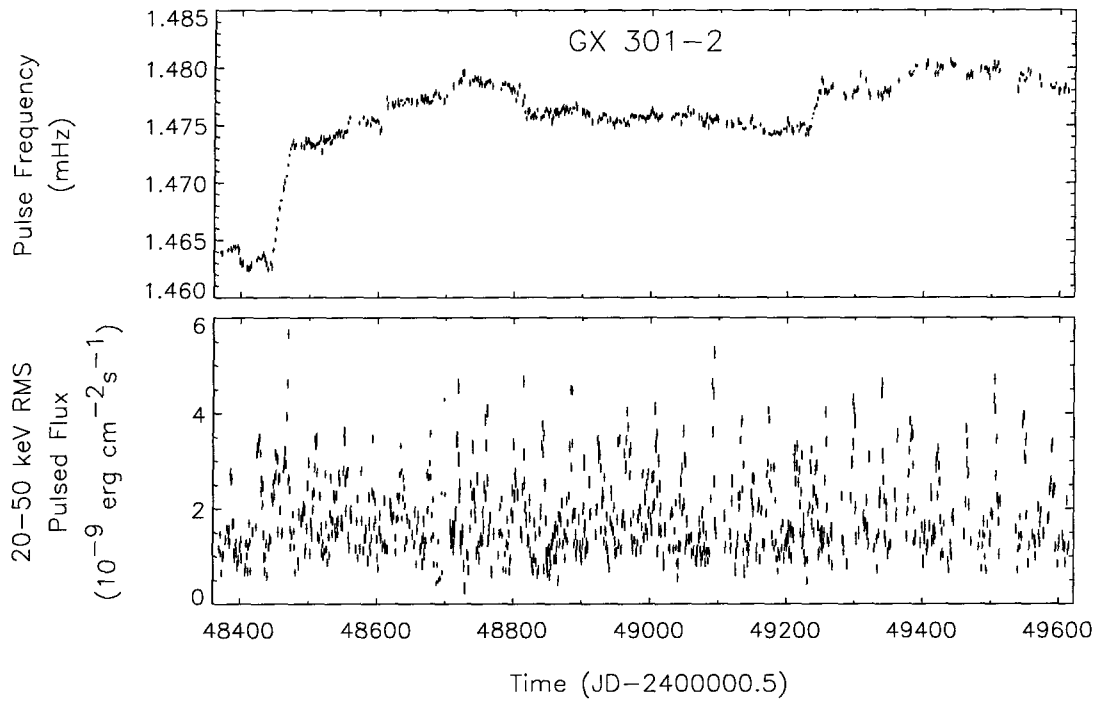

Figure 4.11: GX301–2 frequency and pulsed flux measurements from BATSE. The intrinsic spin frequencies, which have been orbitally corrected using parameters from Koh et al.(1997), were measured at 2–day intervals by searching the Fourier power spectrum of the 15–55 keV CONT data for the strongest signal in a range around the previously observed pulse frequency (see Appendix B.1.1). The pulsed fluxes were measured at 2–day intervals by assuming an exponential spectrum with a e–folding energy of 10 keV (see Appendix B.2.3).

GX 301–2. — *Ariel 5* discovered 700 s pulsations from GX 301-2 (4U 1223-62) (White et al. 1976) and subsequent observations revealed the neutron star to be in a 41.5 day eccentric ($e = 0.47$) orbit (Sato et al. 1986) around the supergiant Wray 977 (Parkes et al. 1980; Kaper et al. 1995). Between 1975 and 1985, the neutron star was, on average, neither spinning up nor down, indicative of wind accretion. However, a prolonged period of spin–up at $\dot{\nu} \approx 2 \times 10^{-13}$ began in 1985 (Nagase 1989).

Detailed discussion of BATSE observations have appeared elsewhere (Koh et al. 1997). BATSE observed two rapid spin-up episodes with $\dot{\nu} \approx$ (3–5) $\times 10^{-12}$ Hz s^{-1}, each lasting ~30 days, probably indicating the formation of a transient accretion disk. Except for these spin-up episodes, there are virtually no net changes in ν on long time scales, suggesting that the long-term spin-up trend observed since 1985 may be due entirely to brief ($\approx$ 30 d) spin-up episodes similar to those we have discovered. In addition to confirming

the previously known flare which occurs ≈ 1.4 d before periastron, BATSE occultation and pulsed-flux measurements folded at the orbital period reveal a smaller flare near apastron (Pravdo et al. 1995; Koh et al. 1997). Orbital parameters measured with BATSE are consistent with previous measurements, with improved accuracy in the orbital epoch (Koh et al. 1997, Table 1.2). Simultaneous pulsed and occultation fluxes measured near periastron yield a 20–55 keV peak-to-peak pulsed fraction of ≈ 0.5 (Koh et al. 1997).

4.4 High-Mass Transient Systems

BATSE has discovered four new high-mass, transient accreting pulsars (GRO J1008–57, GRO J1948+32, GRO J2058+42, and GRO J1750–27), two of which (GRO J2058+42 and GRO J1008–57) have repeated. In addition, BATSE has observed multiple outbursts of the previously known transient accreting pulsars 4U 0115+63, GS 0834–43, 2S 1417–62, A 0535+26, 4U 1145-619 and EXO 2030+375, and a single outburst from A 1118–615. Outburst times and durations are shown in Figure 4.12.

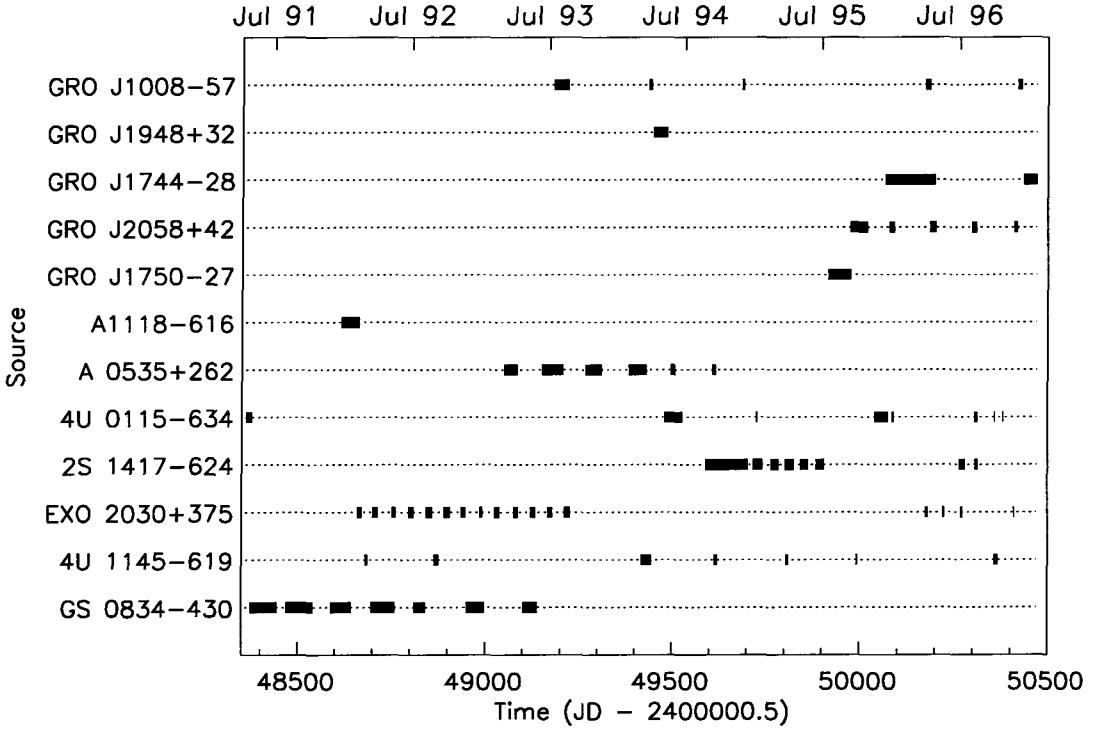

Figure 4.12: Outburst times for all transient accreting pulsars observed by BATSE.

BATSE has observed a series of regularly-spaced outbursts from several transient pulsars. This was the case for GRO J1008–57 (5 outbursts), GRO J2058+42 (5 outbursts), A 0535+26 (6 outbursts), 4U 0115–634 (4 outbursts), 2S 1417–62 (8 outbursts), EXO 2030+375 (17 outbursts), 4U 1145–619 (7 outbursts) and GS 0834–430 (7 outbursts). In some cases one or more outbursts were missing from the sequence. In the case of GS 0834–43 the spacing of the final two outbursts was irregular.

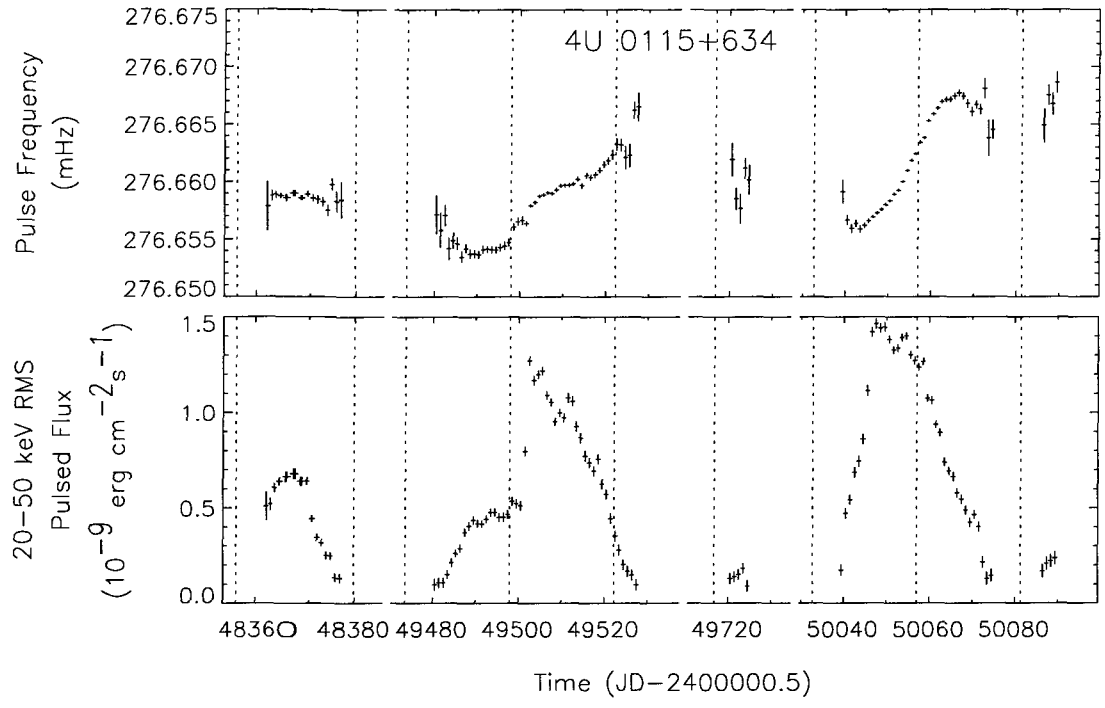

Figure 4.13: 4U 0115+634 frequency and flux measurements from BATSE. The intrinsic spin frequencies, which have been orbitally corrected using the orbital parameters discussed in the text, were determined at 1–day intervals by epoch folding the 20–50 keV DISCLA data at a range of trial frequencies (see Appendix B.1.2). The pulsed fluxes were determined at 1–day intervals by assuming an exponential spectrum with an e–folding energy of 15 keV (see Appendix B.2.3). The gaps in Figure 4.13 are extended intervals when the source was undetectable with BATSE.

4U 0115+634. — *SAS-3* discovered 3.6 s pulsations from 4U 0115+634 in 1978 (Cominsky et al. 1978) and subsequent pulse-timing revealed the pulsar to be in a 24 d eccentric orbit (Rappaport et al. 1978) around the heavily reddened Be Star, V635 Cas (Johns et al. 1978). To date, BATSE has observed 5 outbursts from 4U 0115+634. A 48 day outburst from 1994 May 7 – June 24 (MJD 49480–49528) (Scott et al. 1994; Wilson, Finger, & Scott 1994) showed a sudden rise in pulsed flux at the middle of the outburst, shortly following periastron passage (MJD 49498.1). A 36 day outburst from 1995 November 17 – December 27 (MJD 50039–50075) (Finger et al. 1995) was also seen by *GRANAT*/WATCH (Sazonov & Sunyaev 1995). This was immediately followed in 1996 January by a short weak outburst. Not shown in Figure 4.13 is a 10 day outburst in August 1996 (Scott et al. 1996).

We estimated the epoch of periastron for the outbursts in 1991 April, 1994 May–June, and 1995 November–December by fitting the phase measurements for each data set

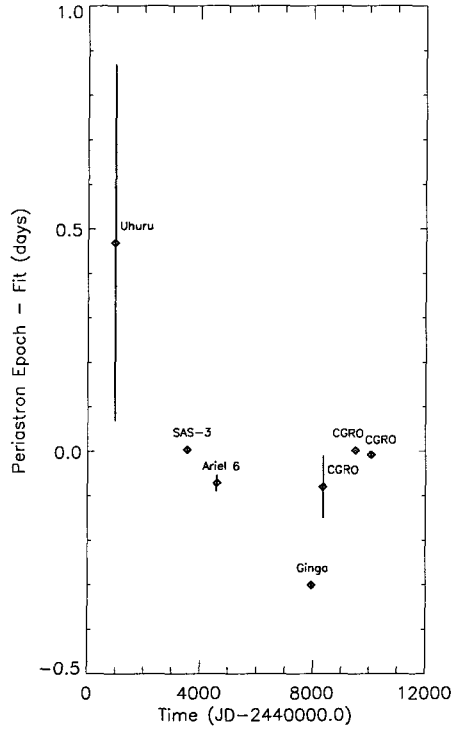

Figure 4.14: Measurements of the 4U 0115+63 periastron epoch. The plot shows the periastron epochs minus the linear ephemeris MJD $49279.2677 + 24.317037 * n$ where n is an integral number of orbits. This ephemeris is discussed in the text. The epoch measurements have been determined from Uhuru (Kelley et al. 1981), SAS-3 (Rappaport et al. 1978), Ariel 6 (Rickets et al. 1981), *GINGA* (Tamura et al. 1992) and this work. Excluding the *GINGA* measurement, the observations are consistent with a constant orbital period.

with a polynomial in pulse emission time using the orbital elements from Rappaport et al.(1978), but allowing the epoch of periastron to vary. This resulted in periastron epochs of MJD 48355.44(7), 49498.1232(15) and 50057.4015(32), which are plotted in Figure 4.14 along with previous determinations. The *GINGA* result (Tamura et al. 1992) deviates from the trend of the other points. This may be due to an incorrect phase connection in that poorly sampled data set. Discarding this point, we find a best fit linear ephemeris of the periastron epoch T_p =MJD49279.2677(34)+n×24.317037(62). The frequencies in Figure 4.13 are orbitally corrected using this ephemeris in combination with the remaining Rappaport et al. (1978) elements.

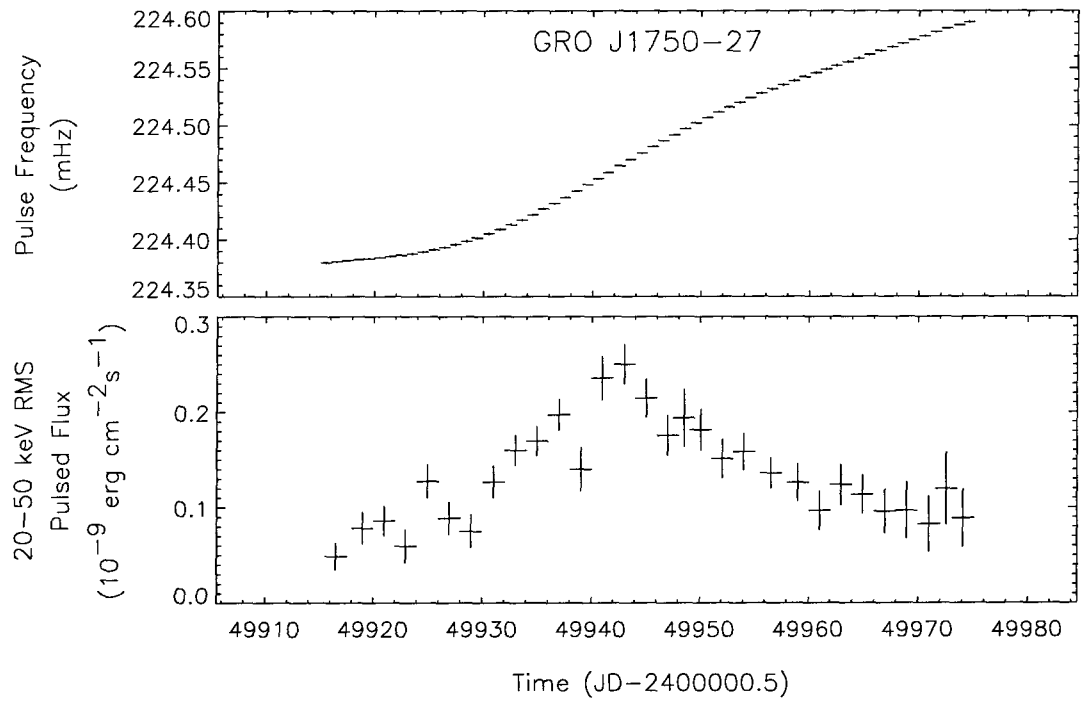

Figure 4.15: GRO J1750-27 spin frequency and pulsed flux measurements from BATSE. The intrinsic spin frequencies, which have been orbitally corrected using parameters from Scott et al.(1997), were determined at 1–day intervals from fits of phase measurements of the 20–50 keV DISCLA data (see Appendix B.1.3). The pulsed fluxes were determined at 1–day intervals by assuming an exponential spectrum with an e–folding energy of 20 keV (see Appendix B.2.3).

GRO J1750-27. — BATSE discovered and observed a single 60 d outburst from the 4.4 s accreting pulsar GRO J1750-27 from 1995 July 7 to September 18 (MJD 49915–49978)

(Wilson et al. 1995b; Scott et al. 1997). Pulse timing revealed an eccentric 29.82 d orbit. A 0.5° localization with BATSE (Koh et al. 1995) motivated an *ASCA* TOO which successfully localized the object to $\approx 2'$ (Dotani et al. 1995). Although no optical counterpart has been reported, the orbital period and pulse period of GRO J1750-27 place it squarely in the Be transient region of the Corbet Diagram (Figure 1.1). Steady spin–up with a peak value of 3.8×10^{-11} Hz s^{-1} coupled with a correlation between the spin–up rate and the pulsed flux strongly suggests accretion from a disk (Scott et al. 1997).

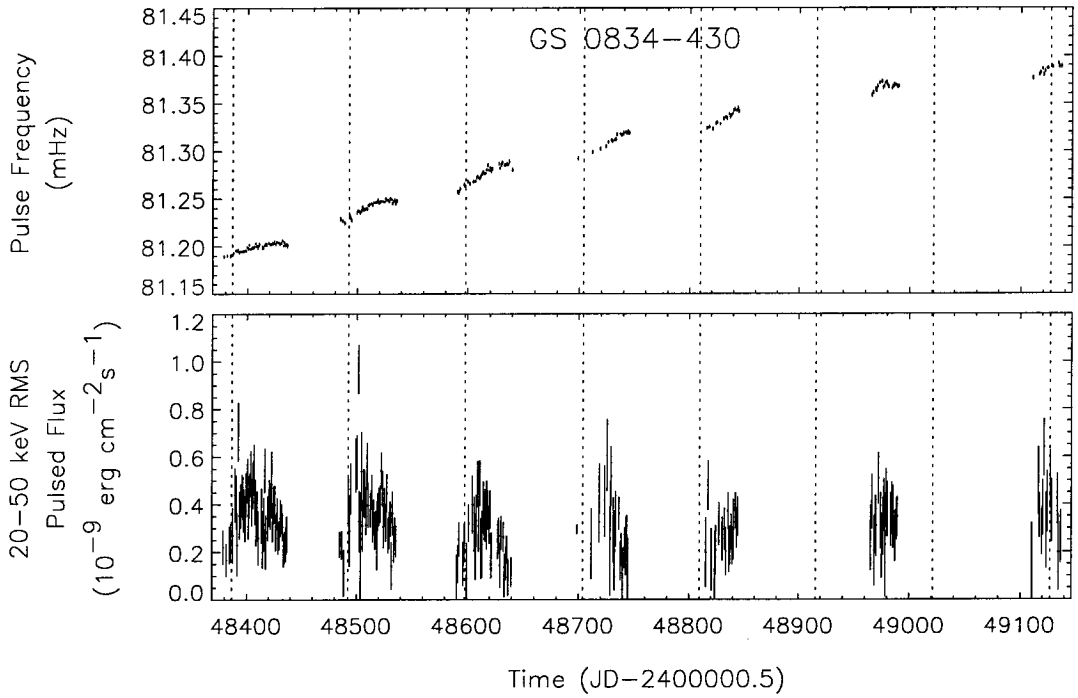

Figure 4.16: GS 0834-430 frequency and flux measurements from BATSE. The intrinsic spin frequencies, which have been orbitally corrected using parameters from Wilson et al.(1997), were determined at 1-day intervals from the power spectra of the 20–70 keV CONT data (see Appendix B.1.1). The pulsed fluxes were determined at 1–day intervals by assuming an exponential spectrum with an e–folding energy of 14 keV (see Appendix B.2.3).

GS 0834-430. — GS 0834-430 was first detected in 1990 February by *GRANAT/WATCH*, but confusion with the X-ray burster MX 0836-42 made unambiguous identification difficult (Lapshov et al. 1992). Subsequent observations with *GINGA* revealed 12.3 s pulsations (Aoki et al. 1992). The optical counterpart is still unknown. A detailed discussion

of BATSE observations has appeared elsewhere (Wilson et al. 1997). To date, BATSE has observed 7 outbursts with durations of 30–70 days, the first 5 of which were spaced at 105–107 d intervals and the last 2 of which were unevenly spaced (Wilson et al. 1997). The eccentricity e and semi-major axis $a_x \sin i$, given in Table 1.2. are individually poorly determined due to large spin-up torques during the outbursts, but $e \times a_x \sin i = 15^{+6}_{-1}$ lt-s is well constrained, thus establishing that the orbit is eccentric. This and the recurrent outburst behavior is strongly reminiscent of the Be transients, although GS 0834-430 falls below the Be-binary trend on the Corbet diagram (Figure 1.1). Pulsations are seen in the energy range 20–70 keV, and simultaneous 20–70 keV pulsed and Earth occultation DC flux measurements on 1991 June 15–28 1991 (MJD 48422–48435), September 19–October 3 (MJD 48518–48532), December 15–27, (MJD 48605–48617) and 1992 July 16–29 (MJD 48819–48832) yielded consistent peak-to-peak pulsed fractions of 10–15%, and marginal evidence for an increase of pulsed fraction with energy. The pulse profiles vary with both energy and time (Wilson et al. 1997).

2S 1417–624. — *SAS-3* discovered 17.6 s pulsations from 2S 1417–624 in 1978 (Kelley et al. 1981a) and the companion was later identified to be a 17th magnitude OB star (Grindlay, Petro, & McClintock 1984). Detailed discussion of BATSE observations have appeared elsewhere (Finger, Wilson & Chakrabarty 1996). BATSE observed a large outburst of 2S 1417–624 from 1994 August 29 – December 11 (MJD 49593–49697), followed by a sequence of five smaller outbursts of diminishing amplitudes occuring every ~40 days (Finger, Wilson, & Chakrabarty 1996), and two later outbursts (not shown). At the peak of the initial outburst, pulsations were detected up to 100 keV. The pulse profile is double-peaked and the ratio of the flux in the two peaks changed systematically during the initial outburst. The binary orbit was measured by a pulse timing analysis, assuming that the accretion torque was correlated with the measured pulsed flux. During the large outburst the spin-up rate reached $\dot{\nu} \simeq 4 \times 10^{-11}$Hz s^{-1}.

GRO J1948+32. — BATSE discovered and observed a single, 35 day outburst from the 18.7 s X-ray pulsar GRO J1948+32 from 6 April to 12 May 1994 (MJD 49448–49482) and localized the source to within 10 deg^2 (Chakrabarty et al. 1995a). The pulse

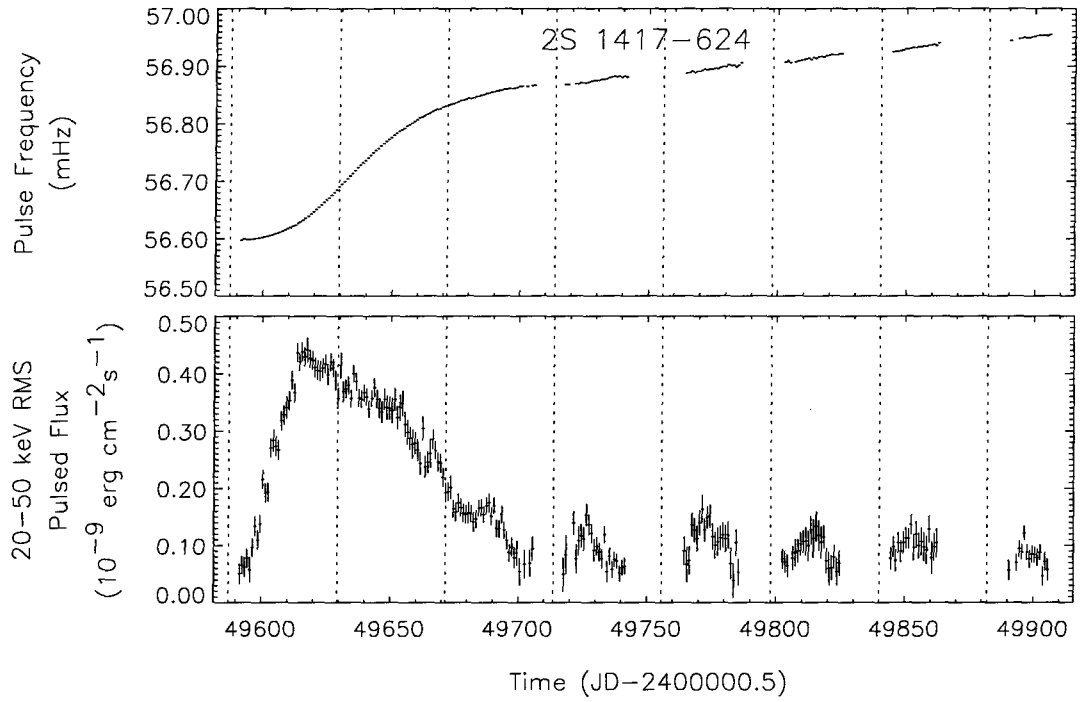

Figure 4.17: 2S 1417–624 frequency and pulsed flux measurements from BATSE. The intrinsic spin frequencies, which have been orbitally corrected using parameters from Finger, Wilson & Chakrabarty (1996) , were determined at 1–day intervals by epoch-folding the 20-50 keV DISCLA data (see Appendix B.1.2). The pulsed fluxes were determined at 1–day intervals by assuming a Comptonized spectrum model of the form $F(E) = AE^{\lambda}\exp(-E/kT)$, with $\lambda = 1.6$ and $kT = 11.9$ keV (Finger, Wilson, & Chakrabarty 1996) (see Appendix B.2.3). The orbit was determined assuming a correlation between pulsed flux and accretion torque, which could potentially introduce modulations in the apparent rate of spin-up during the sequence of outbursts following the main outburst.

frequency showed a modulation suggestive of orbital variation over less than a full cycle. The 20–75 keV pulsed flux reached a maximum of 50 mCrab on the 5th day of the outburst. There is evidence for spectral variability uncorrelated with time or intensity (Chakrabarty et al. 1995a). The system is probably a Be transient, although an orbit could not be uniquely measured and the companion has not been identified.

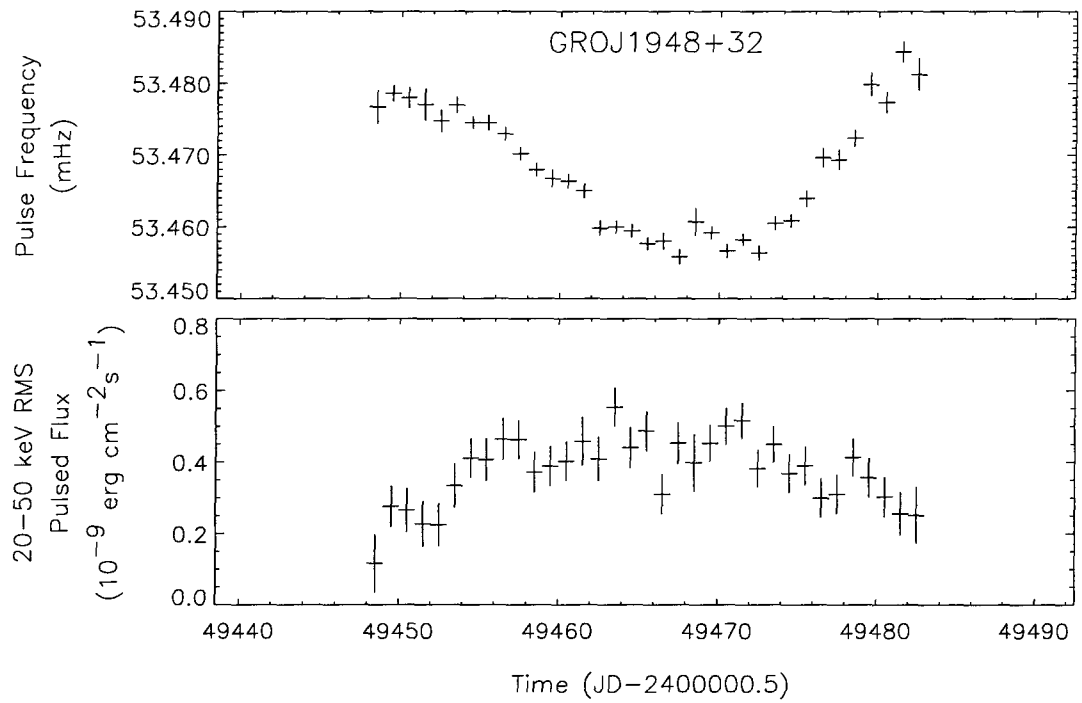

Figure 4.18: GRO J1948+32 frequency and pulsed flux measurements from BATSE. The pulse frequencies, which has not been orbitally corrected as the orbital parameters are unknown, were determined at 1-day intervals from the power spectra of the 20–70 keV CONT data (see Appendix B.1.1). The pulsed fluxes were obtained by assuming an exponential spectrum with an e–folding energy of 15 keV (see Appendix B.2.3).

EXO 2030+375. — *EXOSAT* discovered 41.7 s pulsations from EXO 2030+375 during a strong outburst of ~80 d duration starting in May 1985, and observed a smaller outburst in October 1985 (Parmar et al. 1989). The companion was later identified as a B0 Ve star (Coe et al. 1988). The *EXOSAT* observations found an orbital period of ≈46 d and a strong correlation of both the accretion torque and pulse shape with luminosity, although the orbit and accretion torque could not be separately measured.

Detailed discussions of the BATSE observations of EXO 2030+375 have appeared elsewhere (Stollberg et al. 1993a; Stollberg et al. 1994). During the interval 1992 February 8 – 1993 August 26 (MJD 48661–49226), 13 consecutive outbursts of EXO 2030+375 were seen with durations of 7–19 d, spaced at approximately 46 d intervals (Wilson et al. 1992; Stollberg et al. 1994). A few detections of marginal statistical significance preceded and followed the sequence of outbursts. Over these 13 outbursts, EXO 2030+375 spun up at a mean rate of $\dot{\nu}_s \simeq 1.3 \times 10^{-13}\,\mathrm{Hz\,s^{-1}}$. The pulse profile is double peaked with no

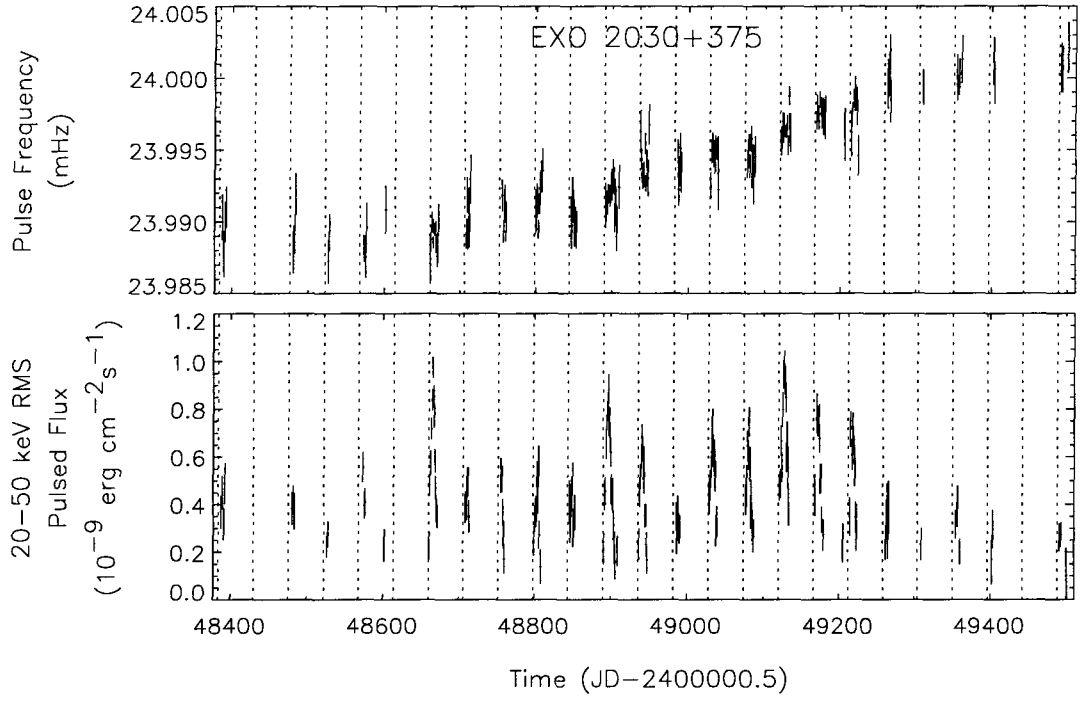

Figure 4.19: EXO 2030+375 frequency and flux measurements from BATSE. The intrinsic spin frequencies, which have been orbitally corrected using parameters from Stollberg et al.(1994), were determined at 1-day intervals from the power spectra of the 20–70 keV CONT data (see Appendix B.1.1). The pulsed fluxes were determined at 1–day intervals by assuming an exponential spectrum with an e–folding energy of 20 keV (see Appendix B.2.3).

evidence for spectral differences between the two peaks (Stollberg et al. 1993a) and no pulse profile variations as were seen by EXOSAT (Parmar, White, & Stella 1989). This sequence of outbursts has allowed the first unambiguous determination of the orbital parameters (Stollberg et al. 1994), shown in Table 1.2. indicating that the outbursts all began at or shortly after periastron passage. The orbit measured with BATSE has been used to determine the correlation between luminosity, L, and accretion torque, N, in the *EXOSAT* May–August 1985 outburst, yielding a functional dependence $N \propto L^{1.2}$ (Reynolds et al. 1996).

The source was quiescent for 2.5 years before being detected by BATSE again in April and May 1996 (Stollberg et al. 1996). These two outbursts occurred ~5 d prior to periastron passage. The latest outbursts were detected in July and November 1996. The spin frequency of the latest outbursts indicate that during quiescence EXO 2030+375 had spun down at a rate $\dot{\nu} \simeq -3.4 \times 10^{-14}$ Hz s^{-1}. Simultaneous 30–70 keV pulsed and Earth

occultation DC flux measurements on MJD 49120–49131 yielded a peak-to-peak pulsed fraction of 0.36(5) (Stollberg et al. 1994).

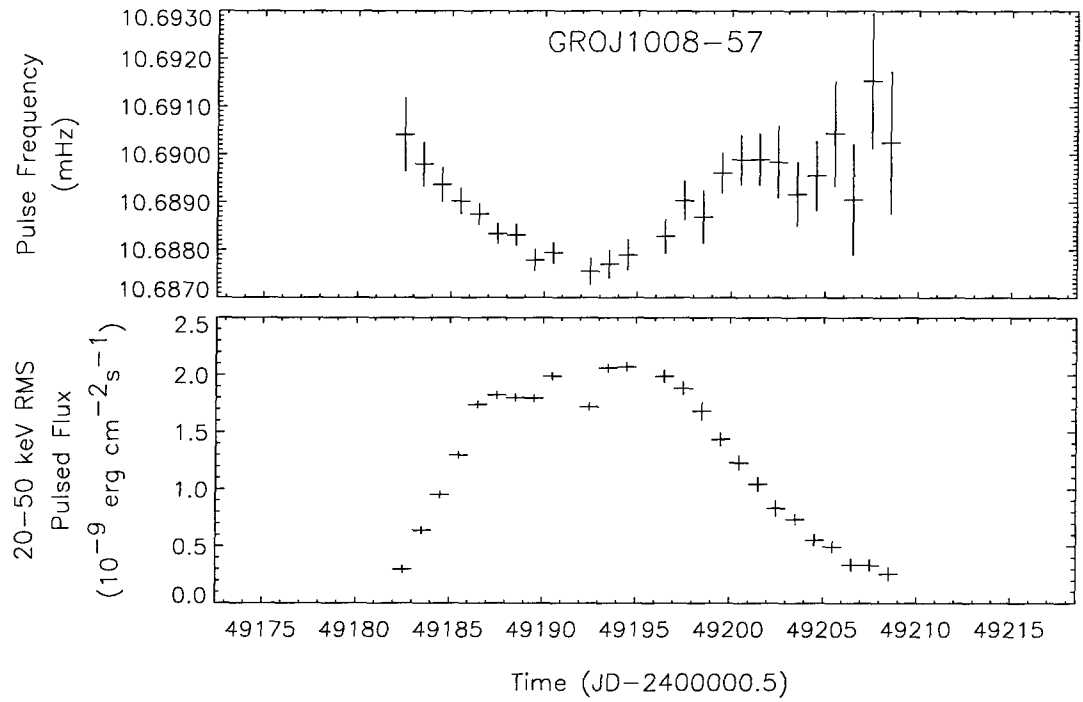

Figure 4.20: GRO J1008-57 frequency and flux measurements from BATSE. The pulse frequencies, which have not been orbitally corrected as the orbital parameters are unknown, were determined at 1-day intervals from the power spectra of the 20–70 keV CONT data (see Appendix B.1.1). The pulsed fluxes were determined at 1–day intervals by assuming an exponential spectrum with an e–folding energy of 20 keV (see Appendix B.2.3).

GRO J1008–57. — BATSE discovered 93.5 s pulsations and observed a 33 day outburst from J1008–57 (Stollberg et al. 1993b) from 14 July to 16 August 1993 (MJD 49182–49215). A preliminary discussion of the BATSE observations of GRO J1008–57 appeared in Wilson et al.(1994b). The source localization to 2.5° by the Earth-occultation technique (Stollberg et al. 1993b) and later by OSSE (Grove et al. 1993), ASCA (Tanaka 1993), and *ROSAT* (Petre & Gehrels 1993) to 15′. Coe et al.(1994a) later identified the companion to be a Be star. GRO J1008–57 has a hard spectrum, with pulsations observed from 20–160 keV. The peak-to-peak pulsed fractions, averaged over the interval MJD 49186–49195, are 0.66(9) (20–30 keV), 0.65(7) (30–40 keV), 0.69(7) (40–50 keV), and 0.76(15) (50–70 keV). Four additional outbursts, not shown in Figure 4.20, were observed during March

1994, November 1994, and March 1996. The very weak and short duration later outbursts occurred at multiples of ≈248 days, indicating that this may be the orbital period of the system.

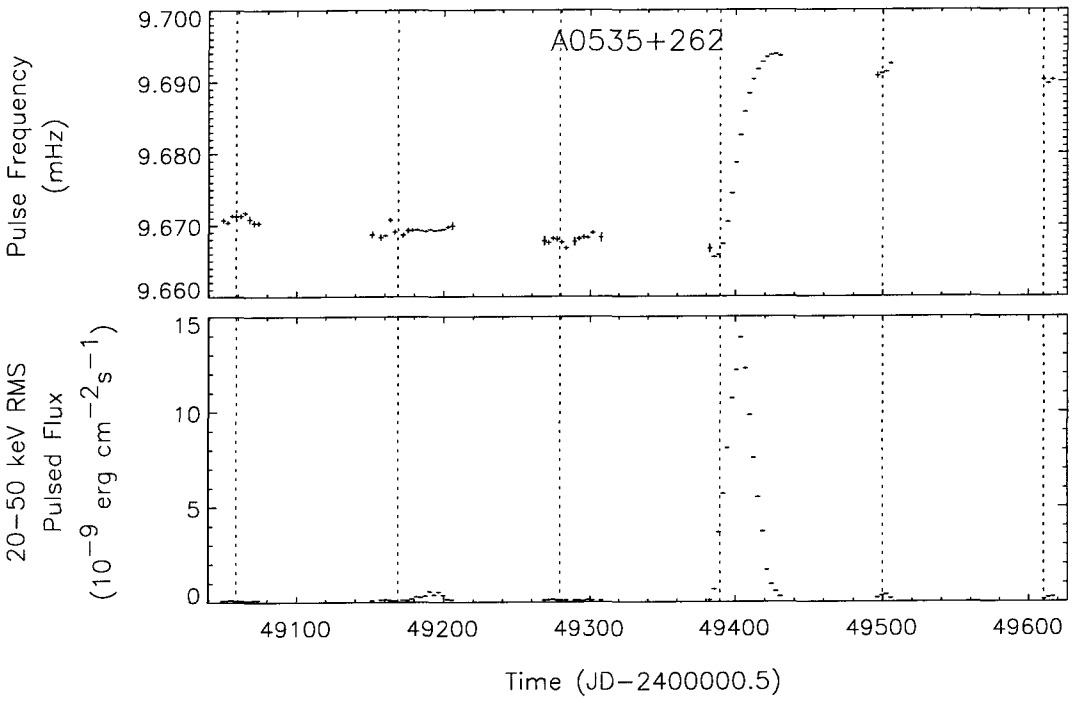

Figure 4.21: A0535+262 frequency and pulsed flux measurements from BATSE. The frequencies, which have been orbitally corrected using orbital parameters from Finger et al. 1994, were determined at 3–day intervals from fits to phase measurements made using the 20–50 keV DISCLA data (see Appendix B.1.3). The pulsed fluxes were measured at 1–day intervals by assuming an exponential spectrum with an e–folding energy of 20 keV (see Appendix B.2.3).

A 0535+26. — *Ariel 5* discovered 103 s pulsations from A 0535+26 in 1975 (Rosenberg et al. 1975; Coe et al. 1975) and its companion is the Be star HDE 245770 (Stier & Liller 1976, Hutchings et al. 1978). The 111 d orbital period of A 0535+26 was first inferred from the spacing of X-ray outbursts (Nagase et al. 1982). The binary undergoes frequent outbursts with a wide range of intensities, the brightest reaching 3 Crab in the 2–10 keV band (Giovannelli & Graziati 1992).

Detailed discussions of BATSE observations of A 0535+26 have appeared elsewhere (Finger et al. 1994; Finger, Wilson, & Harmon 1996). BATSE has observed 6 outbursts

spaced roughly at the orbital period, the 4th of which is a "giant" outburst that occurred from 28 January 1994–20 March 1994 (MJD 49380–49430) and reached a peak flux of 8 Crab in the BATSE energy band. There was little or no spin-up during the normal outbursts, spin-down between outbursts, but rapid spin-up during the giant outburst, suggesting accretion from a disk. The giant outburst showed enough dynamic range that the relation between accretion torque and pulsed flux could be tested directly (see Chapter 7).

BATSE has provided the first measurement of the binary orbit, and detection of Quasi-Periodic Oscillations (QPO) during the giant outburst (Finger et al. 1994; Finger, Wilson, & Harmon 1996). A cyclotron absorption line at 110 keV was reported by OSSE (Grove et al. 1995), which is also evident in the BATSE pulsed flux spectrum. The pulse shape is complex and highly variable with both energy and intensity as shown in Figure 4.22. Fluxes could be measured with the occultation method only during the giant outburst, and these yielded a 20–50 keV peak-to-peak pulsed fraction of > 0.8 at low flux and decreased to about 0.3 at the highest flux.

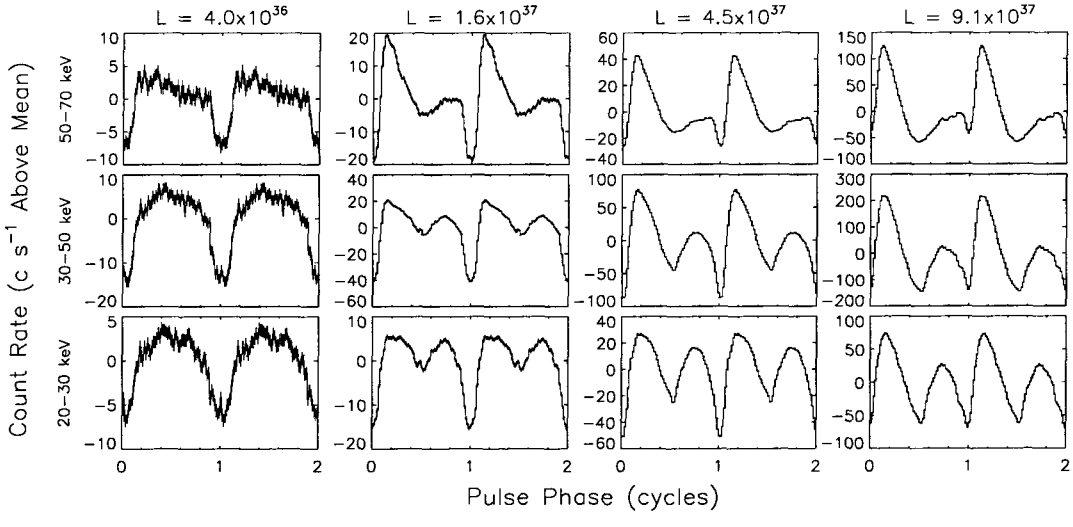

Figure 4.22: Pulse profiles of A0535+262 during the giant outburst in February–March 1994, obtained by epoch-folding CONT data. Profiles in three energy bands are given for four time intervals. The mean luminosity L in ergs s^{-1} is given for each time interval. The time intervals are February 15.1-17.6 ($L = 9.1 \times 10^{37}$), February 25.0-March 1.5 ($L = 4.5 \times 10^{37}$), March 5.0-8.6 ($L = 1.6 \times 10^{37}$), and March 13.1-15.6 ($L = 4.0 \times 10^{36}$). Luminosities were calculated from 20-100 keV fluxes based on occultation measurements by assuming a distance of 2 kpc and assuming the 20–100 keV band contains 45% of the bolometric flux.

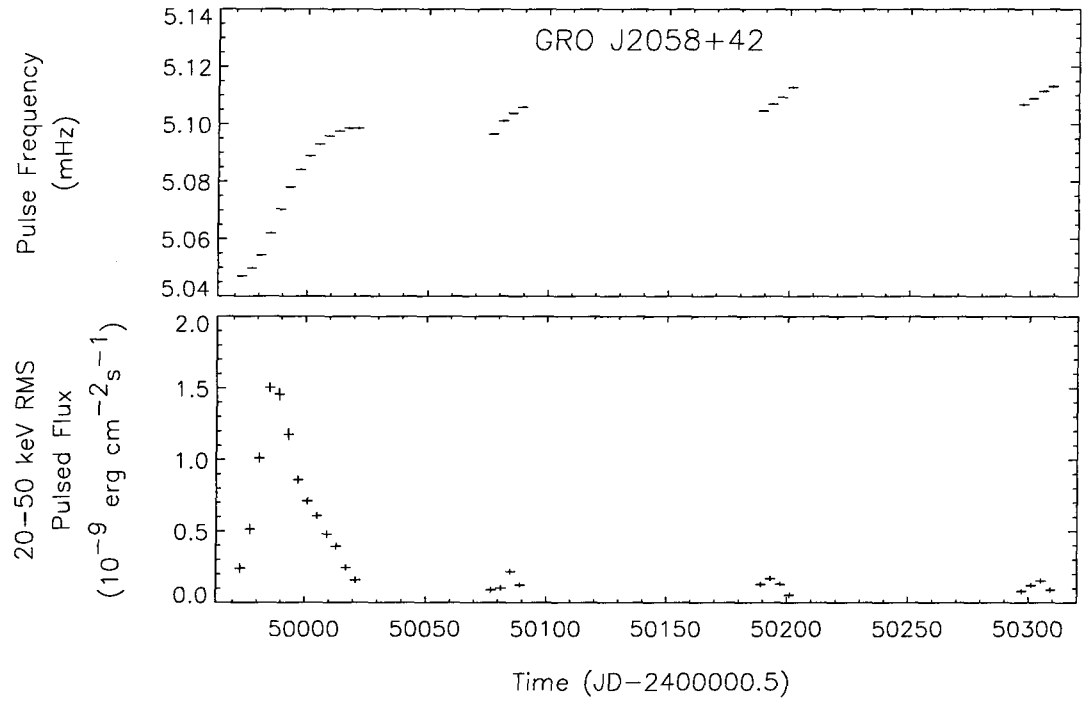

Figure 4.23: GRO J2058+42 frequency and flux measurements from BATSE. The spin frequencies, which have not been orbitally corrected as the orbital parameters are unknown, were determined at 4–day intervals by epoch folding the 20–50 keV DISCLA data at a range of trial frequencies (see Appendix B.1.2). The pulsed fluxes were determined at 4–day intervals by assuming an exponential spectrum with an e–folding energy of 20 keV (see Appendix B.2.3).

GRO J2058+42. — BATSE discovered 198 s pulsations and observed an initial 46 day outburst from GRO J2058+42 (Wilson et al. 1995a) from 1995 September 14 to October 30 (MJD 49974-50020). The source was localized to a $1^\circ \times 4^\circ$ error box with BATSE using both pulsed and Earth occultation data. OSSE scans further reduced the size of the error box to $30' \times 60'$ (Grove 1995), and target-of-opportunity scan with the *RXTE* /PCA in November 1996 reduced the error region to a $4'$ circle (Wilson, Strohmayer, & Chakrabarty 1996). The optical counterpart has not been determined. The total flux, as measured by Earth occultation, peaked at about 300 mCrab (20–50 keV). The large initial outburst was followed by a sequence of 4 much smaller outbursts with pulsed 20–50 keV fluxes peaking at 15-20 mCrab, the first 3 of which are shown in Figure 4.23. The outbursts were spaced by $\approx$ 110 days, which is likely to be the orbital period.

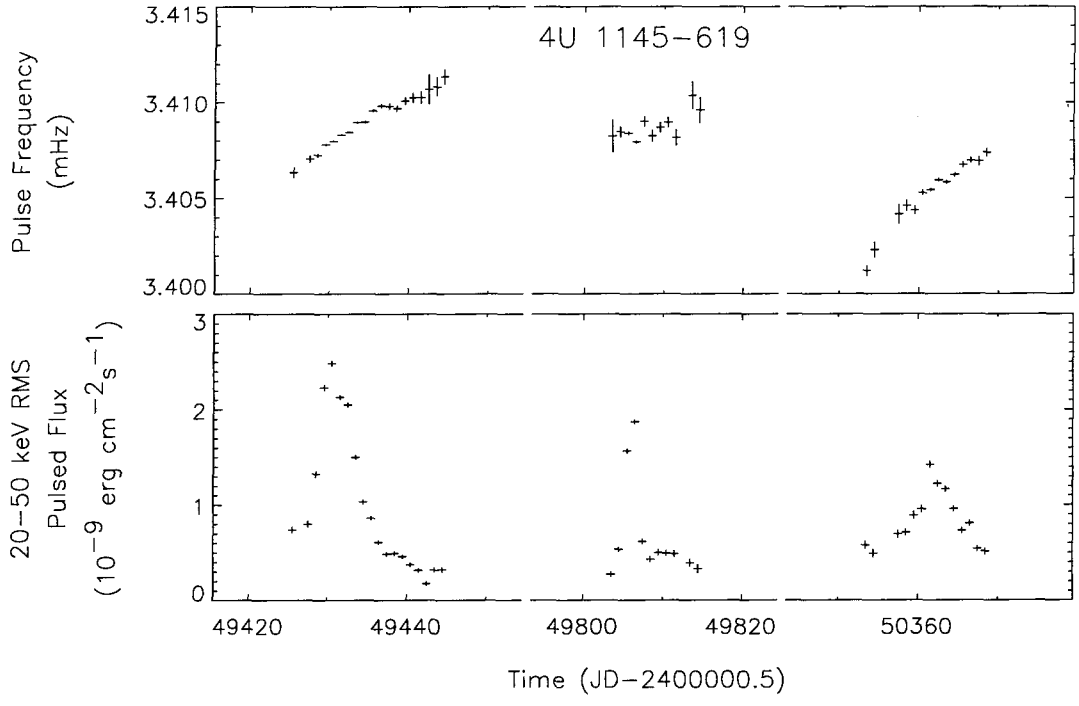

Figure 4.24: 4U 1145-619 frequency and pulsed flux measurements from BATSE. The pulse frequencies, which have not been orbitally corrected as not all the orbital parameters are known, were determined at 1-day intervals by epoch folding the 20–50 keV DISCLA data. The pulsed fluxes were determined at 1–day intervals by assuming an exponential spectrum with a e–folding energy of 15 keV (see Appendix B.2.3).

4U 1145–619. — *Ariel 5* discovered 292.5 s pulsations from 4U1145–619 in 1977 (White et al. 1978). The companion is the 9th magnitude Be star Hen 715 (Dower et al. 1978; Hammerschlag-Hensberge et al. 1980; Bianchi & Bernacca 1980), which exhibits emission lines and has an equatorial rotational velocity of $v \sin i = 290\text{km } s^{-1}$ (Hammerschlag-Hensberge et al.1980, Bianchi and Bernacca 1980). An orbital period of 186.5 d was inferred from the recurrence times of outbursts, which typically last $\approx$ 10 d (Watson, Warwick, & Ricketts 1981; Priedhorsky & Terrell 1983). Pulse frequency variations over multiple EXOSAT observations imply an eccentricity of $e \gtrsim 0.6$ (Cook & Warwick 1987). To date, BATSE has observed 7 outbursts, of which three are shown. The separation between the BATSE outbursts is in good agreement with the 186.5 d period.

A 1118–616. — *Ariel 5* discovered 406.5 s pulsations from A 1118-616 in 1974 (Ives, Sanford, & Bell-Burnell 1975) and the optical companion was later identified to be

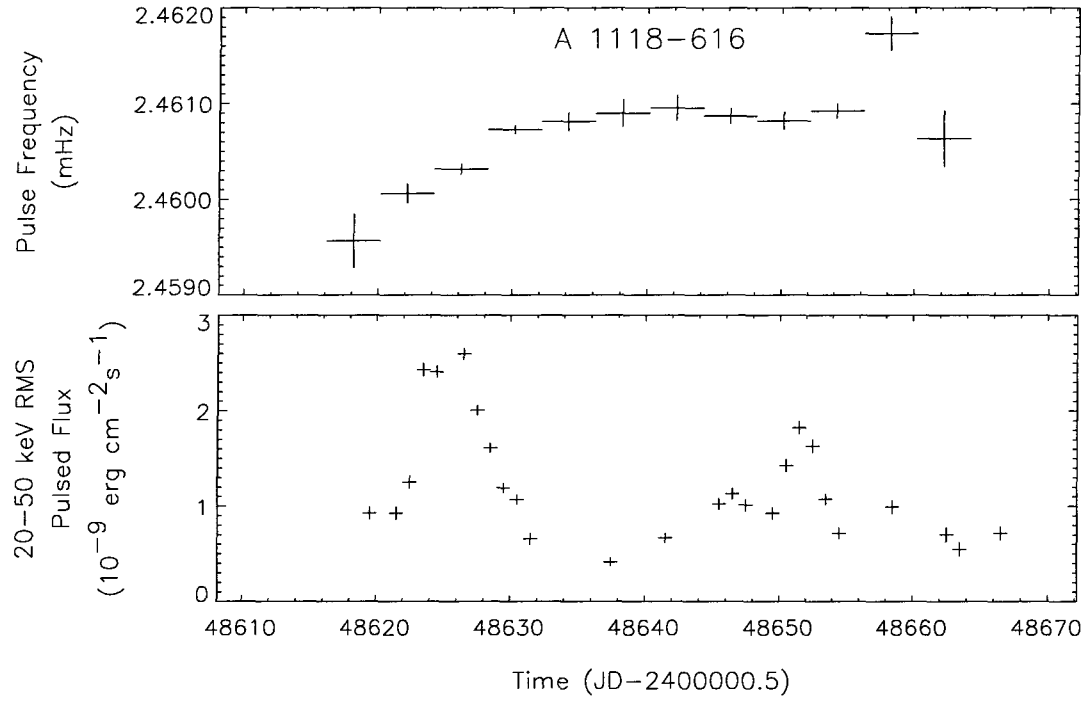

Figure 4.25: A 1118–616 frequency and pulsed flux measurements from BATSE. The spin frequencies, which have not been orbitally corrected as the orbital parameters are unknown, were determined by Coe et al.(1994b) at 4–day intervals by epoch folding the 20–50 keV DISCLA data at a range of trial frequencies (see Appendix B.1.2). The pulsed fluxes were determined at 1–day intervals by assuming an exponential spectrum with an e–folding energy of 15 keV (see Appendix B.2.3).

the Be star He 3-640/Wray 793 (Chevalier & Ilovaisky 1975; Heinze 1976; Wray 1976). Since the initial discovery, no outbursts were observed until BATSE detected one from 1991 December 30 – 1992 January 10 (MJD 48621–48633). This outburst reached a 20–70 keV pulsed intensity of $\approx$14 $c\ s^{-1}$ on 1992 January 3, followed by approximately 50 days of erratic flaring behavior with a maximum on 1992 February 1(MJD 48654) (Coe et al. 1994b). The WATCH experiment on *GRANAT* independently detected and monitored the outburst (Lund, Brandt, & Castro-Tirado 1994), which was also observed by the IUE and ground-based telescopes (Coe et al. 1994b). The X-ray outburst was accompanied by an increase in H_α emission and an IR excess, indicative of an extended disk around the companion star (Coe et al. 1994b). Pulsed emission is detected from 20–100 keV at the peak of the outburst.

Chapter 5

Rapid Spin–Up Episodes in the Wind–Fed Accreting Pulsar GX 301–2 [1]

5.1 Introduction

An accretion-powered pulsar consists of a rotating magnetized neutron star accreting material transferred from a binary companion. In systems with evolved low mass companions, mass transfer occurs via Roche-lobe overflow and is mediated by an accretion disk. If the companion star has high mass, the neutron star can accrete directly from the stellar wind. One such wind-fed system is GX 301–2 (4U 1223–62), a 680s, accreting pulsar in a 41.5 day eccentric ($e = 0.47$) orbit around the supergiant companion Wray 977 (Sato et al. 1986) (hereafter S86). Pulsations of ≈ 700 s were first detected in this binary in 1975 (White et al. 1976). The X-ray mass function is $31.8 M_{\odot}$, making the minimum companion mass $\approx 35 M_{\odot}$ for a $1.4 M_{\odot}$ neutron star. The B2 Iae spectral classification of Wray 977 (Parkes et al. 1980) implies that the star has already evolved off the main sequence and is at least 10^6 years old.

We have observed GX 301–2 continuously with the BATSE instrument from 1991 April to December 1994 and independently re-determined the binary orbital parameters. These are consistent with S86's measurements, but we have obtained a substantially better measurement of the time of periastron passage. This improvement permits accurate removal of orbital effects from the observed pulsed frequency history, yielding the intrinsic neutron

[1] Extracted with changes from "Rapid Spin–Up Episodes in the Wind Fed Accreting Pulsar GX 301–2" in *The Astrophysical Journal*, 479, 933–947, by D. T. Koh, L. Bildsten, D. Chakrabarty, R. W. Nelson, T. A. Prince, B. A. Vaughan, M. H. Finger, R. B. Wilson and B. C. Rubin. Used by permission of the authors.

star spin frequency. Figure 5.1 shows the intrinsic neutron star frequency for the last twenty years. From 1975-1985, the neutron star was, on average, neither spinning up or down, much like other wind accretors. However, a prolonged period of spin-up at $\dot{\nu} \approx 2 \times 10^{-13}$ Hz s^{-1} began in roughly 1985.

The neutron star regularly flares in X-rays $\approx$ 1.4 days before periastron passage (S86) and several stellar wind accretion models have been proposed to explain the magnitude of the flares and their orbital phase dependence (White & Swank 1984; Haberl 1991). In addition to the well-known maximum just before periastron passage, the 20-55 keV BATSE pulsed flux history folded at the orbital period reveals a secondary maximum close to apastron, which is difficult to explain in a spherically symmetric stellar wind.

We begin in section 5.2 by discussing the BATSE data used in our analysis and quantifying the enhanced sensitivity obtained by subtracting the *GRO* orbital variations from the raw data. The orbit determination and resulting intrinsic spin frequency measurements are then presented. Section 5.3 contains a discussion of the stellar properties of the optical companion, Wray 977. Through a careful consideration of the parameters of the binary system, we have placed an upper limit on the mass and radius of the companion, which argues against the reclassification by Kaper et al. (1995) (hereafter K95) of Wray 977 as a B1 Ia+ hypergiant. In section 5.4 we examine critically the possible mass transfer and accretion mechanisms at work in GX 301–2 and raise some theoretical issues that need to be addressed for this binary. Specifically, we show that most features of the folded flux profile can be understood if the neutron star were moving in the plane of a dense, slowly expanding circumstellar disk around Wray 977, whose existence was first postulated by Pravdo et al. (1995) . We close in section 5.5 by arguing that that the neutron star is primarily a wind-fed accretor, but that transient accretion disks can sometimes form which rapidly spin-up the pulsar. We also summarize our results and suggest observations which may resolve some of the outstanding questions.

5.2 BATSE Observations and Frequency Measurements

BATSE consists of eight identical uncollimated detectors positioned on the corners of the *GRO* spacecraft, providing an all-sky monitor of hard X-ray and γ-ray flux (Fishman et al. 1989b). We used the CONT data (16 energy channels at 2.048 s resolution) from the BATSE large-area detectors (LADs), each of which has an effective area of $\approx$ 1000 cm^2 from

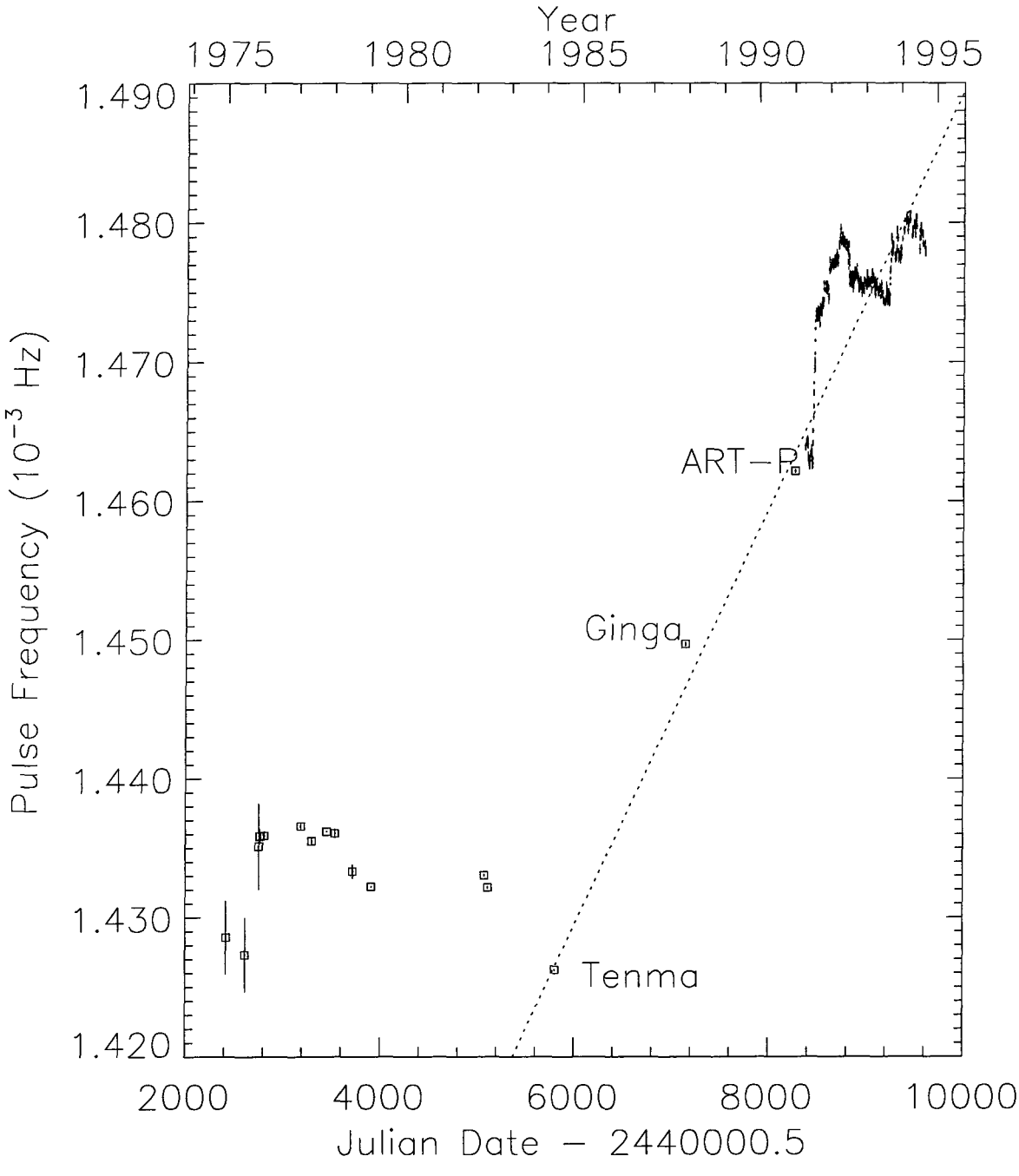

Figure 5.1: Pulse frequency history of GX 301–2 reduced to the solar system barycenter. The historical data are mostly taken from Nagase (1989). Also shown is a 1991 measurement with ART-P/*GRANAT* (Lutovinov et al. 1994), and our 1991-1994 measurements with BATSE. The dashed line is the best linear fit to the *TENMA*, *GINGA*, and ART-P measurements which shows the spin-up trend that began in 1984. The gap near JD 2,448,700 is due to a tape recorder failure on *GRO*.

30-200 keV. For frequency measurements, we used data in the approximate range 15-55 keV (channels 0-3). We only use channels 1-3 for flux measurements, as channel 0 is not well calibrated.

We begin by subtracting the mean background count rate (using the model of Rubin et al. 1996) from the raw data. The resultant reduction in the noise at low frequencies is displayed in Figure 3.1, where we show the power spectrum of the BATSE LAD background for CONT channel 1 (20-33 keV) before and after background subtraction. At frequencies $\nu \gtrsim 0.02$ Hz, the noise is consistent with Poisson counting statistics for the observed mean count rate of $C = 423.72$ c s^{-1}. However, near the second (dominant) harmonic of GX 301–2 ($f = 0.003$ Hz), the noise level of the background-subtracted data is ≈ 4 times the Poisson level. This translates into 1-day and 2-day 5 σ detection threshold signal amplitudes of $\approx$ 0.8 cts s^{-1} and 0.6 cts s^{-1} respectively for this channel. These thresholds agree with those obtained from simulations of injecting $\nu \approx 0.003$ Hz signals of varying amplitudes (1-20 cts s^{-1}) into the CONT channel 1 raw data. These signals were fully recovered, indicating that the background subtraction does not introduce any systematic effects.

In order to make a time series for the frequency searches, we summed CONT channels 0-3 data weighted by the cosine squared [1] of the viewing angle for each detector and reduced all our timing observations to the solar system barycenter using the Jet Propulsion Laboratory DE-200 solar system ephemeris (Standish et al. 1992). The barycentric pulse frequency for each 1-day data segment was determined by searching the corresponding Fourier power spectrum for the strongest signal in a small range around the previously observed pulse frequency, always leading to detections near periastron (≈ 5 days before and after). The neutron star was only detected $\approx 50\%$ of the time outside this orbital phase interval. By increasing each observation interval to two days, we detected pulses away from periastron about 85% of the time.

Pulse profiles were constructed by folding the time series of each (channel, detector) combination at the period determined from the Fourier power spectrum search. Profiles for which the second (dominant) harmonic is present at $> 95\%$ confidence are considered detections. We typically detected a pulse in CONT channels 1 (20-30 keV), 2 (30-45 keV) and 3 (45-55 keV) for two day observations which detected the pulsar (at $> 4\sigma$) in the

[1] The angular response of the BATSE LADs deviates from the usual $\cos\theta$ law below 100 keV due to energy-dependent absorption by the metal and plastic shielding. Although the exact angular response depends on the intrinsic source spectrum, $\cos^2\theta$ is a good approximation over the range of power-law spectra typical for accreting pulsars (Chakrabarty 1996).

summed (CONT channels 0-3) data. It was rare to see a pulse in channel 4 except near periastron passage. We never detected a pulse above channel 4, even in two day observations. Figure 5.2 shows the pulse profiles as a function of channel for MJD 48582-48583 and MJD 48632-48633. No significant pulse shape changes are evident.

5.2.1 Measuring the Neutron Star Orbit

The neutron star orbit was first measured by S86 through a joint fit of pulse time-of-arrival (TOAs) data from *Ariel 5*, *SAS 3* and *Hakucho* observations. The orbital parameters they measured are shown in Table 5.1. The dashed line in Figure 5.3 displays the orbit-induced frequency derivative, $\dot{\nu}_{\rm orb}$, as a function of time for two orbits from S86's parameters. Due to the large eccentricity of the system, $\dot{\nu}_{\rm orb}$ changes abruptly over ≈ 4 days in the vicinity of the periastron passage. The 1-σ error in the extrapolation of the time of periastron passage from S86 to the present date is ≈ 1 day, clearly inadequate for correcting the observed frequencies to the pulsar rest frame. Hence, even if all other orbital parameters have remained constant since S86's data, it is essential to redetermine the best-fit time of periastron. We now describe our new measurement of this parameter, which gives the solid line in Figure 5.3.

A pulse profile template was constructed by accumulating 235 two day profiles of channel 1 data from the detector with the best view of GX 301-2 for MJD 48370-49354. Rather than use the traditional cross-correlation technique to find the shift between a pulse profile and a template, we employed a cross spectrum technique (Bendat & Piersol 1986, see Appendix A. In addition to computing the phase shift more accurately, this technique defines the statistical contributions to TOA errors. Both techniques assume that the pulse shape noise is white (Appendix A and Deeter & Boynton (1985)), whereas the background at low frequencies (Rubin et al. 1996) reddens the pulse shape noise. To alleviate this, we filtered the pulse profiles in the frequency domain by attenuating their harmonic components by the ratio of the expected white noise power to the measured noise power at the harmonic frequency (Deeter & Boynton 1985). In the vicinity of periastron passage, $0.85 \lesssim \phi_{\rm orb} \lesssim 1.1$, GX 301-2 was usually bright enough to measure a TOA once per day. At other orbital phases, accurate TOA's could only be obtained at 2-day intervals.

Measuring the neutron star orbit is complicated by the need to decouple the orbital Doppler delays from any intrinsic changes in the neutron star rotation rate. This is

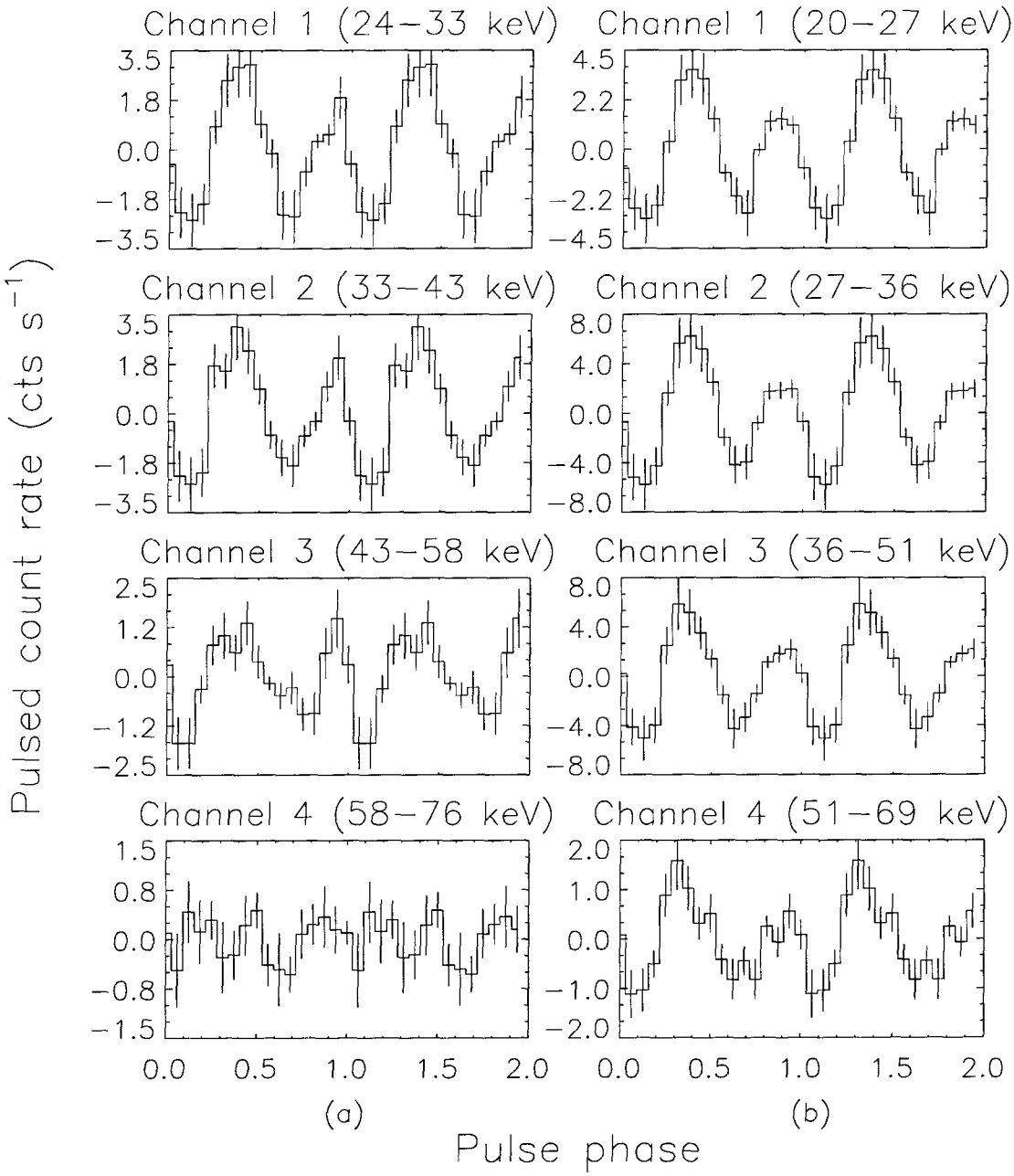

Figure 5.2: Pulse profiles as a function of energy for GX 301–2 during the interval (a) MJD 48622-48623 (orbital phase 0.68) and (b) MJD 48632-48633 (orbital phase 0.92). Two pulses are shown for each channel, and all channels are displayed relative to the same pulse phase. The energy edges for each CONT channel of BATSE detector 0 in (a) and 7 in (b) are indicated. The pulse shapes are uncorrected for the rapid change in detector response as a function of energy in the (20-75) keV range. While the double-peaked profile characteristic of this pulsar is clearly visible in channels 1-3, the pulse is only detected in channel 4 on MJD 48632-48633.

Table 5.1. GX 301–2 Orbital Parameters

Parameter	Sato†	BATSE†	(BATSE+Sato)†¶
P_{orb} (d)	41.508 ± 0.007	41.488 ± 0.009	41.498 ± 0.002
$a_x \sin i$ (lt-sec).....	371.2 ± 3.3	370.0 ± 4.0	368.3 ± 3.7
e	0.472 ± 0.011	0.462 ± 0.014	0.462 ± 0.014
$\omega(^\circ)$	309.9 ± 2.6	311.3 ± 1.5	310.4 ± 1.4
T_0‡ (MJD)	$43,906.06 \pm 0.16$	$48,802.85 \pm 0.13$	$48,802.79 \pm 0.12$

† Quoted uncertainties are single-parameter 1-σ confidence limits.

¶ P_{orb} in this column was obtained by comparing the T_0's in the first 2 columns and assuming that P_{orb} remained constant over this interval. The other 4 orbital parameters in this column were obtained by performing a least squares fit with P_{orb} fixed.

‡ Time of periastron passage.

especially true near periastron, where orbital accelerations are large and the torques on the neutron star might also increase. Variations in the intrinsic pulse period prohibited us from maintaining an accurate pulse count over more than one orbit, so we employed a "hybrid" approach to determining the orbit. We write the pulse emission times as

$$t'_n = t'_0 + \frac{n}{\nu_0} - n^2 \frac{\dot{\nu}}{2{\nu_0}^3} \tag{5.1}$$

where t'_0 is the emission time epoch and ν_0 and $\dot{\nu}$ are the pulse frequency and its derivative at t'_0. The arrival times are then $t_n = t'_n + g(t'_n)$ where $g(t'_n)$, the orbital time delay, is parametrized by five Keplerian orbital parameters: the projected semi-major axis $a_{\rm x} \sin i$ (where i is the inclination angle between the line of sight and the orbital angular momentum vector, defined to lie in the first quadrant), the orbital period $P_{\rm orb}$, the eccentricity e, the longitude of periastron ω, and the orbital epoch T_0 (defined as the epoch of periastron passage).

The five orbital parameters, along with independent t'_0, ν_0 and $\dot{\nu}$ for each orbit, were simultaneously estimated by a least-squares fit of the TOA's. To minimize any bias introduced by possibly large $|\dot{\nu}|$ values at periastron, we typically begin timing in the vicinity

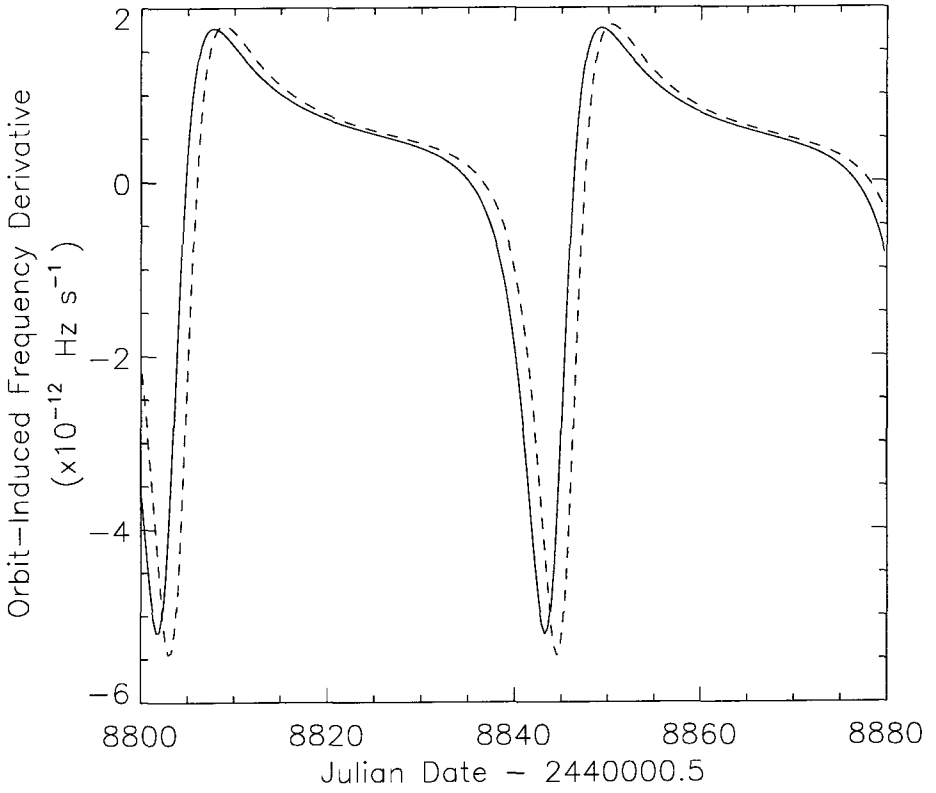

Figure 5.3: The orbit-induced frequency derivative of the pulsar, $\dot{\nu}_{\rm orb}$, as a function of time for two orbits. The solid line is from our orbital parameters, while the dashed line is from the orbital parameters of S86.

of apastron (orbital phase = 0.5) and only used data from orbits for which a pulse could be detected over most ($\gtrsim$ 80%) of the orbit. Sudden torque fluctuations and low fluxes rendered $\approx$ 50% of the orbits unusable for TOA analysis.

We varied all 5 orbital parameters in our fitting, starting with S86's parameters as the initial guess. By comparing our best fit T_0 to that of S86, and assuming that $P_{\rm orb}$ has remained constant over this interval, we obtained a refined value of $P_{\rm orb} = 41.498 \pm 0.002$ d. We then fix $P_{\rm orb}$ at this value and allow the other 4 orbital parameters to vary. These orbital parameters, together with those determined by S86 and those determined from the BATSE data only, are shown in Table 5.1. There are no statistically significant differences in the orbital solutions, and thus no evidence for apsidal motion or orbital decay at present. Figure 5.4 shows the best-fit delay curve with our model of ν_0 and $\dot{\nu}$ removed from each timing

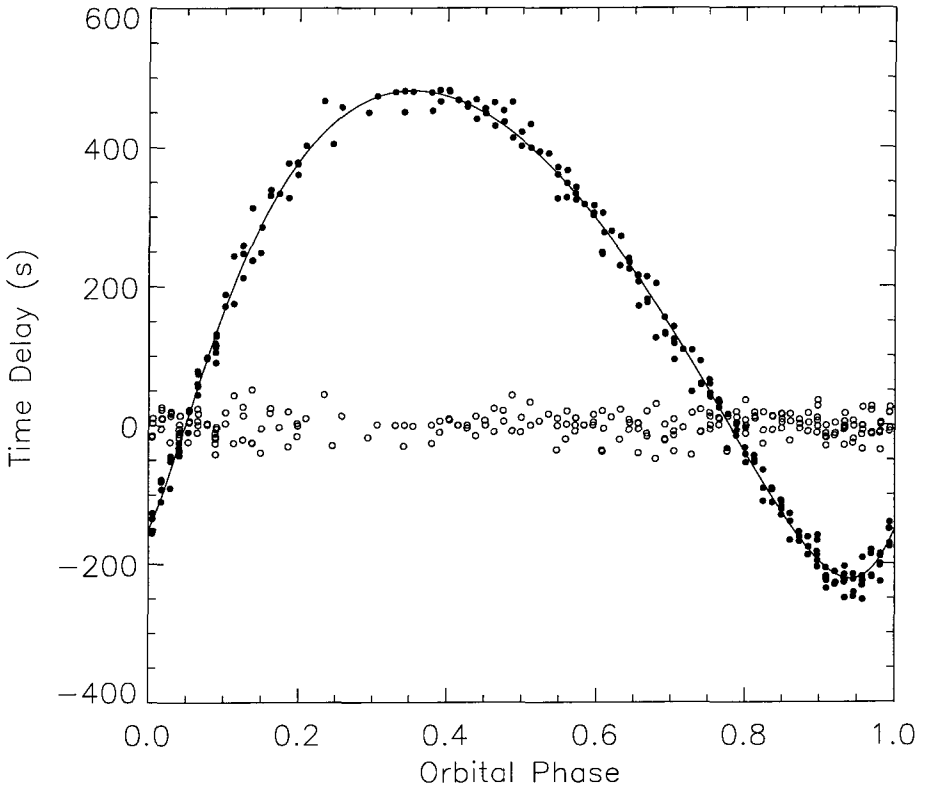

Figure 5.4: Time delays for the pulse arrival times as a function of the orbital phase of GX 301–2 after removing our best model for the intrinsic variations in the spin period. The data plotted are from the interval MJD 48370-49354. The solid circles are the delay times, the solid curve is the best-fit orbital model, and the open circles are the residuals.

interval. The statistical errors in the TOAs computed by the cross-spectrum technique are $\approx$ 3-6 s, much smaller than the RMS arrival time fit residuals of $\approx$ 20 s. Since we do not know the origin of this discrepancy, we assigned a constant error of 20 s to all TOAs when performing the orbital fit.

5.2.2 The Neutron Star Spin Frequency History

The neutron star spin frequency history from MJD 48370–49612 is shown in Figure 5.5. The star generally experiences fluctuating accretion torques with $\langle|\dot{\nu}|\rangle \approx 2.5 \times 10^{-14}$ s^{-2} – 2.2×10^{-13} s^{-2}. On $\sim$ yearly time scales, the star alternates between mild spin-up and spin-down, with $\langle|\dot{\nu}|\rangle \approx 2.0 \times 10^{-13}$ s^{-2}. However, there are also two dramatic spin-up episodes (MJD 48440–48463 and MJD 49230–49245), which we discuss below. In

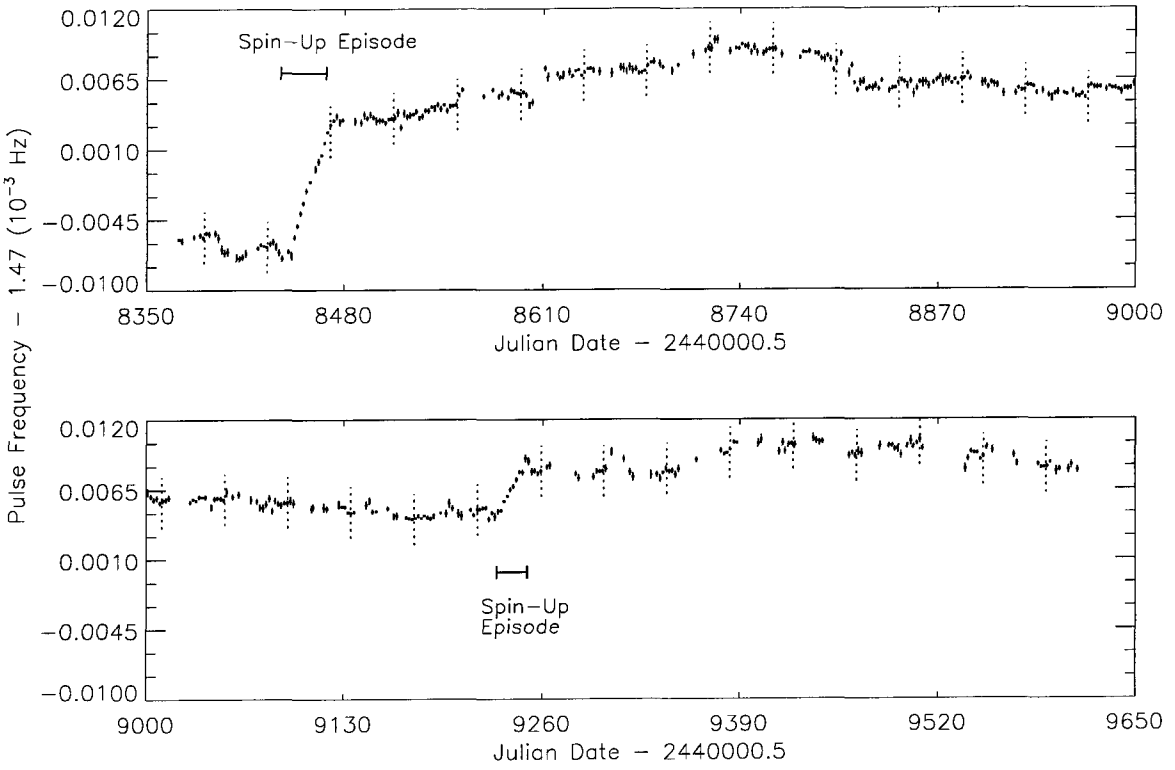

Figure 5.5: The intrinsic neutron star spin frequency in GX 301–2 from MJD 48370-49612. Dotted lines indicate periastron passages. We also mark the two rapid spin-up episodes.

order to search for systematic torque variations with orbital phase, we folded the frequency derivative measurements at P_{orb}. These frequency derivatives were computed by taking time derivatives of 2-day frequency measurements, excluding the 2 major spin–up episodes. There is no strong evidence for spin-up or spin-down torques at any particular orbital phase.

5.2.3 Hard X-Ray Spectrum and Flux Measurements

The pulse is detected in CONT channels 1 to 4 (20-75 keV) in the vicinity ($\pm$5 days) of periastron passage. Outside of periastron, it is only detected in channels 1 to 3 (20-55 keV). We extended the pulse detections to channel 5 by combining data for many days. We first folded all channels of the CONT data (only from the detector with the smallest viewing angle to the source) at 1-day intervals at the known pulse frequencies, as determined from our FFT search. A coherent pulse profile was built up from these 1-day profiles by measuring the phase shift between each daily profile and the running sum with a

cross-correlation analysis, phase shifting the profiles, and adding to the running sum those profiles of high signal-to-noise. For each profile included into the running sum, a running sum of the corresponding detector response matrices was also kept.

We generated four different spectra, which spanned a range of luminosities and orbital phases, with data near periastron, near apastron, away from periastron and apastron, and from the spin-up episodes. The count rate energy distributions were fitted by a power-law photon spectrum of the form $(dN/dE)_{pl} \propto (E/30\text{keV})^{-\gamma}$ and an optically thin thermal bremsstrahhlung (OTTB) spectrum of the form $(dN/dE)_{OTTB} \propto (1/E)\exp(-E/kT)g_{ff}(E,kT)$, where g_{ff} is the velocity-averaged Gaunt factor. The coverage of the different spectra and their corresponding best fit spectral parameters are shown in Table 5.2.

Figures 5.6 show the spectral fits to the near periastron data for both models. The reduced χ^2 for the OTTB fit is 1574 while that for the power-law fit is 2369. Although the OTTB is a better representation of the spectrum, the 25-100 keV pulsed fluxes inferred from the power-law and OTTB fits are almost identical at respectively 1.175 and 1.197 $\times$ 10^{-9}erg cm^{-2}. We could not detect any appreciable changes in spectral shapes, so that flux differences are largely reflected by changes in C_{30}, which is dN/dE evaluated at $E = 30$ keV. Since the power-law yields a good measure of the flux in the bandpass, we fixed γ at 4.5 and measured the pulsed flux every 2 days. Only pulse profiles from channels 1-3 (20-55 keV) were used, as we do not always detect the pulse in channel 4 (55-75 keV). The count rate in a pulse profile was obtained by assuming that each profile is a shifted, scaled version of the template. The method used to find the amplitude scaling, I, is detailed in section 3.3.2. Only data from the detector with the best viewing angle to the source were used. For all 2-day data segments which registered detections in at least channels 1 and 2, C_{30} was computed (for $\gamma = 4.5$). Figure 5.7 shows the (20-55) keV pulsed flux as a function of time for MJD 48370-49612. This plot shows that the flux is always high at periastron and drops off dramatically outside of periastron.

Figure 5.8 displays these flux measurement folded at the orbital period, excluding the 2 spin-up episodes which we will discuss separately. Consistent with earlier observations (S86, Chichkov et al. 1995; Pravdo et al. 1995), we find that the pulsed flux peaks slightly before periastron, at orbital phase 0.956 ± 0.022. A smaller flare occurs near apastron at orbital phase 0.498 ± 0.057 and was also found by Pravdo et al. (1995) and Chichkov et al. (1995). The typical periastron flare is a change in the 20-55 keV flux from 1.0×10^{-9}

Table 5.2. GX 301–2 Spectral Parameters

Coverage	Power-law†	OTTB†‡
Periastron	$\gamma = 4.675 \pm 0.010$	$kT = 14.40 \pm 0.06$
$(0.80 < \phi_{orb} < 1.10)$	$C_{30} = 1.450 \pm 0.003$	$C_{30} = 2.25 \pm 0.07$
Apastron	$\gamma = 4.527 \pm 0.019$	$kT = 13.58 \pm 0.10$
$(0.35 < \phi_{orb} < 0.65)$	$C_{30} = 0.816 \pm 0.004$	$C_{30} = 1.36 \pm 0.07$
Others	$\gamma = 4.338 \pm 0.020$	$kT = 14.47 \pm 0.12$
$(0.10 < \phi_{orb} < 0.35$ and	$C_{30} = 0.580 \pm 0.003$	$C_{30} = 0.93 \pm 0.06$
$0.65 < \phi_{orb} < 0.80)$		
Spin-up Episodes	$\gamma = 4.761 \pm 0.033$	$kT = 14.00 \pm 0.17$
(MJD 48450-48470 and	$C_{30} = 1.387 \pm 0.009$	$C_{30} = 2.20 \pm 0.20$
MJD 49231-49250)		

†C_{30} is dN/dE evaluated at $E = 30$ keV and has units of 10^{-3} cm^{-2} s^{-1} keV^{-1}

†kT in units of keV

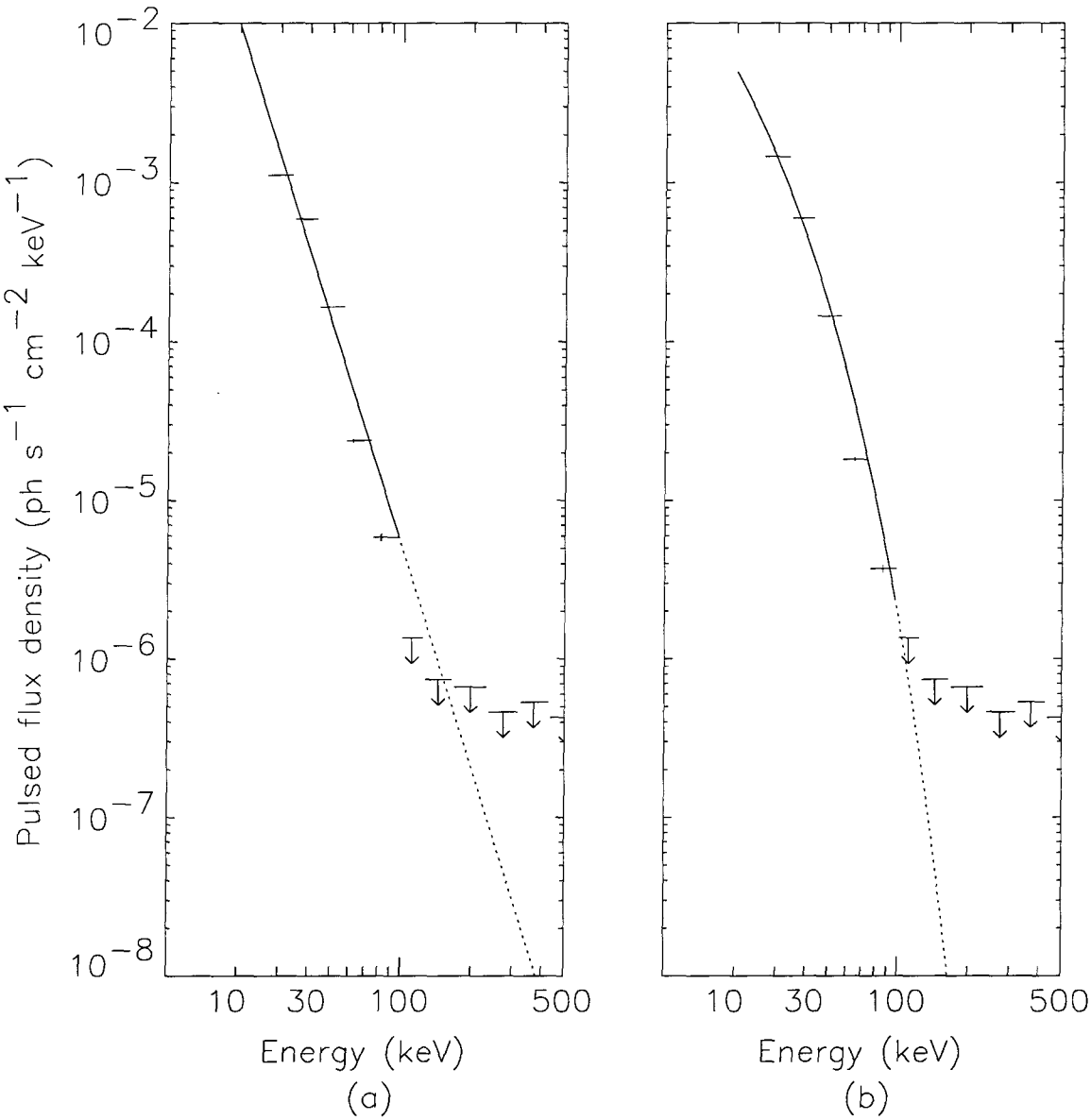

Figure 5.6: The phase and time-averaged pulsed photon spectrum of GX 301–2 for all days in the vicinity of periastron passages ($0.80 < \phi_{orb} < 1.10$). (a) The solid line represents the best fit to the spectral model $dN/dE = C_{30}(E/30\text{keV})^{-\gamma}$, for which $\gamma = 4.675 \pm 0.010$ and $C_{30} = (1.4498 \pm 0.0030)\ 10^{-3}$ cm^{-2} s^{-1} keV^{-1}. (b) The solid line is the best fit OTTB model with $kT = 14.40 \pm 0.06$ keV and a value at 30 keV of $(2.25 \pm 0.06)\ 10^{-3}$ cm^{-2} s^{-1} keV^{-1} for the same data set, which is a better fit according to χ^2.

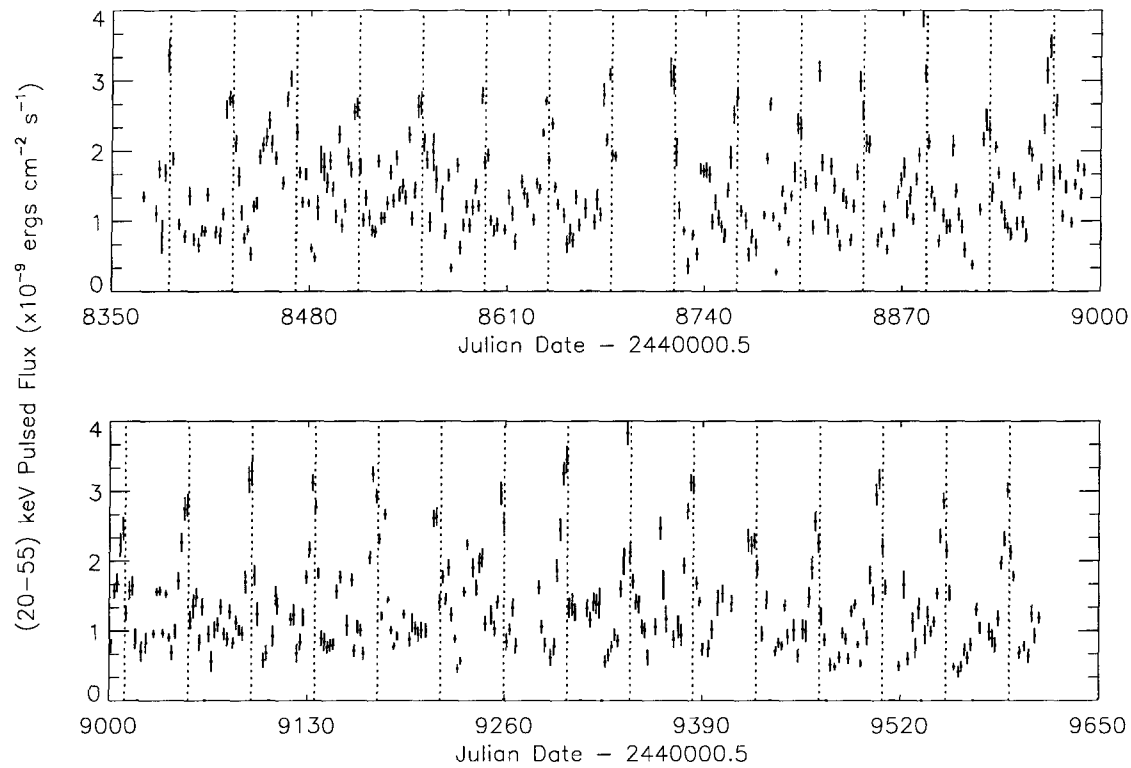

Figure 5.7: The 20-55 keV pulsed flux for GX 301–2 from MJD 48388-49612. These fluxes were found for a presumed photon number index of 4.5 and using only the detector with the smallest viewing angle to the source.

ergs cm^{-2} s^{-1} to 2.7×10^{-9} ergs cm^{-2} s^{-1}. For a typical apastron flare, the 20-55 keV flux increases from 1.0×10^{-9} ergs cm^{-2} s^{-1} to 1.4×10^{-9} ergs cm^{-2} s^{-1}. The flux is high enough near periastron to be measured by the Earth occultation technique (Harmon et al. 1992). The few simultaneous measurements show that the pulsed 20-55 keV flux is about one-half of the (unpulsed+pulsed) component. Multiple observations by *GRANAT*/WATCH from MJD 47900-49300 yield an average 1-20 keV flux at periastron of $\approx 3.6 \times 10^{-8}$ ergs cm^{-2} s^{-1} (Chichkov et al. 1995). Thus, only ≈ 8 % of the total flux is detected as pulsed emission in the BATSE bandpass.

5.3 Inferences about the Optical Companion

There have been many observations of the massive stellar companion of GX 301–2. Here, we first constrain the mass and radius of the companion and then discuss the

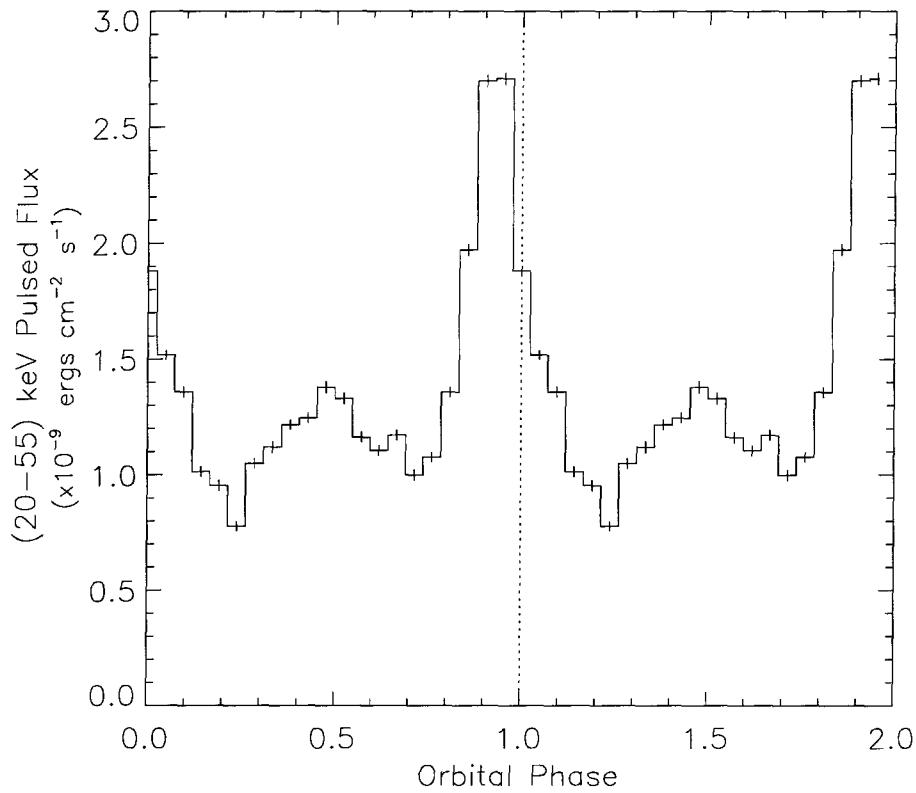

Figure 5.8: The 20-55 keV pulsed flux for GX 301–2 from MJD 48388-49612 as a function of orbital phase. Fluxes from the spin-up episodes (MJD 48440-48463 and MJD 49230-49245) have been excluded. The periastron flare peaks at orbital phase 0.956 ± 0.022. Another significant peak occurs at orbital phase ≈ 0.5. Orbital phases 0 and 1 are periastron passages.

properties of its stellar wind.

5.3.1 Constraints on the Mass and Radius of the Optical Companion

We now combine our orbital measurements with K95's measurements to constrain the mass and radius of the optical companion. Wray 977 is a supergiant with $V = 10.83$ (Hammerschlag-Hensberge, Zuiderwijk, & van den Heuvel 1976), $B - V = 1.76$ (Bord et al. 1976). K95's spectral classification (B1 Ia+) implies $T_{\rm eff} \approx 20{,}000$ K, an intrinsic color index of $(B - V)_0 = -0.20$ (Bohm-Vitense 1981) and a bolometric correction for the V band $BC_V = -1.87$ (Schmidt-Kaler 1982). The bolometric flux, corrected for reddening ($A_V = 5.88$), is then $F_{\rm bol} \approx 1.45 \times 10^{-6}$ erg cm^{-2} s^{-1}. The resulting relationship between

the companion radius, R_c and the distance to the binary, D is

$$R_c \approx 17.7 R_\odot \left(\frac{D}{1\mathrm{kpc}}\right)\left(\frac{20,000\mathrm{K}}{T_{\mathrm{eff}}}\right)^2. \tag{5.2}$$

The orbital period and projected semi-major axis of the neutron star orbit yield a mass function

$$f(M_x) = \frac{(M_c \sin i)^3}{(M_x + M_c)^2} = 31.8\ M_\odot \tag{5.3}$$

which requires the companion mass, M_c, to be $\geq 35 M_\odot$ for a neutron star mass of $M_x = 1.4 M_\odot$.

A star this massive can only reach the effective temperature of a B-type star through nuclear evolution for $\geq 10^6$ years. For the purposes of constraining the companion mass, we derived a $L(M)$ relation from the Schaller, Schaerer & Maeder (1992) models of massive (between 24 and 81 $M_\odot$) evolved stars with $T_{\mathrm{eff}} \approx 20,000$ K for both high and low metallicity. The resulting relationship

$$L \approx 3 \times 10^5 L_\odot \left(\frac{M}{30 M_\odot}\right)^{1.8} \tag{5.4}$$

scales with mass as one would obtain from the Eddington standard model (Hansen & Kawaler 1994) (for a mean molecular weight $\mu = 0.6$) when, as appropriate for this mass range, radiation pressure is becoming appreciable. This $L(M)$ relation is slightly brighter than that for zero-age main sequence due to the helium enrichment of the core. The Thomson scattering appropriate for these stars implies that they radiate at a rate nearly independent of their radius, so that we can use this $L(M)$ for the full range of masses in the interpolated range.

The hatched region in Figure 5.9 denotes the companion radius as a function of mass using the $L(M)$ relation in equation (5.4) and taking $20,000\ \mathrm{K} < T_{\mathrm{eff}} < 22,000\mathrm{K}$. We have chosen a range of effective temperatures to reflect some of the uncertainty in spectral type. The radius of the star must lie below the dark solid line, as no eclipse is observed, so that $M_c > 39 M_\odot$. The star must also be smaller than the physical separation at periastron (denoted by the light solid line), placing an upper limit of $M_c <$ 80-100 $M_\odot$ depending on T_{eff}.

A more stringent mass constraint comes from considering the tidal distortion of the companion during periastron passage. The $l = 2$ f-mode will establish an equilibrium tide when its natural frequency, ω_f, is much larger than the characteristic perturbing frequency

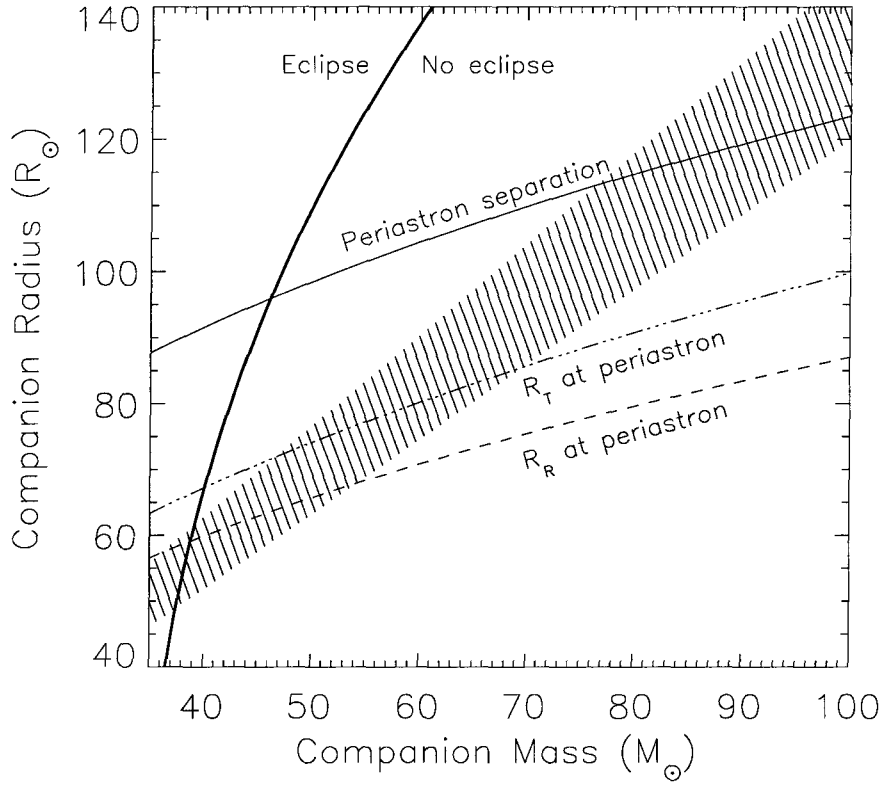

Figure 5.9: Mass-radius constraints to the optical companion of GX 301–2, Wray 977. The upper heavy solid line is the condition for an eclipse. The $R(M)$ relation for the companion is shown by the hatched region, where we allow for some uncertainty in $T_{\rm eff}$. The lower solid line is the separation between the neutron star and stellar companion at periastron. The Roche (tidal) lobe at periastron is denoted by the dashed (dot-dashed) line.

at periastron passage, $\Omega_p = (1-e^2)^{1/2}2\pi/(P_{\rm orb}(1-e)^2)$ (Kumar, Ao & Quataert 1995). The massive star is well represented by an $n = 3$ polytrope, which is very centrally condensed and has $\omega_f^2 = 8.2GM_c/R_c^3$ for $l = 2$ (Cox 1980). Using the $L(M)$ relation above, we find that $P_f \approx 3{\rm d}(20,000/T_{\rm eff})^3(M/40M_\odot)^{0.85}$, so that $\omega_f/\Omega_p \approx 4.5$. The dynamical tide also excites a resonant response (which would not be in instantaneous equilibrium), but the amplitude scales as $\exp(-\alpha_e\omega_f/\Omega_p) \sim 10^{-3}$ with $\alpha_e \approx 1.3e^{-0.25}$ (e is the orbital eccentricity). Thus, the companion star essentially responds adiabatically even at periastron, and we can safely assume that it is instantaneously in tidal equilibrium. We thus use the fitting formulae of Joss & Rappaport (1984) for estimating both the Roche (co-rotating) and tidal (no rotation)

lobe of the star at periastron. We view the tidal lobe as a limiting case since the measured rotational velocity, $v \sin i_r \approx 70$ km s^{-1} (Parkes et al. 1980), is much less than that needed for co-rotation at the periastron period.

The Roche and tidal radii are plotted in Figure 5.9. If we require that the star not overflow its tidal lobe at periastron, then $M_c < 70 M_\odot$, $R_c < 85 R_\odot$ and $D < 5.8$ kpc for $T_{\rm eff} = 22,000$ K while $M_c < 47 M_\odot$, $R_c < 72 R_\odot$ and $D < 4.1$ kpc for $T_{\rm eff} = 20,000$ K. If the star does not overflow the Roche lobe at periastron, then $M_c < 55 M_\odot$, $R_c < 68 R_\odot$ and $D < 4.3$ kpc for $T_{\rm eff} = 22,000$ K. These are all consistent with $D \approx 1.8$ kpc inferred by Parkes et al. (1980). We are nearly in conflict with K95's conclusions that the binary is at $D = 5.3$ kpc and has $L = 1.3 \times 10^6 L_\odot$. This requires a $68 M_\odot$ star with a radius so large as to only be marginally consistent with the tidal constraint for an unusually high effective temperature of $T_{eff} \gtrsim 21,100$ K. Masses this large have rarely been measured dynamically. One of the most massive Wolf Rayet stars with a dynamical mass limit is WR22 (HD92740), with $M > 72 M_\odot$ (Rauw et al. 1996). Further optical and near-UV observations of Wray 977 are needed to better constrain $T_{\rm eff}$ and L.

There are three other known pulsars accreting from the winds of supergiant companions: Vela X–1, 4U 1538–52 and 4U 1907+09. The companion mass for GX 301–2 is more than twice that of Vela X–1 and 4U 1538–52, for which $M_c \approx 20 M_\odot$ (Nagase 1989). In contrast to the high eccentricity of GX 301-2, the orbits of Vela X–1 and 4U 1538–52 are nearly circular, potentially due to more rapid circularization in the tighter orbit and larger age of these systems.

5.3.2 The Stellar Wind

The optical spectrum has P-Cygni line profiles in the hydrogen Balmer (up to Hγ) and Helium emission lines, thus indicating a strong stellar wind (Parkes et al. 1980, K95). The interstellar extinction prohibits measuring the terminal wind velocity from UV resonance lines, in which case K95 assumed that $v_\infty = 400$ km s^{-1} and found $\dot{M}_W \lesssim 10^{-5}$ M$_\odot$ yr^{-1}. The Hα equivalent width measured by K95 is 7.1 Å, which is larger than that of 5.2 for η^1 Sco, a well-known B hypergiant. This led K95 to suggest that Wray 977 was exceedingly luminous. This might very well be the case and, if true, only exacerbates the difficulties discussed above with overfilling the tidal lobe at periastron.

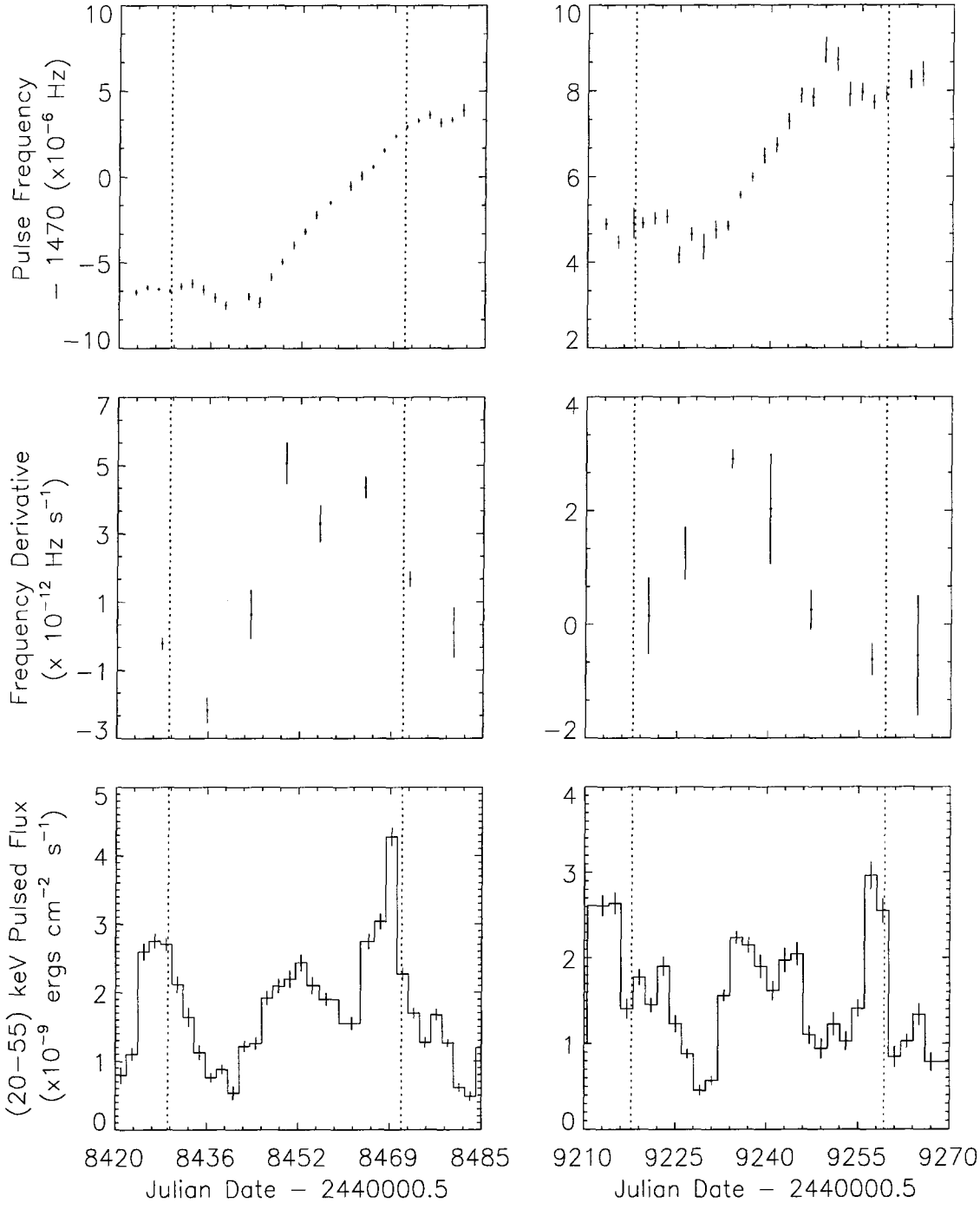

Figure 5.10: Frequency, frequency derivative and pulsed flux during the spin-up episodes which occurred on MJD 48440-48463 (left panel) and MJD 49230-49245 (right panel). The vertical dotted lines denote periastron passage. The onset of spin-up is accompanied by an increase in the 20-55 keV flux. The 20-55 keV flux averaged over MJD 48443-48458 (orbital phase 0.35-0.70) is $(1.889 \pm 0.037) \times 10^{-9}$ ergs cm^{-2} s^{-1}, while for MJD 49233-49245 (orbital phase 0.37-0.66) it is $(1.926 \pm 0.042) \times 10^{-9}$ ergs cm^{-2} s^{-1}.

5.4 Mass Transfer and Accretion onto the Neutron Star

GX 301–2 can accrete from the stellar wind of its companion, but the two rapid and long-lasting spin-up episodes are unusual for stellar wind accretion. Comparable events have not been seen in other persistent high-mass X-ray binaries accreting via winds. In contrast, matter transferred from an accretion disk to the neutron star has a definite sense of angular momentum and can give rise to a monotonic increase in the neutron star spin frequency.

5.4.1 The Two Rapid Spin-Up Episodes

Figure 5.10 shows ν, $\dot{\nu}$ and the pulsed hard X-ray flux for the two rapid spin-up episodes: MJD 48440-48463 (left panel) and MJD 49230-49245 (right panel). The measured $\dot{\nu}$ values between MJD 48443-48463 and MJD 49231-49245 are $\dot{\nu} \approx 4.5 \times 10^{-12}$ Hz s^{-1} and $\dot{\nu} \approx 3.0 \times 10^{-12}$ Hz s^{-1} respectively, giving a spin-up time scale $\approx \nu/\langle\dot{\nu}\rangle \approx 10$ yrs. The steady spin-up strongly suggests that the neutron star is accreting from an accretion disk during these intervals. The fluxes are also higher than usual for these orbital phases. The 20-55 keV flux averaged over MJD 48443-48458 (orbital phase 0.35-0.70) is $(1.889 \pm 0.037) \times 10^{-9}$ ergs cm^{-2} s^{-1}, whereas the folded flux history averaged over the same orbital phase yields $(1.216 \pm 0.008) \times 10^{-9}$ ergs cm^{-2} s^{-1}. For the second spin-up episode, the 20-55 keV flux averaged over MJD 49233-49245 (orbital phase 0.37-0.66) is $(1.926 \pm 0.042) \times 10^{-9}$ ergs cm^{-2} s^{-1}, compared to the folded flux history value for the same orbital phase of $(1.239 \pm 0.010) \times 10^{-9}$ ergs cm^{-2} s^{-1}.

The magnetospheric radius must be less than the co-rotation radius $r_{\rm co} = 1.3 \times 10^{10}$ cm (where a Keplerian disk co-rotates with the neutron star) in order for the material to flow freely along the magnetic field lines and onto the neutron star. The maximum specific angular momentum transferred to the neutron star is then $l_{\rm max} \equiv (GM_{\rm x} r_{\rm co})^{1/2}$. This allows us to set a lower limit on $\dot{M}$ given $\dot{\nu}$, as $N_{\rm obs} = 2\pi I \dot{\nu} < \dot{M} l_{\rm max}$ (Chakrabarty et al. 1993). We then find for $M_{\rm x} = 1.4 M_{\odot}$,

$$\dot{M} > 2 \times 10^{-10} M_{\odot} \text{ yr}^{-1} \left(\frac{\dot{\nu}}{3 \times 10^{-12} \text{ s}^{-2}}\right) \left(\frac{R}{10 \text{ km}}\right)^2 \tag{5.5}$$

where $I = 0.4 M_{\rm x} R^2$ is the neutron star moment of inertia (Ravenhall & Pethick 1994). The measured $\dot{\nu}$ values of 4.5×10^{-12} Hz s^{-1} and 3.0×10^{-12} Hz s^{-1} imply $L_{\rm x} > 3 \times 10^{36}$ erg s^{-1}, in agreement with the 1-20 keV *GRANAT*/WATCH luminosity measurements (Chichkov

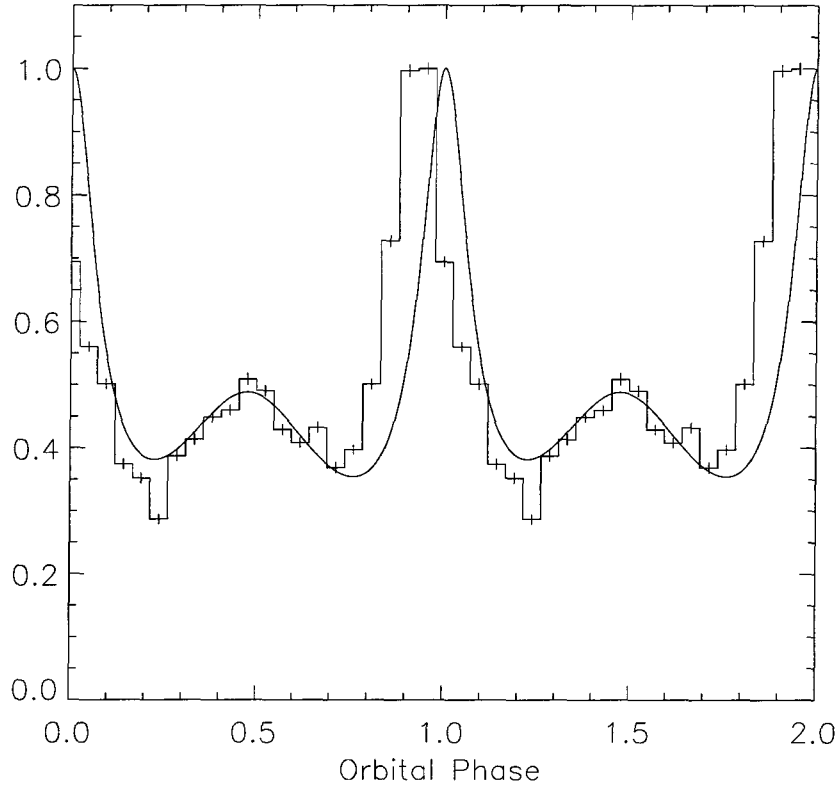

Figure 5.11: A comparison of the folded flux history and the fit obtained using a circumstellar disk model with the following parameters: $v_0 = 0.5$ km s^{-1}, $v_{\rm rot,w} = 80$ km s^{-1}, $\alpha = 1$ and $n = 3.7$. Both the fit and the histogram have been normalized by their respective peak values.

et al. 1995) of $\approx 10^{37}$ ergs s^{-1} at periastron for a distance of 1.8 kpc. Of course, the magnetosphere could be closer to the star than the co-rotation radius.

Both spin-up events begin just after periastron. The infrequent occurrence of these episodes argues against the hypothesis that the event is triggered by tidal overflow at periastron. However, especially if the companion is as luminous as K95 infer, the episodes might be accretion of matter ejected in a mass-loss episode from the star, similar to what is seen from luminous blue variables (LBVs). The luminosity, mass and $T_{\rm eff}$ of Wray 977 put it squarely in the regime where LBVs undergo large scale mass loss episodes every 2-10 years (Stothers & Chin 1995). It may be that the expelled matter is captured predominantly at periastron, in which case the delay between periastron passage and the onset of the torque is the viscous time scale in the accretion disk. The total mass accreted by the neutron star

during a spin-up episode is $> 2 \times 10^{-11} M_{\odot}$, comparable to the mass in an $\alpha = 0.1$ [2] disk of outer radius $R \sim 10^{10}$ cm, for which the viscous time is about 10-30 days, the same as the duration of the spin-up event.

5.4.2 Accretion from the Companion's Wind

Excluding the spin-up episodes, the neutron star experiences torques of both signs, independent of orbital phase, resulting in nearly no frequency change over our observation interval. This is consistent with two-dimensional simulations of wind accretion by Fryxell and Taam (1988) and Taam and Fryxell (1989). They showed that accretion from a stellar wind is highly time-dependent; transient accretion disks form and persist for a few flow times across the accretion diameter ($\sim$ hours for GX 301–2) before dissipating, only to be replaced by disks rotating in the opposite direction. This flip-flop behavior results in large specific angular momentum transfer on short time scales, but little net angular momentum change on long time scales.

This behavior motivates the simplest model of super-sonic Bondi-Hoyle accretion from the spherical wind of the companion, which predicts the neutron star accretion rate, $\dot{M}$, to be

$$\dot{M} = \frac{\dot{M}_W G^2 M_x^2 \delta^3}{a^2 v_W^4(a)} \tag{5.6}$$

where a is the distance between the companion and the neutron star, v_W is the wind velocity at the neutron star and $\delta = v_W / v_{rel}$, where v_{rel} is the relative velocity between the neutron star and the wind. Following Castor, Abbott & Klein (1975), we write

$$v_W(r) = v_\infty \left(1 - \frac{R_c}{r}\right)^\beta \tag{5.7}$$

where v_∞ is the terminal velocity of the wind and $\beta = 0.5$. A refined treatment by Friend & Abbott (1986) yields $\beta = 0.8$, the value which we adopt. However, the spherical wind model does not predict the observed secondary flux peak at $\phi_{orb} \approx 0.5$. Moreover, for $\dot{M}_W = 3 \times 10^{-6}$ $M_\odot$ yr^{-1} and $v_\infty \approx 1000$ km s^{-1} (Parkes et al. 1980), we get $\dot{M} \approx 4 \times 10^{-10}$ $M_\odot$ yr^{-1} at periastron and a ratio of the maximum to minimum flux of ≈ 50. If we adopt $v_\infty = 400$ km s^{-1} (K95), then the maximum to minimum flux ratio drops to $\approx$ 12. Both of these are inconsistent with our observed ratio of 4. Other experiments have measured this ratio, yielding values of ≈ 4 (*Ariel 5*, 2-15 keV) (Watson, Warwick, & Corbet

[2] The typical range of α is $\sim$ 0.01–1 (Frank, King, & Raine 1992)

1982), $\approx$ 10 *GRANAT*/WATCH, 8-20 keV) (Chichkov et al. 1995), $\approx$ 20 (*HEAO 1*, 13-40 keV) (Rothschild & Soong 1987), and 50 (*EXOSAT*, 0.9-21 keV) (Haberl 1991), possibly suggesting changes in the density profile of the wind.

The inability of the radiatively driven wind model to predict the peak at apastron motivated the circumstellar disk model of Pravdo et al. (1995). Though there is no direct observational evidence for a circumstellar disk, recent work by Ignace, Cassinelli & Bjorkman (1996) has shown that even moderate rotation (like that seen in Wray 977) can lead to formation of an equatorially enhanced wind and perhaps a circumstellar disk.

For simplicity, we assume that the neutron star moves within a circumstellar disk modeled as (Waters et al. 1989)

$$\rho(r) = \rho_0 \left(\frac{r}{R_c}\right)^{-n} \tag{5.8}$$

$$v_{r,w}(r) = v_0 \left(\frac{r}{R_c}\right)^{n-2} \tag{5.9}$$

$$v_{\rm rot,w}(r) = v_{\rm rot,c} \left(\frac{r}{R_c}\right)^{-\alpha} \tag{5.10}$$

where r is the distance from the star, $v_{\rm r,w}$ and $v_{\rm rot,w}$ are respectively the radial and rotational components of the wind velocity and $v_{\rm rot,c}$ is the rotational velocity of the star. A finite $v_{\rm r,w}$ shifts the location of the accretion peaks and breaks their temporal symmetries. We fix $v_{rot,w} = 80$ km s^{-1} (allowing for a higher value than the $v \sin i$ measurement) and $\alpha = 1$ (assuming that the disk material conserves angular momentum). The observed periastron/apastron flux ratio then requires $n = 3.7$, within the range of $3 \leq n \leq 3.75$ derived for 6 known Be/X-ray binaries (Waters et al. 1988). The symmetrical apastron peak implies $v_0 \lesssim 1$ km s^{-1}. Although observations of known Be-stars suggest ($2 \lesssim v_0 \lesssim 20$) km s^{-1}, its value is largely uncertain (Lamers & Waters 1987). We adopt $v_0 = 0.5$ km s^{-1} in our fit to the folded flux history which is shown in Figure 5.11. Pravdo et. al. (1995) suggested that if the orbital plane was inclined with respect to that of the disk, then the neutron star may intersect the disk slightly before periastron, resulting in a pre-periastron flux peak. However, the displacement required to reproduce the observed shift implies a pre-apastron peak at an orbital phase $\approx$ 0.3, which is not observed.

So, neither of these accretion models predict the pre-periastron peak of the orbit-folded flux profile, for which many explanations have been proposed. Leahy (1991) and Haberl (1991) suggested that enhanced mass loss from the inner Lagrangian point L1 near

periastron would form a gas stream (Stevens 1988) and accrete onto the neutron star prior to periastron. Leahy's model fit the flux and column density measurements of *TENMA* only at orbital phases $0.75 \lesssim \phi_{\rm orb} \lesssim 1.2$. Haberl's model predicts another flux peak at orbital phase 0.3, when the neutron star intersects the gas stream a second time. which we do not observe. However, we note that the orbital phase of the peak in Haberl's model strongly depends on the shape of the gas stream which in turn depends on the radial wind velocity profile, a poorly known quantity due to, for example, ionization effects.

Chichkov et al. (1995) suggested that the heating of the stellar wind by the X-rays from the neutron star would reduce the Bondi-Hoyle accretion rate prior to periastron. This occurs when the sound speed of the X-ray heated gas becomes larger than the relative velocity between the neutron star and the stellar wind. The supply of matter to the neutron star then prematurely shuts off sometime before periastron passage. Another possible source of variability in the Bondi-Hoyle accretion is direct modification of the stellar wind properties by the X-ray heating and ionization (Ho & Arons 1987a, 1987b; Blondin 1994) This has not been investigated in detail for this eccentric system and might yield some new insights.

5.5 Conclusions

The two rapid spin-up episodes we observed are the most striking features in the spin frequency history of GX 301–2. The steady spin-up strongly suggests the temporary formation of an accretion disk about the neutron star. Aside from these episodes, there is virtually no net change in the spin frequency of the neutron star on yearly time scales. This suggests that the neutron star primarily accretes from the stellar wind of the companion; if accretion disks form at all, they must generally alternate between prograde and retrograde directions on time scales $\lesssim$ 4 d. However, the 2 spin-up episodes observed (Figure 5.5) strongly suggest that a long-lived ($\approx$ 30 d) accretion disk with a definite sense of rotation can sometimes form to spin up the neutron star. Since the net change in neutron star spin period in nearly four years of BATSE observations is due almost entirely to the two spin-up episodes, it is possible that the measured decrease in the period of $\approx$ 25 s since 1984 (Figure 5.1) is entirely due to spin-up episodes similar to the two we have observed, with a recurrence time scale $\approx$ 2 years. This interpretation is also consistent with the secular spin-up rate extrapolated from the previous decade of observations. The pre-1984 frequency

history does not exhibit this secular trend, implying that similar spin-up episodes may not have occurred during that era.

In addition to the well-known flux maximum just before periastron passage, the pulsed flux history folded at the orbital period reveals a secondary maximum close to apastron, which is difficult to account for in a spherically symmetric radiatively driven wind. Accretion from a circumstellar disk might explain this phenomena, but is by no means unique. It might be profitable to apply the X-ray heating and ionization scenario of Ho & Arons (1987a, 1987b) to this eccentric wind-few system. A careful consideration of the parameters of the binary system (see Figure 5.9) has allowed us to place an upper limit on the mass and radius of the companion, which argues against the reclassification by Kaper et al. (1995) of the star as a B1 Ia+ hypergiant. More detailed optical observations (particularly a spectral and luminosity classification) of this object would better constrain its mass, radius and distance.

The question remains as to what causes the formation of the transient accretion disks and what sets their $\sim$ yearly recurrence time scale. We speculated here that formation of these transient disks is related to episodic mass loss from the companion. Simultaneous multi-wavelength observations of GX 301–2 during the next spin-up episode may help answer these questions, as well as provide new insights into the mechanism of mass transfer in wind-fed accreting binaries.

Chapter 6

Spin Evolution of Accretion Powered Pulsars

6.1 Introduction

The single most important attribute which distinguishes the different classes of accretion powered pulsars is their long term spin evolution, which is strongly dependent on the mode of mass transfer from the companion to the the neutron star. For example, pre–BATSE X-ray missions, complemented by optical observations, established that wind–fed systems are characterized by random walks in frequency while disk–fed systems exhibit steady spin–up. Although these observations motivated models which accounted for the main features in the long–term spin evolution of disk–fed sources (Rappaport & Joss 1977; Ghosh & Lamb 1979), several problems remained. For example, Cen X–3 and Her X–1 exibited a spin–up rate much smaller than that predicted by Equation 1.6, while the wind–fed system GX 301–2 appears to have undergone steady spin–up since 1985, implying the surprising presence of a steady accretion disk. As Figure 4.1 shows, some of these apparent discrepancies arise from sparse coverage of pre–BATSE observations which mask important features in the long term frequency histories.

An excellent demonstration of how the continuous monitoring ability of BATSE has revised our picture of spin evolution in accreting pulsars is shown in Figs 6.1 and 6.2. The most natural interpretation of the sparse frequency histories obtained before 1991 is that both Cen X–3 and OAO 1657–415 are undergoing secular spin–up. However, as the dense frequency sampling from BATSE shows, the secular spin–up trend in each of the two systems is actually a residual effect of the alternating spin–up and spin–down episodes which characterize the Cen X–3 and OAO 1657–415 frequency history. Although this explains why

Cen X–3 and OAO 1657–415 are spinning up on a time scale much longer than that predicted by Equation 1.7, it also raises new questions, as discussed in detail below.

In the following sections, we describe new features in the frequency evolution of persistent accreting pulsars revealed by BATSE observations. we discuss the implications of the BATSE observations for current models of spin–evolution and highlight the intriguing questions raised by these observations. As the spin–evolution of transient accreting pulsars are strongly correlated with the mass accretion rate, the discussion for these sources will be deferred to Chapter 7, where we discussion torque–luminosity relations in accreting pulsars.

6.2 Torque Switching in Persistent Sources

An examination of the frequency histories of persistent sources plotted in Chapter 4 and the long term frequency histories in Figure 4.1 reveal torque switching to be a very common behavior among the persistent sources monitored by BATSE. Of the 8 persistent sources monitored by BATSE, the ones that do not exhibit steady spin–up/spin–down on time scales of $\gtrsim$ 10 d are those which populate the non Roche Lobe filling supergiants region of the Corbet diagram: Vela X–1, GX 301–2 and 4U 1538–52. (For Her X–1, the BATSE measurements are too sparse for us to assess the presence of this torque switching behavior.) The sources which clearly exhibit torque switching are: 4U 1626–67, GX 1+4, Cen X–3 and OAO 1657–415. 4U 1626–67, GX 1+4 and Cen X–3 are clearly in the Roche–Lobe overfilling region of the Corbet diagram while OAO 1657–415 borders the underfilled Roche Lobe supergiants and Roche Lobe filling supergiants regions. Table 6.1 summarizes the quantities which characterize the torque reversals in such systems. Unlike 4U 1626–67 and GX 1+4 for which only one long–term reversal has been observed, multiple torque reversals have been observed for Cen X–3 and OAO 1657–415, and the corresponding distribution of frequency derivatives and durations of spin–up/spin–down episodes are histogrammed in Figures 6.3, 6.4, 6.5 and 6.6. We note that all the measured spin–up rates, $\dot{\nu}_{\rm su}$ are within a factor of ≈ 4 of the characteristic spin–up rate, $\dot{\nu}_{\rm char}$ computed from the estimated mass accretion rates and assuming that $r_{\rm m} = r_{\rm co}$. This is reassuring as it shows that the simple torque model described in Chapter 1 is at least qualitatively correct.

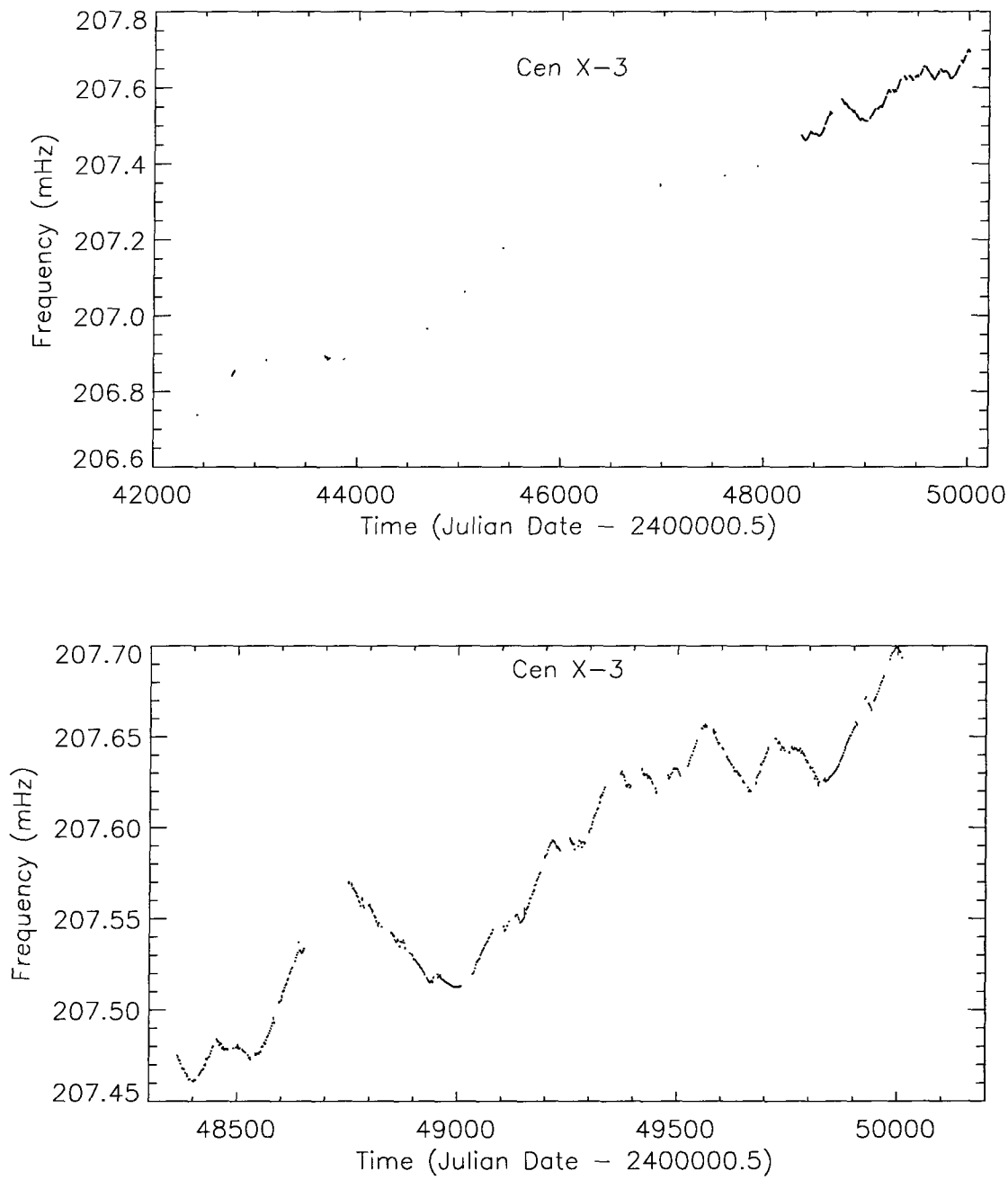

Figure 6.1: Frequency histories of Cen X–3. Upper panel: The long-term frequency history of Cen X–3. Lower panel: High resolution BATSE measurements of the intrinsic spin frequencies of Cen X–3.

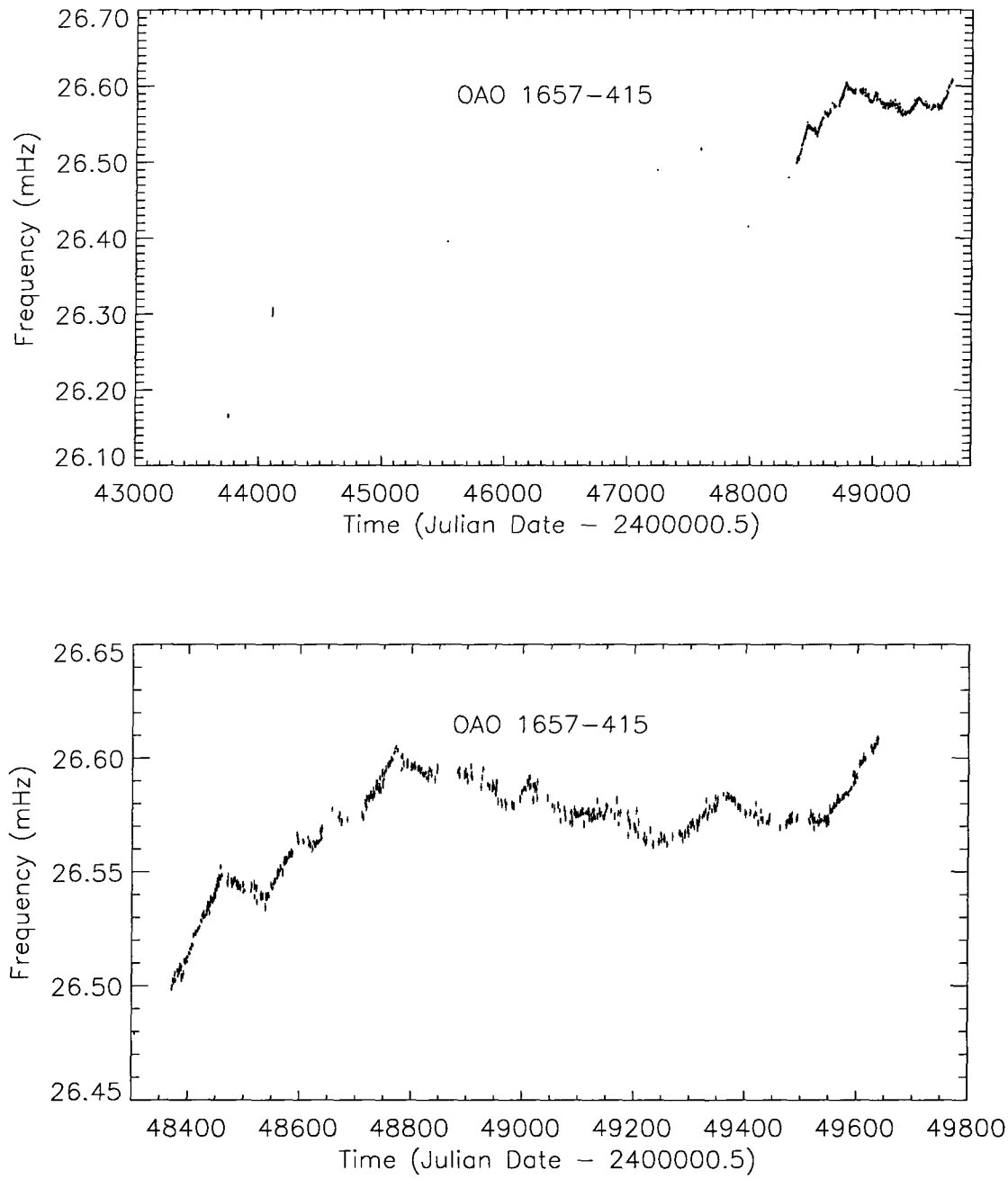

Figure 6.2: Frequency histories of OAO 1657–415. Upper panel: The long-term frequency history of OAO 1657–415. Lower panel: High resolution BATSE measurements of the intrinsic spin frequencies of OAO 1657–415.

For every source, the characteristic magnitude of the spin–up rate is *always* greater than that for spin–down, although they are all within a factor of $\approx$ two of each other. In both Cen X–3 and OAO 1657–415, the transitions occur on a $\lesssim$ 10 d time scale, shorter than what BATSE can resolve. Unfortunately, the torque transitions in 4U 1626–67 and GX 1+4 took place before the launch of BATSE.

In the basic model of accretion in a disk–fed system described in Chapter 1, accretion onto the neutron star occurs when the magnetospheric radius, $r_{\rm m}$ is less than the co–rotation radius, $r_{\rm co}$, resulting in spin–up. When $r_{\rm m} > r_{\rm co}$, the centrifugal barrier expels matter from the neutron star, resulting in spin–down (the propeller effect). While the observed spin–up episodes in the various sources mentioned earlier can be accounted for by this basic model, the spin–down episodes are harder to explain, since the propeller effect predicts spin–down to be accompanied by a significant decrease in luminosity. In the following subsections, we discuss three broad classes of models, all extensions of the basic one, which could be invoked to explain the observed spin–down and torque switching behavior:

- Prograde accretion disk interacting with pulsar magnetosphere.
- Transitions between standard Keplerian disks and sub–Keplerian advection–dominated flow (ADAF).
- Alternating prograde and retrograde accretion disks.

We briefly summarize the key features of each model, critically assess their applicability to each of the sources exhibiting torque switching behavior, and finally suggest additional observations which may resolve existing ambiguities.

6.2.1 Prograde Accretion Disk Interacting with Pulsar Magnetosphere

One of the most widely cited models in this class is that of Ghosh & Lamb (1979) (GL), who asserted that the torque on a disk–fed pulsar is the sum of two components

$$N = N_{\rm mat} + N_{\rm mag} \tag{6.1}$$

where $N_{\rm mat} = \dot{M}_{\rm acc}\sqrt{GM_{\rm x}r_{\rm m}}$ is the torque contribution from the accretion of matter while $N_{\rm mag}$ is the contribution from the interaction between the accretion disk and the magnetic field lines that thread it. Beyond the co-rotation radius, the accretion disk rotates at a speed slower than that of magnetic field lines, causing the latter to be swept back and resulting

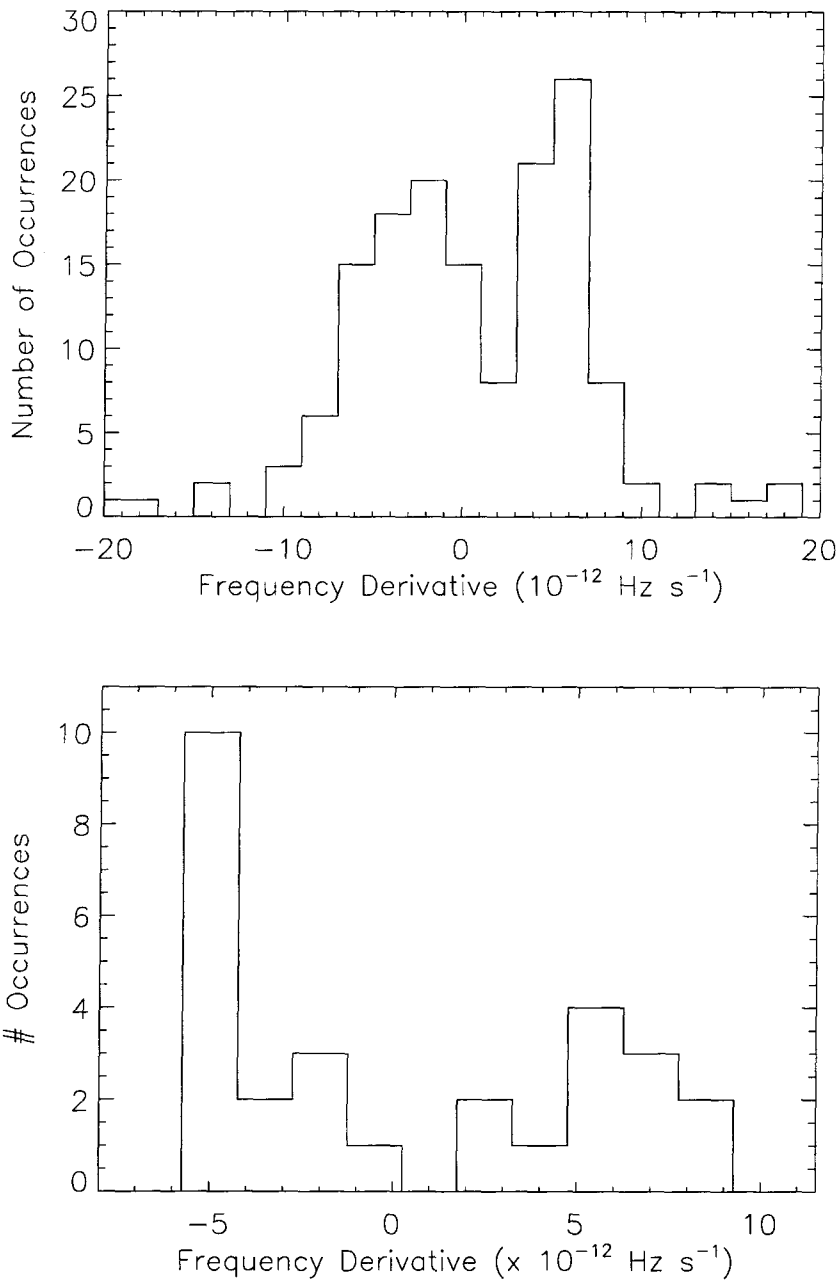

Figure 6.3: Upper Panel: Histogram of frequency derivatives for Cen X–3. The frequency derivatives were derived from frequencies measured at 4–day intervals from the power spectra of the 20–50 keV DISCLA data. Lower Panel: Each frequency derivative here was obtained by performing a linear fit to all frequency measurements in a particular spin–up/spin–down episode.

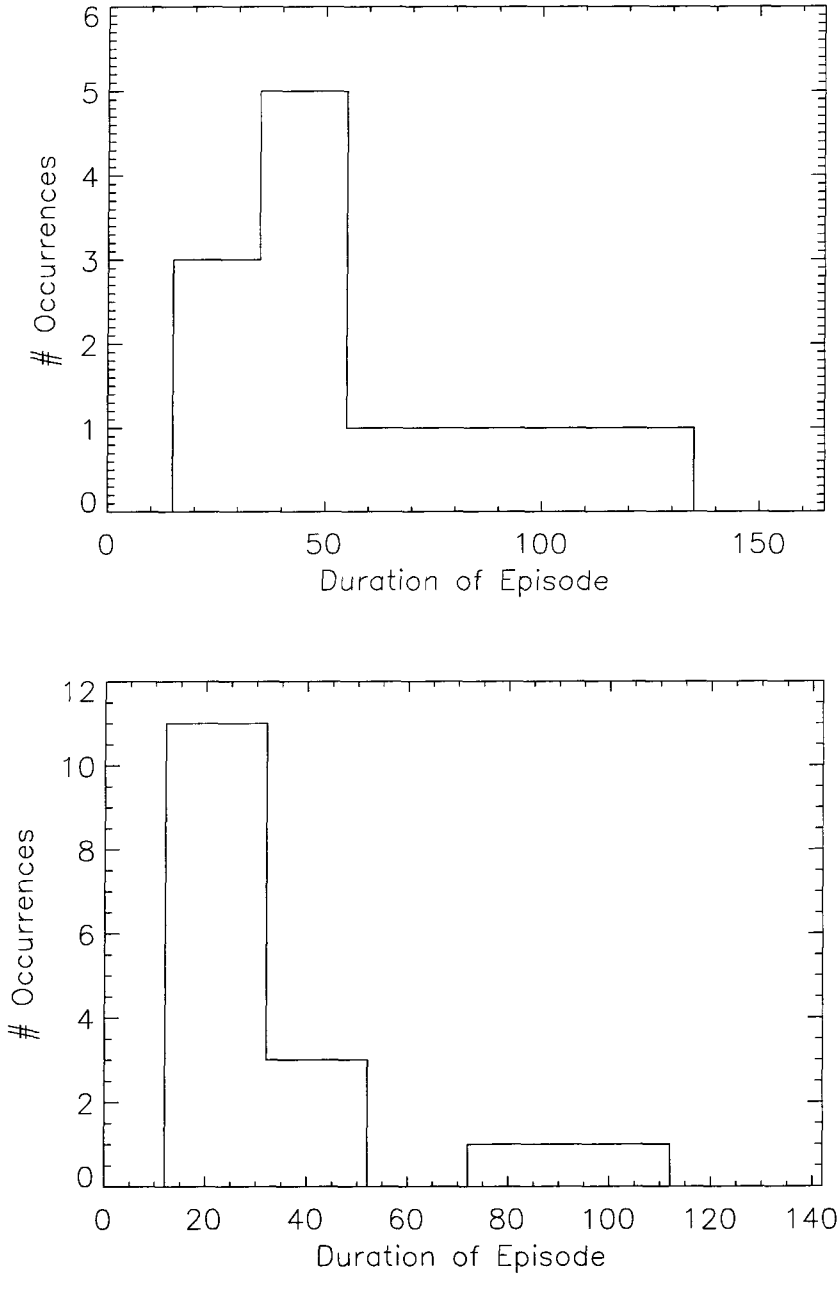

Figure 6.4: Distribution of durations of spin–up (upper panel) and spin–down (lower panel) episodes for Cen X–3.

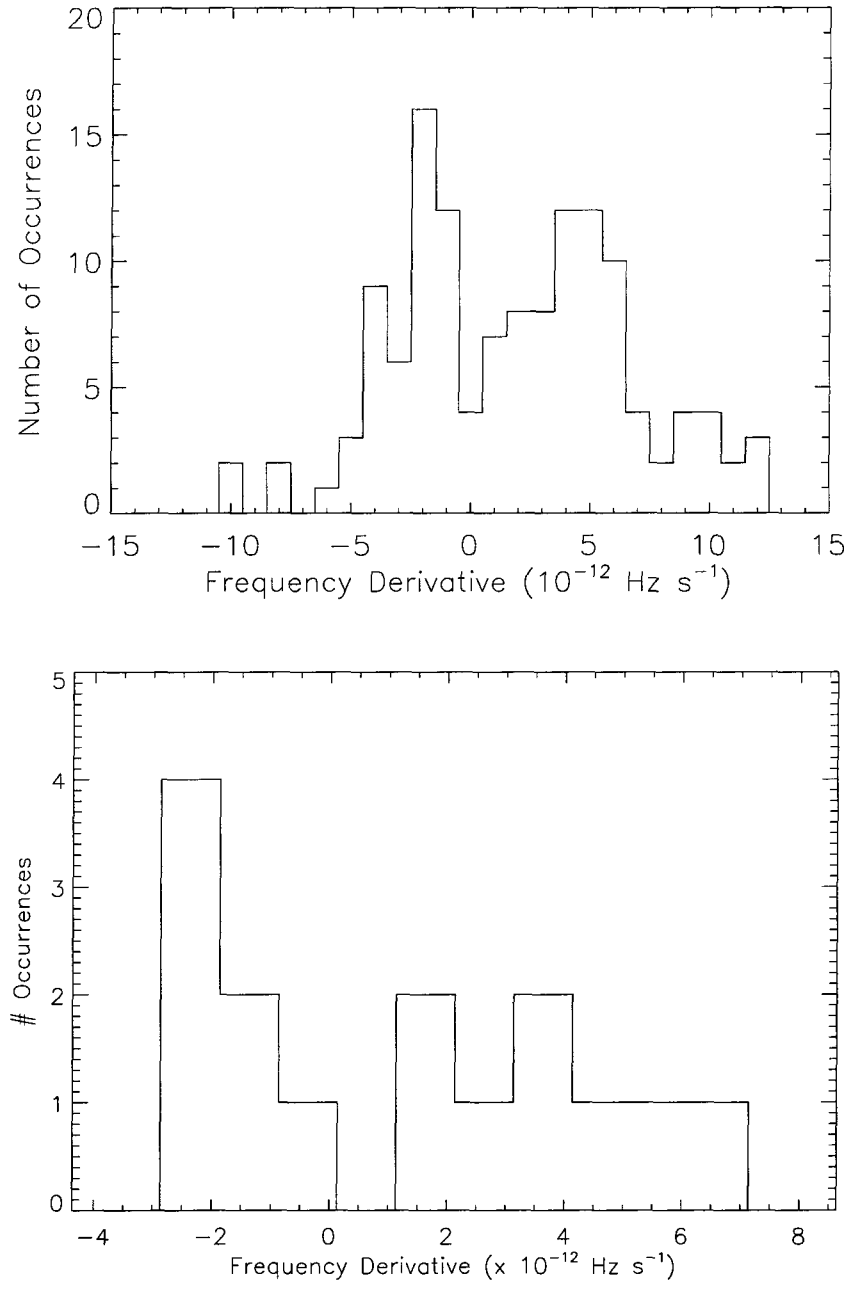

Figure 6.5: Upper Panel: Histogram of frequency derivatives for OAO 1657–415. The frequency derivatives were derived from frequencies measured at 4–day intervals from the power spectra of the 20–50 keV DISCLA data. Lower Panel: Each frequency derivative here was obtained by performing a linear fit to all frequency measurements in a particular spin–up/spin–down episode.

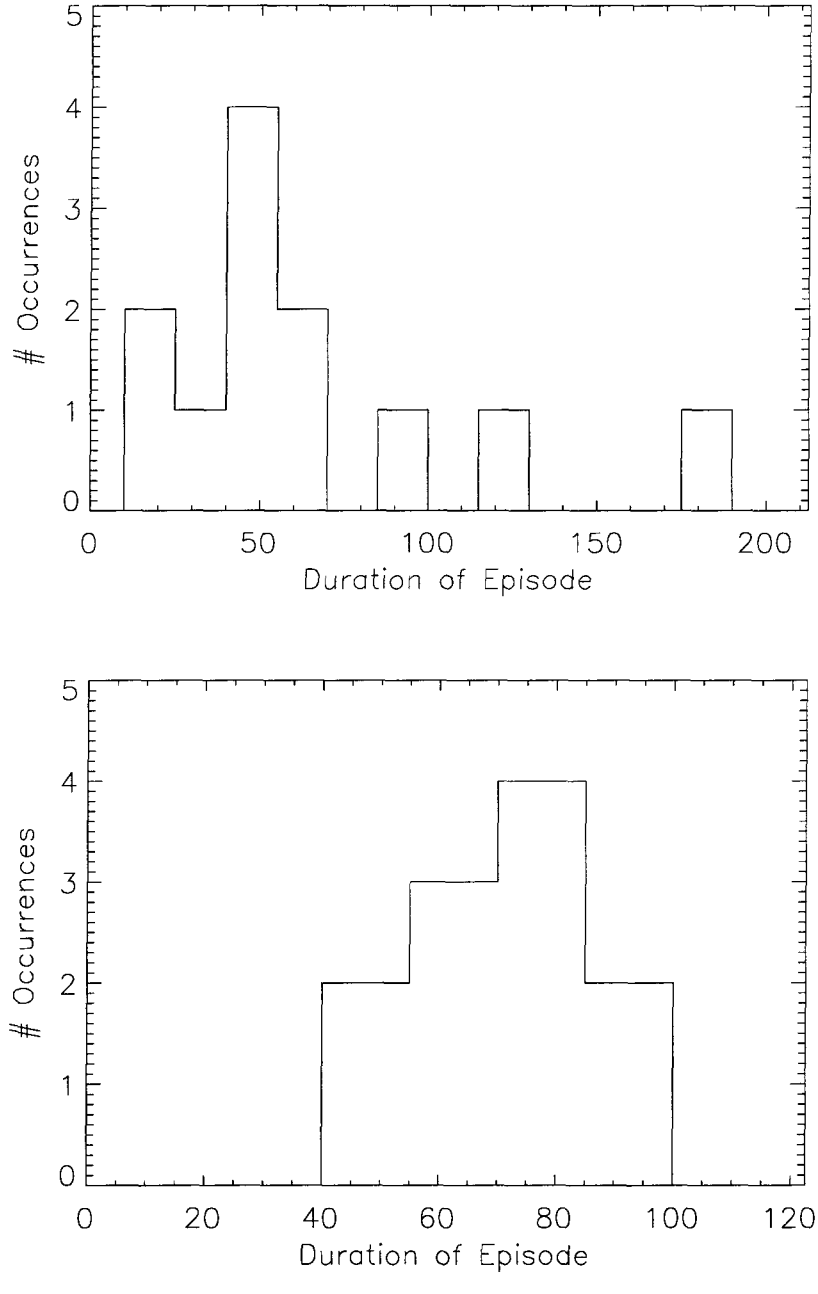

Figure 6.6: Distribution of durations of spin–up (upper panel) and spin–down (lower panel) episodes for OAO 1657–415.

Table 6.1. Characteristics of Torque Reversals

Source	$\dot{\nu}_{\rm char}$[1]	$\lvert\dot{\nu}_{\rm su}\rvert$[2]	$t_{\rm su}$[3]	$\lvert\dot{\nu}_{\rm sd}\rvert$[4]	$t_{\rm sd}$[5]	$B_{\rm p}^{\rm min}$[6]
GX 1+4 [7]	6.6	6.026(1)	$\gtrsim$ 13 yrs	3.5348(1)	$\gtrsim$ 13 yrs	358
4U 1626–67 [8]	2.6	0.854(7)	$\gtrsim$ 12 yrs	0.7175(4)	$\gtrsim$ 5 yrs	5
Cen X–3 [9]	22.8	6.28(7)	55(31) days	4.94(8)	$\approx$ 34(24) days	5
OAO 1657–415 [10]	–	5.50(8)	63(45) days	2.45(9)	68(14) days	40

[1]Characteristic spin–up rate expected for observed mass accretion rate, computed by assuming $r_{\rm m} = r_{\rm co}$ in Equation 1.6.

[2]Spin–up rate in units of 10^{-12} Hz s^{-1}.

[3]Characteristic duration of spin–up episode.

[4]Spin–down rate in units of 10^{-12} Hz s^{-1}.

[5]Characteristic duration of spin–down episode.

[6]Minimum dipole field strength in units of 10^{12} G, inferred from $\dot{\nu}_{\rm su}$ and assuming source to be spinning at equilibrium See Section 6.2.1 for details.

[7]Only 1 torque reversal observed. Values of $|\dot{\nu}|$ taken from Chakrabarty et al.(1997b). $\dot{M}_{\rm acc}$ used in computation of $\dot{\nu}_{\rm char}$ taken from Chakrabarty & Roche (1997).

[8]Only 1 torque reversal observed. Values of $|\dot{\nu}|$ taken from Chakrabarty et al.(1997a). $\dot{M}_{\rm acc}$ used in computation of $\dot{\nu}_{\rm char}$ taken from Chakrabarty (1997).

[9]Values of $|\dot{\nu}_{\rm su}|$ and $|\dot{\nu}_{\rm sd}|$ have been respectively averaged over positive and negative values measured. (Figure 6.3 upper panel.) Values of t quoted are respective average (with standard deviation) of those histogrammed in Figure 6.4. $\dot{M}_{\rm acc}$ used in computation of $\dot{\nu}_{\rm char}$ taken from Nagase (1989).

[10]Values of $|\dot{\nu}_{\rm su}|$ and $|\dot{\nu}_{\rm sd}|$ have been respectively averaged over positive and negative values measured. (Figure 6.5 upper panel.) Values of t quoted are respective average (with standard deviation) of those histogrammed in Figure 6.6. No estimate of $\dot{\nu}_{\rm char}$ can be made because companion is unidentified and distance is unknown.

in a spin–down torque. For slow rotators, defined as those with spin frequencies much less than the equilibrium frequencies ($\omega_{\rm spin} \ll \Omega_{\rm K}(r_{\rm m}) = (GM/r_{\rm m}^3)^{1/2}$), the above spin–down contribution is small and GL estimates that $N_{\rm mag} \approx 0.4\ N_{\rm mat}$, so that $N \approx 1.4\ N_{\rm mat}$. However, for fast rotators ($\omega_{\rm spin} \approx \Omega_{\rm K}(r_{\rm m})$) $N_{\rm mag}$ can be negative with $-N_{\rm mag} > N_{\rm mat}$. This results in spin–down, even though accretion is taking place. To explain the spin–down in Cen X–3 and Her X–1, Ghosh & Lamb (1979) argued that both these sources are fast rotators rotating close to their equilibrium frequencies of $\Omega_{\rm K}(r_{\rm m})$, and that decreases in the mass accretion rates cause $r_{\rm m}$ to increase, thus increasing the magnitude of the spin–down torque $N_{\rm mag}$ and resulting in spin–down.

In the other models (Anzer & Borner 1980; Arons et al. 1984; Lovelace, Romanova, & Bisnovatyi-Kogan 1995), spin–down results from the the loss of angular momentum in a magnetohydrodynamic outflow: outflowing material moves along rigid magnetic field lines like beads on a wire, gaining angular momentum from the star as it is forced to corotate. The resultant spin-down torque is given by $N \sim \dot{M}_{\rm w}\sqrt{GMr_\alpha}$, where $\dot{M}_{\rm w}$ is the mass loss rate in the wind and r_α is the Alfven radius within which the magnetic field becomes dynamically important.

All of the current models involving disk–magnetosphere interaction are problematic within the context of our BATSE observations. The similarities between the spin–up and spin–down magnitudes in Table 6.1 require not only step–like changes in the mass accretion rates, but also fine tuning in their magnitudes. This is especially implausible in 4U 1626–67, where the mass accretion rate is likely governed by the loss of angular momentum through gravitational radiation (Chakrabarty et al. 1997a). Moreover, none of these models inherently favor positive torques and hence cannot explain why the characteristic spin–up rates are always larger than the spin–down rates for all the four sources.

The requirement by these models that the pulsar be spinning close to equilibrium is also problematic for some sources as it results in unusually high dipole magnetic field strengths. For accretion to take place, the magnetospheric radius must be less than the co–rotation radius: $r_{\rm m} < r_{\rm co}$. From Equation 1.5, the mass accretion rate onto the neutron star must thus satisfy the lower bound

$$\dot{M}_{\rm min} = 6.26 \times 10^{-10}\ M_\odot\ {\rm yr}^{-1} \left(\frac{R_{\rm x}}{10\ {\rm km}}\right)^2 \left(\frac{\dot{\nu}}{10^{-12}\ {\rm Hz\ s}^{-1}}\right) \left(\frac{\rm s}{P}\right)^{1/3} \qquad (6.2)$$

and from Equation 1.8, the corresponding dipole magnetic field, $B_{\rm p}$ is given by

$$B_{\rm p} \gtrsim 0.177 \times 10^{12}\ {\rm G} \left(\frac{P}{\rm s}\right)^{7/6} \left(\frac{\dot{M}_{\rm min}}{10^{-10} M_{\odot}\ {\rm yr}^{-1}}\right)^{1/2}. \quad (6.3)$$

The dipole fields derived this way are tabulated in Table 6.1. The values for OAO 1657–415 and GX 1+4 are unusually large, especially as they are lower limits. Cyclotron resonance features (CRFs) have yet to be detected in OAO 1657–415 and GX 1+4. Nevertheless, an independent estimate of $B_{\rm p}$ for these two sources can be obtained from their respective spectral cut–off energy, $E_{\rm c}$, as the *GINGA* GDB experiment found a clear correlation between the cyclotron resonance energy and $E_{\rm c}$ in 9 accreting pulsars (Makishima & Mihara 1992). Although we caution that the CRF and $E_{\rm c}$ are typically close together in the observed spectra and the separate fits used to extract each of these parameters may introduce a slight inherent correlation, it is still useful to infer the B fields of OAO 1657–415 and GX 1+4 using this method. In OAO 1657–415 and GX 1+4, $E_{\rm c} \approx 18$ keV and 10 keV respectively, (White, Swank, & Holt 1983), corresponding to $B_{\rm p} \approx 4 \times 10^{12}$ G and 2×10^{12} G, which are in good agreement with the inferred dipole field strengths for the 9 pulsars with clear CRFs. The huge discrepancies between the values of $B_{\rm p}$ inferred from spectral cutoff and those determined by assuming equilibrium cast additional doubt on the applicability of such models.

6.2.2 Transitions Between Standard Keplerian disks and sub–Keplerian Advection–dominated Flow (ADAF)

Yi, Wheeler & Vishniac (1997) proposed that the torque reversals are caused by the transition of standard Keplerian accretion disks to sub–Keplerian advection–dominated flows (ADAF). They argued that when the mass accretion rate onto the neutron star falls beneath a critical level, $\dot{M}_{\rm crit}$, the accretion disk evolves into a optically thin, low density state. When this happens, the accretion disk is said to be in an advective state in which radiative losses become inefficient and most of heat generated from orbital energy dissipation is advected onto the compact object (Narayan & Yi 1995b). The hot accretion disk can no longer be geometrically thin and becomes sub–Keplerian. Under the assumption that the neutron star is initially spinning close to equilibrium, the sub–Keplerian angular frequency at the magnetospheric radius becomes less than the neutron star rotational frequency, and a spin–down torque results. Yi, Wheeler & Vishniac (1997) also argued that the time scale

for transitions to ADAF flows are expected to be less than the local thermal time scale or the disk viscous–thermal time scale, which is $\sim 10^3$ s.

The most attractive aspect of this model is that it naturally accounts for the very short time scales over which the observed torque transitions take place. However, as Nelson et al.(1997) pointed out, fine tuning of the sub–Keplerian flow velocity profile is required to account for similarities in the magnitude of spin–up and spin–down torques. Moreover, as explained in the previous subsection, the spin equilibrium requirement is problemmatic.

6.2.3 Alternating Prograde and Retrograde Disks

Nelson et al.(1997) proposed that the torque reversals are manifestations of disk reversals, thus reviving similar suggestions by Makishima et al.(1988) and Dotani et al.(1989) to explain the secular spin–down trend in GX 1+4. As Nelson et al.(1997) pointed out, the retrograde disk model naturally accounted for the bimodal distribution of torques in Cen X–3 and OAO 1657–415, the similarities in magnitudes between the spin–up and spin–down rates in Table 6.1, the fact that all torque transitions observed in GX 1+4, 4U 1626–67 and Cen X–3 involve a change in direction, and the observed correlation between the BATSE 20–50 keV pulsed flux and *spin–down* torque in GX 1+4 (Chakrabarty et al. 1997b). The disk reversal model also eliminates the equilibrium requirement which led to unusually high dipole fields in GX 1+4 and OAO 1657–415.

Despite these merits, the disk reversal model does not account for why the spin–up torques are consistently larger then the spin–down torques. Moreover, a critical question which the disk reversal model must address is the mechanism by which a retrograde disk forms. The need to resolve this question is especially compelling in 4U 1626–67 and Cen X–3, as there is substantial evidence to suggest that these systems overflow or are close to overflowing their Roche Lobes (see sections below). Due to orbital motion, matter from the companion which escapes through the inner Lagrangian point L_1 has high specific angular momentum relative to the neutron star of $l \sim d^2\Omega_{\rm orb}$, where d is the separation between the neutron star and the L_1 point, and $\Omega_{\rm orb}$ is the angular orbital velocity of the neutron star. It is thus hard to imagine retrograde disk formation under these circumstances.

A possible resolution of this dilemma is provided by the two–dimensional hydrodynamical simulations of Blondin, Stevens & Kallman (1991), who showed that wind accretion and Roche Lobe overflow are actually limiting cases of the wind enhancement induced by

neutron star tidal effects on the stellar companion. Hence, even a companion star that is close to overfilling its Roche Lobe could still exhibit properties of wind accretion.

As long as wind accretion takes place, disk reversals are not only plausible, but expected. Two–dimensional hydrodynamical simulations (Fryxell & Taam 1988; Taam & Fryxell 1989; Blondin et al. 1990) have shown that accretion from a stellar wind is highly time–dependent; transient accretion disks of alternating directions form due to changing flow patterns of the wind, which occurs on the time scale of several flow times across the accretion cylinder

$$\tau \sim 10^6 \left(\frac{v_{\rm rel}}{10^7 {\rm cm\ s^{-1}}} \right)^{-3} {\rm s} \tag{6.4}$$

where $v_{\rm rel}$ is the relative velocity between the neutron star and the stellar wind. Three–dimensional simulations by Ruffert et al.(1997) also revealed similar alternating accretion disks. The lifetime of of the accretion disk is expected to be longer than τ, since the material in the accretion disk disspates on a viscous time scale given by (Frank, King, & Raine 1992)

$$t_{\rm visc} \sim 4.3\ \alpha^{-4/5} \left(\frac{\dot{M}_{\rm acc}}{10^{-10}\ M_\odot\ {\rm yr^{-1}}} \right)^{-3/10} \left(\frac{R_{\rm d}}{10^{10}\ {\rm cm}} \right)^{5/4} {\rm d} \tag{6.5}$$

where $\alpha \sim 0.01$–1 for a standard Shakura–Sunyaev disk, $\dot{M}_{\rm acc}$ is the neutron star mass accretion rate and $R_{\rm d}$ is the accretion disk radius. The analytical treatment by Lubow & Shu (1975) indicates that for a wide range of binary mass ratios, $R_{\rm d} \approx 0.1\times$ the binary separation. However, Papaloizou & Pringle (1977) showed that dissipative transport of angular momentum spreads the disk out until the tidal torques from the companion are sufficient to remove the angular momentum required for the material to accrete. In this case, $R_{\rm d} \approx 0.9\ R_{\rm L}$, where $R_{\rm L}$ is the neutron star Roche radius.

In the following sections, we attempt to characterize the wind properties in each of the four torque switching systems and argue that accretion of this wind can plausibly account for the observed properties of these systems. We consider two types of winds: radiatively driven winds and X–ray excited thermal winds.

Radiatively driven winds are associated with evolved stars and are accelerated through line absorption of the stellar radiation by the wind material (Castor, Abbott, & Klein 1975; Abbott 1982). The velocity profile of such winds can be characterized by (Friend & Abbott 1986)

$$v(r) = v_\infty \left(1 - \frac{R_{\rm c}}{r} \right)^{0.8} \tag{6.6}$$

where r is the distance from the star, and v_∞ is the terminal velocity of the wind. Typically, $v_\infty \approx 3\ v_{\rm esc}$, with $v_{\rm esc}$ being the escape velocity of the companion. The expected mass accretion rate onto the neutron star is given by Equation 5.6.

The concept of an X–ray excited thermal wind was first proposed by Basko et al.(1977) as a possible mass transfer mechanism in Her X–1. Such winds arise from neutron star induced X–ray heating of the of the companion surface. The thermal wind consists of two regimes, the lower of which is in approximate hydrostatic and thermal equilibrium with the star while the upper is thermally unstable and results in a high velocity outflow. According to Basko et al.(1977), the mass loss rate of a thermal wind is given by

$$\dot{M}_{\rm thermal} = 4\pi R_{\rm c}^2 f \tag{6.7}$$

where $f = \rho v$ is the surface mass flux given by

$$f = g(x) P_{\rm min} \Phi^{-1/2}. \tag{6.8}$$

In the above equation, $\Phi = GM_{\rm c}/R_{\rm c}$ is the gravitational potential at the stellar surface, while $P_{\rm min}$, the pressure above which thermal instability occurs, is given by (Voit & Shull 1988)

$$P_{\rm min} = 5 \times 10^{-11} \left(\frac{F_{\rm x}}{\rm ergs\ cm^{-2}\ s^{-1}} \right) \tag{6.9}$$

where $F_{\rm x}$ is the X–ray flux at the stellar surface. For an externally illuminated thermal wind, Basko et al.(1977) showed that $g(x) \approx 0.8$.

Unlike radiatively driven winds which have been extensively studied both analytically and numerically, X–ray excited winds are still poorly understood. While analytical expressions exist for estimating the wind velocity and neutron star accretion rate for a radiatively driven wind, corresponding equations for a X–ray excited wind do not yet exist. Hence, our treatment of X–ray excited winds will be largely qualitative.

OAO 1657–415

Although the optical companion of OAO 1657–415 has yet to be identified, the orbital parameters derived from BATSE timing, together with the resultant constraints on the companion type (Chakrabarty et al. 1993), allow us to estimate the possible mass outflow from the companion and the Bondi–Hoyle accretion rate in this system.

Chakrabarty et al.(1993) inferred the companion to be a blue supergiant of spectral type B0–B6, mass 14–18 $M_\odot$, and radius 25–32 $R_\odot$. These allow us to estimate the

companion effective temperature, $T_{\rm eff}$, the mass loss rate in a radiatively driven wind, $\dot{M}_{\rm W}$, the stellar wind terminal velocity, v_∞, the stellar wind velocity at the neutron star, $v_{\rm W}$, and $v_{\rm rel}$. These quantities and the associated assumptions are summarized in Table 6.2.

The most obvious problem is that, even for the higher limit of $\dot{M}_{\rm W}$, the Bondi–Hoyle mass accretion rate onto the neutron star (Equations 5.6 and 5.7) is $\dot{M}_{\rm acc} \sim 3 \times 10^{-11}\ M_\odot\ {\rm yr}^{-1}$, which is much smaller than the lower limit of $\sim 10^{-9} M_\odot\ {\rm yr}^{-1}$ inferred from the typical spin–up rate.

However, X–ray induced ionization of the stellar wind could drastically alter this estimate, due to the sensitive dependence of the Bondi–Hoyle accretion rate on the stellar wind velocity (Ho & Arons 1987c; Stevens & Kallman 1990). Since stellar winds are accelerated through line absorption of the stellar radiation by the wind material (Castor, Abbott, & Klein 1975; Abbott 1982), X–ray induced ionization depletes the supply of accelerable ions, and slows down the stellar wind considerably. Quantitatively, this effect becomes important when the parameter, ξ, defined as (Tarter, Tucker, & Salpeter 1969; McCray & Hatchett 1975)

$$\xi = \frac{L_x}{n(R_\xi) R_\xi^2} \tag{6.10}$$

exceeds a threshold, $\xi_{\rm crit}$. In this equation, $L_{\rm x}$ is the bolometric X–ray luminosity, $n(r) = \dot{M}_{\rm W}/(4\pi m_p v_{\rm W}(r) r^2)$ is the number density of the wind (assumed to be primarily hydrogen), and R_ξ, is the distance from the neutron star at which accelerable ions in the wind are depleted (the Strömgren distance). Ho & Arons (1987) estimated $\xi_{\rm crit} \approx 10^4$ ergs cm s^{-1} for the radiative force cutoff but Stevens (1991) argued that this is an overestimate and proposed a value of $\xi_{\rm crit} \approx 100$ ergs cm s^{-1} instead. Using $L_{\rm x} = 1.4 \times 10^{37}$ ergs s^{-1} and wind parameters from Table 6.2, we find $\xi \gtrsim 100$ ergs cm s^{-1} at distances of $r \gtrsim 1.1\ R_{\rm c}$ from the companion. The resultant attenuation in wind velocity is difficult to quantify, but a factor of 8–10 decrease in the terminal velocity is consistent with the findings of both Ho & Arons (1987) and Stevens & Kallman (1990). With the lower $v_{\rm rel}$, the range of Bondi–Hoyle mass accretion rate increases to $2 \times 10^{-10} \lesssim \dot{M}_{\rm acc} \lesssim 10^{-8}\ M_\odot\ {\rm yr}^{-1}$, and there now exists a range of mass accretion rates larger the lower bound inferred from Equation 6.2.

Aside from a radiatively driven wind, an X–ray excited wind could also exist in OAO 1657–415. Adopting $L_{\rm x} = 1.4 \times 10^{37}$ ergs s^{-1}, and and applying Equations 6.9, 6.8 and 6.7, we obtain a flux of $F_{\rm x} \approx 4.8 \times 10^{11}$ erg cm^{-2} s^{-1} at the surface of the companion and a mass loss rate of $\dot{M}_{\rm therm} \sim 5 \times 10^{-7} M_\odot\ {\rm yr}^{-1}$. In comparison, the range of mass loss

Table 6.2. Inferred Properties of OAO 1657–415

Quantity	Value
Spectral Type [1]	B0–B6
Companion Mass [1] ($M_\odot$)	$14 \lesssim M_c \lesssim 18$
Companion Radius [1] ($R_\odot$)	$25 \lesssim R_c \lesssim 32$
Inclination Angle [2]($^\circ$)	$60 \lesssim i < 90$
Mass ratio	$10 \lesssim q \lesssim 15$
Semi–major axis	$a \approx 56 R_\odot$
Effective Temperature (K)	$12400 \lesssim T_{\rm eff} \lesssim 25700$
Mass loss rate [3]($M_\odot$ yr^{-1})	$2.8 \times 10^{-8} \lesssim \dot{M}_W \lesssim 1.5 \times 10^{-6}$
Stellar wind terminal velocity [4] (km s^{-1})	$v_\infty \approx 1400$
Wind velocity at neutron star [5] (km s^{-1})	$v_{\rm W}(r = a) \approx 800$ km s^{-1}
Stellar wind – neutron star (km s^{-1}) relative velocity	$v_{\rm rel} \approx 850$

[1]From Chakrabarty et al.(1993).

[2]Lower limit obtained by requiring companion radius to be less than Roche radius (Chakrabarty et al. 1993).

[3]Assumes $\log(-\dot{M}_W) = 1.769 \log(L/L_\odot) - 1.676 \log(T_{\rm eff}) - 8.158$, determined empirically by fitting observed mass loss rates for 271 stars of spectral types O through M (de Jager, Nieuwenhuijzen, & van der Hucht 1988).

[4]Assumes $v_\infty = 3 v_{\rm esc}$ (Abbott 1982).

[5]Assumes $v_{\rm W}(r) = v_\infty (1 - R_c/r)^{0.8}$ (Friend & Abbott 1986).

rates for the radiatively driven wind is $2.8 \times 10^{-8} \lesssim \dot{M}_{\rm rad} \lesssim 1.5 \times 10^{-6} M_{\odot}$ yr^{-1}. In section 6.2.4, we argue that $\dot{M}_{\rm rad} \approx \dot{M}_{\rm thermal}$ in OAO 1657–415.

Adopting $\alpha = 1$ in Equation 6.5, the expected lifetime of an accretion disk formed is $\sim$ 300 d, which is in good agreement with the measured durations (see Figure 6.6).

Cen X–3

The companion of Cen X–3 is the O6–8 supergiant V779 Cen (Krzeminski 1974; Rickard 1974; Hutchings et al. 1979). Accretion in this source has been believed to occur through Roche Lobe overflow because its Eddington–like bolometric luminosity (Nagase 1989) requires an implausibly strong stellar wind, which is at odds with the absence of P–Cygni line profiles (Hutchings et al. 1979). Moreover, the optical light curves also suggest Roche Lobe overflowing in the companion (van Paradijs & Zuiderwijk 1977).

As in OAO 1657–415, X–ray heating of the stellar wind is important and could decrease the wind velocity enough to sustain the high bolometric luminosity even with Bondi–Hoyle accretion. However, Day & Stevens (1993) showed that $\xi \approx 300 > \xi_{\rm crit}$ just above the stellar photosphere at a distance $r = 1.01\ R_c$. Since this is most likely within the critical point of the radiatively driven wind acceleration zone (Castor, Abbott, & Klein 1975), Day & Stevens (1993) argued that the mass loss rate of the companion is severely suppressed and that a radiatively driven wind will not form. Instead, they proposed that in Cen X–3, X–ray heating of the stellar surface could give rise to a thermal wind. Adopting $L_{\rm x} = 10^{38}$ ergs s^{-1}, the X–ray flux at the surface of the companion is $F_{\rm x} \approx 3.5 \times 10^{13}$ erg cm^{-2} s^{-1}, and Day & Stevens (1993) arrived at a stellar mass loss rate of $\dot{M}_{\rm therm} \sim 4 \times 10^{-6} M_{\odot}$ yr^{-1}.

Day & Stevens (1993) also discovered that the column density $N_{\rm H}$ changes (derived from *EXOSAT* data) over an eclipse are too drastic to be explained by a radiatively wind : the absorption dropped by two orders of magnitude during egress over an orbital phase of 0.1. Day & Stevens (1993) suggested that a radiatively driven wind from the non X–ray illuminated side of the neutron star would be ionized when it enters the X–ray illuminated zone. This leads to an excess of non–accelerable ions which are localized to the limb of the companion star, possibly giving rise to the drastic column density changes observed as the neutron star enters and emerges from an eclipse.

Additional support for a X–ray excited wind in Cen X–3 is provided by high res-

olution spectroscopy with *ASCA* over an eclipse (Ebisawa et al. 1996). These observations revealed K α emission lines from highly ionized ions: hydrogenic and helium–like Fe (6.7 and 6.97 keV), hydrogenic S (2.64 keV), Si (2.01 keV), Mg (1.25 keV) and Ne (1.02 keV) and possibly helium–like Si (1.84–1.86 keV). As Ebisawa et al.(1993) pointed out, the 6.97 keV line implies the presence of naked Fe nuclei. The presence of copious quantities of highly ionized ions strongly support the argument by Day & Stevens (1993) that a radiatively driven wind cannot exist in this system. Ebisawa et al.(1993) also discovered that whereas the line flux of the 6.4 keV line decreased by about an order of magnitude during the eclipse, implying a small emission region for this line, the other line fluxes decreased by factors of $\lesssim 3$, implying that the corresponding emission region is more extended than that of the companion star. This may be hard to reconcile with the expectation of Day & Stevens (1993) that the X–ray excited wind is a narrow stream, but we note that the dynamics and flow geometry of the X–ray excited wind has yet to be investigated in detail.

Adopting $\alpha = 1$ in Equation 6.5, the expected lifetime of an accretion disk formed is ~ 50 d, which is in good agreement with the measured durations (see Figure 6.4).

4U 1626–67

In 4U 1626–67, the companion is likely a low–mass (0.02–0.06 $M_{\odot}$) degenerate He or CO dwarf (Chakrabarty et al. 1997a). Motivated by *ASCA* spectroscopy which revealed a strong emission–line complex of Ne lines from *ASCA*, Angelini et al.(1995) proposed that the companion is a He–burning star which underfills its Roche Lobe and that mass transfer to the neutron star occurs through a radiatively driven wind. While Ne is a by–product of He–burning and the absence of Fe lines in the *ASCA* spectra supports the unevolved nature of the companion, X–ray heating in this compact system is undoubtedly more severe than in Cen X–3, thus nullifying the radiatively driven wind hypothesis. We hence apply the same analysis performed by Day & Stevens (1993) for Cen X–3 to 4U 1626–67 to evaluate the plausibility of a thermal wind in this system.

Adopting the probable 42–min orbital period determined from optical photometry (Middleditch et al. 1981), and a companion mass of $M_{\rm c} \approx 0.04 M_{\odot}$, the semi–major axis $a \approx 0.45 R_{\odot}$. In order for the companion to remain within its Roche Lobe, $R_{\rm c} \lesssim 0.06 R_{\odot}$. From the secular spin–up rate, Chakrabarty (1997a) inferred the accretion rate onto the neutron star to be $\dot{M}_{\rm acc} \gtrsim 2 \times 10^{-10}\ M_{\odot}\ {\rm yr}^{-1}$. This corresponds to a bolometric luminosity

of $L_{\rm x} \gtrsim 2.5 \times 10^{36}$ ergs s^{-1}, which implies a flux of $F_{\rm x} \approx 2 \times 10^{14}$ ergs s^{-1} at the surface of the companion and a mass loss rate of of $\dot{M}_{\rm therm} \sim 10^{-9} M_{\odot}$ yr^{-1}. The inferred mass accretion rate requires an efficient capture rate of $\dot{M}_{\rm acc}/\dot{M}_{\rm W} \gtrsim 0.2$. We note that since $M_{\rm x} \gg M_{\rm c}$, the neutron star dominates the potential well and should capture most, if not all, of the wind.

Adopting $\alpha = 0.01$ in Equation 6.5, the expected lifetime of an accretion disk formed is ~ 1 yr, which is in roughly consistent with the measured duration of ~ 10 yrs.

GX 1+4

The companion for GX 1+4 is the M5 III giant V2116 OPHIUCHI (Davidsen, Malina, & Bowyer 1977). Extensive optical observations by Chakrabarty & Roche (1997) yielded spectral and luminosity classifications which are consistent with V2116 Oph being either a first–ascent giant branch (FGB) star or an asymptotic giant branch (AGB) star. On the basis of the intestellar extinction being rather low for the inferred distance to the companion if were an AGB star, Chakrabarty & Roche (1997) favored an FGB companion. Although extensive optical observations by Chakrabarty & Roche (1997) supported the presence of an accretion disk, they argued that steady accretion from Roche Lobe overflow will be very short–lived ($\lesssim 10^6$ yr), and hence improbable. Instead, they proposed that V2116 Oph does not overflow its Roche Lobe, but accretes a slow ($\sim$ 10 – 100 km s^{-1}) dense stellar wind which could give rise to alternating prograde and retrograde disks.

Although the orbital solution for GX 1+4 has yet to be determined, we can still make meaningful estimates of the companion mass loss rates using the properties inferred by Chakrabarty & Roche (1997). For a FGB companion, $M_{\rm c} \approx 0.8$–$2 M_{\odot}$, $R_{\rm c} \approx 50$–$100\ R_{\odot}$, $L_{\rm x} \approx (0.08$–$3) \times 10^{38}$ ergs s^{-1} and $P_{\rm orb} \gtrsim 280$ d. Assuming a circular orbit, we obtain $\dot{M}_{\rm therm} \sim 3 \times 10^{-7} M_{\odot}$ yr^{-1}. For an AGB companion, $M_{\rm c} \approx 0.8$–$10 M_{\odot}$, $R_{\rm c} \approx 210$–$270\ R_{\odot}$, and $L_{\rm x} \approx (1$–$2) \times 10^{38}$ergs s^{-1} and $P_{\rm orb} \gtrsim 280$ d. Assuming a circular orbit, we obtain $\dot{M}_{\rm therm} \sim 6 \times 10^{-5} M_{\odot}$ yr^{-1}.

Chakrabarty and Roche (1997) also noted that stringent non–detections of radio emission from GX 1+4 (Seaquist, Krogulec, & Taylor 1993; Fender et al. 1997) constrained the mass loss rate to $\dot{M}_{\rm W} \lesssim 10^{-6}\ M_{\odot}$, which provides additional support for a FGB companion.

Adopting $\alpha = 1$ in Equation 6.5, the expected lifetime of an accretion disk formed

is $\sim$ 20 yr, which is in good agreement with the measured duration of $\sim$ 10 yrs.

6.2.4 Discussion

While we have by no means established with certainty that accretion from an X–ray excited thermal wind gives rise to the torque switching episodes observed, we have shown this interpretation to be plausible. Although we still do not understand the details of the thermal winds sufficiently to perform a more quantitative analysis, we can nevertheless adopt a phenomenological approach. Not only does this allow us to test the self–consistency of our model, more importantly, it may also enable us to predict and characterize the behavior of potentially torque switching systems like Her X–1 and SMC X–1 which could not be monitored continuously by BATSE.

Table 6.3 summarizes the key inferred properties of the four torque reversing systems. A plot of the typical durations of spin–up ($t_{\rm su}$) and spin–down episodes ($t_{\rm sd}$), against $v_{\rm orb}$ reveals a clear anti–correlation (Figure 6.7) with a power law index of $\approx -3/2$. We speculate that this is related to the fact that the time scale over which flow directions in the stellar wind change falls off with $v_{\rm rel}$ with a power law index of -3 (Equation 6.4). The discrepancy between these two power law indices may reflect the weaker dependence on $v_{\rm rel}$ of the flow reversal times scale in actual three–dimensional flows, in contrast to the two–dimensional hydrodynamical simulations of Fryxell & Taam (1988) and Taam & Fryxell (1989) on which Equation 6.4 is based.

We now apply this phenomenological insight to Her X–1 and SMC X–1. For Her X–1, $v_{\rm orb} \approx 220$ km s^{-1}, similar to those of Cen X–3 and OAO 1657–415. We hence expect Her X–1 to exhibit torque switching on a time scale of $\approx$ 50 d. We further speculate that spin–down rates in Her X–1 are smaller than the spin–up rates. This could plausibly account for why the long term spin–up rate of the source inferred from sparse observations by pre–BATSE instruments (summarized in Nagase (1989)) is much smaller than that predicted by Equation 1.6. For SMC X–1, $v_{\rm orb} \approx 300$ km s^{-1}, which should imply a torque switching time scale similar to those of Cen X–3 and OAO 1657–415. However, the long term spin–up rate (from observations summarized in Nagase (1989)), $\dot{\nu} \approx 2.7 \times 10^{-11}$ Hz s^{-1}, is in good agreement with that predicted by Equation 1.6, which implies that the torque switching time scale in SMC X–1 $>$ 16 years. One possible reason for this discrepancy is that the source is super–Eddington, with $L_{\rm x} \approx 5 \times 10^{38}$ ergs s^{-1} (Nagase 1989) and this excites a very

Table 6.3. Key Properties of Selected Accreting Pulsars

Source	F_x [1]	$\dot{M}_W$ [2]	$\lvert\dot{\nu}_{su}\rvert$ [3]	$\lvert\dot{\nu}_{sd}\rvert$ [4]	$\dot{M}_{acc}$ [5]	ϵ [6]	η [7]
SMC X–1	680	15000	27	NA	20	1.3×10^{-3}	≈ 0
GX 1+4	0.055	280	6.026(1)	3.5348(1)	0.76	2.7×10^{-3}	≈ 0
4U 1626–67	2000	1	0.854(7)	0.7175(4)	0.29	2.8×10^{-1}	≈ 0
Cen X–3	350	4000	6.28(7)	4.94(8)	2.6	6.5×10^{-4}	≈ 0
OAO 1657–415	4.8	1000	5.50(8)	2.45(9)	0.93	9.3×10^{-4}	≈ 1
Vela X–1	2.4	2000	NA	NA	0.42 [8]	2.1×10^{-4}	≈ 10

[1]Neutron star irradiated X–ray flux at companion in units of 10^{-11} ergs s^{-1}.

[2]Mass loss rate from companion in units of $10^{-9} M_\odot$ yr^{-1} (includes both radiative, $\dot{M}_{rad}$, and thermal, $\dot{M}_{therm}$, components.

[3]Typical spin–up episode frequency derivative in units of 10^{-12} Hz s^{-1}. (See Table 6.1).

[4]Typical spin–down episode frequency derivative in units of 10^{-12} Hz s^{-1}. (See Table 6.1).

[5]With the exception of Vela X–1, minimum mass accretion rate onto neutron star in units of $10^{-9} M_\odot$ yr^{-1}. Inferred from $\dot{f}_{su}$ using Equation 6.2.

[6]$\epsilon = \dot{M}_{acc}/\dot{M}_W$.

[7]$\eta = \dot{M}_{rad}/\dot{M}_{therm}$.

[8]Inferred from bolometric X–ray flux and estimated distance to companion (Nagase 1989).

strong thermal wind of $\dot{M}_{\rm therm} \sim 10^{-5}\ M_\odot\ {\rm yr}^{-1}$, which is more than a factor of 10 larger than any of those in Table 6.3. In this case, the unusually high density of the X–ray excited stream could result in angular momentum transfer of constant sign, as demonstrated in the 2–D hydrodynamical simulations of Blondin, Stevens & Kallman (1991). As in Cen X–3, the severe X–ray heating of the companion completely suppresses the formation of a radiatively driven wind.

A comparison of Cen X–3 and OAO 1657–415 is also instructive, since they populate different parts of the Corbet diagram, and have experienced many more transitions than 4U 1626–67 and GX 1+4. Both sources share very similar frequency histories: episodes of steady spin–up and spin–down, resulting in a bimodal distribution in frequency derivative which is positively biased. Yet, there are subtle differences: while *all* transitions in Cen X–3 resulted in a change in the torque direction, some transitions in OAO 1657–415 are from steady spin–up/spin–down to random walk behavior reminiscent of those observed in the non–Roche–Lobe overfilling supergiant sources.

These differences could have arisen because Cen X–3 accretes exclusively from a X–ray excited wind while OAO 1657–415 accretes from both a X–ray excited wind and a radiatively driven wind. It may be that during episodes of steady spin–up and spin–down, OAO 1657–415 is primarily powered by the X–ray excited wind while the radiatively driven wind dominates the mass transfer during periods of random walk. The similarities and differences between Cen X–3 and OAO 1657–415 can also be understood phenomenologically within the context of the Corbet diagram. Just as OAO 1657–415 resides in the boundary between the non Roche Lobe overfilling and Roche Lobe overfilling regions, its frequency behavior exhibits both types of characteristics. As for Cen X–3, which clearly resides in the disk–fed region of the Corbet diagram, no signatures of wind–fed systems are present.

Valuable phenomenological insights can also be obtained by comparing OAO 1657–415 to Vela X–1. The 8.96 d orbit and B0.5Ib supergiant companion of Vela X–1 bears a close resemblance to those of OAO 1657–415. Yet, the persistent random walk behavior of the Vela X–1 frequency history contrasts starkly with the steady spin–up/spin–down behavior of OAO 1657–415. We argue that the broad range of torque behavior spanned by SMC X–1, GX 1+4, 4U 1626–67, Cen X–3, OAO 1657–415 and Vela X–1 can be parametrized in terms of the ratio $\eta = \dot{M}_{\rm rad}/\dot{M}_{\rm thermal}$.

Using the stellar mass loss rate equation in Table 6.2, we estimate $\dot{M}_{\rm rad} \sim 2 \times$

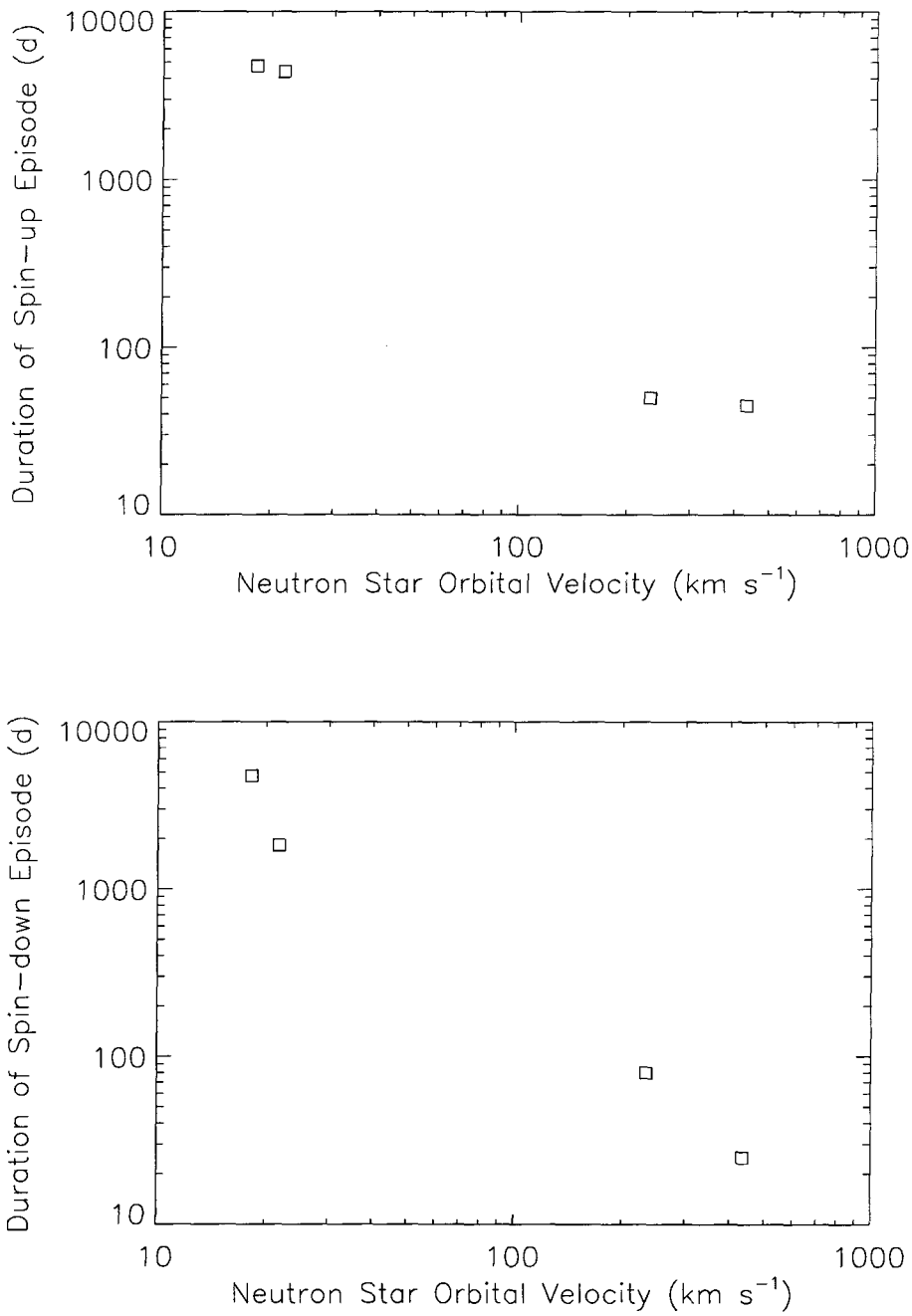

Figure 6.7: Upper Panel: Typical duration of spin–up episodes plotted against neutron star orbital velocities for the four torque switching sources. Lower Panel: Typical duration of spin–up episodes plotted against neutron star orbital velocities. The sources are, from left to right: GX 1+4, 4U 1626–67, OAO 1657–415, Cen X–3. A clear anti–correlation is observed in both plots.

10^{-6} $M_\odot$ yr^{-1} in Vela X-1. Adopting $L_x = 5 \times 10^{36}$ ergs s^{-1}, we find $F_x \approx 2.4 \times 10^{11}$ erg cm^{-2} s^{-1} and $\dot{M}_{\rm therm} \sim 3 \times 10^{-7}$ $M_\odot$ yr^{-1}, thus yielding $\eta \approx 10$. At the other extreme, $\eta \approx 0$ for GX 1+4, 4U 1626–67 and Cen X–3. We speculate that $\eta \approx 1$ for OAO 1657–415 since it exhibits spin behavior intermediate between these two groups of objects. If, as mentioned earlier, the steady spin–up/spin–down behavior of OAO 1657–415 results from the accretion of the thermal wind while the random walk behavior results from the accretion of the radiatively driven wind, we do not expect any significant changes in X–ray luminosities between these different states of behavior. This is consistent with our observations, assuming that the BATSE pulsed fluxes track the bolometric flux.

Physical arguments also support this phenomenological unification scheme. As mentioned by Day & Stevens (1993), the X–ray excited wind in a system close to Roche Lobe overfilling is likely to be a dense tidal stream flowing from the companion to the neutron star, and the simulations of Blondin, Stevens & Kallman (1991) and Fryxell & Taam (1988)show that this large asymmetry could result in angular momentum transfer of constant sign.

As mentioned earlier, the theory of X–ray excited winds is still relatively undeveloped. However, if the torque switching systems are indeed fed by such winds, several important properties of these winds can be inferred. The 2–D hydrodynamical simulations of Fryxell & Taam (1988) require a moderate wind density gradient perpendicular to the accretion flow of $0.005 < \epsilon_\rho < 0.25$ for accretion disk reversals. Here, ϵ_ρ is the ratio between the accretion radius and the length scale over which the density varies. In addition, a similar set of simulations by Fryxell & Taam (1989) require a small velocity asymmetry of $\epsilon_v \approx 0.01$ and a high Mach number of ≈ 10 for durations of spin–up/spin–down to be approxmately equal, as was observed in Cen X–3 and OAO 1657–415 (see Table 6.1). Here, ϵ_v is the ratio between the accretion radius and the length scale over which the velocity varies. Since the simulations performed are 2–D, the exact magnitudes of these numbers should not be taken too seriously. Nevertheless, the qualitative picture they portray will be useful in guiding the development of more detailed theories of X–ray excited winds.

6.2.5 Observational Tests and Future Directions

While the retrograde disk model appears to be the most viable of all the ones proposed to date, it is by no means the final word and we urge additional observations to

test its claims.

The presence of an accretion disk can be inferred from the observation of an UV emission line split by the disk rotation. For the eclipsing systems Cen X–3, OAO 1657–415 and Her X–1, the order of disappearance of the split lines yields the rotational sense of the disk: the blue wing of the line disappears first in a prograde disk while the red wing disappears first in a retrograde disk. However, as Nelson et al.(1997) pointed out, this may prove difficult in the high–mass systems due to overwhelming contaminating emission from the companion.

High resolution spectroscopy similar to those carried out for Cen X–3 and 4U 1626–67 should be carried out for GX 1+4 and OAO 1657–415 using *ASCA*. The detection of highly ionized ions supports the presence of an X–ray excited wind and for an eclipsing system like OAO 1657–415, the relative change in emission line strengths across an eclipse could yield valuable information on the geometry of the wind. Optical spectroscopy should also be carried out as this probes the companion mass loss rate and wind velocity for a radiatively driven wind (see for example Parkes et al.(1980), which should be present only in OAO 1657–415. Such observations could also reveal the importance of X–ray heating effects in OAO 1657–415: fluctuations in X–ray emission should induce changes in the P–Cygni profiles of the stellar wind, from which the velocity of the stellar wind can be inferred. The optical counterpart of OAO 1657–415, with a limiting magnitude of $V = 18$, has yet to be identified, but observations over the several months could yield positive results (D. Chakrabarty, private communication).

We also advocate simultaneous, continuous optical and X–ray observations before, during and after a torque reversal as the relationship between optical features, frequency derivatives and X–ray luminosities could yield valuable insights into the torque switching mechanism. A broad–band collimated instrument such as *RXTE*/PCA should be used for the X–ray observations as this allows the bolometric fluxes to be measured. The column densities inferred from the 2–60 keV spectra could also reveal possible changes in the interaction of the X–ray excited wind and the neutron star during a torque reversal. The enhanced sensitivity of *RXTE*/PCA also enables far more precise measurements of the times of torque reversals than those obtainable from BATSE. This allows us to investigate the possible dependence of torque reversals on orbital phase.

6.3 Accretion Disks in non Roche–Lobe Overfilling Systems

The puzzling presence of transient accretion disks in non Roche–Lobe overfilling systems is not confined to OAO 1657–415, but extends to GX 301–2 as well. Figure 5.1 shows the long–term frequency history of GX 301–2 and the BATSE observations in greater detail. A perfectly legitimate interpretation of the sparse frequency history obtained before 1991 is that the GX 301–2 frequency history random walked for ≈ 8 years after its discovery but that from 1984, a steady accretion disk formed in the source, leading to the observed secular spin–up of $\dot{\nu} \approx 2 \times 10^{-13}$ Hz s^{-1}.

The BATSE observations, however, revealed two steady and rapid spin-up episodes, with $\dot{\nu} \approx$ (3-5) $\times 10^{-12}$ Hz s^{-1}, each lasting for about 30 days. As explained in Chapter 5, they probably represent the formation of transient accretion disks in this wind-fed pulsar. Except for these spin-up episodes, there are virtually no net changes in the neutron star spin frequency on long time scales. These observations suggest that the decrease in the period of ≈ 25 s since 1984 is due entirely to brief (≈ 30 d) spin-up episodes similar to those we have discovered, with a recurrence time scale ≈ 2 yrs. This interpretation is also consistent with the secular spin-up rate extrapolated from the previous decade of observations. The pre-1984 frequency history does not exhibit this secular trend, implying that similar spin-up episodes may not have occurred during that era.

As in OAO 1657–415, the mechanism responsible for the formation of these accretion disks remains unclear, although in the case of GX 301–2, it may be related to episodic mass loss from the companion (see Chapter 5).

Chapter 7

Torque Luminosity Relations in Accreting Pulsars [1]

7.1 Introduction

Accretion flows onto a strongly magnetized star differ significantly from those onto an unmagnetized one. The strong magnetic field, B, disrupts the accretion flow at a distance r_A from the stellar surface, where the magnetic stress becomes comparable to the ram pressure of the accreting matter. Thus, r_A is given by (Pringle & Rees 1972; Lamb, Pethick, & Pines 1973)

$$\frac{B(r_A)^2}{8\pi} \approx \frac{1}{2}\rho(r_A)v(r_A)^2 \tag{7.1}$$

where ρ is the density of the accreting matter and v its velocity. Assuming a dipolar magnetic field, spherical accretion and free fall velocity of the accreting matter, r_A is given by

$$r_{\rm A} = \left(\frac{\mu^4}{2GM_{\rm x}\dot{M}^2}\right)^{1/7} \simeq 6.8\times10^8 \text{ cm} \left(\frac{\mu}{10^{30} \text{ G cm}^3}\right)^{4/7} \left(\frac{10^{-10}\ M_\odot \text{ yr}^{-1}}{\dot{M}_{\rm acc}}\right)^{2/7} \left(\frac{1.4M_\odot}{M_{\rm x}}\right)^{1/7} \tag{7.2}$$

where $\dot{M}_{\rm acc}$ is the mass accretion rate and μ and $M_{\rm x}$ are respectively the magnetic moment and mass of the accreting star. If $r_{\rm A} < r_{\rm co}$, the co–rotation radius, the accreting matter gets attached to the rotating field lines and are channeled to the poles of the accreting star.

[1] Adapted, with new results added, from "Observations of Accreting Pulsars", of which I was a major contributing author, to appear in the Astrophysical Journal Supplements 1997, 113, #2, by L. Bildsten, D. Chakrabarty, J. Chiu, M. H. Finger, D. T. Koh, R. W. Nelson, T. A. Prince, B. C. Rubin, D. M. Scott, M. Stollberg, B. A. Vaughan, C. A. Wilson and R. B. Wilson. Used by permission of the authors.

In many situations, the accreting matter possesses too much angular momentum to accrete radially, but first forms an accretion disk in which excess angular momentum is removed through viscous forces. In this case, the distance from the star at which the accretion flow becomes disrupted is modified to $r_{\rm m} = \xi r_{\rm A}$. Estimates for ξ range from 0.52 (Ghosh & Lamb 1979) to ≈ 1 (Arons 1993; Ostriker & Shu 1995; Wang 1996). Assuming that all the angular momentum of the accreting matter is transferred to the star, the latter will experience a spin–up torque (Pringle & Rees 1972; Rappaport & Joss 1977)

$$N = 2\pi I\dot{\nu} \approx \dot{M}\sqrt{GM_{\rm x}r_{\rm m}}\ . \tag{7.3}$$

Since $r_{\rm m} \propto \dot{M}^{-2/7}$, the expected relationship between the spin–up rate $\dot{\nu}$ and the bolometric luminosity L is given by

$$\dot{\nu} \propto L^{6/7} \tag{7.4}$$

since $L = GM_x\dot{M}/R$. This assumes that all of the accretion energy is converted to radiation.

While the exact relationship varies depending on additional refinements to this simple model, Equation 7.4 illustrates that measurements of $\dot{\nu}$ and L probes the interaction between the stellar magnetosphere and the accretion disk. The importance of understanding disk–magnetospheric interactions stems from its pervasiveness across a wide spectrum of astrophysical systems including accreting pulsars, magnetized CVs (Frank, King, & Raine 1992) and T–Tauri stars (Konigl 1991). Despite being widely contrasting systems, many of their evolutionary and observational characteristics are believed to be governed by the common physics of accretion flows onto a magnetized object. Hence, new insights gained on accretion flows in one class of systems are expected to be easily generalized to the others.

Accreting pulsars are the best systems for probing the disk–magnetospheric interactions. The compact nature of the neutron star implies a small moment of inertia which translates into measurable torques on short time scales of days instead of years for CVs and T–Tauri stars, thus allowing for dynamical probes of disk–magnetospheric interaction. The energy released per unit mass accreted is also by far the highest in neutron stars, hence leading to comparatively more systems which are detectable and studied.

7.2 Strengths and Weaknesses of BATSE

As Chapter 6 has demonstrated, the sparse observations provided by pre–BATSE instruments masked important features in the frequency and flux histories which severely

limit the ability of these earlier data to probe torque–luminosity relations accurately. This problem is especially acute for transient sources, which are highly variable and are only detectable during outbursts, when they briefly become the brightest X–ray sources in the sky for $\sim$ weeks. The continuous monitoring ability of BATSE resolves many of the problems posed by the old sparse data sets. However, we highlight that BATSE observations suffer from several limitations.

Ideally, tests of torque–luminosity relations in accreting pulsars require bolometric flux measurements as these are believed to be excellent tracers of the mass accretion rate $\dot{M}_{\rm acc}$. As mentioned earlier in Chapter 1, the spectra of most known accreting pulsars can be characterized by a flat power–law with index α of 0–1 up to a cut–off energy, $E_{\rm c} \approx$ 10–20 keV, after which it falls off exponentially. Thus, most of the luminosity from an accreting pulsar resides in the energy range $\approx$ 2–20 keV. Since $L_{\rm x} = GM_{\rm x}\dot{M}_{\rm acc}/R_{\rm x}$, the pulsed and unpulsed flux from 2–20 keV (the bolometric flux) should be a good tracer of $\dot{M}_{\rm acc}$.

Unfortunately, BATSE detects only photons with energies $E \gtrsim 20$ keV. Moreover, BATSE data are background limited and except for extremely bright sources ($\gtrsim$ 100 mCrab) for which the pulsed and unpulsed components can be measured using the Earth occultation technique (Harmon et al. 1992), only the pulsed component can be measured. Hence, if we used only BATSE fluxes for studies of torque–luminosity correlations, we often assume that pulsed fluxes at $E > 20$ keV track the corresponding bolometric fluxes. This is not necessarily a good assumption because of spectral changes across different observations, and BATSE is unable to detect spectral changes at $E \lesssim 20$ keV. Even at $E \gtrsim 20$ keV, the relatively low signal–to–noise in each of the individual CONT channels typically preclude accurate determination of the spectra on $\approx$ daily time scales. Hence, we are often forced to assume a constant spectral shape in order to derive the fluxes.

Nevertheless, we can sometimes verify this assumption through simultaneous observations by BATSE and *RXTE*/ASM, which measures the 2–10 keV bolometric flux. When this is not possible, arguments on spectral changes outside of the BATSE energy range and spectral information from previous pointed observations can also be used to evaluate the plausibility of whether the BATSE fluxes tracked the bolometric fluxes.

In the following sections, we review what BATSE has taught us about torque–luminosity relations in accreting pulsars. Aside from transient sources during outbursts, we also studied all sources persistent in the BATSE band which exhibit spin–up and/or spin–down episodes with durations of at least tens of days, as these suggest the presence of

accretion disks. Spin–up and/or spin–down episodes are detected in several sources which span a wide range of the Corbet diagram. The differentiation in spin behavior among the different classes of sources permits separate aspects of known accretion models to be tested. Though the insights in accretion flows gained from studying a single source are limited because of the many uncertainties involved, a far clearer and more compelling picture emerges when we piece together the individual fragments. This allows us to realistically and critically assess the strengths and weaknesses of each model.

7.3 Transient Sources

When transient sources go into outburst, many of them become the brightest X–ray sources in the sky, typically lasting several weeks. For all transients with known orbital parameters (GRO J1744–28, GRO J1750–27, A 0535+262, 4U 0115–634, 2S 1417–624, EXO 2030+375), BATSE observations revealed outbursts to be accompanied by steady spin–up lasting $\sim$ weeks, strongly suggesting the presence of an accretion disk. In addition, from the last frequency measurement and the first frequency measurement of two consecutive outbursts, Finger et al.(1994a) inferred a spin–down rate of $\dot{\nu} = -2.2(6) \times 10^{-13}$ Hz s^{-1} in A 0535+26 during quiescence. Since the mass accretion rate is much reduced between outbursts, this spin–down could be a manifestation of the propeller effect.

The wide dynamic range in luminosities and frequency derivatives exhibited by some of the transient sources also makes them ideal for testing Equation 7.4, which underlies the basic model of accretion. Two such transient systems detected by BATSE and which have known orbital parameters are GRO J1744–28 (Finger et al. 1996) and A 0535+262 (Finger, Wilson, & Harmon 1996). Figure 7.1 shows the measured frequency derivatives, $\dot{\nu}$ vs fluxes, F, for these two sources, and the best fit to the power-law $\dot{\nu} \propto F^{\gamma}$ (Bildsten et al. 1997). The frequency and flux measurements obtained by *EXOSAT* during an outburst of the transient source EXO 2030+375 (Parmar et al. 1989), combined with the orbital determination of this source by BATSE (Stollberg et al. 1994), allowed Reynolds et al.(1996) to determine a value for γ. Table 7.1 summarizes the values of γ obtained in the above investigations.

All the measured values of γ are $\approx 4\,\sigma$ greater than the expected value of 6/7. For A 0535+262 and GRO J1744–28, however, the BATSE fluxes may not track the bolometric fluxes. Moreover, in A 0535+262, there may be variations in the pulse profile shape. The

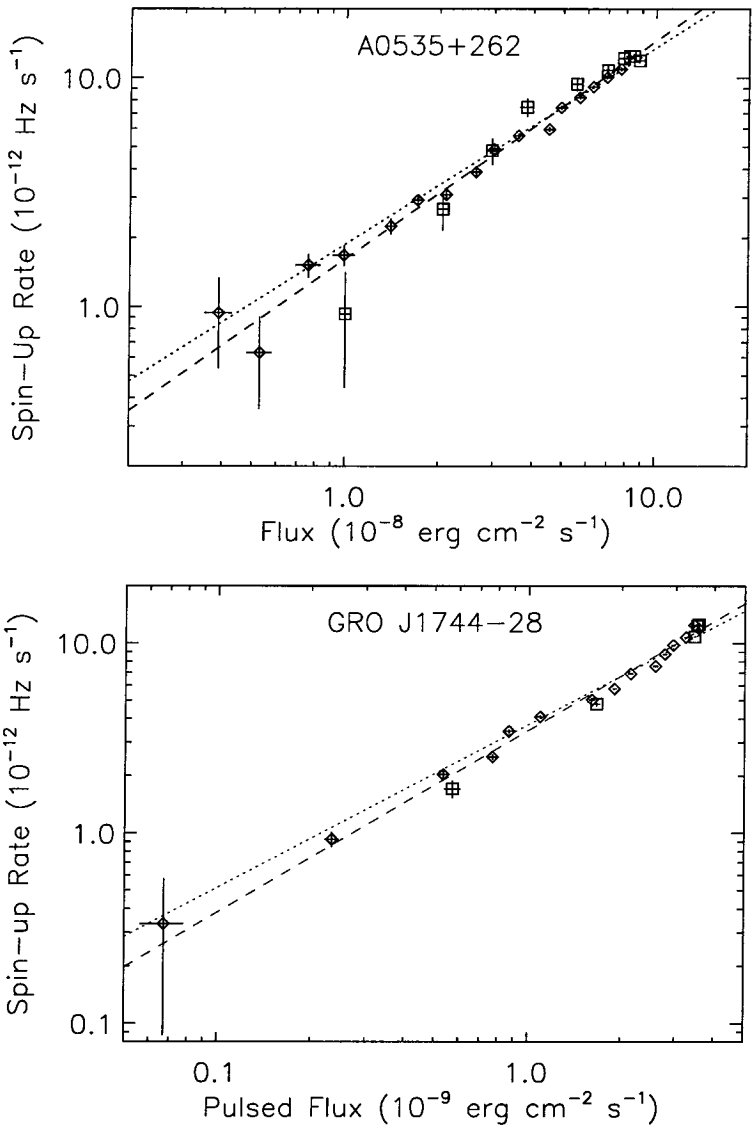

Figure 7.1: Observed relationships between fluxes and frequency derivatives. Upper panel: Spin-up rate of A 0535+262 during the 1994 giant outburst versus the measured total 20–100 keV flux, determined from Earth occultation measurements. Bottom panel: Spin-up rate of GRO J1744-28 during the December 1995-March 1996 outburst versus the 20-50 keV R.M.S. pulsed flux. For both sources the square symbols are from the outburst rise, and the diamond symbols are from the outburst decline. The dotted curves are power-laws with the expected index of 6/7, while the dashed curves are best fit powers-laws. The best fit index for A 0535+262 is 0.951(26) and that for GRO J1744–28 is 0.957(26). Figure is from Bildsten et al.(1997).

Table 7.1. Torque Luminosity Index for Transient Sources

Source	Flux Description	γ
A 0535+262	20–100 keV pulsed+unpulsed	0.951(26)
GRO J1744–28	20–50 keV R.M.S pulsed	0.957(26)
EXO 2030+375	1–10 keV pulsed + unpulsed	≈ 1.2 [1]

[1]There is no formal uncertainty because Reynolds et al. (1996) found the χ^2 of the fit to be formally unacceptable.

discrepancy in EXO 2030+375 is not expected, since the *EXOSAT* 1–10 keV flux should be a good tracer of the bolometric flux (Parmar et al. 1989). Worse still, the value of $\gamma \approx 1.2 > 1$ implies that the magnetospheric radius *increases* as the mass accretion rate is increased, opposite that predicted by Equation 7.2. However, Parmar, White & Stella (1989b) found a strong dependence of the pulse profile shape on luminosity, implying changes in the beaming pattern which could have resulted in the discrepancy in γ. We also note that Reynolds et al.(1996) did not provide an error estimate for the value of γ because the χ^2 of the fit was formally unacceptable, implying that either the basic torque model is inapplicable for EXO 2030+375, or that the measured flux is not a good measure of the mass accretion rate. To distinguish between these two alternatives, the effects of beaming pattern changes on pulse profiles and measured fluxes should be studied and quantified. The analysis should then be repeated with the adjusted fluxes.

Aside from effects unaccounted for in the data, the discrepancy in γ could be attributable to the oversimplified assumptions used in the derivation of Equation 7.4. The pulsar magnetic field need not be purely dipolar (Arons et al. 1984), and for magnetic fields with multipole components, Equation 7.4 can be generalized to

$$\dot{\nu} \propto L^{[4(n+1)-6/(4(n+1)-5]} \tag{7.5}$$

where n is the order of the dominant magnetic field component (e.g. $n = 2$ for a purely

dipole field and $n = 3$ for a purely quadrupole field). However, the γ's measured for A 0535+26 and GRO J1744–28 require a $n = 5$ dominant component in the B field, which is rather implausible. Hence, while higher order multipole components could increase the value of γ, it is not expected to be resolve the the discrepancies between the measured and expected values.

7.4 Persistent Sources

Although the fluxes and frequency derivatives of persistent sources do not exhibit a wide enough dynamic range for the determination of γ, torque reversals exhibited by many of these sources cannot be accommodated by the basic model alone. This allows us to probe extensions of the basic model which were originally formulated to explain how spin–down and accretion can take place concurrently in accreting pulsars. As mentioned before in Chapter 6, these models can be divided into three broad classes:

- Prograde accretion disk interacting with pulsar magnetosphere.
- Transitions between standard Keplerian disks and sub–Keplerian advection–dominated flow (ADAF).
- Alternating prograde and retrograde accretion disks.

These models have been described in detail in Chapter 6. In the following section, we discuss the implications for these models of BATSE observations of 4U 1626–67, GX 1+4, Cen X–3, and OAO 1657–415.

7.4.1 4U 1626–67 and GX 1+4

Chakrabarty (1997a) performed a careful study of the fluxes of 4U 1626–67 before and after the torque reversal, which included fluxes determined from all archival observations. Although this study revealed that the energy spectrum of 4U 1626–67 changed appreciably during the torque transition, it was not clear if the bolometric luminosity changed significantly before and after the torque transition.

In contrast to the extremely smooth spin–down experienced by 4U 1626–67, the GX 1+4 spin–down is more erratic, with significant fluctuations in the frequency derivatives. BATSE observations revealed a surprising *correlation* between the pulsed 20–50 keV

pulsed flux and the *spin–down* torque (Chakrabarty et al. 1997a). A fit of the observed fluxes and frequency derivatives for one of the extended spin–down episodes to $-\dot{\nu} \propto F^{\gamma}$ yielded $\gamma = 0.48 \pm 0.01$. As Chakrabarty et al. (1997a) explained, this anti–correlation may be due to the pulsed flux being a poor tracer of the bolometric flux. However, no significant spectral changes were observed in the BATSE energy range for different torque and luminosity states, and spectral changes at energies below the BATSE range need to be drastic to account for the factor of 7 change observed in the BATSE fluxes (Chakrabarty et al. 1997a). Unfortunately, the relative dimness of the source after *RXTE*/ASM began operation makes it difficult to establish whether the BATSE pulsed 20–50 keV fluxes tracked the *RXTE*/ASM 2–10 keV fluxes (D. Chakrabarty, private communication). Nevertheless, we find it reasonable to assume henceforth that the BATSE fluxes are a good tracer of the bolometric fluxes in GX 1+4.

With this assumption, the observed torque luminosity anti–correlation is at odds with the first class of models requiring the pulsars to be spinning near equilibrium because they require *lower* accretion rates for enhanced spin–down torque. Moreover, the BATSE fluxes during a bright spin–down flare centered at MJD 49238 (see Figure 4.5) reached intensities similar to those of a bright spin–up interval near MJD 49700 without triggering a similar reversal (Chakrabarty et al. 1997b), which is at odds with the hypothesis that the pulsar is spinning near equilibrium.

Nelson et al.(1997) argue that the observed correlation between the flux and spin–down torque, as well as the similarity in magnitudes between the secular spin–up and spin–down rates (see Table 6.1), can be naturally accounted for by a retrograde accretion disk. As argued earlier in Chapter 6, disk formation through accretion from an X–ray excited wind is plausible in both systems.

7.4.2 Cen X–3 and OAO 1657–415

The short torque reversal time scales for Cen X–3 and OAO 1657–415 result in many more spin–up/spin–down episodes than the single pair observed to date in each of 4U 1626–67 and GX 1+4. Whereas the torque reversals observed to date in these two sources occurred before the launch of *GRO*, BATSE's continuous coverage of frequency and flux changes in Cen X–3 and OAO 1657–415 across multiple torque reversals provides additional means to test the accretion models.

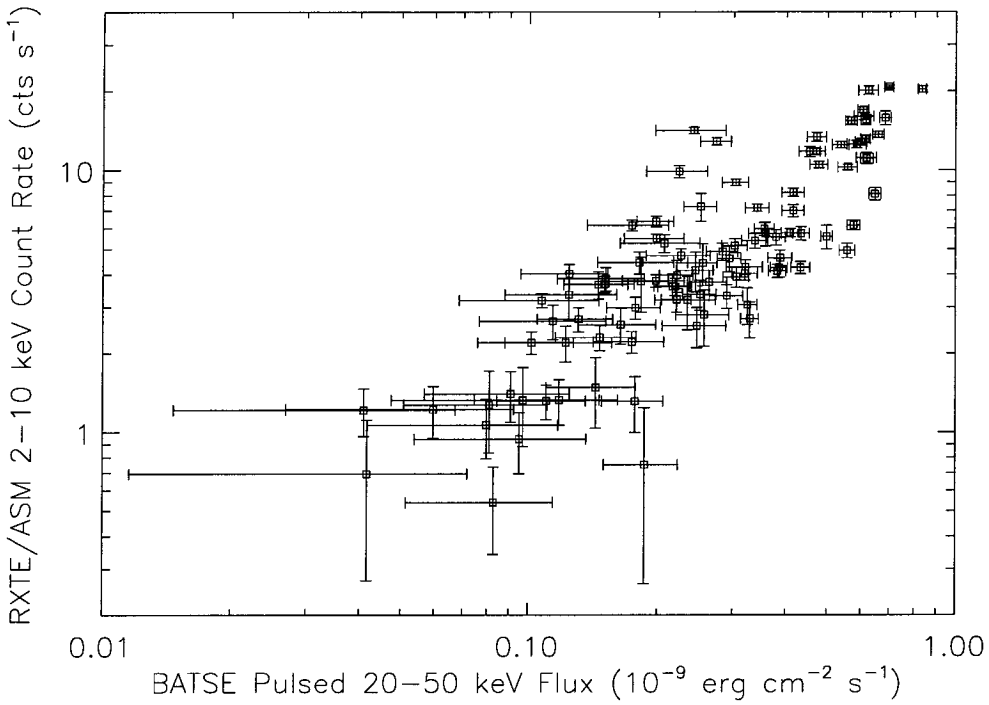

Figure 7.2: The *RXTE*/ASM bolometric 2–10 keV count rate plotted against the BATSE pulsed 20–50 keV flux for Cen X–3, showing a clear correlation. The correlation coefficient is ≈ 0.6. The ASM count rates, measured daily from MJD 50087–50485, are all corrected to the count rate that would be measured by a single SSC (ASM camera) if the source were at the center of the field of view and all 8 anodes were operating. The BATSE fluxes are measured at 2–day intervals by assuming an exponential spectrum with a e–folding energy of 12 keV (See Appendix).

To address the question of whether the BATSE fluxes for Cen X–3 and OAO 1657–415 tracked the respective bolometric fluxes, we plotted the *RXTE*/ASM 2–10 keV count rates vs. the BATSE 20–50 keV pulsed fluxes for these sources in Figures 7.2 and 7.3. The plot for Cen X–3 reveals a clear correlation between the BATSE fluxes and ASM count rates, with a correlation coefficient of ≈ 0.6, suggesting that the BATSE fluxes are a good tracer of the bolometric flux for this source.

However, the plot for OAO 1657–415 does not show any clear correlation, with a correlation coefficient of ≈ 0.1. This could be due to the large errors in the ASM count rates. We also computed the average spectra for each spin–up/spin–down episode for OAO 1657–415 and found that there was significant spectral variability in the 20–75 keV (CONT

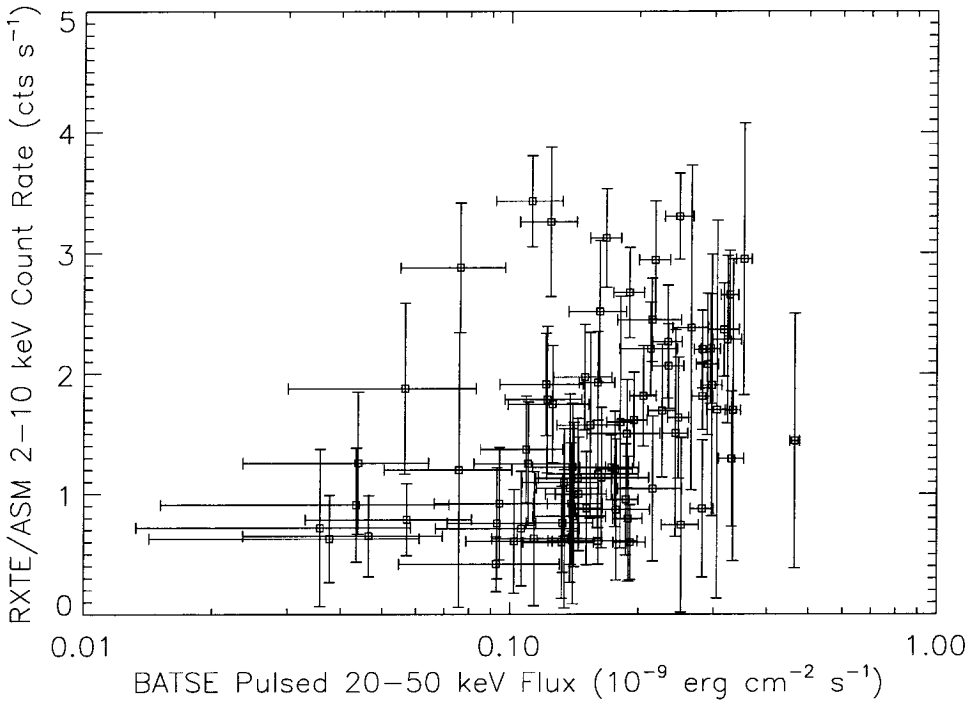

Figure 7.3: The *RXTE*/ASM bolometric 2–10 keV count rate plotted against the BATSE pulsed 20–50 keV flux for OAO 1657–415, showing no clear correlation. The correlation coefficient is ≈ 0.1. The ASM count rates, measured daily from MJD 50087–50485, are all corrected to the count rate that would be measured by a single SSC (ASM camera) if the source were at the center of the field of view and all 8 anodes were operating. The BATSE fluxes are daily by assuming an exponential spectrum with a e–folding energy of 12 keV (See Appendix). There is evidence for Spectral variability in OAO 1657–415, and the assumption of a constant spectrum could have masked an existent bolometric–pulsed flux correlation. Unfortunately, the BATSE CONT data does not possess sufficient signal–to–noise to permit precise determination of the spectrum on time scales of several days.

Channels 1–4) range, with kT in an OTTB fit ranging from $\approx$ 30–40 keV. This results in an additional uncertainty of $\approx 20\%$ in the fluxes plotted in Figure 7.3 as these were derived by assuming a constant spectral model. A combination of these two factors could have masked an existent correlation between the ASM and BATSE fluxes.

Figures 7.4 and 7.5 show the BATSE fluxes and ASM count rates plotted against the frequency derivatives for Cen X–3 and OAO 1657–415 respectively. No correlation is apparent in either case.

Since the frequency derivatives appear relatively constant during each spin–up/spin–

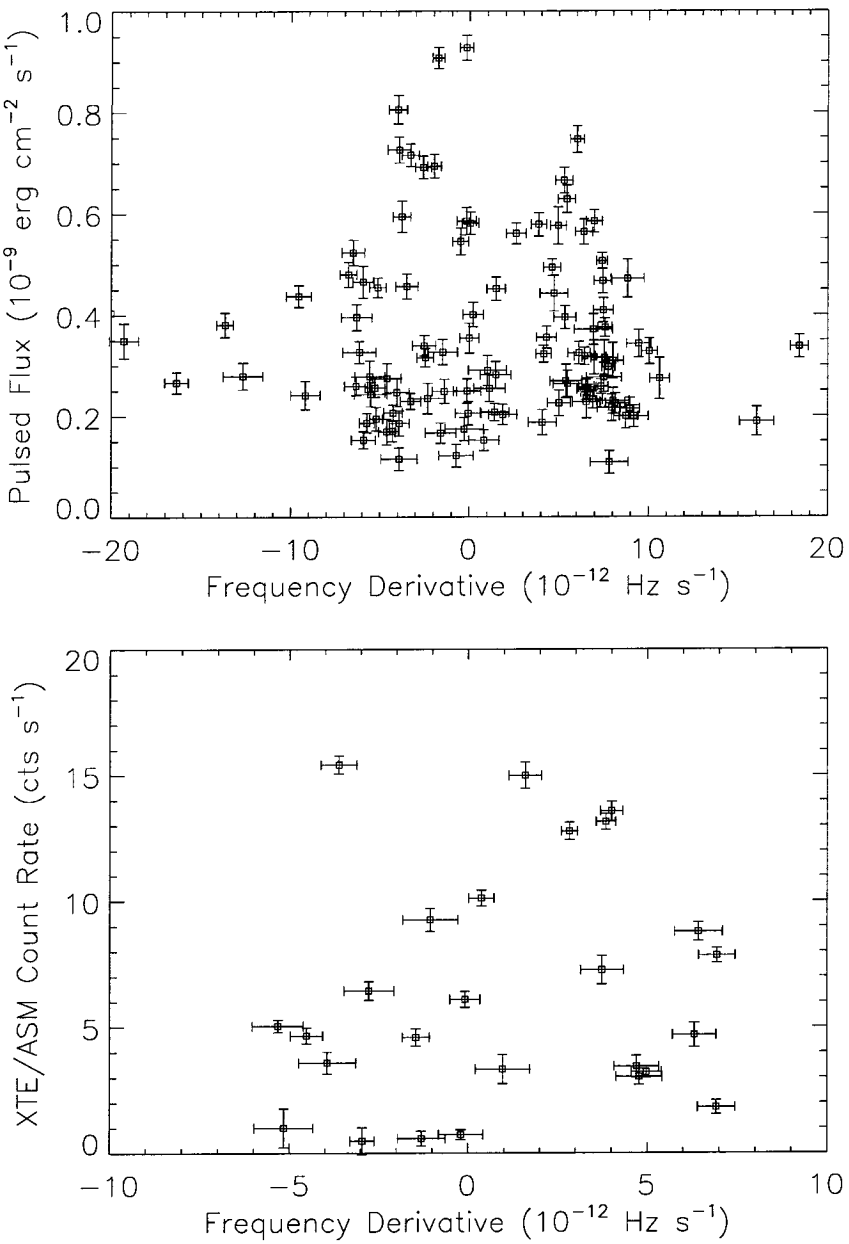

Figure 7.4: Upper panel: The BATSE 20–50 keV pulsed fluxes plotted against frequency derivatives for Cen X–3. The pulsed fluxes are obtained at 2.1–day intervals by assuming an exponential spectrum with a e–folding energy of 12 keV (See Appendix). The frequency derivatives are derived from frequencies measured at 4–day intervals from the power spectra of the 20–50 keV DISCLA data. Lower panel: The bolometric 2–10 keV *RXTE*/ASM bolometric count rate plotted against frequency derivatives measured from BATSE data (using an identical procedure as described above). The ASM count rates, measured daily from MJD 50087–50485, are all corrected to the count rate that would be measured by a single SSC (ASM camera) if the source were at the center of the field of view and all 8 anodes were operating.

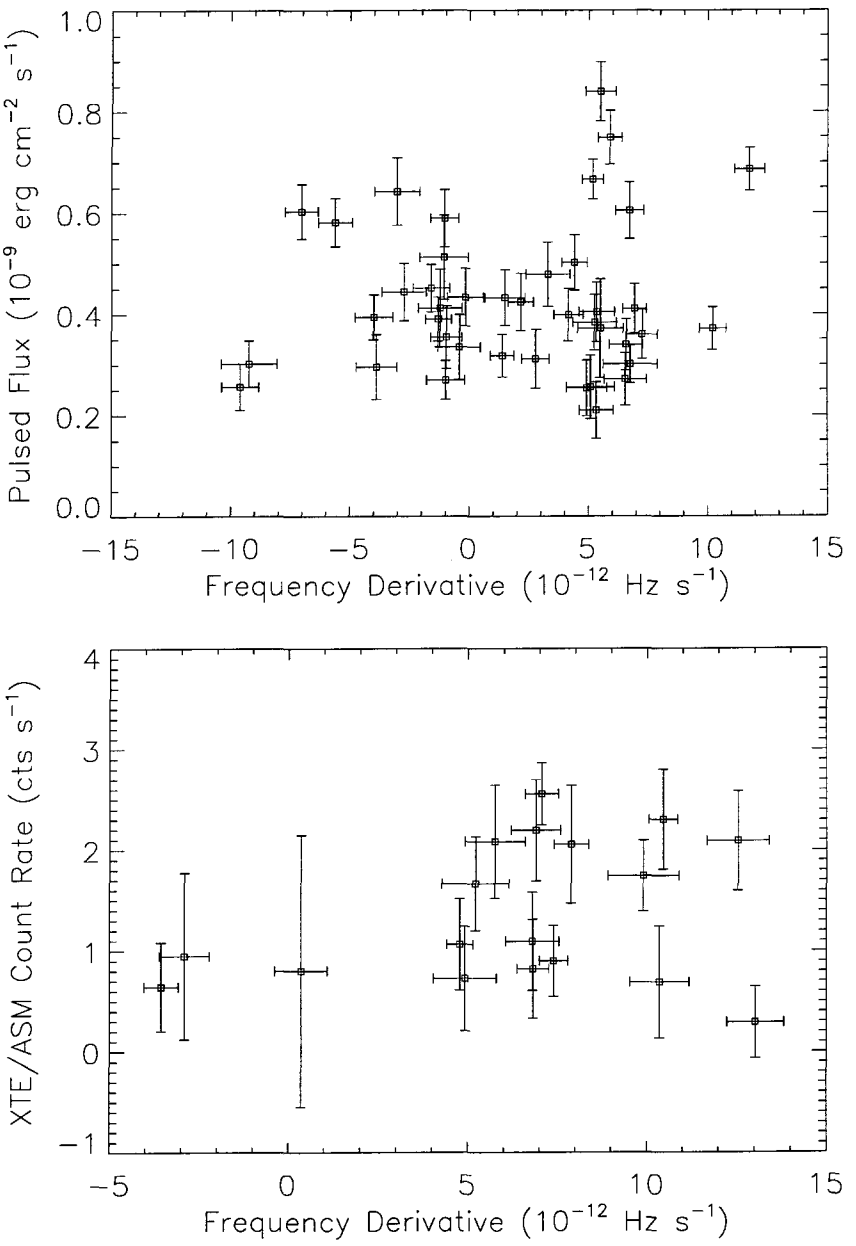

Figure 7.5: Upper panel: The BATSE 20–50 keV pulsed fluxes plotted against frequency derivatives for OAO 1657–415. The pulsed fluxes are are obtained daily by assuming an exponential spectrum with a e–folding energy of 20 keV (See Appendix). The frequency derivatives are derived from frequencies measured at 4–day intervals from the power spectra of the 20–50 keV DISCLA data. Lower panel: The bolometric 2–10 keV *RXTE*/ASM bolometric count rate plotted against frequency derivatives measured from BATSE data (using an identical procedure as described above). The ASM count rates, measured daily from MJD 50087–50485, are all corrected to the count rate that would be measured by a single SSC (ASM camera) if the source were at the center of the field of view and all 8 anodes were operating. The excess in positive frequency derivatives is due an extended spin–up episode from $\approx$ 10240–10485.

down episode for both Cen X–3 and OAO 1657–415, we can further check the above results by performing a linear fit to the frequencies for the entire episode to obtain the frequency derivative and averaging the fluxes for the entire episode. Figures 7.6 and 7.7 show the 20–50 keV pulsed flux averaged over each spin–up/spin–down episode vs the corresponding frequency derivative for the two sources. Once again, no correlation is apparent, reinforcing our earlier result.

The absence of any significant correlation between torque and luminosity is at odds with the basic torque–luminosity model of disk accretion (Equation 7.4), especially for Cen X–3 where we established that the BATSE fluxes tracked the bolometric fluxes. In both sources, we did not observe any trends between fluxes of adjacent spin–up/spin–down and spin–down/spin–up episodes. This casts doubt on all the torque models requiring near equilibrium spin frequencies as they assert that a transition from spin–down(spin–up) to spin–up(spin–down) is caused by a increase(decrease) of the mass accretion rates. The absence of torque–luminosity correlation or anti–correlation also casts doubt on the retrograde disk model. However, we note that in OAO 1657–415, two flares involving a $\approx$ 6 times increase in the BATSE pulsed 20–50 keV fluxes were associated with the torque reversals centered respectively at $\approx$ MJD 48770 and MJD 49000. This behavior bears a striking resemblance to that observed in the 2–D numerical simulations of wind accretion by Taam & Fryxell (1989). They found that when the transient accretion disks predicted by their simulations alternate sense, the mass accretion rates increase rapidly, leading to flare like activity. Although this lends support to the retrograde disk model for OAO 1657–415, we highlight that the flares were observed in only two torque reversals.

Yi, Wheeler and Vishniac (1997) asserted that transitions from a Keplerian disk to a sub–Keplerian ADAF flow occur when the mass accretion rate falls below a critical rate of $\dot{M}_{\rm crit} \sim 10^{-11}$–$10^{-10}\ M_\odot\ {\rm yr}^{-1}$. This estimate is based on the detailed calculations of Narayan & Yi (1995b), who showed that $\dot{M}_{\rm crit} \sim \alpha^2 \dot{M}_{\rm Edd}$, where α refers to the parameterization used in the Shakura–Sunyaev disk (see Equation 6.5). This range of $\dot{M}_{\rm crit}$ is clearly at odds with the mass accretion rate onto Cen X–3, which is $\dot{M}_{\rm acc} \sim 9 \times 10^{-9}\ M_\odot\ {\rm yr}^{-1}$ as inferred from the bolometric luminosity (Nagase 1989). However, transitions to ADAF flows could also occur at high accretion rates, at which the optical depth becomes so large that radiation is unable to escape in less than the flow time across the accretion disk (Narayan & Yi 1994; Narayan & Yi 1995b). Unfortunately, the corresponding $\dot{M}_{\rm crit}$ estimate is unavailable because Narayan & Yi (1995b) carried out the detailed analysis only for the case of

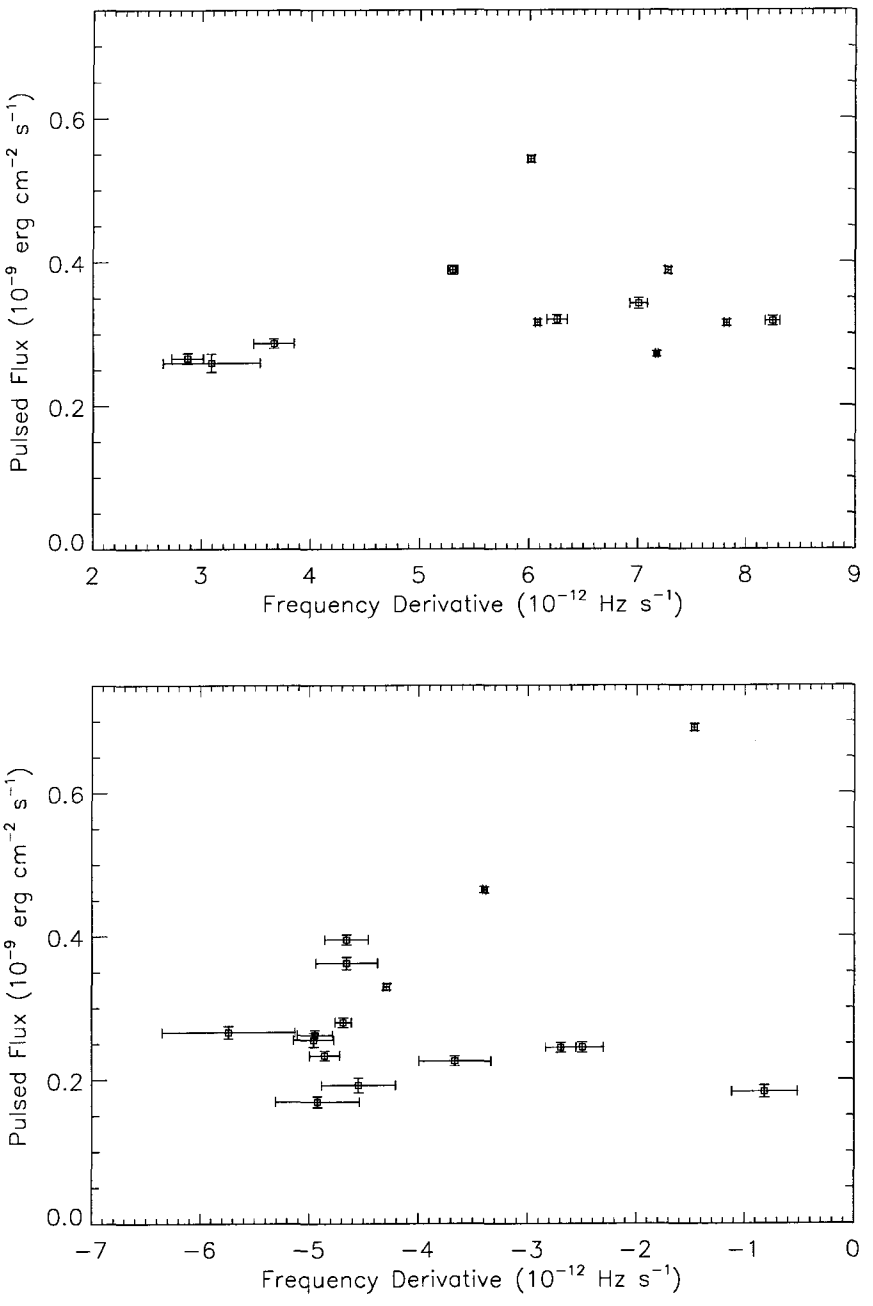

Figure 7.6: Upper panel: The BATSE 20–50 keV pulsed fluxes plotted against frequency derivatives for the spin–up episodes in Cen X–3. Each pulsed flux value has been averaged across over the entire spin–up episode concerned. The corresponding frequency derivative was obtained by performing a linear fit to all frequency measurements in the spin–up episode. Lower panel: The exact same quantities as above, for spin–down episodes. No correlation is apparent in either case.

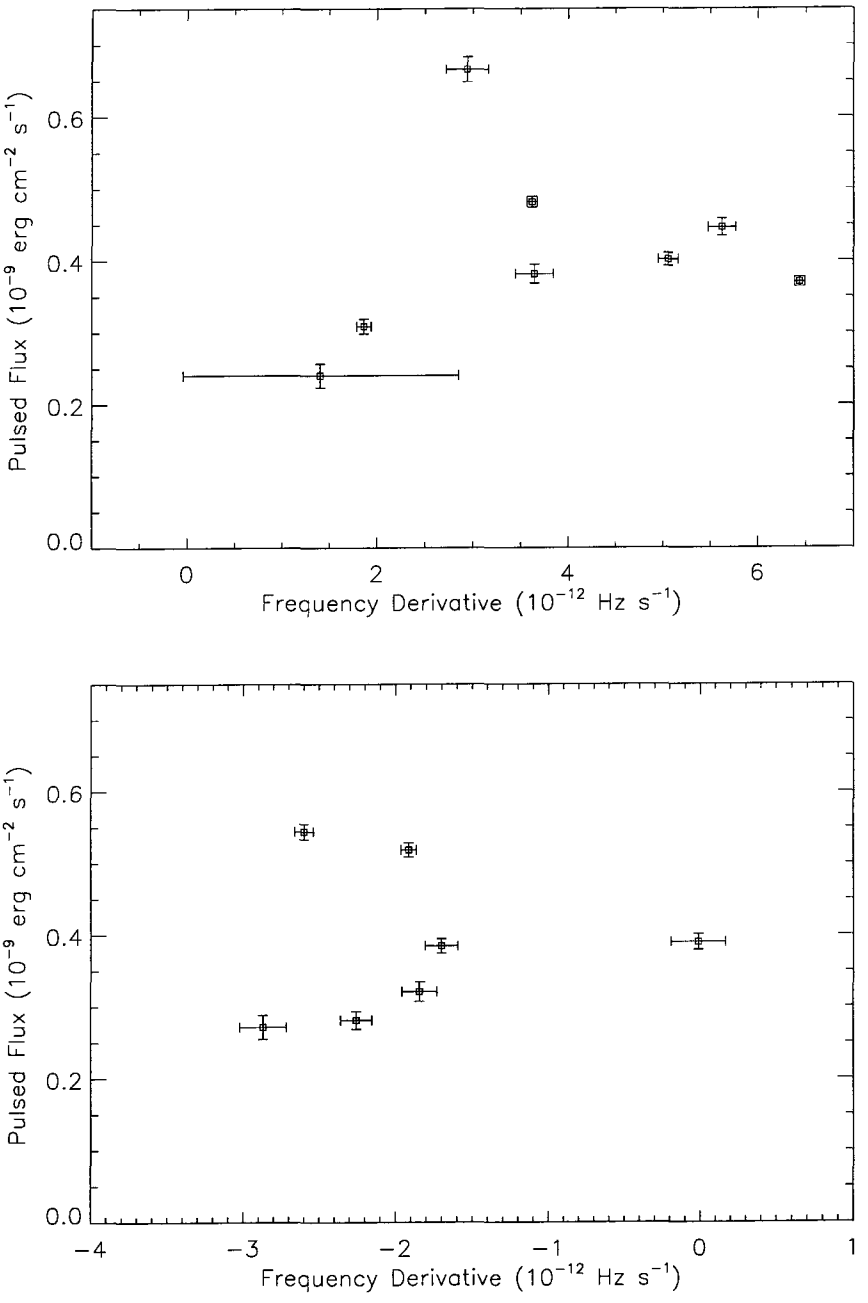

Figure 7.7: Upper panel: The BATSE 20–50 keV pulsed fluxes plotted against frequency derivatives for spin–up episodes in OAO 1657–415. Each pulsed flux value has been averaged across over the entire spin–up episode concerned. The corresponding frequency derivative was obtained by performing a linear fit to all frequency measurements in the spin–up episode. Lower panel: The exact same quantities as above, for spin–down episodes. No correlation is apparent in either case.

low mass accretion rates. Nevertheless, since transitions to ADAF flows occur either below or above a critical mass accretion rate, there should be a systematic trend between fluxes of adjacent spin–up/spin–down and spin–down/spin–up episodes. As mentioned earlier, we did not observe this trend in Cen X–3 and OAO 1657–415.

7.5 Overall Assessment

Having applied the different torque models to account for the spin evolution and torque–luminosity relations in a wide spectrum of accreting pulsars, we can critically assess each model.

The simple model of pulsar spin–up through disk–fed accretion mediated by a magnetosphere at distance $\approx 100\ R_x$ from the neutron star surface is at least qualitatively correct. First, there is reasonable agreement between the measured and characteristic spin–up rates for GX 1+4, 4U 1626–67 and Cen X–3 (Table 6.1). This is complemented by the steady spin–up and strong correlation between the measured fluxes and spin–up rates in the transient sources A 0535+262, GRO J1744–28 and EXO 2030+375. Although fitting the spin–up rates and fluxes to $\dot{\nu} \propto F^{\gamma}$ yields γ's which are significantly larger than the expected value of 6/7, the discrepancies could possibly be accounted for by factors such as the pulsed BATSE fluxes not being a good tracer of the mass accretion rates, pulse shape changes and spectral changes.

Unfortunately, this success does not carry over to the more sophisticated models which build upon the basic one to account for both accretion and spin–down. All the models involving disk–magnetospheric interaction could neither plausibly explain the spin evolution nor the torque–luminosity relations in the torque switching sources. First, their requirement that the sources be spinning close to equilibrium result in unusually high magnetic fields of $\sim 10^{14}$ G in some sources like GX 1+4. These models also require fine tuning in mass accretion and/or mass loss rates to account for the similarities in the magnitudes of the observed spin–up/spin–down rates. The observed fluxes and spin–up (spin–down) rates in both Cen X–3 and OAO 1657–415 are uncorrelated, whereas a correlation (anti–correlation) is expected. The correlation between the *spin–down* rates and fluxes in GX 1+4 is opposite that expected. The prediction by these models that a torque transition from spin–down(spin–up) to spin–up(spin–down) is caused by an increase(decrease) of the mass accretion rates has also been seriously challenged by the OAO 1657–415 and Cen X–3 data, which do not exhibit such

trends. The substantial observational evidence in direct contradiction with the predictions of these models suggests that these models may be fundamentally flawed.

Like the models just discussed, the ADAF model of Yi, Wheeler and Vishniac (1997) also requires equilibrium because otherwise, a transition to sub–Keplerian flow may result only in a change in the torque magnitude instead of a reversal. The critical mass accretion rate, $\dot{M}_{\rm crit}$, predicted for a torque reversal to take place is more than two orders of magnitude less than the Eddington rates observed in Cen X–3. Torque reversals could occur at very high mass accretion rates, but this possibility has not been investigated in detail. Nevertheless, the expected trend in fluxes between adjacent spin–up/spin–down and spin–down/spin–up episodes was not observed.

The prograde–retrograde disk interpretation of Nelson et al.(1997) resolves some of the most pressing problems faced by the above models. First, it can naturally account for the similarities in the spin–up and spin–down torque magnitudes, and the correlation between the *spin–down* rates and fluxes in GX 1+4. We have also shown in Chapter 6 that disk reversals through accretion of an X–ray excited thermal wind is plausible in GX 1+4, 4U 1626–67, Cen X–3 and OAO 1657–415. However, the disk reversal model does not account for why the magnitudes of the spin–up torques are consistently larger than those of spin–down torques. Also, the expected correlation between fluxes and both spin–up and spin–down torques are seen in neither Cen X–3 nor OAO 1657–415. Although this model makes no specific prediction of how the fluxes behave during a torque reversal, the two torque reversal associated flares observed in OAO 1657–415 are reminiscent of those observed in the 2–D hydrodynamical simulations of Taam & Fryxell (1989). Though not completely satisfactory, the disk reversal model appears more promising than the other ones.

7.6 Future Directions

BATSE observations have shown that current models of torque luminosity relations in accreting pulsars are inadequate or even fundamentally flawed. New advances in this area may require the emergence of a new paradigm which will benefit tremendously from coordinated observational and theoretical efforts.

Although we have often substantiated our assumption of BATSE pulsed fluxes tracking the bolometric fluxes, multiple sensitive observations with pointed instruments,

such as *RXTE*/PCA, will be invaluable since they not only unambiguously yield bolometric fluxes, but will also reveal spectral changes which could affect the data interpretation. The much enhanced sensitivity of such observations will also significantly reduce uncertainties and cast the results on much firmer footing. Simultaneous optical observations which complement the pointed X–ray observations may also shed new light on the interaction between the companion and the neutron star during a torque reversal.

The poor agreement between data and the current models may also suggest that approximate analytical treatments of the notoriously complicated physics which govern the accretion flows are unfeasible. While computational requirements have limited simulations done to date to fairly detailed 2–D hydrodynamical flows (Fryxell & Taam 1988; Taam & Fryxell 1989; Blondin et al. 1990; Blondin, Stevens, & Kallman 1991) and simple 3–D ones (see Ruffert (1997) and references therein), the advent of parallel computers with ever increasing speed, memory and I/O access rates will enable extensive 3-D magneto-hydrodynamic simulations to be carried out. Such simulations, coupled with refined observations, should yield fresh insights into the nature of accretion flows in magnetized systems.

Chapter 8

The Population of Be Transients [1]

8.1 Introduction

A Be–transient pulsar is an accreting pulsar in which the companion is a main–sequence OB star which exhibits strong H and He emission lines and IR continuum excess. Comprehensive reviews of the properties of Be–transients can be found in van den Heuvel & Rappaport (1987) and Apparao (1994) , and we provide a brief synopsis here.

The characteristic emission lines and IR continuum excess are believed to be manifestations of a slowly out-flowing, dense circumstellar disk in the equatorial plane of the companion. The companion star typically rotates at a velocity close to break–up, resulting in expulsion of matter along the equatorial plane which fuels the circumstellar disk. Away from the equatorial plane, the density of the circumstellar disk falls off quickly and at the poles, the outflow is primarily a fast, radiatively driven wind typical of those found in the companions of non–Roche Lobe overfilling supergiant systems.

The neutron star orbits in Be–transients are typically wide ($15 \lesssim P_{\rm orb} \lesssim 200$ d) and eccentric ($0.3 \lesssim e \lesssim 0.8$). The wide orbits and unevolved nature of the companions imply Roche Lobe under-filling, and one mode of mass transfer to the neutron star is through accretion of the circumstellar wind. The large eccentricity results in strong orbital phase dependence of the X–ray luminosity, L, with the ratio $L_{\rm max}/L_{\rm min} \geq 100$. For systems in which the neutron star orbital plane coincides with the equatorial plane of the companion,

[1] Adapted, with changes and additional material added, from "Observations of Accreting Pulsars," of which I was a major contributing author, to appear in the Astrophysical Journal Supplements 1997, 113, #2, by L. Bildsten, D. Chakrabarty, J. Chiu, M. H. Finger, D. T. Koh, R. W. Nelson, T. A. Prince, B. C. Rubin, D. M. Scott, M. Stollberg, B. A. Vaughan, C. A. Wilson and R. B. Wilson. Used by permission of the authors.

$L_{\max}$ occurs close to periastron. Otherwise, the light-curve as a function of orbital phase will exhibit two local maximum, each corresponding to intersection of the neutron star with the equatorial plane. Such increases in luminosity at predictable orbital phases are known as normal outbursts (Motch et al. 1991), and typically last for days to tens of days. Normal outbursts have been observed by BATSE in EXO 2030+375 (Figure 4.19), A 0535+262 (Figure 4.21), GRO J2058+42 (Figure 4.23), 2S 1417–624 (Figure 4.17), and GS 0834–430 (Figure 4.16).

A qualitatively different type of outbursts identified by Motch et al.(1991) are termed giant outbursts. In contrast to normal outbursts, the start times of giant outbursts are uncorrelated with orbital phase and they occur much less frequently, about once every several years for each source. Whereas normal outbursts last for a fraction of an orbit, giant outbursts typically extend over several orbits. X–ray emission stronger than those of normal outbursts by up to a factor of 10 are accompanied by steady spin–up, which is strongly suggestive of angular momentum transfer to the neutron star from an accretion disk. It is generally believed that the accretion disk and the ensuing outburst result from episodic mass loss from the rapidly rotating companion. Giant outbursts have been observed by BATSE in A 0535+26 (Figure 4.21), 2S 1417–624 (Figure 4.17), 4U 0115+63 (Figure 4.13), 4U 1145–619 (Figure 4.24), GRO J2058+42 (Figure 4.23), GRO J1750–27 (Figure 4.15), and A 1118–616 (Figure 4.25).

8.2 Motivation

Of the 44 known accreting pulsars, 29 are Be–transient systems, and even without accounting for the 4 systems discovered by BATSE, Be–transient systems are clearly the single largest class of accreting pulsars. Moreover, in view of the sparse and non–uniform sky coverage of pre–BATSE instruments, the known Be–transients clearly represent only a small fraction of the Galactic population.

Many models on the evolution of high mass X–ray binaries (see for example, Meurs and van den Heuvel (1989) and Dalton and Sarazin (1995)) make specific predictions of the Galactic population of Be/neutron–star binary systems. Although the fraction of this population which are also pulsars is unknown, this number would nevertheless be an upper limit to the Galactic population of Be–transients. A realistic estimate of the latter thus allows the validity of evolutionary models of Galactic X–ray binary population to be tested.

The Galactic population of Be–transients have been estimated before by Rappaport & van den Heuvel (1982) and Meurs & van den Heuvel (1989), and both arrived at a number of several thousand. However, the sparse and non–uniform coverage of pre–BATSE instruments resulted in several non–quantifiable ambiguities in their analysis. The continuous, uniform and all–sky coverage provided by BATSE removed many of these problems. In the following section, we describe how statistical arguments applied to BATSE detection of giant outbursts allow us to estimate the Galactic population of Be–transients.

We restrict our analysis to giant outbursts because of two key characteristics which simplify the analysis. Although the exact mechanism which governs giant outbursts is not unambiguously understood, they are thought to result from stochastic processes like rotational instabilities or mode–switching of non–radial pulsations which trigger sudden enhanced mass loss from the companion (see Slettebak (1988) for a review.) Both pre–BATSE (Motch et al. 1991) and BATSE observations of giant outbursts (Figure 4.12) reveal that they neither occur at specific orbital phases nor regular intervals, thus supporting their stochastic nature. It is hence reasonable to characterize giant outbursts from transient sources as a Poisson process.

Using the distances inferred from the optical counterparts to the sources which exhibit giant outbursts where they are available (see Nagase (1989)) [2] we find that the peak 20–50 keV pulsed luminosities of these outbursts are in the range of $(1-10)\times 10^{36}$ erg s^{-1}. Since the optically inferred distances are typically accurate to at best a factor of ≈ 2, this observed range is not inconsistent with the the assumption that giant outbursts are standard candles. We also note that the two giant outbursts observed by BATSE in 4U 0115+63 have 20–50 keV fluxes which are within ≈ 7 % of each other, thus providing further justification for the standard candle assumption.

8.3 Be–transient Population Estimation

BATSE has detected 11 transients with high mass companions (mostly Be stars) between 1991 April and 1997 January (MJD 48370–50464). This is a complete sample at 20–50 keV of transient sources with pulsed fluxes in excess of $F_{\rm min} \approx 2\times 10^{-10}$ erg cm^{-2} s^{-1}. They have a mean Galactic latitude of 1.3°, a mean absolute Galactic longitude, $|\ell|$, of 81.3°,

[2] For GRO J1750–27, we assumed a Galactic Center distance of 8.5 kpc, inferred from the column density of $N_{\rm H} = 2\times 10^{22}$ cm^{-2} measured by *ASCA* (Dotani et al. 1995).

and are concentrated at galactic longitudes $60° \lesssim |\ell| \lesssim 90°$. This may be due to clustering in nearby spiral arms. Of these 11, 7 have exhibited giant outbursts as described in the previous section and their galactic locations are plotted in Figure 8.1. Of these 7, giant outbursts in A 0355+26, 2S 1417–624, 4U 0115+63, 4U 1145–619 and GRO J2058+42 were identified by their high pulsed flux and spin-up rate relative to other outbursts from these sources. The single outburst from GRO J1750–27 was identified as a giant outburst from its peak spin up rate ($\dot{\nu} \approx 4 \times 10^{-11}\,\mathrm{Hz\,s^{-1}}$). The single outburst from A 1118–616 was identified through its duration ($\sim 50\,\mathrm{d}$) and its large $\dot{\nu} \approx 2 \times 10^{-12}\,\mathrm{Hz\,s^{-1}}$ compared with the largest expected orbital signature (the orbit is unknown), although comparable rates are seen in normal outbursts of 2S 1417–624 and GS 0834–430. Using the distances inferred from the optical counterparts where they are available (see Nagase 1989), we find that the peak 20–50 keV pulsed luminosities of these outbursts are in the range of $(1-10) \times 10^{36}$ erg s^{-1}. This implies that we can detect giant outbursts at distances of at least 11.5 kpc, roughly consistent with the giant outburst detection of GRO J1750–27, near the Galactic center.

Although these outbursts may not be standard candles, it is interesting to ask what sampling distance one would infer from their distribution in ℓ and b, shown in Figure 8.2 if they are standard candles. Given the limited data set, we take a simple model for the Galactic distribution. We assume that the Be transients are distributed as $\exp(-|z|/z_0)$ in the direction perpendicular to the plane and, like the matter in the Galaxy, fall off radially $\exp(-r/r_0)$ away from the Galactic center, where $r_0 = 3.5$ kpc (de Vaucouleurs & Pence 1978). We also assume that our modeling has $\pm\ell$ and $\pm b$ symmetry, we use the absolute values of ℓ and b in this analysis. There may be an intrinsic asymmetry in the ℓ distribution due to the possible clustering of transients along spiral arms. However, since our estimate of the BATSE sampling distance (see below) depends mainly on the b distribution (after integrating over the the ℓ distribution), the effect of this assumption on our results will be minimal.

For a Galactic center distance of 8.5 kpc, we find that the acceptable fits ($\gtrsim$90% confidence) to the cumulative b distribution require a sampling distance in the range of $(35-50)z_0$ (see Figure 8.2). If the Be binaries have the scale height $z_0 \approx 100$ pc of massive stars (Miller & Scalo 1979), then the sampling distance inferred from the latitude distribution is 3–5 kpc. This is consistent with the observed excess of objects in the direction of the Galactic center versus the anti-center, as the sampling distance is of order the exponential scale length in the disk population, r_0. However, kick velocities of $v \sim 450 \pm 90$ km s^{-1} are

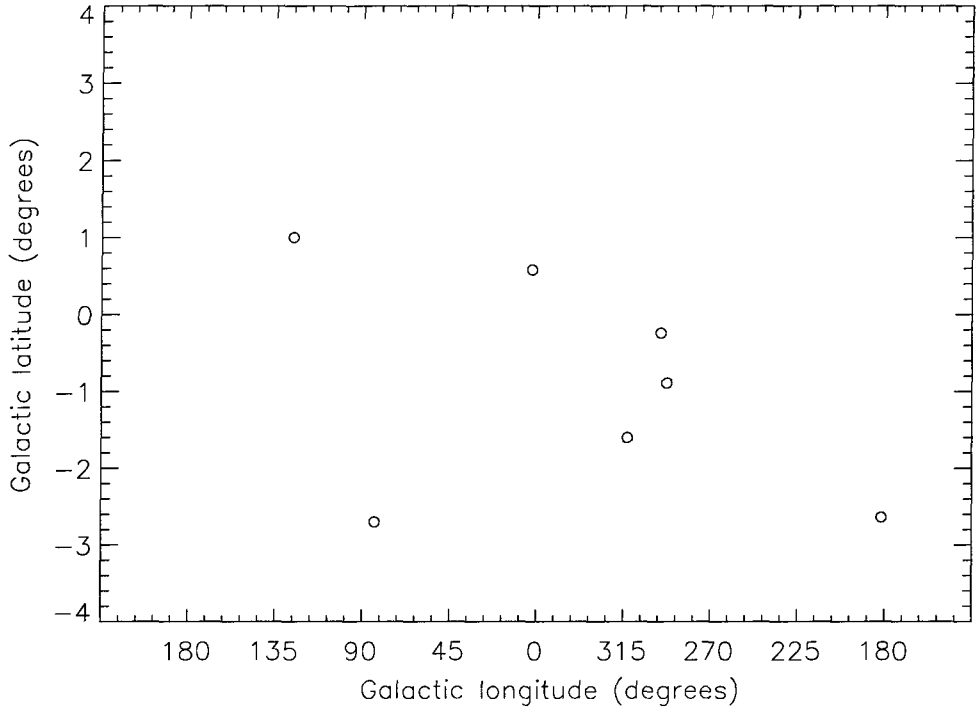

Figure 8.1: Galactic location of BATSE-detected giant outbursts from Be transients. The circles denote the location within the galaxy of those Be transients which were detected by BATSE during giant outbursts.

typically imparted to neutron stars during the supernova (Lyne & Lorimer 1994), potentially increasing the scale height of those which remain in binaries up to $\approx$ 140 pc (Brandt & Podsiadlowski 1995). This helps to make the sampling distance more consistent with our first estimate of 11.5 kpc, but still a bit short. The resolution of this discrepancy may be that the giant outbursts are not standard candles. We note also that our assumption of $\pm b$ symmetry is not strictly correct because the sun is known to lie a vertical distance of $z_\odot \approx$ 15 pc above the Galactic plane (Cohen 1995). Nevertheless, since $z_\odot$ is small compared to both the sampling distance and the expected scale height of Be transients, including the effects of $z_\odot$ will negatively shift the peak of the latitude distribution to $|b| \lesssim 0.2°$, which does not affect our results, especially in light of other larger uncertainties.

In four years, one of the 7 systems has had giant outbursts twice, while the remaining had giant outbursts only once, thus giving a total of 8 outbursts. We define $N_{\rm loc}$ to be the total number of transients which exist within a distance $R_{\rm loc}$ of Earth, and as-

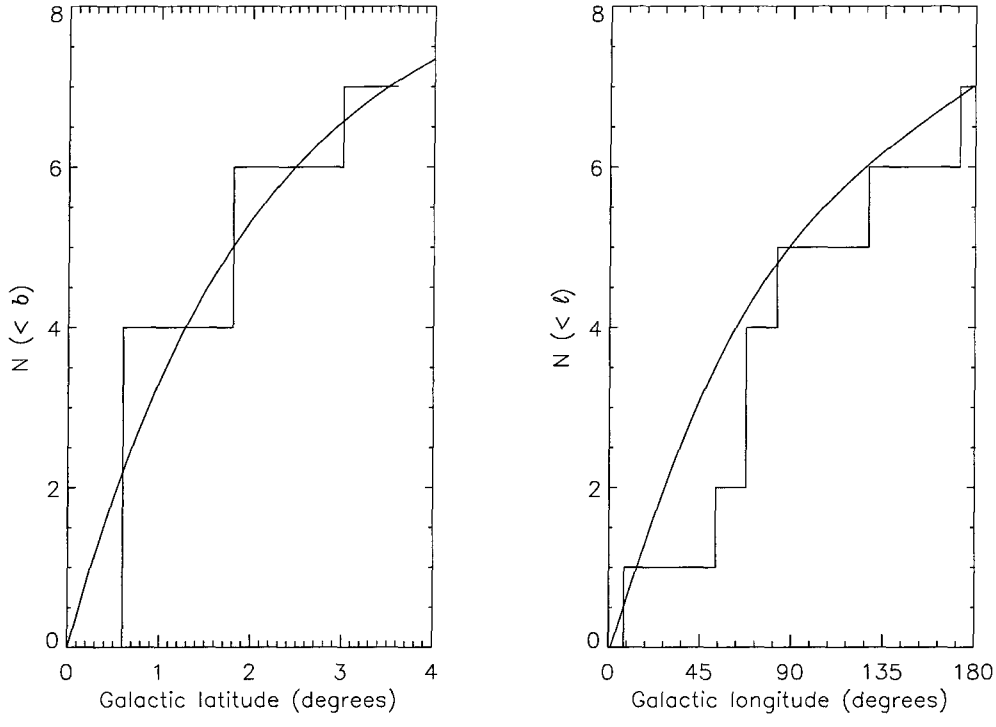

Figure 8.2: Cumulative b distribution (left panel) and cumulative ℓ distribution (right panel) of the 7 Be–transient systems detected by BATSE during giant outbursts: A 0535+262, A 1118-61, GRO J1750-27, GRO J2058+42, 2S 1417-624, 4U 0115+634 and 4U 1145-619. The histogram and solid line respectively represent the actual data and the model prediction. We assume that our modeling has $\pm\ell$ and $\pm b$ symmetry, we use the absolute values of ℓ and b in this analysis. A sampling distance of $40z_0$, with $z_0 = 100\ pc$ gives the best fit to the b distribution and yields an acceptable Kolmogorov-Smirnov statistic. The relatively poor correspondence between the ℓ distribution and the model is due to the clustering of transients at $60° \lesssim \ell \lesssim 90°$.

sume that all the 7 systems from which BATSE had detected giant outbursts are within distance $R_{\rm loc}$ of Earth. If the frequency of giant outbursts is governed by a Poisson process, BATSE's detection of 8 giant outbursts in 4 years implies that the recurrence time scale for each transient is $\tau_{\rm r} \approx N_{\rm loc}/(8/4) = N_{\rm loc}/2$ yrs and that the mean number of giant outbursts expected from each transient in 4 years is $\mu = 8/N_{\rm loc}$. In 4 years, the probability of one transient undergoing two outbursts, 6 undergoing one outburst, and the remainder undergoing no outbursts is given by

$$Pr \propto \left(\frac{N_{\rm loc}!}{7!\ (N_{\rm loc}-7)!}\right)\left(\frac{7!}{1!\ 6!}\right)\left(\frac{\mu^2 e^{-\mu}}{2}\right)(\mu e^{-\mu})^6\ \mu^{(N_{\rm loc}-7)}\ . \tag{8.1}$$

The peak of this function occurs at $N_{\rm loc} \approx 25$, which is the expected total number of transients within a distance of $R_{\rm loc}$ of Earth. This allows us to compute the proportionality constant in the density distribution of Be–transients which, when integrated over the Galactic disk, yields an estimate of the total number of Be transients in the Galaxy, $N_{\rm tot}$. As shown in Figure 8.2, $R_{\rm loc} = 40 z_0$ provides the best fit to the observed cumulative b distribution. For $z_0 = 100$ pc, $R_{\rm m} = 4$ kpc and $N_{\rm tot} \approx 1300$ while for $z_0 = 200$ pc, $R_{\rm m} = 8$ kpc and $N_{\rm tot} \approx 250$. If BATSE could indeed sample out to $R_{\rm loc} = 11.5$ kpc, the estimated distance to GRO J1750–27, $N_{\rm tot} \approx 130$ for $z_0 = 100$ pc. Since our estimate of $N_{\rm loc}$ hinges upon a single transient which exhibited more than one giant outburst, these estimates should be considered crude. However, they are consistent with estimates from evolutionary models of the total number of Be/neutron-star binaries, $\sim 10^4$, most of which are quiescent (Meurs & van den Heuvel 1989; Dalton & Sarazin 1995).

Chapter 9

Summary

Five years of continuous monitoring by BATSE has harvested an unusually rich data set on accreting pulsars which, as demonstrated by the frequency and flux histories in Chapter 4, is unprecedented in breadth, size and uniformity. This has yielded many new important insights into the behavior and evolution of accreting pulsars.

The all–sky, uniform coverage provided by BATSE has allowed us to estimate realistically the Galactic population of Be–transients (Chapter 8). Although the estimate is crude, it will improve with the detection of more giant outbursts from existent or new Be–transients.

The simple model of pulsar spin–up through disk–fed accretion mediated by a magnetosphere at a distance $\approx 100\ R_{\rm x}$ from the neutron star surface appears to be at least qualitatively correct, given the consistency between the characteristic and observed spin–up rates in GX 1+4, 4U 1626–67 and Cen X–3 (see Table 6.1). This is further supported by the reasonable agreement between the theoretical and measured values of γ (the power–law index which relates the spin–up rate and flux) for A 0535+26 and GRO J1744–28.

The dense sampling of frequency histories by BATSE also revealed that Cen X–3 has been spinning up on a much longer time scale than that predicted by the simple model (Equation 1.7) because it is actually undergoing torque reversals every ≈ 50 d. The apparent secular spin–up trend inferred from pre–BATSE observations is simply an artifact of the sparse sampling (Figure 6.1). Even more surprising is the fact that the known persistent sources GX 1+4, 4U 1626–67 and OAO 1657–415 also exhibit similar torque reversals on time scales ranging from weeks to years. This behavior is hard to account for even with extensions to the simple model. Models involving a prograde accretion disk interacting

with the pulsar magnetosphere (Section 6.2.1), or transitions between standard Keplerian disks and sub–Keplerian advection dominated flows (ADAF) (Section 6.2.2) require fine tuning and the pulsar to be spinning close to equilibrium. The alternating prograde and retrograde disk model (Section 6.2.3) appears more plausible than the previous ones, but the expected correlation between the magnitudes of spin–up/spin–down rates and fluxes is neither observed in Cen X–3 nor OAO 1657–415.

BATSE observations have also blurred the distinction between the traditional classes of accreting pulsars. The wind–fed system GX 301–2 exhibited two steady spin–up episodes each lasting $\approx$ 30 d, strongly suggesting the formation of transient accretion disks (Chapter 5). The disk reversal model, if correct, asserts that the supposed Roche Lobe filling systems Cen X–3 and 4U 1626–67 do not actually overflow their Roche Lobe, but that mass transfer from the companion to the neutron star occurs through an X–ray excited thermal wind (Section 6.2.3). An alternative phenomenological classification scheme which appears promising is based on the parameter $\eta = \dot{M}_{\rm rad}/\dot{M}_{\rm therm}$, where $\dot{M}_{\rm rad}$ and $\dot{M}_{\rm therm}$ are respectively the rates of radiatively driven and X–ray excited outflows from the companion (Section 6.2.4).

Although BATSE has yielded many new insights into the behavior and evolution of accreting pulsars, our understanding of these systems is far from complete. In fact, BATSE observations have raised more questions than it answered, especially with respect to the torque reversals observed. Further progress in this area would require a coordinated two–pronged effort. The first is to pursue aggressive simultaneous multi–wavelength campaigns involving BATSE, *RXTE*/PCA and optical telescopes (Section 6.2.5), while the other is to perform ever more realistic and sophisticated 3–D magneto-hydrodynamical simulations with the latest generation of supercomputers (Section 7.6). The vast expanse of uncharted territory which remains to be explored promises to keep the study of accreting pulsars a fertile research area in the foreseeable future.

Appendix A

GX 301–2 Time Delay Measurements Using the Cross Spectrum Technique [1]

The time delay between a pulse template and a folded profile has traditionally been found by maximizing their cross correlation. The statistical error in each phase bin and uncertainty in the cross correlation is easy to find when photon counting statistics dominate the measurement noise. However, it is not so simple to estimate errors for measurements dominated by a background that varies on a time scale comparable to the signal and has a complicated (i.e. not white) power spectrum.

As demonstrated by Figure 3.1, the low frequency noise in BATSE is highly frequency dependent and much stronger than counting noise. However, the noise is "locally Gaussian" (i.e. Gaussian in all narrow ranges of frequencies). We can thus measure the noise at any frequency, and estimate the shift between template and profile for each harmonic using the cross spectrum (Bendat & Piersol 1986). This allows us to find the statistical errors and construct a minimum-variance estimate of the shift. A technique described by Deeter and Boynton (1985) and Boynton and Deeter (1985) to estimate time delays in signal-dominated measurements where changes in pulse shape contribute significantly to the uncertainties is almost equivalent.

Each pulse profile is generated by folding a 2-day long time series at the fundamental pulsar frequency, f_0, into N_b bins. Let $x(k)$ and $y(k)$, $0 \leq k < N_b$ denote the zero-meaned template and the profile respectively. Assuming that the profile is a scaled,

[1] Extracted with changes from "Rapid Spin–Up Episodes in the Wind Fed Accreting Pulsar GX 301–2" in *The Astrophysical Journal*, 479, 933–947, by D. T. Koh, L. Bildsten, D. Chakrabarty, R. W. Nelson, T. A. Prince, B. A. Vaughan, M. H. Finger, R. B. Wilson and B. C. Rubin. Used by permission of the authors.

shifted version of the template, we can model the profile as

$$y_{mod}(k) = \alpha x(k - \tau_0 N_b/P), \tag{A.1}$$

where α is the scaling factor, τ_0 is the time shift, and P is the epoch-folding period. We then expand $x(k)$ and $y(k)$ in Fourier series and treat the Fourier coefficients as statistically independent. Deeter and Boynton (1985) point out that this is not strictly true in the presence of strong background fluctuations with a long coherence length. The difference in phase between each harmonic of the profile and template is a (nearly) statistically independent measure of the shift between the profile and template. The phase difference at harmonic j is found using the cross spectrum, C_j, defined as the product of the Fourier transform of the template, X_j, with the complex conjugate of the Fourier transform of the profile, Y_j: $C_j = X_j Y_j^*$. The argument of C_j is the phase difference in the jth harmonic. If the profile is a shifted, scaled version of the template, then the phase shift at harmonic j, ϕ_j, is given by

$$\phi_j = \arg[C_j] = 2\pi\tau_0 j/P. \tag{A.2}$$

The argument of C_j scales linearly with harmonic number, j, and has slope $2\pi\tau_0/P$. We then find the shift, τ_0, by performing a linear least-squares fit to the observed phase differences, ϕ_j, with τ_0 as the only fit parameter. This is formally equivalent to a weighted average of the ϕ_j of the form

$$\tau_0 = \left(\frac{P}{2\pi}\right)\left(\sum_{j=1}^{N_b/2} j\phi_j/\sigma_j^2\right)\left(\sum_{j=1}^{N_b/2} j^2/\sigma_j^2\right)^{-1} \tag{A.3}$$

where σ_j^2 is variance in the measurement of ϕ_j. Because it was derived from a least-squares statistic, equation A.3 is a minimum variance estimate of the shift between profile and template. It remains to estimate σ_j.

Since the template has much better statistics than the individual profiles, we can measure the phase difference at any harmonic as well as we can measure the phase of the Fourier coefficient of the profile at that harmonic. Determining the uncertainty in the phase shift is equivalent to determining the uncertainty in the phase of a sinusoid. The Fourier transform of the profile at harmonic j, Y_j, is the sum of the Fourier transform of the signal and the noise at ν_j: $Y_j = Y_j^s + Y_j^n$. The phase of Y_j is given by

$$\arg[Y_j] = \arctan[\mathrm{Im}(Y_j)/\mathrm{Re}(Y_j)]. \tag{A.4}$$

The precision with which we can measure phase is independent of phase, and we can assume without loss of generality that the phase of the signal is zero. In that case, $\mathrm{Im}(Y_j^s) = 0$, $\arg[Y_j] \approx \mathrm{Im}(Y_j)/\mathrm{Re}(Y_j)$, and the variance in $\arg[Y_j]$ is given approximately by

$$\mathrm{var}(arg[Y_j]) \simeq \mathrm{var}[\mathrm{Im}(Y_j^n)]/(\mathrm{Re}(Y_j))^2. \tag{A.5}$$

Because the noise is locally Gaussian, $\mathrm{var}[\mathrm{Im}(Y_j^n)] = \mathrm{var}[Y_j^n]/2 = P_j^n/2$, where P_j^n is the noise power at ν_j. Thus the uncertainty in phase is

$$\delta\arg[Y_j] = \left(\frac{P_j^n}{2P_j^s}\right)^{1/2}. \tag{A.6}$$

The variance in the jth phase shift is simply one half the ratio of the signal and noise powers at ν_j, both of which we measure from the daily power spectra.

As higher harmonics are dominated by noise, we only used 7 harmonics in performing the least-squares fit. Even for $j < 7$, we used only high signal-to-noise harmonics for finding τ_0. To probe the validity of our assumptions, the reduced chi-square were computed for all the single parameter fits undertaken to measure time delays. The pulse profiles for GX 301-2 are typically detected in ≈ 3 out of the 7 harmonics. In the vicinity of periastron passage, the number of harmonics detected increases to $\approx$ 4–5. For a single parameter fit with 3 points, the distribution of the reduced chi-square is expected to be

$$f(\chi^2) = \exp(-\chi^2). \tag{A.7}$$

Figure A.1 compares the reduced chi-square histogram for those 173 fits which were significant detections at two or more harmonics to the expected distribution. The same template constructed from 235 2-day folded profiles were used for all the fits. The slight excess of fits with high reduced chi-square arise from the increased number of harmonics detected near periastron passage. The agreement between the actual and expected distribution demonstrates the validity of the assumptions upon which this method is based. In particular, the assumption that all pulse profiles share a common shape seems to have borne out. We highlight this as it is also an important assumption made in our flux estimates.

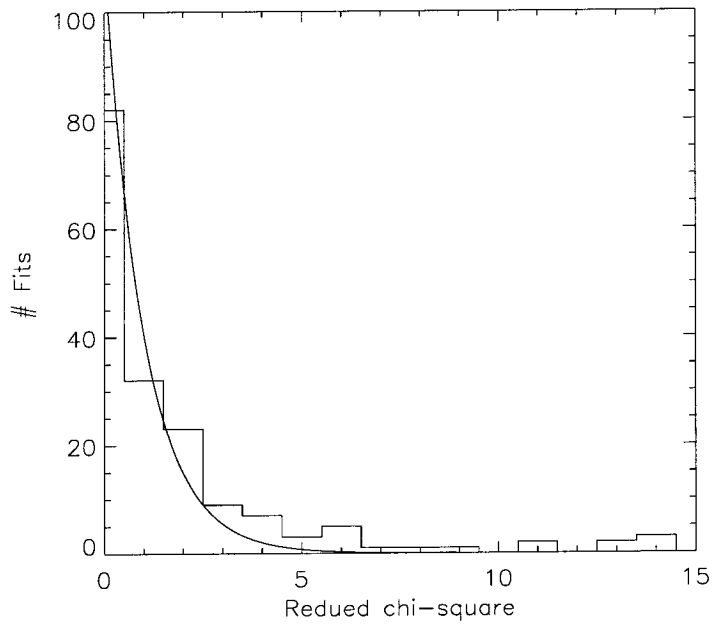

Figure A.1: The chi-square histogram for the 173 single-parameter fits performed. The solid line shows the distribution expected for a single-parameter fit with 3 points. The slight excess of fits with high reduced chi-square are due mainly to the increased number of harmonics detected at orbital phases close to periastron passage.

Appendix B

Details of BATSE Data Analysis Techniques [1]

In this appendix we discuss the various techniques used to measure frequency and flux in the BATSE analysis. Frequency estimation is covered first, followed by pulsed flux.

B.1 Frequency Estimation

B.1.1 Frequency Estimation using Power Spectra

Power spectra were used to compute the frequency histories of 4U 1626–67, GX 1+4, OAO 1657–415, GX 301–2, GS 0834–430, GRO J1948+32, EXO 2030+375 and GRO J1008–52 displayed in § 4, as well as in data files at the COSSC. Power spectra are computed using the Fast Fourier Transform (FFT). Given a contiguous dataset of duration T seconds in N uniform bins of duration T/N, the FFT returns $N/2 + 1$ statistically-independent estimates, a_j, of the amplitude and phase of the variability at frequencies $\nu_j = j/T$, where $0 \leq j \leq N/2$. The normalized power at ν_j is $P_j \equiv |a_j|^2/\bar{P}(\nu_j)$, where $\bar{P}(\nu)$ is the average power, $\langle |a_j|^2 \rangle$, in the vicinity of ν_j (excluding frequencies immediately adjacent to ν_j). This normalization is important because the background power is strongly frequency dependent (see Figure 3.1). Thus defined, $\langle P_j \rangle = 1$. Data collected by BATSE are in uniform bins of duration 2.048 s (CONT data), 1.024 s (DISCLA data) or shorter (PSR data). However, corrections of spacecraft times to the solar system barycenter cause the bins to become nonuniform. We therefore define a new array with bins equispaced in arrival time at the

[1] Extracted with changes from "Observations of Accreting Pulsars", of which I was a major contributing author, to appear in the Astrophysical Journal Supplements 1997, 113, #2, by L. Bildsten, D. Chakrabarty, J. Chiu, M. H. Finger, D. T. Koh, R. W. Nelson, T. A. Prince, B. C. Rubin, D. M. Scott, M. Stollberg, B. A. Vaughan, C. A. Wilson and R. B. Wilson. Used by permission of the authors. This appendix was written mainly by M. H. Finger and B. A. Vaughan.

solar-system barycenter (or in the frame of the neutron star if the orbit is known). An individual time-series bin from the spacecraft will generally overlap two such bins. We can either treat each bin as a delta function at the bin center and add all counts to the appropriate bin in the new array (*whole binning*) or split counts between overlapping bins in proportion to the degree of overlap (*bin splitting*). We choose bin splitting because it performs significantly better than whole binning when $\nu \gtrsim N/2T$ while introducing negligible corrections to the power spectrum.

The response, $R^2(\nu)$, of the power spectrum to a sinusoid of frequency ν decreases with increasing frequency and also depends upon the separation, $\Delta\nu$, between ν and the nearest Fourier frequency, falling off as

$$R^2(\nu) = \mathrm{sinc}^2(\pi\nu/2\nu_{\mathrm{Nyq}})\mathrm{sinc}^2(\pi\Delta\nu T) \tag{B.1}$$

where $\mathrm{sinc}(x) = \sin(x)/x$ and $\nu_{\mathrm{Nyq}} = N/2T$ is the Nyquist frequency. Attenuation at high frequency is intrinsic to binned data and constrains us to use DISCLA and/or PSR data for fast pulsars, but attenuation with $\Delta\nu$ can be circumvented by computing the power at a denser set of frequencies. By appending an array of zeroes of length $(m-1)N$ to the array of data and computing the FFT, we obtain an over-resolved Fourier transform with m times finer frequency spacing, but with frequency bins that are no longer statistically independent. The signature of a sinusoid is no longer in one or two bins, but distributed over $\sim m$ bins. To preserve the definition $\nu_j = j/T$, we allow j to take on $m(N/2)+1$ values in increments of $\epsilon \equiv 1/m$. If the highest power occurs in frequency bin j, then Middleditch (1976) has shown that the best estimate of the signal frequency is given by

$$\nu = \nu_j + \frac{3}{4\pi^2\epsilon T}\left(\frac{P_{j+\epsilon} - P_{j-\epsilon}}{P_j}\right). \tag{B.2}$$

The uncertainty in the frequency (Middleditch 1976; Middleditch & Nelson 1976) is given by

$$\sigma_\nu \simeq \frac{1}{2\pi T}\sqrt{\frac{6}{P_j}}. \tag{B.3}$$

In all cases we use the dominant harmonic for frequency estimation. For double-peaked pulsars (see figure 4.2), the second harmonic usually dominates.

It is worth noting that $\sigma_\nu \propto T^{-3/2}$ (since $P \propto T$), and hence N_d-day power spectra are $N_d^{3/2}$ times more precise than 1-day estimates. However, transform length cannot be increased indefinitely because variations in ν will eventually cause a loss of coherence when

$T^2 \gtrsim \langle \dot{\nu} \rangle$. We call this the *de-coherence time scale* (see Appendix A of Chakrabarty et al. 1997a).

The frequency histories in this paper for OAO 1657–415, GS 0834–430, GRO J1948+32, EXO 2030+375, GRO J1008–52, and 4U 1145–619 were made from daily power spectra of CONT data. These histories and others made from daily power spectra are available in the datasets at the COSSC via:

http://cossc.gsfc.nasa.gov/cossc/COSSC_HOME.html

For the sources 4U 1626–67, GX 1+4 and GX 301–2, multi-day power spectra were used.

B.1.2 Frequency Estimation using Epoch Folding

Spin frequencies were also estimated by epoch folding data at a range of trial frequencies. We use the term "epoch folding" to describe any technique where a pulse phase is assigned to each time bin based upon a model of the spin frequency. In some cases we implemented epoch folding as a fitting procedure. This technique was used with DISCLA data for the histories of Cen X–3, 4U 1538–52, 4U 0115+634, GRO J1750–27, 2S 1417–624, GRO J2058+42, 4U 1145–619 and A 1118–616 shown in Chapter 4. Detection and determination of the pulse frequency are based on the Z^2_m test, which measures the significance of the first m Fourier amplitudes of the epoch-folded pulse profile.

Rather than rebinning the data into uniform phase bins and then epoch folding them, we fit the data using a background model and a low order Fourier expansion in the pulse phase model. Fitting does not require rebinning, and hence avoids the loss of phase resolution inherent to rebinning techniques, which is important when the low time resolution is $\gtrsim P_{\rm spin}$ (Deeter & Boynton 1986). The data are divided into $1 \sim 10$ d intervals, and each interval fit with a model $C(t)$ of the form

$$C(t) \;=\; M(t) \;+\; \sum_{k=1}^{n} \left[A_k \cos 2\pi k\phi(t) + B_k \sin 2\pi k\phi(t) \right], \tag{B.4}$$

where $M(t)$ is a model of the background rate, the harmonic sum is a Fourier representation of the pulse profile, and $\phi(t)$ is the pulse phase, where we generally assume a constant frequency for each interval and use $n = 3$. The background is modeled as a quadratic spline, with segments every 300 s and with value and slope continuous across segment boundaries (but not across gaps). This background modeling procedure is approximately equivalent

to applying a high-pass filter with ν^6 roll off and a roll-off frequency of $\sim$0.002 Hz (500 s). The Z_3^2 statistic is determined for each trial frequency for the best set of fit parameters, $\{A_k, B_k\}$, and values of Z_3^2 near the peak value fitted to determine the frequency. In the case of 4U 1538–52, because of its low frequency, we use the phenomenological background model described in Section 3.5 and Rubin et al.(1996) rather than a quadratic spline.

B.1.3 Frequency Estimation from Fits to Pulse-Phase Measurements

The frequencies histories of GRO J1744-28, Her X–1, Vela X–1, GRO J1750-27 and A 0535+26 shown in Chapter 4 were determined from fits to pulse phase measurements. Phases were determined (for orbital analyses) by epoch folding data over short intervals ($\sim$ 0.5 days) and correlating the resulting pulse profiles with pulse templates to determine phase offsets from the epoch folding phase model. The total phases were then divided into several day intervals and a linear fit in emission time made to the total phases (model plus offset) in each interval to obtain frequencies.

B.2 Pulsed Flux Estimation

B.2.1 What is Pulsed Flux and Pulsed Fraction?

Pulsed flux is the periodically varying part of the flux from a source. Unlike average flux, pulsed flux is not uniquely defined, and we employ two separate definitions for different purposes and for different sources. Let $F(\phi)$ be the flux of a pulse profile at phase ϕ, $0 \leq \phi \leq 1$, let $\bar{F} = \int_0^1 F(\phi)d\phi$ be the average flux, and let $F_{\rm min} = \min[F(\phi)]$ be the minimum flux. We define peak-to-peak pulsed flux as $F_{\rm pulsed} = \int_0^1 (F(\phi) - F_{\rm min})d\phi$, and root-mean-square (RMS) flux as $F_{\rm RMS} = \left[\int_0^1 (F(\phi) - \bar{F})^2 d\phi\right]^{1/2}$. Their relative values depend upon pulse shape. For a square wave they are equal. For a sinusoid, which is a good approximation to most accreting pulsars, $F_{\rm pulsed} = \sqrt{2}F_{\rm RMS}$. Peak-to-peak pulsed flux has intuitive appeal, but it is more difficult to measure since $F_{\rm min}$ is harder to determine than $\bar{F}$. We generally use peak-to-peak pulsed flux for average spectra of many days (see Table 4.1), where S/N is large, and RMS flux for daily estimates, as displayed in § 4. **Pulsed fraction** is the ratio of the pulsed flux to the mean flux (pulsed + unpulsed). It is in general energy dependent.

B.2.2 Peak-to-Peak Pulsed Spectra and Flux

Average energy spectrum and flux using CONT data

To estimate the energy spectrum of the pulsed emission we first compute the pulse count rate in each energy channel by epoch folding $\sim 1\,\mathrm{d}$ of data at a time into $N \lesssim P_{\mathrm{spin}}/\tau$ phase bins, where $\tau = 2.048\,\mathrm{s}$ (CONT data) or $1.024\,\mathrm{s}$ (DISCLA data) and P_{spin} is determined from over-resolved power spectra or from folding, as discussed in B.1. A running average pulse profile is constructed by aligning each day's profile with and adding it to the existing running sum, weighted by its exposure (area times exposure time). Alignment is performed by maximizing the cross correlation between the daily profile and the running sum or using the cross spectrum (see Appendix A). The end result is an average profile in each energy channel (for DISCLA we use only channel 1). Channels with a significant detection are used for spectral fitting. Prior to fitting the profiles are Fourier transformed and all harmonics higher than $n_H \sim 6$ set to zero to reduce the counting noise (see Deeter & Boynton 1986), then inverse transformed. The rate in the minimum phase bin is subtracted from each bin and the resulting rates averaged to obtain the pulsed count rate in each energy channel.

In the following discussion we denote the intrinsic strength of the pulsar signal as s, and the amplitude we measure as a. If the signal-to-noise is low, then the measured amplitude, a, of the pulsar signal, s, is significantly biased by the measurement noise, n, such that $\langle a \rangle > s$. To account for this bias and rigorously estimate the measurement uncertainty we use the probability distribution of the measured amplitude (Thomas 1969; Goodman 1985)

$$p(a|s,n) = \frac{2a}{n^2} \exp\left[\frac{-(a^2+s^2)}{n^2}\right] I_0\left(\frac{2as}{n^2}\right) \qquad (a > 0), \tag{B.5}$$

where I_0 is the zeroth order Bessel function of the first kind. This can be inverted to yield the probability distribution of s (Chakrabarty 1996):

$$p(s|a,n) = \frac{2}{n}\sqrt{\frac{1}{\pi}} \exp\left[\frac{-(a^2+2s^2)}{2n^2}\right] \frac{I_0\left(\frac{2as}{n^2}\right)}{I_0\left(\frac{a^2}{2n^2}\right)} \qquad (s > 0). \tag{B.6}$$

If $a \gg n$, the probability distribution approaches a Gaussian with variance $\sigma^2 = n^2/2$. Because the noise varies with time and energy, we determine n separately for each energy

channel by averaging the power in frequencies in the vicinity of the dominant harmonic in each of the daily power spectra of all days used to construct the average profile.

We determine the incident spectrum by folding standard models through the detector response matrix and varying the model parameters to fit the pulsed count rate in each energy channel. Pendleton et al.(1995) have computed BATSE detector response matrices as a function of viewing angle, θ. The energy edges of the CONT channels are independent of θ but vary with detector (see Figure 2.3). Because a single average profile may contain data from multiple spacecraft orientations (a typical viewing period lasts 1–2 weeks), we compute an average response matrix and average channel edges for the spectral fitting. A photon power-law model, $dN/dE = C_{30}(E/30\,\mathrm{keV})^{-\alpha}$, and an exponential (EXP) model $dN/dE = C_0/E\,\exp(-E/E_f)$, provide reasonable fits to the data. In most cases the EXP model is superior.

An alternative to aligning and averaging daily profiles is to perform a *long coherent fold.* This is only possible for consistently bright, non-eclipsing systems where gaps in the data are short compared with the de-coherence time scale, or where the torque history is smooth. Spectra have been constructed for 4U 1626–67 and GX 1+4 in such a way (Chakrabarty et al. 1997a; Chakrabarty et al. 1997b),

On-Peak Minus Off-Peak Pulsed Spectra and Flux

In another approach to pulsed flux estimation, 5–10 d of CONT data are folded using a phase model determined by fitting pulse phases measured using epoch-folded DISCLA data. An "on-pulse" and "off-pulse" phase interval are chosen by eye and the average rate in the off-pulse interval subtracted from each phase bin, yielding a rate difference in each energy channel for each phase bin.

B.2.3 Daily RMS Flux

Unlike profiles constructed from 10–200 days, daily profiles have low S/N for most sources most of the time. Rather than attempting to fit a spectral model, we generally assume a spectral shape and determine the normalization. Although we use an exponential model in some cases and a power law in others, daily flux histories are not particularly sensitive to the choice of model.

Daily RMS flux from CONT and DISCLA data

For most sources, an RMS flux, $F_{\rm RMS}$, is estimated daily by constructing pulse profiles in flux units. First, the average rate is subtracted from the folded profile from each detector and energy channel. Next, each phase bin, ϕ, of each daily pulse profile for each exposed detector and energy channel is modeled as a phase-dependent exponential spectrum

$$F(E,\phi) = F_0(\phi)(E_0/E)\exp(-(E-E_0)/E_f), \tag{B.7}$$

where $F_0(\phi)$ is the flux at E_0, which depends upon phase, and where E_f is assumed independent of phase. The e–folding energy is not adjusted in the daily fits but rather taken from longer term analysis. The flux as a function of phase is parameterized in terms of a small number m (3–6) of Fourier amplitudes;

$$F_0(\phi) = F_0^{\rm avg} + \sum_{k=1}^{m}[A_k\cos(2\pi k\phi) + B_k\sin(2\pi k\phi)], \tag{B.8}$$

with the Fourier coefficients A_k and B_k determined in the fit. Finally, the RMS flux $F_{\rm RMS}$ is determined as

$$F_{\rm RMS} = \left(0.5\sum_{k=1}^{m}[A_k^2 + B_k^2]\right)^{1/2}. \tag{B.9}$$

This procedure assumes that the pulse shape is independent of energy, which is not in general true. Fluxes in the datasets at the COSSC are determined using this procedure.

DISCLA flux using power spectra

Flux histories have been determined for 4U 1626–67 and GX 1+4 by computing 1–5 d power spectra of the X-ray light curves in DISCLA channel 1 and using the amplitude of the dominant harmonic, in both cases the fundamental, to estimate the pulsed amplitude. The flux is determined by convolving either a power-law or exponential model with the detector response matrix, assuming a power-law index or e–folding energy. This technique assumes a constant spectral shape and pulse profile, and can be used with non-sinusoidal profiles by computing a correction factor between the amplitude of the dominant harmonic and the pulsed flux.

Frequencies and Fluxes from PSR data

PSR data were used in the analysis of GRO J1744–28 because of its short 0.467 s pulse period. As well as data collected explicitly for GRO J1744-28, all applicable PSR data that was collected in a single-sweep mode (with no folding on board) were used. On

the ground the 20-40 keV rates from these data were divided into intervals of $\sim$ 200 s. For each interval an empirical background model quadratic in time was fit to the rates and subtracted. Then the rates in each interval were fitted with an 6th order Fourier pulse model. These (harmonically represented) profiles were then combined over $\sim$ 0.5 d intervals using a phase model, obtained by bootstrapping. The frequencies for GRO J1744–28 shown in Figure 4.6 were obtained by fitting pulse phase measurements based on these profiles. To obtain fluxes, a conversion factor from pulsed count rate to pulsed flux was calculated with the detector response matrices by assuming a spectral form $dN/dE = AE^{-2}\exp(-E/E_{\rm fold})$ with $E_{\rm fold} = 15$ keV.

References

Abbott, D. C. 1982, ApJ, 259, 282

Anzer, U. & Borner, G. 1980, A&A, 83, 133

Aoki, T. et al. 1992, PASJ, 44, 641

Apparao, K. M. V. 1994, Space Sci.Rev., 69, 255

Arons, J. 1993, ApJ, 408, 160

Arons, J., Burnard, D., Klein, R. I., McKee, C. F., Pudritz, R. E., & Lea, S. M. 1984, in High Energy Transients in Astrophysics, ed. S. E. Woosley, (New York: AIP), 215

Basko, M. M., Hatchett, S., McCray, R., & Sunyaev, R. A. 1977, ApJ, 215, 276

Basko, M. M. & Sunyaev, R. A. 1976, MNRAS, 175, 395

Bendat, J. S. & Piersol, A. G. 1986, Random Data, (New York: Wiley)

Bianchi, L. & Bernacca, P. L. 1980, A&A, 89, 214

Bildsten, L. et al. 1997, ApJ, in press

Bildsten, L., Chakrabarty, D., Chiu, J., Finger, M. H., Grunsfeld, J. M., Koh, T., Prince, T. A., & Wilson, R. B. 1994, in Second Compton Symposium, ed. N. Gehrels C. E. Fichtel & J. P. Norris, (New York:AIP Press), 290

Blondin, J. M. 1994, ApJ, 435, 756

Blondin, J. M., Kallman, T. R., Fryxell, B. A., & Taam, R. E. 1990, ApJ, 356, 591

Blondin, J. M., Stevens, I. R., & Kallman, T. R. 1991, ApJ, 371, 684

Bohm-Vitense, E. 1981, ARA&A, 19, 295

Bord, D. J., Mook, D. E., Petro, L., & Hiltner, W. A. 1976, ApJ, 203, 689

Boynton, P. & Deeter, J. 1985, in Workshop on the Timing Studies of X-ray Sources, ed. Satio Hayakawa & Fumiaki Nagase, 13

Brandt, N. & Podsiadlowski, P. 1995, A&A, 274, 461

Castor, J. I., Abbott, D. C., & Klein, R. I. 1975, ApJ, 195, 157

Chakrabarty, D. 1996. Ph.D. Thesis, California Institute of Technology

Chakrabarty, D. 1997, ApJ, submitted

Chakrabarty, D. et al. 1993, ApJ, 403, L33

Chakrabarty, D. et al. 1997a, ApJ, 474, 414

Chakrabarty, D. et al. 1997b, ApJ, 481, L101

Chakrabarty, D., Bildsten, L., Chiu, J., Grunsfeld, J. M., Koh, T., Prince, T. A., Finger, M. H., & Wilson, R. B. 1994a, in Second Compton Symposium, ed. C. E. Fichtel, N. Gehrels, & J. P. Norris, (New York: AIP), 285

Chakrabarty, D., Koh, T., Bildsten, L., Prince, T. A., Finger, M. H., Wilson, R. B., Pendleton, G. N., & Rubin, B. C. 1995a, ApJ, 446, 826

Chakrabarty, D., Koh, T., Prince, T. A., Vaughan, B., Finger, M. H., Scatt, M., & Wilson, R. B. 1995b, IAU Circ., No. 6153

Chakrabarty, D., Prince, T. A., Finger, M. H., & Wilson, R. B. 1994b, IAU Circ., No. 6105

Chakrabarty, D. & Roche, P. 1997, ApJ, submitted

Chevalier, C. & Ilovaisky, S. A. 1975, IAU Circ., No. 2778

Chichkov, M. A., Syunyaev, R. A., Lund, I. Y., Brandt, S., & Castrotirado, A. 1995, Soviet Ast. Lett., 21, 435

Coe, M. J. et al. 1994a, MNRAS, 270, L57

Coe, M. J. et al. 1994b, A&A, 289, 784

Coe, M. J., Carpenter, G. F., Engel, A. R., & Quenby, J. J. 1975, Nature, 256, 630

Coe, M. J., Longmore, A., Payne, B. J., & Hanson, C. G. 1988, MNRAS, 232, 865

Cohen, M. 1995, ApJ, 444, 874

Cominsky, L., Clark, G. W., Li, F., Mayer, W., & Rappaport, S. 1978, Nature, 273, 367

Cominsky, L., Roberts, M., & Finger, M. 1994, in Second Compton Symposium, ed. C. E. Fichtel, N. Gehrels, & J. P. Norris, (New York: AIP), 294

Cook, M. C. & Page, C. G. 1987, MNRAS, 225, 381

Cook, M. C. & Warwick, R. S. 1987, MNRAS, 225, 369

Corbet, R. H. D. 1986, MNRAS, 220, 1047

Corbet, R. H. D., Woo, J. W., & Nagase, F. 1993, A&A, 276, 52

Cox, J. P. 1980, Theory of Stellar Pulsation, (Princeton: Princeton University Press)

Crampton, D., Hutchings, J. B., & Cowley, A. P. 1978, ApJ, 225, L63

Dalton, W. W. & Sarazin, C. L. 1995, ApJ, 440, 280

Davidsen, A., Malina, R., & Bowyer, S. 1977, ApJ, 211, 866

Davidson, K. & Ostriker, J. P. 1973, ApJ, 179, 585

Davison, P. J. N., Watson, M. G., & Pye, J. P. 1977, MNRAS, 181, 73P

Day, C. S. R. & Stevens, I. R. 1993, ApJ, 403, 322

de Jager, C., Nieuwenhuijzen, H., & van der Hucht, K. A. 1988, A&AS, 72, 259

de Jager, O. C., Swanepoel, J. W. H., & Raubenheimer, B. C. 1989, A&A, 221, 180

de Vaucouleurs, G. & Pence, W. D. 1978, AJ, 83, 1163

Deeter, J. & Boynton, P. 1985, in Workshop on the Timing Studies of X-ray Sources, ed. S. Hayakawa & F. Nagase, 29

Deeter, J. E. & Boynton, P. E. 1986, in Proceedings Inuyama Workshop on the Timing Studies of X-Ray Sources, ed. S. Hayakawa & F. Nagase, (Nagoya: Nagoya University), 29

Deeter, J. E., Boynton, P. E., Lamb, F. K., & Zylstra, G. 1989, ApJ, 336, 376

Deeter, J. E., Boynton, P. E., Miyamoto, S., Kitamoto, S., Nagase, F., & Kawai, N. 1991, ApJ, 383,

324

Deeter, J. E., Boynton, P. E., & Pravdo, S. H. 1981, ApJ, 247, 1003

Deeter, J. E., Boynton, P. E., Shibazaki, N., Hayakawa, S., Nagase, F., & Sato, N. 1987, AJ, 93, 887

Dotani, T., Fujimoto, R., Nagase, F., & Inoue, H. 1995, IAU Circ., 6241

Dotani, T., Kii, T., Nagase, F., Makishima, K., Ohashi, T., Sakao, T., Koyama, K., & Tuohy, I. R. 1989, PASJ, 41, 427

Dower, R. G., Apparao, K. M. V., Bradt, H. V., Doxsey, R. E., Jernigan, J. G., & Kulik, J. 1978, Nature, 273, 364

Doxsey, R., Bradt, H. V., Levine, A., Murthy, G. T., Rappaport, S., & Spada, G. 1973, ApJ, 182, L25

Ebisawa, K., Day, C. S. R., Kallman, T. R., Nagase, F., Kotani, T., Kawashima, K., Kitamoto, S., & Woo, J. W. 1996, PASJ, 48, 425

Elsner, R. F., Ghosh, P., & Lamb, F. K. 1980, ApJ, 241, L155

Fender, R. P., Roche, P. D., Pooley, G. G., Chakrabarty, D., Tzioumis, A. T., & Spencer, R. E. 1997, in The Transparent Universe, ed. C. Winkler, T. J. L. Courvoisier, & P. Durouchoux, (Noordwijk: ESA SP–382), 303

Finger, M. H. et al. 1995, IAU Circ., No. 6266

Finger, M. H., Cominsky, L. R., Wilson, R. B., Harmon, B. A., & Fishman, G. J. 1994, in The Evolution of X-ray Binaries, ed. S. S. Holt & C. S. Day, (New York:AIP Press), 459

Finger, M. H., Koh, D. T., Nelson, R. W., Prince, T. A., Vaughan, B. A., & Wilson, R. B. 1996, Nature, 381, 291

Finger, M. H., Wilson, R. B., & Chakrabarty, D. 1996, A&AS, 120, C209

Finger, M. H., Wilson, R. B., & Fishman, G. J. 1994, in Second Compton Symposium, ed. C. E. Fichtel, N. Gehrels, & J. P. Norris, (New York:AIP Press), 304

Finger, M. H., Wilson, R. B., & Harmon, B. A. 1996, ApJ, 459, 288

Finger, M. H., Wilson, R. B., Harmon, B. A., Fishman, G. J., Meegan, C. A., & Paciesas, W. S. 1993, in Compton Gamma Ray Observatory, ed. M. Friedlander, N. Gehrels, & D. J. Macomb, (New York: AIP Press), 386

Finger, M. H., Wilson, R. B., Meegan, C. A., Paciesas, W. S., & Fishman, G. J. 1992, in Compton Observatory Science Workshop, ed. C. R. Shrader, N. Gehrels, & B. Dennis, (Washington: NASA CP–3137), 185

Fishman, G. J. et al. 1989a, in Proc. of the GRO Science Workshop, ed. W. N. Johnson, (Greenbelt: NASA/GSFC), 2–39

Fishman, G. J. et al. 1989b, in Proc. of the GRO Science Workshop, ed. W. N. Johnson, (Greenbelt: NASA/GSFC), 39

Frank, J., King, A., & Raine, D. 1992, Accretion Power in Astrophysics, (Cambridge: Cambridge University Press)

Friend, D. B. & Abbott, D. C. 1986, ApJ, 311, 701

Fryxell, B. A. & Taam, R. E. 1988, ApJ, 335, 862

Ghosh, P. & Lamb, F. K. 1979, ApJ, 234, 296

Giacconi, R., Gursky, H., Kellogg, E., Levinson, R., Schreier, E., & Tananbaum, H. 1973, ApJ, 184, 227

Giacconi, R., Gursky, H., Kellogg, E., Schreier, E., & Tananbaum, H. 1971, ApJ, 167, L67

Giovannelli, F. & Graziati, L. S. 1992, Space Sci.Rev., 59, 1

Goodman, J. W. 1985, Statistical Optics, (New York: Wiley)

Gottwald, M., Steinle, H., Graser, U., & Pietsch, W. 1991, A&AS, 89, 367

Grindlay, J. E., Petro, L. D., & McClintock, J. E. 1984, ApJ, 276, 621

Grove, J. E. 1995, IAU Circ., No. 6239

Grove, J. E. et al. 1993, IAU Circ., No. 5838

Grove, J. E. et al. 1995, ApJ, 438, L25

Haberl, F. 1991, ApJ, 376, 245

Haberl, F., Pietsch, W., Motch, C., & Buckley, D. A. H. 1996, IAU Circ., 6445

Hammerschlag-Hensberge, G. et al. 1980, A&A, 85, 119

Hammerschlag-Hensberge, G., Zuiderwijk, E. J., & van den Heuvel, E. P. J. 1976, A&A, 49, 321

Hansen, C. J. & Kawaler, S. D. 1994, Stellar Interiors, (New York: Springer-Verlag)

Harmon, B. A. et al. 1992, in Compton Observatory Science Workshop, ed. C. R. Shrader, N. Gehrels, & B. Dennis, (Washington: NASA CP–3137), 69

Heinze, K. G. 1976, ApJS, 30, 491

Hellier, C. 1994, IAU Circ., No. 5994

Hiltner, W. A., Werner, J., & Osmer, P. 1972, ApJ, 175, L19

Ho, C. & Arons, J. 1987a, ApJ, 316, 283

Ho, C. & Arons, J. 1987b, ApJ, 321, 404

Ho, C. & Arons, J. 1987c, A&AS, 321, 404

Hughes, J. P. 1994, ApJ, 427, L25

Hutchings, J. B., Bernard, J. E., Crampton, D., & Cowley, A. P. 1978, ApJ, 223, 530

Hutchings, J. B., Cowley, A. P., Crampton, D., van Paradijs, J., & White, N. E. 1979, ApJ, 229, 1079

Ignace, R., Cassinelli, J. P., & Bjorkman, J. E. 1996, ApJ, 459, 671

Illarionov, A. F. & Sunyaev, R. A. 1975, A&A, 39, 185

Ilovaisky, S. A., Chevalier, C., & Motch, C. 1982, A&A, 114, L7

Israel, G. L., Mereghetti, S., & Stella, L. 1994, ApJ, 433, L25

Israel, G. L., Stella, L., Angelini, L., White, N. E., & Giommi, P. 1995, IAU Circ., No. 6277

Ives, J. C., Sanford, P. W., & Bell-Burnell, S. J. 1975, Nature, 254, 578

Iwasawa, K., Koyama, K., & Halpern, J. P. 1992, PASJ, 44, 9

Johns, M., Koski, A., Canizares, C., & McClintock, J. 1978, IAU Circ., No. 3171

Johnson, W. N. et al. 1993, ApJS, 86, 693

Joss, P. C. & Rappaport, S. A. 1984, ARA&A, 22, 537

Kaper, L., Lamers, H. J. G. L. M., Ruymaekers, E., van den Heuvel, E. P. J., & Zuiderwijk, E. J. 1995, A&A, 300, 446

Kelley, R. L., Apparao, K. M. V., Doxsey, R. E., Jernigan, J. G., Naranan, S., & Rappaport, S. 1981a, ApJ, 243, 251

Kelley, R. L., Rappaport, S., & Ayasli, S. 1983, ApJ, 274, 765

Kelley, R. L., Rappaport, S., Brodheim, M. J., Cominsky, L., & Strothers, R. 1981b, ApJ, 251, 630

Kelley, R. L., Rappaport, S., Clark, G. W., & Petro, L. D. 1983, ApJ, 268, 790

Koh, D. T. et al. 1997, ApJ, 479, 933

Koh, T., Chakrabarty, D., Prince, T. A., Vaughan, B. A., Zhang, S. N., Scott, M., Finger, M. H., & Wilson, R. B. 1995, IAU Circ., 6222

Konigl, A. 1991, ApJ, 370, L39

Kouveliotou, C., van Paradijs, J., Fishman, G. J., Briggs, M. S., Kommers, J., Harmon, B. A., Meegan, C. A., & Lewin, W. H. G. 1996, Nature, 379, 799

Koyama, K. et al. 1991a, ApJ, 366, L19

Koyama, K., Kawada, M., Takeuchi, Y., Tawara, Y., Ushimaru, N., Dotani, T., & Takizawa, M. 1990a, ApJ, 356, L47

Koyama, K., Kunieda, H., Takeuchi, Y., & Tawara, Y. 1990b, PASJ, 42, L59

Koyama, K., Kunieda, H., Takeuchi, Y., & Tawara, Y. 1991b, ApJ, 370, L77

Krzeminski, W. 1974, ApJ, 192, L135

Kumar, P., Ao, C. O., & Quataert, E. J. 1995, ApJ, 449, 294

Lamb, F. K., Pethick, C. J., & Pines, D. 1973, ApJ, 184, 271

Lamers, H. J. G. L. M. & Waters, L. B. F. M. 1987, A & A, 182, 80

Lapshov, I. Y., Drenim, V. V., Sunyaev, R. A., Brandt, S., & Lund, N. 1992, Soviet Ast. Lett., 18, 12

Leahy, D. A. 1991, MNRAS, 250, 310

Levine, A., Ma, C. P., McClintock, J., Rappaport, S., van der Klis, M., & Verbunt, F. 1988, ApJ, 327, 732

Levine, A., Rappaport, S., Deeter, J. E., Boynton, P. E., & Nagase, F. 1993, ApJ, 410, 328

Levine, A., Rappaport, S., Putney, A., Corbet, R., & Nagase, F. 1991, ApJ, 381, 101

Lewin, W. H. G., Ricker, G. R., & McClintock, J. E. 1971, ApJ, 169, L17

Lovelace, R. V. E., Romanova, M. M., & Bisnovatyi-Kogan, G. S. 1995, MNRAS, 275, 244

Lubow, S. H. & Shu, F. H. 1975, ApJ, 198, 383

Lund, N., Brandt, S., & Castro-Tirado, A. J. 1994, IAU Circ., No. 5448

Lutovinov, A. A., Grebenev, S. A., Syunyaev, R. A., & Pavlinskii, M. N. 1994, Astron. Lett., 20, 538

Lyne, A. G. & Lorimer, D. R. 1994, Nature, 369, 127

Makishima, K. et al. 1988, Nature, 333, 746

Makishima, K., Kawai, N., Koyama, K., Shibazaki, N., Nagase, F., & Nakagawa, M. 1984, PASJ, 36, 679

Makishima, K., Koyama, K., Hayakawa, S., & Nagase, F. 1987, ApJ, 314, 619

Makishima, K. & Mihara, T. 1992, in Frontiers of X-ray Astronomy, ed. Y. Tanaka & K. Koyama, (Tokyo:Yamada Science Foundation and Universal Academy Press), 327

McClintock, J. E. et al. 1976, ApJ, 206, L99

McClintock, J. E., Canizares, C. R., Bradt, H. V., Doxsey, R. E., Jernigan, J. G., & Hiltner, W. A. 1977, Nature, 270, 320

McCray, R. & Hatchett, S. 1975, ApJ, 199, 196

Mereghetti, S. & Stella, L. 1995, ApJ, 442, L17

Meurs, E. J. A. & van den Heuvel, E. P. J. 1989, A&A, 226, 88

Middleditch, J. 1976. Ph.D. Thesis, University of California, Berkeley

Middleditch, J., Mason, K. O., Nelson, J. E., & White, N. E. 1981, ApJ, 244, 1001

Middleditch, J. & Nelson, J. 1976, ApJ, 208

Miller, G. E. & Scalo, J. M. 1979, ApJS, 41, 513

Motch, C., Stella, L., Janot-Pacheco, E., & Mouchet, M. 1991, ApJ, 369, 490

Murakami, T., Ikegami, T., Inoue, H., & Makishima, K. 1987, PASJ, 39, 253

Nagase, F. 1989, PASJ, 41, 1

Nagase, F. et al. 1982, ApJ, 263, 814

Nagase, F., Corbet, R. H. D., Day, C. S. R., Inoue, H., Takeshima, T., Yoshida, K., & Mihara, T. 1992, ApJ, 396, 147

Narayan, R. & Yi, I. 1994, ApJ, 428, L13

Narayan, R. & Yi, I. 1995a, ApJ, 452, 710

Narayan, R. & Yi, I. 1995b, ApJ, 444, 231

Nelson, R. W. et al. 1997, in Accretion Phenomena and Associated Outflows, ed. D. Wickramasinghe, L. Ferrario, & G. Bucknell, (San Francisco: Astron. Soc. of the Pacific), in press

Ostriker, E. C. & Shu, F. H. 1995, ApJ, 447, 813

Papaloizou, J. & Pringle, J. E. 1977, MNRAS, 181, 441

Parkes, G. E., Mason, K. O., Murdin, P. G., & Culhane, J. L. 1980, MNRAS, 191, 547

Parkes, G. E., Murdin, P. G., & Mason, K. O. 1978, MNRAS, 184, 73P

Parmar, A. N., White, N. E., & Stella, L. 1989, ApJ, 338, 373

Parmar, A. N., White, N. E., Stella, L., Izzo, C., & Ferri, P. 1989, ApJ, 338, 359

Pendleton, G. N. et al. 1995, Nucl. Instr. Methods A, 364, 567

Petre, R. & Gehrels, N. 1993, IAU Circ., No. 5877

Pravdo, S. H., Day, C. S. R., Angelini, L., Harmon, B. A., Yoshida, A., & Saraswat, P. 1995, ApJ, 454, 872

Preece, R. D., Pendleton, G. N., Briggs, M. S., Mallozzi, R. S., Paciesas, W. S., Band, D. L., Matteson, J. L., & Meegan, C. A. 1997, ApJ, submitted

Priedhorsky, W. C. & Terrell, J. 1983, ApJ, 273, 709

Pringle, J. E. & Rees, M. J. 1972, A&A, 21, 1

Rappaport, S., Clark, G. W., Cominsky, L., Joss, P. C., & Li, F. 1978, ApJ, 224, L1

Rappaport, S. & Joss, P. 1977, Nature, 266, 683

Rappaport, S., Joss, P. C., & McClintock, J. E. 1976, ApJ, 206, L103

Rappaport, S., Markert, T., Li, F. K., Clark, G. W., Jernigan, J. G., & McClintock, J. E. 1977, ApJ, 217, L29

Raubenheimer, B. C. 1990, A&A, 234, 172

Rauw, G., Vreux, J. M., Gosset, E., Hutsemekers, D., Magain, P., & Rochowicz, K. 1996, A&A, 306, 771

Ravenhall, D. G. & Pethick, C. J. 1994, ApJ, 424, 846

Reynolds, A. P., Parmar, A. N., Stollberg, M. T., Verbunt, F., Roche, P., Wilson, R. B., & Finger, M. H. 1996, A&A, 312, 872

Rickard, J. 1974, ApJ, 189, L113

Rickets, M. J., Hall, R., Page, C. G., & Pounds, K. A. 1981, Space Sci.Rev., 30, 399

Rosenberg, F. D., Eyles, C. J., Skinner, G. K., & Willmore, A. P. 1975, Nature, 256, 628

Rothschild, R. E. & Soong, Y. 1987, ApJ, 315, 154

Rubin, B. C. et al. 1994, in Evolution of X-ray Binaries, ed. S. S. Holt & C. S. Day, (New York: AIP), 455

Rubin, B. C. et al. 1996, A&AS, 120(4), C687

Rubin, B. C., Finger, M. H., Scott, D. M., & Wilson, R. B. 1997, ApJ, in press

Ruffert, M. 1997, A&A, 317, 793

Safi-Harb, S., Ogelman, H., & Dennerl, K. 1996, ApJ, 456, L37

Sato, N., Nagase, F., Kawai, N., Kelley, R. L., Rappaport, S., & White, N. W. 1986, ApJ, 304, 241

Sazonov, S. & Sunyaev, R. 1995, IAU Circ., No. 6272

Schaller, G., Schaerer, D., & Maeder, G. M. A. 1992, A & AS, 96, 269

Schmidt-Kaler, T. 1982, in Numerical Data and Functional Relationships in Science and Technology, New Series, Volume 2, Astronomy and Astrophysics, ed. K. Schaifers & H. H. Voigt, (Springer Verlag:Berlin), 1

Schmidtke, P. C., Cowley, A. P., McGrath, T. K., & Anderson, A. L. 1995, PASP, 107, 450

Schonfelder, V. et al. 1993, ApJS, 86, 657

Schreier, E., Levinson, R., Gursky, H., Kellogg, E., Tananbaum, H., & Giacconi, R. 1972, ApJ, 172, L79

Schwentker, O. 1994, A&A, 286, L47

Scott, D. M., Finger, M. H., Wilson, R. B., Koh, D. T., Prince, T. A., Vaughan, B. A., & Chakrabarty, D. 1997, ApJ, submitted

Scott, D. M., Finger, M. H., Wilson, R. B., & Prince, T. A. 1994, IAU Circ., No. 5990

Scott, D. M., Finger, M. H., Wilson, R. B., Prince, T. A., & Vaughan, B. 1996, IAU Circ., No. 6450

Seaquist, E. R., Krogulec, M., & Taylor, A. R. 1993, ApJ, 410, 260

Seward, F. D., Charles, P. A., & Smale, A. P. 1986, ApJ, 305, 814

Shore, S. N., Livio, M., & van den Heuvel, E. 1994, in Interacting Binaries, ed. H. Nussbaumer & A. Orr., (Berlin: Springer-Verlag)

Skinner, G. K. 1981, Space Sci.Rev., 30, 441

Slettebak, A. 1988, PASP, 100, 770

Soong, Y., Gruber, D. E., Peterson, L. E., & Rothschild, R. E. 1990, ApJ, 348, 634

Standish, E. M., Newhall, X. X., Williams, J. G., & Yeomans, D. K. 1992, in Explanatory Supplement to the Astronomical Almanac, ed. P. K. Seidelmann, (Mill Valley: University Science), 279

Stella, L., White, N. E., Davelaar, J., Parmar, A. N., Blissett, R. J., & van der Klis, M. 1985, ApJ, 288, L45

Stevens, I. R. 1988, MNRAS, 232, 199

Stevens, I. R. & Kallman, T. R. 1990, ApJ, 365, 321

Stier, M. & Liller, W. 1976, ApJ, 206, 257

Stollberg, M. T. et al. 1993a, in Compton Gamma-Ray Observatory, ed. M. Friedlander, N. Gehrels, & D. J. Macomb, (New York:AIP Press), 371

Stollberg, M. T., Finger, M. H., Wilson, R. B., Harmon, B. A., Rubin, B. C., Zhang, N. S., & Fishman, G. J. 1993b, IAU Circ., No. 5836

Stollberg, M. T., Paciesas, W. S., Finger, M. H., Fishman, G. J., Wilson, R. B., Harmon, B. A., & Wilson, C. A. 1994, in The Evolution of X-ray Binaries, ed. S.S. Holt & C.S. Day, (New York; AIP Press), 255

Stollberg, M. T., Wilson, R. B., Finger, M. H., & Prince, T. A. 1996, IAU Circ., No. 6413

Stothers, R. B. & Chin, C. W. 1995, ApJ, 451, L61

Strickman, M. S. et al. 1996, ApJ, 464, L131

Taam, R. E. & Fryxell, B. A. 1989, ApJ, 339, 297

Tamura, K., Tsunemi, H., Kitamoto, S., Hayashida, K., & Nagase, F. 1992, ApJ, 389, 676

Tanaka, Y. 1993, IAU Circ., No. 5851

Tananbaum, H., Gursky, H., Kellogg, E. M., Levinson, R., Schreier, E., & Giacconi, R. 1972, ApJ, 174, L143

Tarter, C. B., Tucker, W. H., & Salpeter, E. E. 1969, ApJ, 156, 943

Tascione, T. F. et al. 1988, Radio Science, 23, 211

Tawara, Y., Yamauchi, S., Awaki, H., Kii, T., Koyama, K., & Nagase, F. 1989, PASJ, 41, 473

Thomas, J. B. 1969, Introduction to Statistical Communication Theory, (New York: Wiley)

Thompson, D. J. et al. 1993, ApJS, 86, 629

Tjemkes, S. A., Zuiderwijk, E. J., & van Paradijs, J. 1986, A&A, 154, 77

van den Heuvel, E. P. J. & Rappaport, S. 1987, in Physics of Be Stars, ed. A. Slettebak & T. P. Snow, (Reidel: Dordrecht), 291

van der Kils, M. 1988, in Timing Neutron Stars, ed. H. Ogelman & E. P. J. van den Heuvel, (Dordrecht: Kluwer Press), 27

van Kerkwijk, M. H., van Paradijs, J., Zuiderwijk, E. J., Hammerschlag-Hensberge, G., Kaper, L., & Sterken, C. 1995, A&A, 303, 483

van Paradijs, J. & Zuiderwijk, E. J. 1977, A&A, 61, L19

Voit, G. M. & Shull, J. M. 1988, ApJ, 331, 197

Wang, Y. M. 1996, ApJ, 465, L111

Wang, Y. M. & Frank, J. 1981, A&A, 93, 255

Waters, L. B. F. M., Demartino, D., Habets, G. M. H. J., & Taylor, A. R. 1989, A & A, 223, 207

Waters, L. B. F. M., Taylor, A. R., van den Heuvel, E. P. J., Habets, G. M. H. J., & Persi, P. 1988, A & A, 198, 200

Waters, L. B. F. M. & van Kerkwijk, M. H. 1989, A & A, 223, 196

Watson, M. G., Warwick, R. S., & Corbet, R. H. D. 1982, MNRAS, 199, 915

Watson, M. G., Warwick, R. S., & Ricketts, M. J. 1981, MNRAS, 195, 197

White, N. E., Mason, K. O., Huckle, H. E., Charles, P. A., & Sanford, P. W. 1976, ApJ, 209, L119

White, N. E., Nagase, F., & Parmar, A. N. 1995, in X–Ray Binaries, ed. W. H. G. Lewin, J. van Paradijs, & E. P. J. van den Heuvel, (Cambridge: Cambridge U. Press), 1

White, N. E., Parkes, G. E., Sanford, P. W., Mason, K. O., & Murdin, P. G. 1978, Nature, 274, 664

White, N. E. & Pravdo, S. H. 1979, ApJ, 233, L121

White, N. E. & Swank, J. H. 1984, ApJ, 287, 856

White, N. E., Swank, J. H., & Holt, S. S. 1983, ApJ, 270, 711

Wilson, C. A. et al. 1995a, IAU Circ., No. 6238

Wilson, C. A., Finger, M. H., Harmon, B. A., Scott, D. M., Wilson, R. B., Bildsten, L., Chakrabarty, D., & Prince, T. A. 1997, ApJ, 479, 388

Wilson, C. A., Strohmayer, T., & Chakrabarty, D. 1996, IAU Circ., No. 6514

Wilson, R. B. et al. 1992, IAU Circ., No. 5454

Wilson, R. B. et al. 1994a, in Second Compton Symposium, ed. C. E. Fichtel, N. Gehrels, & J. P. Norris, (New York: AIP), 390

Wilson, R. B. et al. 1994b, in Evolution of X-ray Binaries, ed. S. S. Holt & C. S. Day, (New York: AIP), 451

Wilson, R. B., Finger, M. H., Pendleton, G. N., Briggs, M., & Bildsten, L. 1994c, in Evolution of X-ray Binaries, ed. S. S. Holt & C. S. Day, (New York: AIP), 475

Wilson, R. B., Finger, M. H., Pendleton, G. N., Briggs, M., & Bildsten, L. 1994d, in Second Compton Symposium, ed. C. E. Fichtel, N. Gehrels, & J. P. Norris, (New York: AIP), 235

Wilson, R. B., Finger, M. H., & Scott, D. M. 1994, IAU Circ., No. 5999

Wilson, R. B., Zhang, S. N., Scott, M., Harmon, B. A., Koh, T., Chakrabarty, D., Vaughan, B., & Prince, T. A. 1995b, IAU Circ., No. 6207

Wray, J. D. 1976. Ph.D. Thesis, Northwestern University

Yi, I., Wheeler, C., & Vishniac, E. T. 1997, ApJ, 481, L51